

**JAERI-Conf  
98-004**



**PROCEEDINGS OF THE FIRST JAERI-KANSAI INTERNATIONAL  
WORKSHOP ON ULTRASHORT-PULSE ULTRAHIGH-POWER LASERS  
AND SIMULATION FOR LASER-PLASMA INTERACTIONS  
JULY 14-18, 1997,  
KYOTO RESEARCH PARK, KYOTO, JAPAN**

**March 1998**

**Kansai Research Establishment**

**29 - 43 日本原子力研究所  
Japan Atomic Energy Research Institute**

本レポートは、日本原子力研究所が不定期に公刊している研究報告書です。

入手の問合わせは、日本原子力研究所研究情報部研究情報課（〒319-1195 茨城県那珂郡東海村）あて、お申し越してください。なお、このほかに財団法人原子力弘済会資料センター（〒319-1195 茨城県那珂郡東海村日本原子力研究所内）で複写による実費頒布をおこなっております。

This report is issued irregularly.

Inquiries about availability of the reports should be addressed to Research Information Division, Department of Intellectual Resources, Japan Atomic Energy Research Institute, Tokai-mura, Naka-gun, Ibaraki-ken, 319-1195, Japan.

© Japan Atomic Energy Research Institute, 1998

編集兼発行 日本原子力研究所  
印 刷 いばらき印刷(株)

**JAERI-Conf 98-004**

*Proceedings of*  
the First JAERI-Kansai International Workshop  
on  
Ultrashort-Pulse Ultrahigh-Power Lasers  
and  
Simulation for Laser-Plasma Interactions

*in*

*Joint ICFA/JAERI-Kansai International Workshop '97*

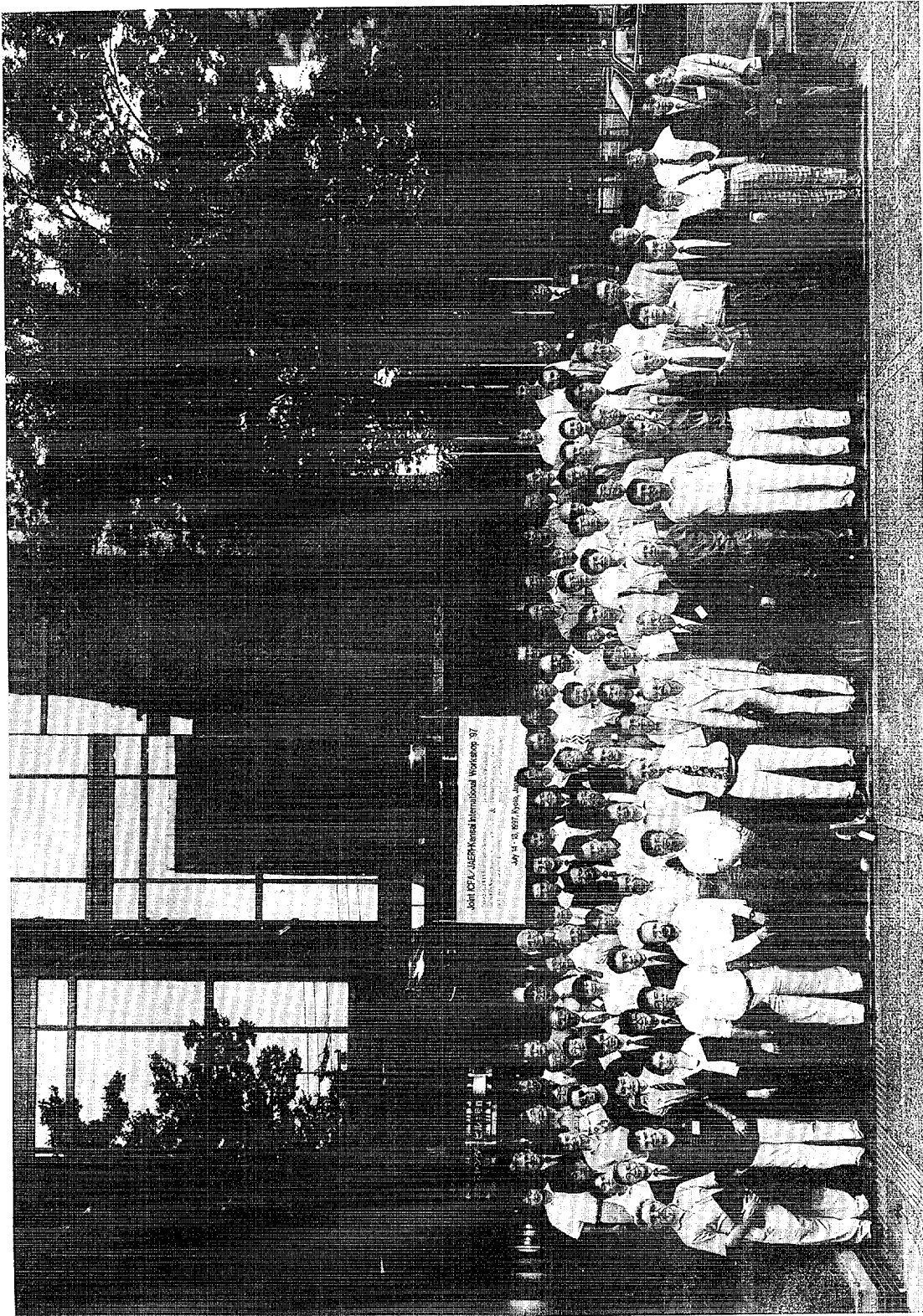
14 to 18 July 1997

Kyoto Research Park

Kyoto, JAPAN

日本原子力研究所

**Japan Atomic Energy Research Institute**



Joint ICFA/JAERI - Kansai International Workshop '97 July 14 - 18, 1997, Kyoto, Japan

Proceedings of the First JAERI-Kansai International Workshop on  
Ultrashort-Pulse Ultrahigh-Power Lasers and Simulation for Laser-Plasma Interactions  
July 14-18, 1997, Kyoto Research Park, Kyoto, Japan

Kansai Research Establishment

Japan Atomic Energy Research Institute  
Higashisiokoji-cho, Simogyo-ku, Kyoto-shi, Kyoto-fu

(Received February 5, 1998)

Records of the First JAERI-Kansai International Workshop, which focused on the subject of "Ultrashort-Pulse Ultrahigh-Power Lasers and Simulation for Laser-Plasma Interactions", are contained in this issue. The First JAERI-Kansai International Workshop was held as Joint ICFA/JAERI-Kansai International Workshop '97 with International Committee for Future Accelerators(ICFA). The number of oral presentations was 27 at the First JAERI-Kansai International Workshop. This report consists of 24 contributed papers.

Keywords: JAERI-Kansai, Ultrashort-Pulse Lasers, Ultrahigh-Power Lasers, Simulation,  
Laser-Plasma Interactions

第1回関西研究所国際ワークショップ論文集

超短パルス、超高出力レーザー

及び

レーザー-プラズマ相互作用のシミュレーション

1997年7月14日～18日、京都リサーチパーク、京都

日本原子力研究所

関西研究所

(1998年2月5日受理)

第1回関西研究所国際ワークショップが「超短パルス、超高出力レーザー及びレーザー-プラズマ相互作用のシミュレーション」のテーマのもとに、1997年7月14日から18日にわたって京都リサーチパークで開催された。本ワークショップは、ICFA (International Committee for Future Accelerators) との合同国際ワークショップ (Joint ICFA/JAERI-Kansai International Workshop '97) として開催された。本論文集は、第1回関西研究所国際ワークショップで講演された27件のうち、論文として投稿された24件を収録している。

## Contents

1. Photon Acceleration Versus Frequency-domain Interferometry for Laser Wakefield	
Diagnostics .....	1
J.M. Dias (Institute Superior Tecnico), L.O. Silva (Institute Superior Tecnico/UCLA) and J.T. Mendonca (Institute Superior Tecnico)	
2. Staged Electron Laser Accelerator (STELLA) Experiment at Brookhaven ATF .....	25
I.V. Pogorelsky, A. van Steenberg, J.C. Gallardo, V. Yakimenko, M. Babzien, K.P. Kusche, J. Skaritka (BNL), W.D. Kimura, D.C. Quimby, K.E. Robinson, S.C. Gottschalk, L.J. Pastwick, L.C. Steinhauser (STI Optronics Inc.), D.B. Cline, Y. Liu, P.He (UCLA), F. Camino, I. Ben-Zvi (SUNY at Stony Brook), R.B. Fiorito, D.W. Rule (NSWC), R.H. Pantell (Stanford Univ.) and J. Sandweiss (Yale Univ.)	
3. Simulation of Intense Laser-Dense Matter Interactions	
- X ray production and Laser absorption - .....	31
Yutaka UESHIMA, Yasuaki KISHIMOTO, Akira SASAKI (JAERI), Yasuhiko SENTOKU (ILE, Osaka Univ.) and Toshiki TAJIMA (JAERI/Univ. of Texas)	
4. Pondermotive Absorption of a Short Intense Laser Pulse in a Non-uniform Plasma .....	37
A.A. Andreev, K.Yu. Platonov (Vavilov State Optical Institute) and K.A. TANAKA (ILE, Osaka Univ.)	
5. Integrated Code Development for Studying Laser Driven Plasmas .....	41
Hideaki TAKABE, Hideo NAGATOMO, Atsusi SUNAHARA, Naofumi OHNISHI, Syuji NARUO and Kunioki MIMA (ILE, Osaka Univ.)	
6. 3d Particle Simulations on Ultra Short Laser Interaction .....	52
Katsunobu NISHIHARA, Takashi OKAMOTO and Hidekazu YASUI (ILE, Osaka Univ.)	
7. Ultra Fast Atomic Process in X-ray Emission by Inner-shell Ionization .....	58
Kengo MORIBAYASHI, Akira SASAKI (JAERI) and Toshiki TAJIMA (JAERI/Univ. of Texas)	
8. Stimulated Raman Backscattering at High Laser Intensities .....	64
Milos M. SKORIC (Vinca Institute), Toshiki TAJIMA, Akira SASAKI (JAERI), Aleksandra MALUCKOV and Moma JOVANOVIC (Univ. of Nis)	
9. Plasma Simulation with the Differential Algebraic Cubic Interpolated Propagation Scheme ....	70
Takayuki UTSUMI (JAERI)	
10. Correlations in a Partially Degenerate Electron Plasma .....	76
Junzo CHIHARA (JAERI)	
11. Time-dependent H-like and He-like Al lines produced by Ultra-short Pulse Laser .....	82
Takako KATO and Masatoshi KATO (NIFS), Ronnie SHEPHERD, Bruce YOUNG, Richard MORE and Al OSTERHELD (LLNL)	

12. Theory and Simulation of Ultra-short Pulse Laser Interactions .....	88
Richard MORE, Rosemary WALLING, Dwight PRICE, Gary GUETHLEIN, Rick STEWART, Steven LIBBY, Frank GRAZIANI and Joann LEVATIN (LLNL)	
13. Modeling of Collisional Excited X-ray Lasers using Short Pulse Laser Pumping .....	96
Akira SASAKI, Kengo MORIBAYASHI, Takayuki UTSUMI and Toshiki TAJIMA (JAERI)	
14. Optical Properties of Cluster Plasma .....	102
Yasuaki KISHIMOTO (JAERI), Toshiki TAJIMA (JAERI/Univ. of Texas) and Mike C. DOWNER (Univ. of Texas)	
15. Array Processors Based on Gaussian Fraction-free Method .....	112
Shietung Peng (Univ. of Aizu), Igor Sedukhin (Hiwada Electronic Corp.) and Stanislav Sedukhin (Univ. of Aizu)	
16. Numerical Simulation of Extremely Chirped Pulse Formation with an Optical Fiber .....	118
Tamitake ITOH, Akihiko NISHIMURA, Kazuyoku TEI, Tohru MATOBA, Hiroshi TAKUMA (JAERI), Mikio YAMASHITA and Ryuji MORITA (Hokkaido Univ.)	
17. Emerging Terawatt Picosecond CO <sub>2</sub> Laser Technology .....	125
I.V. Pogorelsky (BNL)	
18. Next Generation Chirped Pulse Amplification .....	131
John NEES, Subrat BISWAL, Gerard MOUROU (Univ. Michigan), Akihiko NISHIMURA and Hiroshi TAKUMA (JAERI)	
19. Flashlamp Pumped Ti-sapphire Laser for Ytterbium Glass Chirped Pulse Amplification .....	136
Akihiko NISHIMURA, Akira OHZU, Akira SUGIYAMA, Yoichiro MARUYAMA, Takashi ARISAWA, Hiroshi TAKUMA (JAERI), Edward ERICKSON (EEA), Susumu OWADA, Sousuke SATOU (RASEL), John NEES, Subrat BISWAL and Gerard MOUROU (Univ. Michigan)	
20. Efficient Chirped-Pulse Amplification of Sub-20 fs Laser Pulses .....	139
Shinichi MATSUOKA and Koichi YAMAKAWA (JAERI)	
21. Development of Laser Diode-Pumped High Average Power Solid-State Laser for the Pumping of Ti:sapphire CPA System .....	145
Yoichiro MARUYAMA, Kazuyoku TEI, Masaaki KATO, Yoshito NIWA, Sayaka HARAYAMA, Masaki OBA, Tohru MATOBA, Takashi ARISAWA and Hiroshi TAKUMA (JAERI)	
22. Development of All Solid-State, High Average Power Ultra-Short Pulse Laser for X-ray Generation -High Average Power CPA System and Wavefront Control of Ultra Short Laser Pulse- .....	150
Sayaka HARAYAMA, Katsuaki AKAOKA, Kazuyoku TEI, Masaaki KATO, Yoshito NIWA, Yoichiro MARUYAMA, Toru MATOBA, Takashi ARISAWA and Hiroshi TAKUMA (JAERI)	

23. 80-W cw TEM <sub>00</sub> IR Beam Generation by use of a Laser-diode-side-pumped Nd:YAG Rod Laser .....	156
Susumu KONNO, Shuichi FUJIKAWA and Koji YASUI (Advanced Technology R & D Center, Mitsubishi Electric Corporation)	
24. Reliability of Czochralski-grown $\beta$ -BaB <sub>2</sub> O <sub>4</sub> (BBO) Devices .....	162
Nobuhiko UMEZU, Tatsuo FUKUI, Tsutomu OKAMOTO, Hiroyuki WADA, Kouichi TATSUKI, Kenji KONDO and Shigeo KUBOTA (Research Center, Sony Corporation)	
Appendix Program of Joint ICFA/JAERI-Kansai International Workshop '97 .....	168
Author Index .....	184
Keyword Index .....	187

# 1. Photon Acceleration versus Frequency-domain Interferometry for Laser Wakefield Diagnostics

J. M. Dias<sup>1</sup>, L. Oliveira e Silva<sup>1,2</sup>, and J. T. Mendonça<sup>1</sup>

<sup>1</sup>*GoLP/Centro de Física de Plasmas, Instituto Superior Técnico, 1096 Lisboa Codex, Portugal*

<sup>2</sup>*Department of Physics and Astronomy, University of California at Los Angeles,*

*Los Angeles, CA 90095, U.S.A.*

## Abstract

A detailed comparison between the photon acceleration diagnostic technique and the frequency-domain interferometric technique for laser wakefield diagnostics, by using ray-tracing equations is presented here. The dispersion effects on the probe beam and the implications of an arbitrary phase velocity of the plasma wave are discussed for both diagnostic techniques. In the presence of large amplitude plasma wave and long interaction distances significant frequency shifts can be observed. The importance of this effect on the determination of the phase and frequency shifts measurements given by each of the two diagnostic techniques, is also analyzed. The accuracy of both diagnostic techniques is discussed and some of their technical problems are reviewed.

## I. INTRODUCTION

In recent years, there has been great interest in the generation of large amplitude electron plasma waves because of their potential application for particle acceleration. One of the most promising schemes of electron plasma waves production is the laser wakefield accelerator. One of the most important goals of the research in this field is the development of experimental techniques to characterize the plasma wave generated by the laser. The first measurements of the temporal and spatial characteristics of the electron density perturbation in a laser wakefield accelerator, were reported recently. These experiments, carried out by researchers at the École Polytechnique de Paris [1] and at the University of Texas at Austin [2], were based on the measurement of the phase shift suffered by a probe laser pulse in the laser wakefield, using the frequency-domain interferometric technique [3,4].

In parallel, another experiment was performed by our group in collaboration with the Laboratoire de Optique Appliquée in France with the aim of studying the photon acceleration mechanism in the interaction of short laser pulses with relativistic ionization fronts [5]. We were able to obtain an estimate for the velocity of the ionization front and its maximum electron density, clearly pointing out the feasibility of a new diagnostic tool based on the measurement of the frequency-shift suffered by a probe laser pulse interacting with coherent relativistic structures (e.g. laser wakefield) in laser produced plasmas.

In this paper a detailed comparison of this two diagnostic techniques is carried out. A numerical simulation based on the ray tracing equations for the probe laser pulse is employed to calculate the frequency shift due to photon acceleration of the laser pulse co-propagating with the plasma wave. The same simulation also allow us to determine the phase shift of the laser pulse propagating in the laser wakefield relative to another laser pulse which propagates in the unperturbed plasma. Comparing both results we are then able to evaluate the importance of the frequency shift, induced by the plasma wave, on the determination of the phase shift. On the other hand, due to nonlinear effects [6] and 3D effects [7], it is clear that the group velocity of the driving beam, responsible for the wakefield excitation, can

be considerably different from the velocity obtained from the linear dispersion relation in a plasma ( $v_{g\ linear} = c\sqrt{1 - \omega_p^2/\omega^2}$ , where  $\omega_p$  is the plasma frequency and  $\omega$  is the laser pulse frequency). Due to this difference we have analyzed the regimes where the phase velocity of the wakefield is different from the group velocity of the probe pulse (which obeys the linear dispersion relation).

This paper is organized as follows. In Section II, we present the working principles of the two diagnostics, stressing the major technical characteristics of the frequency-domain interferometric technique and pointing out the most important aspects of a photon acceleration diagnostic. In Section III we first present, for the sake of completeness, the ray tracing equations used in the simulations and the calculation of the relative phase shift. The expressions for the wakefield scaling laws are also given and the results of the simulations are presented for several scenarios corresponding to different wakefield time/length scales and phase velocities. Finally, in the last section, we state the conclusions.

## II. DIAGNOSTIC PRINCIPLES

### A. Frequency-domain Interferometry

The objective of this diagnostic technique is to measure the phase shift suffered by a probe laser pulse travelling in a plasma perturbation (laser wakefield), relatively to another unaffected laser pulse (reference pulse). The experimental principle is as follows: An high-intense and ultra-short laser pulse (pump pulse) ionizes a gas at the focal region and excites the electron density perturbation called laser wakefield. A double pulse beam (probe and reference pulses) is focused on the same axis. Co-propagating with the plasma density wave  $n_e(z, t)$  the probe pulse will experience an optical phase shift  $\Delta\phi$  proportional to  $n_e(z, t)$ , while the reference pulse, which precedes the pump pulse, passes the interaction region unperturbed. The relative phase shift between these two probing pulses is then measured by the frequency-domain interferometric technique. The relative position in time of the

three laser pulses (reference, pump and probe) are illustrated in Fig. 1.

The frequency-domain interferometric technique is based on a temporal recombination of the probe and the reference pulses in a spectrometer. The temporal beating creates a system of fringes in the frequency domain. The position of the fringes depends on the relative phase between the two pulses. This phase difference  $\Delta\phi$  can be obtained in a straightforward way from the power spectrum  $I(\omega)$  recorded by the CCD camera or diode-array detector. To extract the phase information from the spectral domain we calculate the inverse Fourier transform of  $I(\omega)$

$$\begin{aligned}\mathcal{F.T.}[I(\omega)] &= \frac{1}{\sqrt{2\pi}} \int_{-\infty}^{\infty} I(\omega) e^{i\omega t} dt \\ &= 2h(t') + e^{i\Delta\phi} h(t' - \Delta t) - e^{-i\Delta\phi} h(t' + \Delta t)\end{aligned}\quad (1)$$

where  $h(t')$  is the inverse Fourier transform of the original probe pulses. Thus, it is clear that the phase information is contained on the sidebands centered at  $t' = \pm\Delta t$ . If  $\Delta t$  is sufficiently large the sidebands are separated from the autocorrelation terms  $h(t')$  at  $t' = 0$  and it is possible to extract a complex-value, that contains the phase information, by calculating the phase angle of  $\mathcal{F.T.}[I(\omega)]$  at the  $t' = \pm\Delta t$  point.

It should be noted that in this diagnostic technique it is normally assumed that the group velocity of the probe pulses and the phase velocity of the plasma wave are identical, i.e.,  $v_{g_{probe}} = v_p$ . So, the probe pulse stays always in phase with the density perturbation sampling only a small portion of the plasma wakefield during its propagation. Let us Consider the case where the laser wakefield is of the periodic form

$$n_e(z, t) = \delta n_e(z) \sin(k_p(z - v_p t)) + n_{e0}\quad (2)$$

where  $v_p$  is the phase velocity and  $k_p$  is the wavenumber of the density perturbation  $\delta n_e$  excited in an homogeneous plasma background  $n_{e0}$ . The maximum measured phase in the frequency-domain interferograms is the integrated phase shift of the probe pulse after passing through the interaction region

$$\Delta\phi = \int_{-\infty}^{\infty} \frac{2\pi}{\lambda_0} [\eta_{probe}(z) - \eta_{ref}(z)] dz\quad (3)$$

where  $\lambda_0$  is the wavelength of the probe and reference pulses. The plasma refractive index seen by the probe pulse  $\eta_{probe}(z) = \sqrt{1 - \frac{\delta n_e(z) + n_{e0}}{n_c}}$  and the plasma refractive index  $\eta_{ref}(z) = \sqrt{1 - \frac{n_{e0}}{n_c}}$  seen by the reference laser pulse are determined by the amplitude of the laser wakefield  $\delta n_e(z)$  and by the unmodulated plasma  $n_{e0}$ , respectively (where  $n_c$  is the critical density for the two laser pulses).

Finally, by sweeping the probe pulse along a period or more of the plasma wave with a time delay line, it is possible to reconstruct the wakefield oscillation with an amplitude given by eq.(3) and a wavelength identical to that of the plasma wave,  $\lambda_p = 2\pi/k_p$ .

At this point it is important to notice that the above description [1,2] of the phase shift, suffered by the probe pulse, leaves out the contribution of the frequency shift of the pulse. The dependence of the group velocity of the probe pulse on the local plasma density  $v_{gprobe}(\delta n_e)$  is also not taken into account.

Apart from these two weaknesses, one of the most important characteristics of this diagnostic technique is its high sensitivity to small density perturbations. This comes from the fact that in this interferometric technique the signal is placed on a carrier (frequency-domain fringes) and uses phase-sensitive lock-in detection in order to avoid stray light, pump leakage and detector defects problems.

## B. Photon acceleration technique

Strictly speaking, photon acceleration was the name initially proposed by Wilks *et al.* [8] to label the frequency shift produced by a wakefield. But it can also be used to describe the frequency shift in other configurations [9]- [11].

Let us consider a plasma wave described by  $\delta n_e = \delta n_{e0} \sin(k_p \zeta)$ , where  $\zeta = z - v_p t$  is the perturbation frame, and assume a low-intensity probe laser pulse centered around  $\zeta = 0$ , with a pulse length  $\sigma_z \ll 2\pi/k_p$ . As we can see by the illustration of Fig.2, the local density at the front of the laser pulse will be less than that at the back of the pulse. Since the phase velocity is proportional to the plasma density, the phase velocity of the pulse at the front

is slower than at the back of the pulse. Hence, the phase peaks at the back move faster than those at the front of the laser pulse (represented here as a wave packet) the wavelength decreases and the frequency increases. For small shifts and considering that the laser pulse stays in phase with the plasma wave ( $v_{g_{probe}} = v_p$ ), the frequency will be up-shifted according to [12]

$$\Delta\omega \simeq \frac{\omega_p^2}{2\omega_0} \frac{\delta n_{e0}}{n_{e0}} \Delta z k_p \cos(k_p \zeta) \quad (4)$$

where  $\omega_p$  is the plasma frequency of the unperturbed plasma,  $\omega_0$  the frequency of the laser pulse, and  $\Delta z$  is the propagation distance.

From eq.(4) we can easily map the plasma wave (i.e., plasma wakefield) by putting the probe laser pulse at different positions of the plasma oscillation  $\zeta$ , like in the frequency-domain interferometry diagnostic technique, described in the previous sub-section. Notice that eq.(4) is only valid for very small frequency shift  $\Delta\omega \ll \omega_0$ . This is usually true for the present laser wakefield experiments, but in future experiments with long propagation distances and large plasma wave amplitudes the frequency shifts can be of the order the frequency of the laser pulse. In this picture a more general theory must be used. Recently, a new approach to describe this phenomenon using the Hamiltonian formulation of photon or ray-tracing equations [11,13] provided a more general description of the photon acceleration mechanism. Generally, the solution of the ray-tracing equations set can only be obtained numerically, but fully analytical results can, however, be achieved for some electron density perturbation like a ionization front. For instance, we can easily calculate the frequency shift which occurs when a wave packet (classical analog of a photon) crosses over an ionization front without reflection [11]

$$\Delta\omega = \frac{\omega_{p0}^2}{2\omega_0} \frac{\beta}{1 \pm \beta} \quad (5)$$

where the initial frequency of the photon, is much higher then maximal frequency of the plasma behind the ionization front, i.e.,  $\omega_0 \gg \omega_{p0}$ . The signs + (respectively, -) pertain to the counter-propagation (respectively, co-propagation) case where the velocity propagation of the ionization front is  $v_p = \beta c$ .

Recent results of an experiment performed by us [5] have shown a very good agreement with this ray-tracing formalism. The results of the frequency up-shift in the co and counter-propagation setups of this experiment allowed us to determine the electron plasma density and the ionization front velocity, by using the 2D version of the eq.(5) [5]. This clearly points to the feasibility of a photon acceleration diagnostic for relativistic coherent structures in laser produced plasmas, based on the measurement of the frequency shift suffered by a ultra-short low-intensity probe laser pulse. It is very important to mention that, in this new description of the frequency-shift diagnostic technique, the assumption  $v_{gprobe} = v_p$  is no longer necessary and the small frequency shifts limitation does not exist.

### III. RAY-TRACING SIMULATIONS

The results presented in this Section are based on the numerical integration of the photon, (short laser pulse) trajectories described by the ray-tracing equations, in presence of a laser wakefield. The pulse length is not considered and the probe pulse is only characterized by its frequency and wavenumber. When the laser pulse propagates in the presence of electron density perturbation, the linear dispersion relation is assumed valid:

$$\omega^2 - k^2 c^2 - \omega_p^2(z - v_p t) = 0 \quad (6)$$

where  $\omega$  is the frequency,  $k$  is the wavenumber and  $\omega_p(z - v_p t)$  is the plasma frequency associated to the density perturbation which propagates with the phase velocity  $v_p$ . This equation (6) is valid in two conditions: i) the electromagnetic wave packet does not disturb the electron density perturbation, and ii) the time scale  $\tau_p$  of the perturbation is much higher than the period of the wave packet, i.e.,  $2\pi/\omega \ll \tau_p$  and the same in spatial scale  $2\pi/k \ll \tau_p v_p$ . These conditions are usually satisfied when the probing is an ultra-short and a low-intensity pulse, with a frequency much higher than the electron plasma frequency. The dispersion relation (6) can be inverted to express the frequency  $\omega$  as a function of the other variables  $k$ , and  $t$ . We can then obtain for the ray-tracing equations:

$$\frac{dz}{dt} = \frac{\partial \omega}{\partial k} = c \sqrt{1 - \frac{\omega_p^2(z, t)}{\omega^2}} \quad (7)$$

$$\frac{dk}{dt} = -\frac{\partial \omega}{\partial z} = -\frac{1}{2\omega} \frac{\partial \omega_p^2(z, t)}{\partial z} \quad (8)$$

These equations allow us to calculate the wavenumber of the probe laser pulse at each point of its trajectory. Knowing the wavenumber we obtain in a straightforward way the frequency shift by applying the dispersion relation (see eq.(6))

$$\Delta\omega(z, t) = \sqrt{k^2(z, t)c^2 + \omega_p^2(z, t)} - \omega_0 \quad (9)$$

where  $k(z, t)$  is the pulse wavenumber and  $\omega_p(z, t)$  is the plasma frequency of the wakefield at a point  $(z, t)$  along the laser pulse trajectory.  $\omega_0$  is the pulse frequency before interacting with the plasma wave. To determine the phase shift suffered by the laser pulse in the wakefield we use the same ray-tracing trajectories

$$\phi_{probe}(z, t) = \int_0^z k(z, t) dz - \int_0^t \omega(z, t) dt \quad (10)$$

where  $k(z, t)$  and  $\omega(z, t)$  are the wavenumber and frequency function along the ray-tracing trajectory. We can then easily determine the accumulated phase shift relative to one pulse propagating in an unmodulated plasma

$$\Delta\phi(z, t) = \phi_{probe}(z, t) - \phi_{ref}(z, t) \quad (11)$$

The phase of the reference pulse can be written in the form

$$\phi_{ref}(z, t) = \int_0^z k_0 - \frac{\omega_0}{v_{gref}} dz \quad (12)$$

where  $k_0$  and  $\omega_0$  are the unchanged wavenumber and frequency of the reference pulse, respectively. The constant group velocity of the reference laser pulse  $v_{gref}$  is given by

$$v_{gref} = \frac{k_0 c^2}{\sqrt{k_0^2 c^2 + \omega_{p0}^2}} = c \sqrt{1 - \frac{\omega_{p0}^2}{\omega^2}} \quad (13)$$

where  $\omega_{p0}$  is the plasma frequency of the homogenous unmodulated plasma.

The numerical simulations were based on the classical fourth-order Runge-Kutta method with a time step of  $dt = 0.1$  fs to integrate the ray-tracing equations (see eq.(7)-(8)). We applied the trivial trapezoidal rule of the Newton-cotes formulas [14] to determine the phase shift integrals,(10) and (12).

A brief description of the laser wakefield scaling laws is shown in the next sub-section. The simulations presented in the others sub-sections are divided in two parts. First, we will discuss the importance of not considering the group velocity of the probe pulse constant and equal to the phase velocity of the wakefield ( $v_{gprobe}(z, t) \neq v_p$ ). The trajectories with large frequency shifts are analyzed in the second part of the numerical results, where the impact of this effect on the two diagnostic techniques is also discussed.

### A. Laser Wakefield Scaling Laws

Here we present the expressions for the laser wakefield excitation in the linear nonrelativistic two-dimensional (2D) regime. Using the solution of the linearized 2D fluid equations given by [15,16], we have in terms of the normalized vector potential  $a_L$  of the pump pulse, the second-order density perturbation

$$\begin{aligned} \frac{\delta n_e}{n_{e0}} = & \frac{a_L^2(\zeta, r)}{2} + k_p \int_{\zeta}^{\infty} \sin [k_p(\zeta - \zeta')] \frac{a_L^2(\zeta, r)}{2} d\zeta' \\ & - \frac{1}{k_p} \int_{\zeta}^{\infty} \sin [k_p(\zeta - \zeta')] \\ & \times \left[ \frac{1}{r} \frac{\partial}{\partial r} r \frac{\partial}{\partial r} \frac{a_L^2(\zeta, r)}{2} \right] d\zeta' \end{aligned} \quad (14)$$

where  $\zeta$  is the longitudinal speed-of-light-frame coordinate  $\zeta = z - v_p t$ . Now assuming that the pump beam is Gaussian in the radial direction and that the longitudinal pulse shape is also Gaussian, we have:

$$a_L^2(\zeta, r) = a_0^2 e^{-(\zeta/\sigma_z)^2} e^{-(r/\sigma_r)^2} \quad (15)$$

Substituting in (14) we can obtain [2]

$$\frac{\delta n_e}{n_{e0}} = \frac{a_0^2}{2} e^{-(r/\sigma_r)^2} \left[ 1 + \frac{4}{(k_p \sigma_r)^2} \left\{ 1 - \left( \frac{r}{\sigma_r} \right)^2 \right\} \right] \times \sqrt{\pi} \left[ k_p \sigma_z e^{-(k_p \sigma_z)^2/4} \right] \sin(k_p \zeta) \quad (16)$$

where  $k_p = \left( \frac{4\pi e^2}{m_e c^2} \right) n_e$  is the wavenumber of the plasma wave.

For better understanding of our calculations, we will work with laboratory-oriented parameters of pump pulse energy  $E_0$ , pulsewidth  $\sigma_z = c\tau/(2\sqrt{\ln 2})$  (where  $\tau$  is the FWHM pulsewidth) and center wavelength  $\lambda_0$ . In terms of these parameters and using the following relations

$$a_0^2 = \frac{I}{\left( \frac{\pi^2 m_e c^2}{2} \frac{1}{r_e/c} \frac{1}{\pi \lambda_0^2} \right)} \quad (17)$$

$$I = \frac{c}{\sqrt{\pi}} \frac{E_0}{\pi \sigma_z \sigma_r^2} \quad (18)$$

where  $r_e$  is the classical electron radius and  $m_e$  its mass, we rewrite (16) as

$$\frac{\delta n_e}{n_{e0}} = \frac{2}{\pi^2 \sqrt{\pi}} \left( \frac{\lambda r_e}{\sigma_r^2} \right)^2 \frac{1}{\sqrt{r_e^3 n_e}} \frac{E_0}{m_e c^2} e^{-(r/\sigma_r)^2} e^{-\pi r_e n_e \sigma_z^2} \times \left\{ \pi r_e n_e \sigma_r^2 + \left[ 1 - \left( \frac{r}{\sigma_r} \right)^2 \right] \right\} \sin(k_p \zeta) \quad (19)$$

For a Gaussian focus,  $\sigma_r$  varies longitudinally as  $\sigma_r^2 = \sigma_{r0}^2 [1 + (z/z_r)^2]$ , where the Rayleigh range is  $z_r = (2\pi/\lambda)\sigma_{r0}^2$ . Of particular interest is the  $n_{e0}$  which maximizes  $\delta n_e$ . For this we use the reduced expression in 2D limit for the resonant density given by [2] ( $n_{res} = 1/2\pi r_e \sigma_z^2$ ).

Finally, the requirement that  $\delta n_e/n_{e0} \leq 1$  in the laser focus, imposes a minimum size to the laser focal spot,  $\sigma_{r0}$ . In our simulations we used this limit to optimize our density perturbation. For simplicity, we have decided to analyze, in all the simulations, only the trajectories at  $r = 0$  and so (19) comes

$$\frac{\delta n_e}{n_{e0}} = \frac{2}{\pi^2 \sqrt{\pi}} \left( \frac{\lambda r_e}{\sigma_r^2} \right)^2 \frac{1}{\sqrt{r_e^3 n_e}} \frac{E_0}{m_e c^2} e^{-\pi r_e n_e \sigma_z^2} \times \left[ \pi r_e n_e \sigma_r^2 + 1 \right] \sin(k_p \zeta) \quad (20)$$

## B. Propagation velocity effects

As it was mentioned in previous Sections, it is currently assumed that the probe laser pulse stays always in phase with plasma wave, i.e.,  $v_{gprobe} = v_p$ . This is not completely true for two reasons: i) the probe group velocity depends on the local electron plasma density  $v_{gprobe}(z, t) = c\sqrt{1 - \omega_p^2(z, t)/\omega}$  at each point of the pulse trajectory (see eq.(7) and (8)); ii) the phase velocity of the wakefield  $v_p$ , which is nearly equal to the group velocity of the pump laser pulse, can be considerably different from the velocity given by linear dispersion relation in a plasma ( $v_{gpump} \neq c\sqrt{1 - \omega_p^2/\omega}$ ), due to nonlinear and 3D effects. These two aspects of the velocity effects in the probe pulse are discussed separately in this Subsection.

For these simulations we have considered typical parameters for the pump laser pulse used in recent laser wakefield experiments [1,2]:  $E_0 = 2.5mJ$ ,  $\tau_{pump} = 100fs$  ( $\sigma_z = 18\mu m$ ) which can be focused down to  $\sigma_{r0} \approx 3.6\mu m$  (for  $\delta n_e/n_{e0} \leq 1$ ) in the 2D resonant plasma density of  $n_{e0} \approx 1.74 \times 10^{17}cm^{-3}$ . Finally, because in this type of experiments the probe pulse is usually a small fraction of the pump beam, we use the same wavelength for both beams  $\lambda_0 = 800nm$ .

In Fig.3(a) and (b) we present the phase and frequency shift of the probe pulse, after interacting with the plasma perturbation, for different time and space delays. These delays enable us to insert the probe pulse at different positions of the laser wakefield and to sample different regions of the plasma wave oscillations. In Fig.3(a) we compare the phase shift obtained for  $v_{gprobe} = v_p$  (dashed curve) with the phase shift considering the probe pulse group velocity as a function of the local density  $v_{gprobe}(\delta n_e(z, t))$  (solid curve). The phase velocity of the plasma perturbation in this case is given by the group velocity of a pump laser pulse in a homogeneous unmodulated plasma density  $n_{e0}$  ( $v_p = c\sqrt{1 - \frac{\omega_{p0}^2}{\omega^2}}$ ). From this figure it is clear that the obtained phase shift oscillation is amplified when we consider that the probe group velocity depends on the local electron plasma density. So the measured phase shift can mislead us in the estimation of the plasma wave amplitude. This can be explained by the fact that in this situation we are comparing the probe pulse phase and the

reference pulse phase at the same spatial point but at different times, due to the difference in their group velocities. On the other hand, the frequency shift [see Fig.3(b)] remains the same in both cases.

Now, let us assume that the phase velocity  $v_p$  of the wakefield is no longer equal by the group velocity of the pump, but is an independent parameter. For  $v_p = 0.9c$  the simulations are shown (solid curves) in Fig.4(a) and (b) for the probe pulse phase and frequency shifts, respectively. Comparing these results with the previous ones (dashed curves), we notice that the wavelength of the phase shift oscillation, as well as the frequency shift oscillation, are enlarged by nearly 12 percent, and that the amplitudes are slightly smaller. So, in this case, the wavelength measured by the probe pulse phase or by the frequency shift will be larger than the wavelength plasma wakefield ( $\lambda_{measured} \approx 1.12\lambda_p$  for  $v_p = 0.9c$ ). To overcome this problem we need an independent measure of the phase velocity of the plasma wakefield, which can be obtain by comparing the frequency shift in co and in counter-propagation, as demonstrated in recent photon acceleration experiments [5].

### C. Large frequency shifts effects

Another assumption, normally taken in the measurements of the laser wakefield, is to consider that the frequency shift suffered by the probe laser pulse is so small that can be neglected for phase shift calculations. This is usually true in the present day experiments, but in the near future it will be possible to excite larger plasmas perturbations with the help of more powerful lasers, and to make them propagate along larger distances [17] which will lead to much larger frequency shifts. To examine the importance of a large frequency shift on the frequency-domain interferometry we have changed the pump laser pulse parameters: we have increased the pulse energy to  $E_0 = 100mJ$  and compressed the pulse duration to  $\tau_{pump} = 30fs$  ( $\sigma_z \approx 5.4\mu m$ ). The new plasma wakefield perturbation obtained from the scaling laws of section III A is  $\delta n_e \approx 1.93 \times 10^{18}cm^{-3}$  in the laser focus ( $\sigma_{r_0} \approx 8.2\mu m$  for  $\delta n_e/n_{e0} \approx 1$ ).

From Fig.5(b) we can see that the frequency shift suffered by the probe pulse is of the same order of its initial frequency. In this simulation, the frequency shift can go up to  $\Delta\lambda \approx 200nm$  for a probe laser wavelength of  $\lambda_0 = 800nm$ , in case of red-shift. Like in the simulations of Fig.3, the frequency shift reaches its positive and negative maximum values when the pulse is positioned in the regions of the strongest negative and positive gradients of the electron density perturbation, respectively. But, in the present situation the maximum up-shift ( $\Delta\lambda_+ \simeq 113nm$ ) is much smaller than the maximum downshift ( $\Delta\lambda_- \simeq 196nm$ ). This nonlinear effect comes from the fact that the frequency shift at each point of the ray-tracing trajectory of the probe pulse is inversely proportional to its frequency (see eq.(8)).

The curves presented in the Fig.5(a) are the phase shifts of the probe pulse given by the eq.(10)-(12) where the frequency shift contribution is taken into account (solid curve) and the phase shifts obtained by neglecting these using (3) (dashed curve). Comparing these two curves we can notice that not only the phase shift oscillations become much stronger, but it also reveals a similar nonlinear behavior, e.g,  $\Delta\phi_- > \Delta\phi_+$ . This can be explained by observing Fig.6.

This is a typical plot of the frequency-shift  $\Delta\lambda$  (solid) and phase-shift  $\Delta\phi$  (dashed) along the probe pulse trajectory through the laser wakefield. From this plot it is visible that the phase shift of the probe pulse does not tend to a constant value, in contrast with the frequency-shift. This is due to the fact that the final frequency of the probe pulse is very different from the reference pulse frequency (which is constant) and the phase difference between these two pulses continuously increases as long as they propagate inside the plasma. So, the consequence of this is that for large frequency-shift, the measured phase shift will be strongly dependent on the plasma length.

This can lead to phase shifts several times larger than  $\pi$ . For instance, in the simulations of Fig.5, where the total propagation distance inside the plasma is  $\Delta z \approx 30z_r$ , the phase shift oscillations reach amplitudes of  $\approx 11\pi$  (peak to peak). This is an additional difficulty for the frequency-domain interferometry diagnostic technique. In fact, to map the wakefield oscillations the time delay step  $\Delta t$ , for this diagnostic technique, must be small enough to enable

us to count all the displaced fringes in the frequency-domain interferograms. Theoretically the upper limit for the time delay step  $\Delta t$  is given by

$$\Delta t \leq \frac{T_p}{4(\Delta\phi_{pp}/\pi)} \quad (21)$$

where  $T_p = \lambda_p/v_p$  is the plasma wave period and  $\Delta\phi_{pp}$  is the expected phase shift oscillation amplitude (peak to peak).

Before the conclusions we should discuss the limits of viability for each of the two diagnostic techniques. In order to illustrate these limits we build up a map representing the pump laser parameters, energy  $E_p$  versus pulse length  $\tau_p$  (see Fig.7). For each set of parameters, the corresponding laser wakefield scaling is obtained for the optimized situation  $\delta n_e/n_{e0} \approx 1$  at the 2D limit for the resonant density, as already discussed in section III A. We will now explain the criteria used to define the limiting curves. The solid curve is given when the frequency shift  $\Delta\omega_{shift}$  measured by the photon acceleration technique equals the spectral width of the probe pulse  $\Delta\omega_{pFWHM}$

$$\Delta\omega_{shift} = \Delta\omega_{pFWHM} \quad (22)$$

Because it is very difficult to measure a frequency shift smaller than the spectral width, this technique is only valid above this curve.

The frequency-domain interferometry technique is limited by the measured phase shift  $\Delta\phi$ , which should stay lower than  $2\pi$ . We have plotted two curves above which this diagnostic technique is not valid: one (dotted curve) considering the phase shift as given by the refraction index  $\Delta\phi_k$  (see eq.(3)) and the other (dashed curve) retaining the contribution of the frequency variation  $\Delta\phi_{k,\omega}$  (see eq. (10)-(12)). In this map we also represent two lines which define the goal of  $100\text{GeV}/m$  for accelerating gradients, already obtained in recent experiments [18]. The lines correspond to the 2D and 1D limits of the resonant density. A close analysis of this map clearly shows that the more favorable diagnostic technique for the future laser wakefield accelerators is photon acceleration .

#### IV. CONCLUSIONS

In this work we have presented a detailed comparison between two different diagnostic techniques for plasma wakefields. Using the ray-tracing equations we were able to analyze the dispersion (group velocity) and frequency-shift effects, that are neglected in the current literature on frequency-domain interferometry, but can be of great importance in the interpretation of future experiments. By simulating the time-delay scanning of the plasma oscillations we were able to identify these effects in both diagnostic techniques.

Our numerical simulations show that, for frequency-domain interferometry, the wakefield oscillation reconstructed from the measured phase shifts is significantly modified in both amplitude and frequency, if we include the dispersion effects in the probe beam and assume that the plasma wave phase velocity is different from the group velocity of the driver laser beam. On the contrary, for the photon acceleration technique, the results are not affected by these dispersion effects and the phase velocity of the laser wakefield can be determined by complementing the co-propagation with the counter-propagation measurements.

We have also considered that for future laser wakefield experiments (with more powerful laser beams which will excite larger plasma waves over longer distances) the frequency shift of the probe beam cannot be considered negligible. In fact, we were able to identify for the first time the non-linear effect of the frequency shift given by the photon acceleration mechanism for both diagnostic techniques. Moreover, we have also studied the influence of a large frequency shift on the phase measurements made with the frequency-domain interferometry. In this case the frequency of the probe pulse is completely different from that of reference one. So the phase difference will depend, not only the plasma length, as we have noticed, but also on the dispersive optics which are in their path before reaching the detector device. This fact added to the complexity of measuring phase shifts much higher than  $\pi$  and the difficulty of using the frequency-domain interferometry of two laser beams with very different frequencies, will be the major drawback of this laser wakefield diagnostic technique. On the other hand, the large frequency shifts play in favor of the photon acceleration diagnostic

technique due to the fact that the external contributions for the of data, such as, stray light, pump leakage and detector defects are no longer a technical problem. For all the reasons discussed above we believe that photon acceleration will become the most powerful diagnostic technique, in future laser wakefield accelerator experiments.

## REFERENCES

- [1] J.R. Marquès *et al*, "Temporal and Spatial Measurements of the Electron Density Perturbation Produced in the Wake of an Ultrashort Laser Pulse," *Phys. Rev. Lett.*, vol. 76, pp. 3566-3569, 1996.
- [2] C.W. Siders *et al*, "Laser Wakefield Excitation and Measurement by Femtosecond Longitudinal Interferometry," *Phys. Rev. Lett.*, vol. 76, pp. 3570-3573, 1996; C.W. Siders *et al*, "Plasma-Based Accelerator Diagnostics Based upon Longitudinal Interferometry with Ultrashort Optical Pulses," *IEEE Trans. Plasma Sci.*, vol. 24, no. 2, pp. 301-315, April 1996.
- [3] E. Tokunaga, A. Terasaki, and T. Kobayashi, "Frequency-domain interferometer for femtosecond time-resolved phase spectroscopy," *Opt. Lett.*, vol. 17, pp. 1131-1133, Aug. 1992; "Femtosecond phase spectroscopy by use of frequency-domain interference," *J. Opt. Soc. Amer. B*, vol. 12, no. 5, pp. 753-771, 1995.
- [4] J.P. Geindre *et al*, "Frequency-domain interferometer for measuring the phase and amplitude of a femtosecond pulse probing a laser-produced plasma," *Opt. Lett.*, vol. 19, pp. 1997-1999, Dec. 1994.
- [5] J.M. Dias *et al*, "Experimental Evidence of Photon Acceleration of Ultrashort Laser Pulses in Relativistic Ionization Fronts," *Phys. Rev. Lett.*, vol. 78, no. 25, pp. 4773-4776, June 1997.
- [6] C.D. Decker and W.B. Mori, "Group velocity of large amplitude electromagnetic waves in a plasma," *Phys. Rev. Lett.*, vol. 72, pp. 490-493, 1994; *Phys. Rev. E*, vol. 51, pp. 1364-1375, 1995.
- [7] E. Esarey, P. Sprangle, M. Pilloff, and J. Krall, "Theory and group velocity of ultrashort, tightly focused laser pulses," *J. Opt. Soc. Amer. B*, vol. 12, pp. 1695-1703, 1995.
- [8] S.C. Wilks *et al*, "Photon accelerator," *Phys. Rev. Lett.*, vol. 62, no. 22, pp. 2600-2603,

1989;

- [9] M. Lampe, E. Ott and J.H. Walker, "Interaction of electromagnetic waves with a moving ionization front," *Phys. Fluids*, vol. 10, pp. 42-54, 1978.
- [10] J.T. Mendonça , "Nonlinear interaction of wavepackets," *J. Plasma Phys.*, vol. 22, pp. 15, April 1979.
- [11] J.T. Mendonça and L. Oliveira e Silva, "Regular and stochastic acceleration of photons," *Phys. Rev. E*, vol. 49, no. 4, pp. 3520-3523, April 1994.
- [12] E. Esarey, A. Ting, and P. Sprangle, "Frequency shifts induced in laser pulses by plasma waves," *Phys. Rev. A*, vol. 42, pp. 3526-3531, 1990.
- [13] L. Oliveira e Silva and J.T. Mendonça, "Photon Acceleration in Superluminous and Accelerated Ionization Fronts," *IEEE Trans. Plasma Sci.*, vol. 24, no. 2, pp. 316-322, April 1996.
- [14] W.H. Press, S.A. Teukolsky, W.T. Vetterling, and B.P. Flannery, "Numerical Recipes in C. The art of scientific computing", Cambridge Univ. Press, 2nd Edition, 1992.
- [15] L.M. Gorbunov and V.I. Kirsanov, "Excitation of plasma waves by an electromagnetic wave packet," *Sov. Phys. JETP*, vol. 66, no. 2, pp. 290-294, Aug. 1987.;
- [16] E. Esarey, A. Ting, P. Sprangle, and G. Joyce, "The laser Wakefield," *Comments Plasma Phys. Controlled Fusion*, vol. 12, no. 4, pp. 192-204, 1989.;
- [17] P. Sprangle, E. Esarey, J. Krall, A. Ting, and G. Joyce, "Propagation and guiding of intense laser pulses in plasmas," *Phys. Rev. Lett.*, vol. 69, pp. 2200-2203, 1993.
- [18] A. Modena *et al*, "Electron acceleration from the breaking of relativistic plasma waves," *Nature*, vol. 337, pp. 606-608, 1995.

## FIGURES

FIG. 1. Schematic visualization of the pump pulse, trailing wakefield, and two probe pulses.

FIG. 2. Schematic of laser pulse frequency upshifting by a plasma wave where  $v_{gprobe} \simeq v_p \simeq c$ .

FIG. 3. Wakefield oscillation map given by the numerical results for phase shift (a) and frequency shift (b) for different space delays, assuming that  $v_{gprobe} = v_p$  (dashed curves) or that probe the pulse group velocity depends on the local plasma density  $v_{gprobe}(\delta n_e(z, t))$  (solid curves). In (b) the dashed curve and the solid overlap.

FIG. 4. Wakefield oscillation map giving the phase shift (a) and the frequency shift (b) for the propagation velocity of the plasma wave of  $v_p = 0.9c$  (solid curves) different from the group velocity of a laser pulse (dashed curves).

FIG. 5. Wakefield oscillation map giving the phase shift (a) and the frequency shift (b) for the new pump laser pulse parameters:  $E_0 = 100mJ$ ,  $\tau_{pump} = 30fs$ . The calculated phase shifts at (a) are obtained by neglecting the frequency shift of the probe pulse (dashed curve) and by retaining it (solid curve).

FIG. 6. Typical plot of the frequency-shift  $\Delta\lambda$  (solid) and phase-shift  $\Delta\phi$  (dashed) at each point of the probe pulse trajectory through the laser wakefield centered at  $z/z_r = 0$ .

FIG. 7. Map of the pump laser pulse parameters (pulse energy versus length). Solid curve defines the limit where the frequency shift is equal the spectral width of the probe pulse (defines the zone where the photon acceleration technique is applicable,  $\Delta\omega_{shift} > \Delta\omega_{pFWHM}$ ). Dashed and dotted curves limit the zone of applicability of the frequency-domain interferometry. The vertical lines indicate the  $100GeV/m$  goal for the future plasma accelerators as predicted by the 2D and 1D scaling laws.

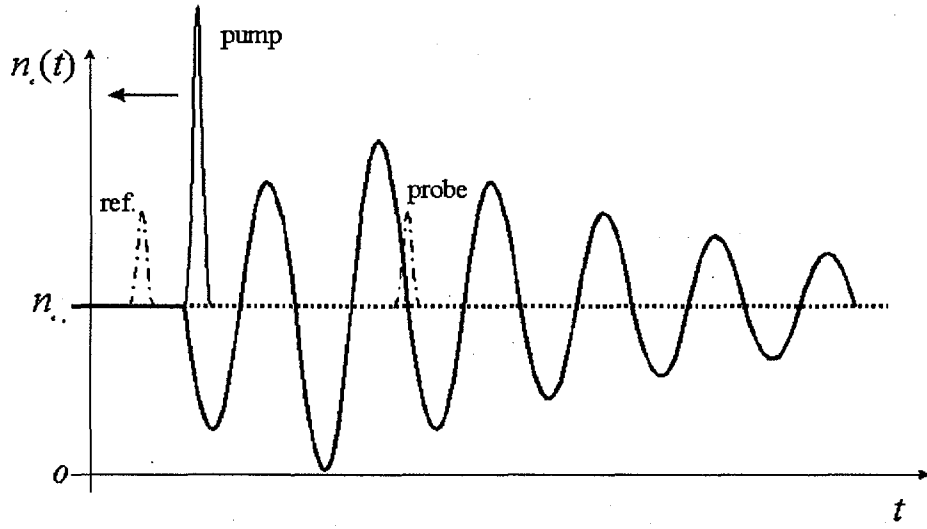


Fig. 1

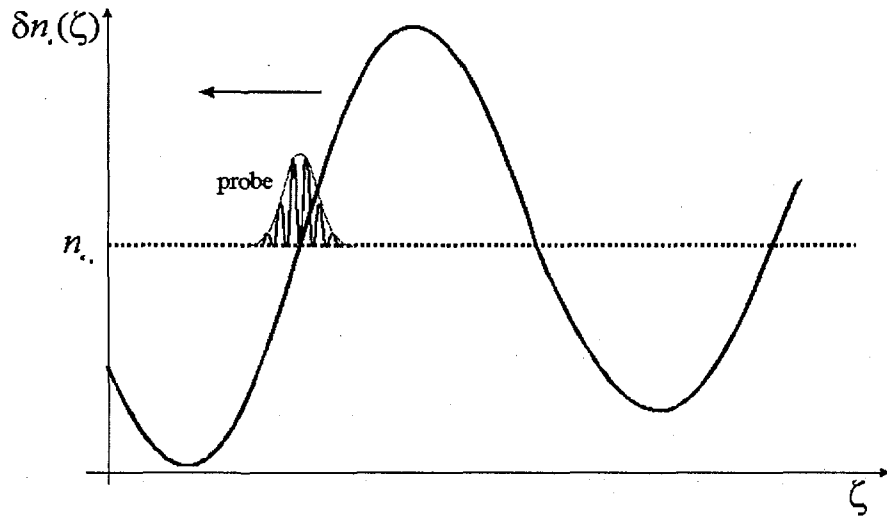


Fig. 2

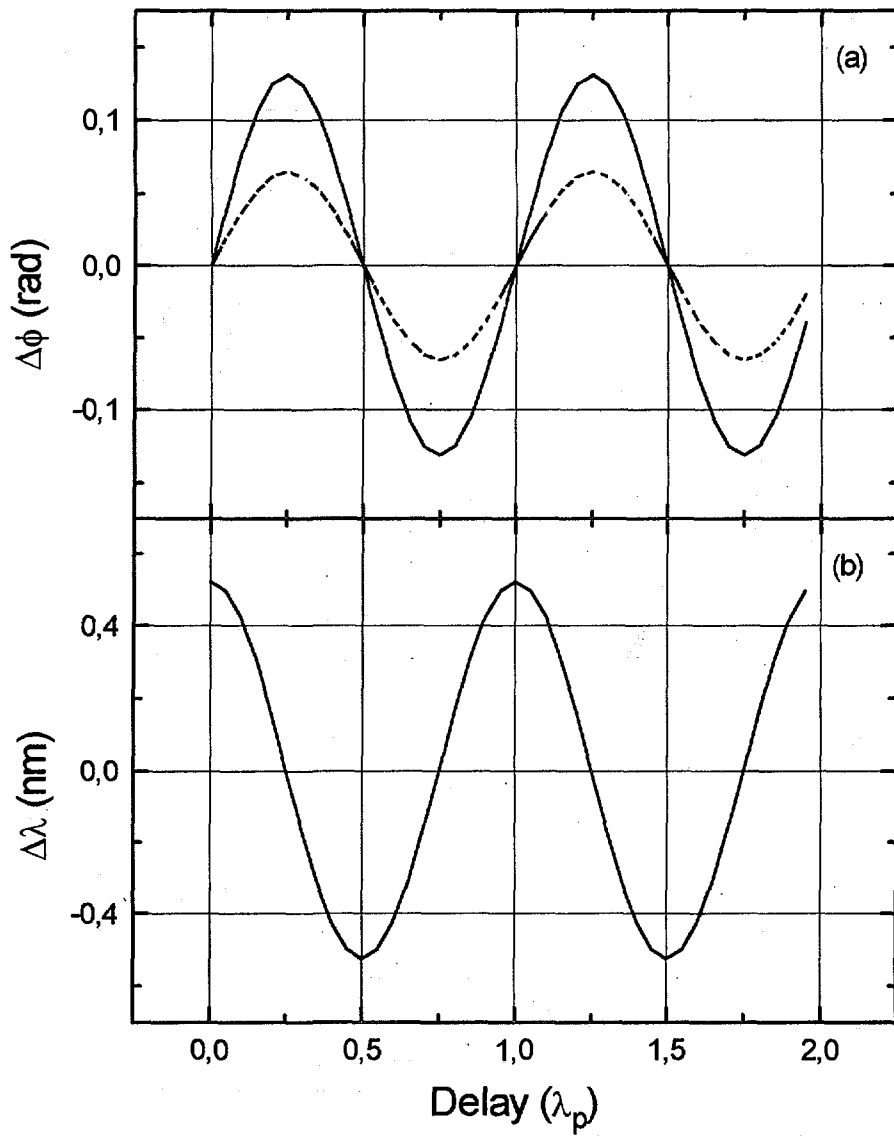


Fig. 3

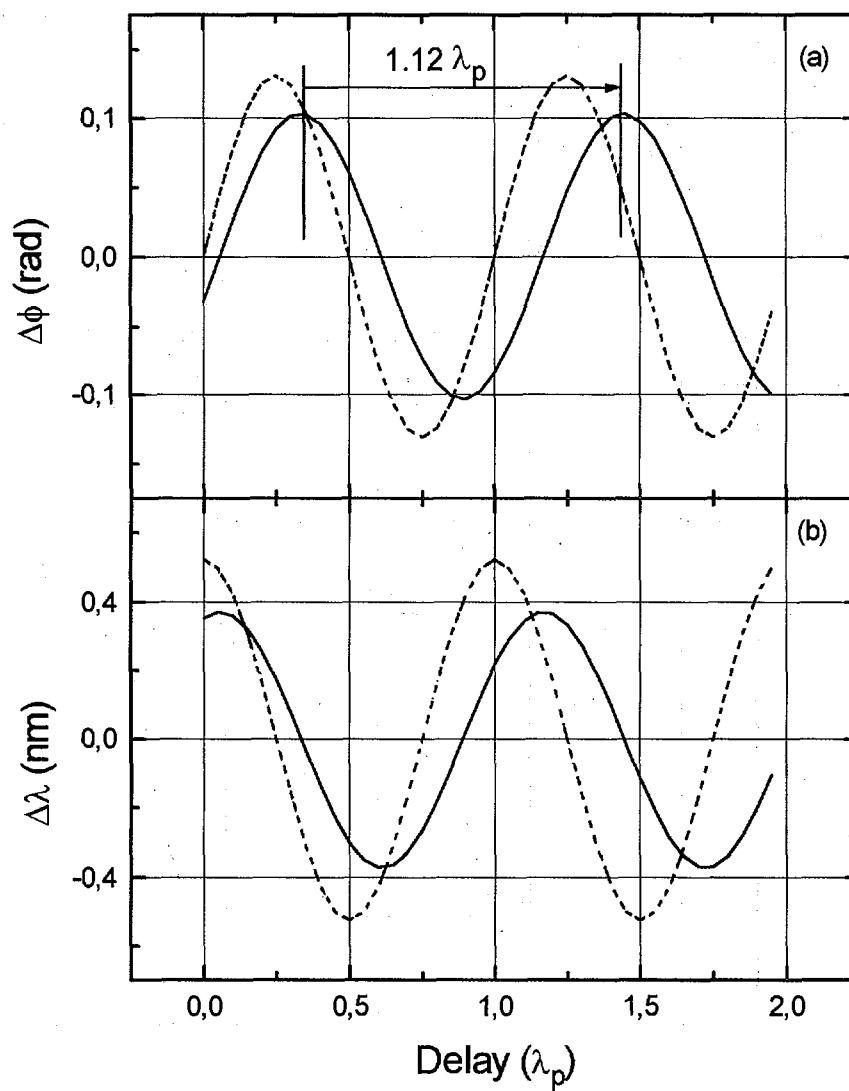


Fig. 4

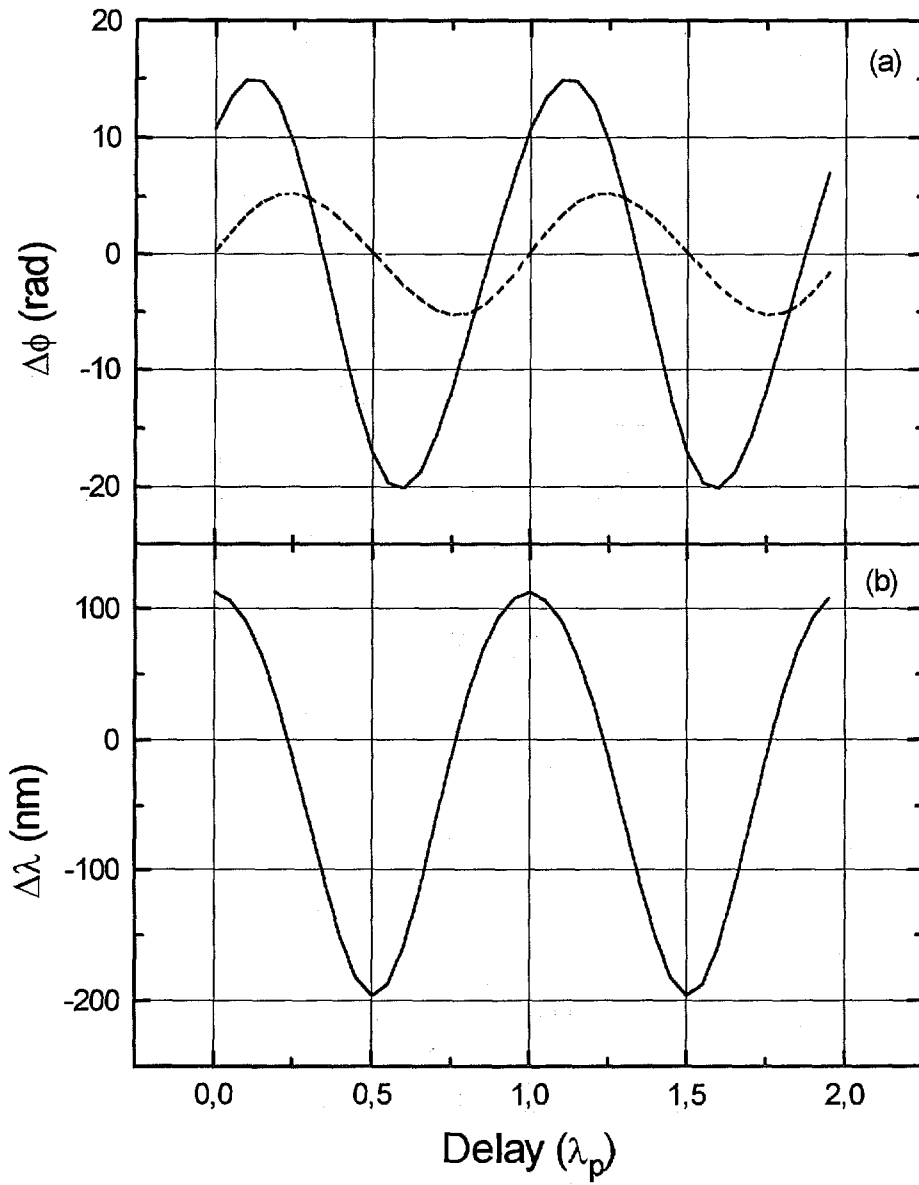


Fig. 5

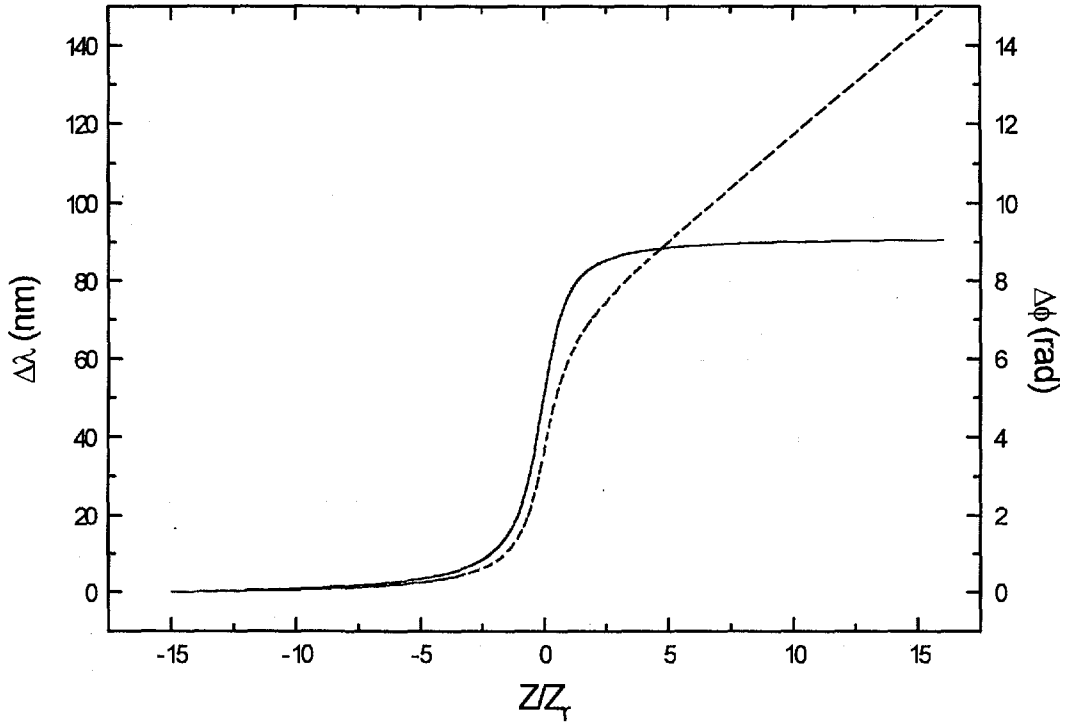


Fig. 6

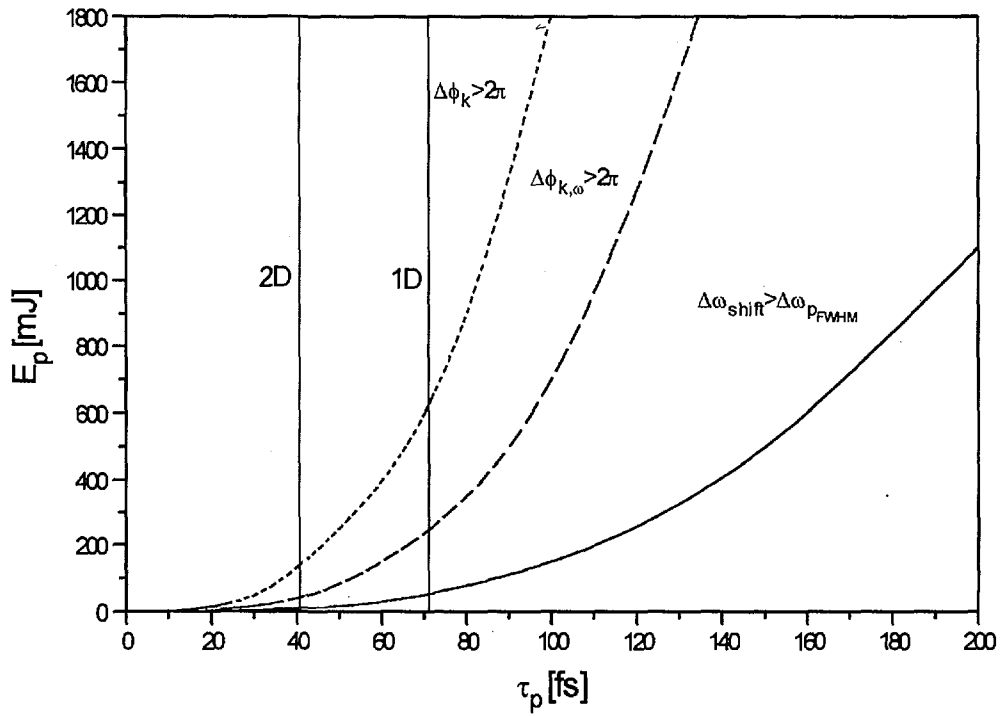


Fig. 7

## 2 . Staged Electron Laser Accelerator (STELLA) Experiment at Brookhaven ATF

I.V. Pogorelsky<sup>\*a</sup>, A. vanSteenbergen<sup>a</sup>, J.C. Gallardo<sup>a</sup>, V. Yakimenko<sup>a</sup>, M. Babzien<sup>a</sup>, K.P. Kusche<sup>a,b</sup>,  
 J. Skaritka<sup>a</sup>, W.D. Kimura<sup>b</sup>, D.C. Quimby<sup>b</sup>, K.E. Robinson<sup>b</sup>, S.C. Gottschalk<sup>b</sup>, L.J. Pastwick<sup>b</sup>,  
 L.C. Steinhauer<sup>b</sup>, D.B. Cline<sup>c</sup>, Y. Liu<sup>c</sup>, P. He<sup>c</sup>, F. Camino<sup>d</sup>, I. Ben-Zvi<sup>d</sup>, R.B. Fiorito<sup>e</sup>, D. W. Rule<sup>e</sup>, R.H.  
 Pantell<sup>f</sup>, and J. Sandweiss<sup>g</sup>

a - Brookhaven National Laboratory, b - STI Optronics Inc., c - UCLA, d - SUNY at Stony Brook,  
 e - Naval Surface Warfare Center, f - Stanford University, g - Yale University

**Abstract.** The STELLA experiment is being prepared at the BNL Accelerator Test Facility (ATF). The goal of the experiment is to demonstrate quasi-monochromatic inverse Cherenkov acceleration (ICA) of electrons bunched to the laser wavelength period. Microbunches on the order of 2  $\mu\text{m}$  in length separated by 10.6  $\mu\text{m}$  will be produced using an inverse free electron laser (IFEL) accelerator driven by a CO<sub>2</sub> laser. The design and simulations for two phases of this experiment including demonstration of 10 MeV and 100 MeV acceleration are presented.

### 1. INTRODUCTION

The STELLA experiment is a program to demonstrate inverse Cherenkov acceleration of microbunches produced during the IFEL acceleration process. Generation of microbunches much shorter than the oscillating driver field period is a prerequisite for producing highly monochromatic, low emittance electron beams in accelerators. This problem has not been addressed yet for laser linac schemes, such as ICA [1] or IFEL [2], driven at optical or IR frequencies, which are at least 10,000 times faster than conventional RF linac fields. Note also that generation of femtosecond electron bunches, which will be accomplished during the STELLA program, has potential applications beyond laser acceleration. For example, via Compton scattering such bunches may enable generation of extremely short duration x-ray pulses over a wide spectral range which can be used in many different applications.

The STELLA experiment is a natural merge of the two ICA and IFEL laser acceleration experimental programs which have been conducted at the ATF for several years. Both ICA and IFEL are driven by the ATF high-power CO<sub>2</sub> laser and use the high-brightness 50-MeV, 10-ps electron beam produced by the RF linac. The ICA program has essentially completed its major objectives demonstrating energy modulation using the Fontana-Pantell radially-polarized, axicon-focused laser beam geometry [3]. In this experiment the electrons interacted over all phases of the light wave resulting in both accelerated and decelerated particles. To achieve high acceleration of a significant proportion of electrons requires prebunching them to the laser wavelength period and then resonance interaction with the laser EM wave in the ICA cell. Meeting this demand, the ATF IFEL experiment has recently demonstrated microbunch generation, which has been detected using a coherent transition radiation diagnostic [4].

In this paper we discuss the design and simulations for two phases of the STELLA experiment including demonstration of 10 MeV and 100 MeV acceleration.

### 2. STELLA DESIGN

The principal diagram in Fig.1 illustrates the layout of the STELLA experiment which is located at the end of the ATF electron beamline #1. Quadrupoles not shown on the drawing focus the e-beam through a 3 mm diameter hole in a metal mirror used to direct the laser beam into the IFEL waveguide. Triplet #1 refocuses the e-beam inside the IFEL. The ICA cell is separated from the exit of the IFEL by a 190-cm

- Contact author: BNL, 725C, Upton, NY 11973; fax: (516) 344-5801; pogore@bnlarm.bnl.gov

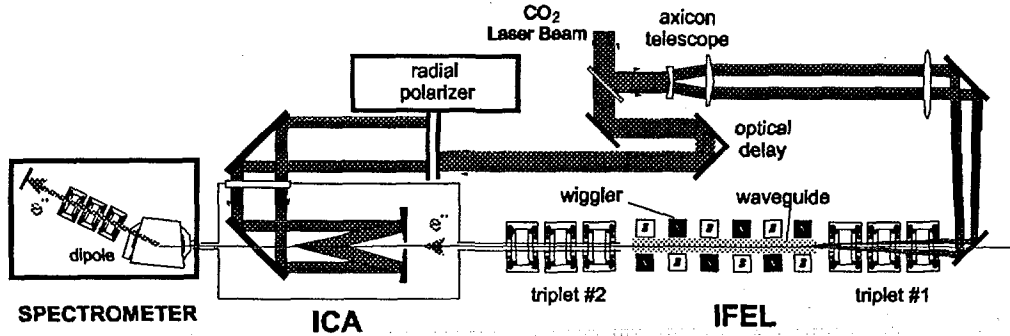


FIGURE 1. Principal diagram of STELLA experiment

TABLE 1. STELLA design parameters

PARAMETER	VALUE
<b>Initial e-Beam Parameters</b>	
Energy	50 MeV
Energy spread	±0.15%
Normalized emittance	0.5 mm-mrad
<b>IFEL and Drift Space</b>	
Laser power	5 MW
Wiggler Length	47 cm
Wiggler period	3.33 cm
Wiggler gap	4 mm
Peak field	1 T
Waveguide	60cm×2.8mm
Energy modulation	1.2%
Drift distance	190 cm
Bunch length	~1 μm
<b>ICA</b>	
Laser power	10 GW
Cherenkov angle	20 mrad
Interaction length	6.5 cm
Hydrogen pressure	1.7 atm
Net acceleration	10 MeV
Output energy spread	±1 MeV

drift space. In between there is Triplet #2 which refocuses the e-beam into the ICA cell. To satisfy the phase matching Cherenkov condition, the ICA cell is filled with ~1.7 atm of hydrogen gas. It is separated from the vacuum beamline by 1-μm thick diamond windows for transmission of the 50-MeV electron beam. After interacting with the laser beam inside the ICA cell, the e-beam leaves to the spectrometer.

The CO<sub>2</sub> laser beam will be divided into two beams using a beamsplitter. A relatively small amount of laser power will be sent to the IFEL in order to modulate the energy just enough so that the peak bunching occurs at the end of the drift region at the entrance to the ICA stage. To avoid striking the central hole for the e-beam in the mirror which introduces the laser beam into the IFEL, the laser beam will be annular in shape. To create this shape, the laser beam will be sent through an axicon telescope.

A sapphire tube with 60-cm length and 2.8-mm ID is used to channel the laser energy through the IFEL wiggler with an attenuation factor of 0.2 dB/m. Approximately 90% coupling of the laser energy into the HE<sub>11</sub> mode inside the waveguide has been synthesized.

Due to the location of various devices it will be necessary to delay the ICA laser beam with respect to the IFEL laser beam. This delay will utilize an optical trombone and will also be used to fine tune the phase between the two laser pulses sent to the IFEL and ICA cell.

After passing through a radial polarization converter optical system, the annular shaped laser beam is introduced into the ICA gas cell and focused by an axicon mirror along the e-beam axis. Self-interference of the axicon-focused radially polarized laser beam results in Bessel distributions for the longitudinal (accelerating) and radial (focusing) components of the electric field as is shown in Fig.2. The focusing field described by the J<sub>1</sub> distribution is 90° out of phase with the accelerating field described by the J<sub>0</sub> function.

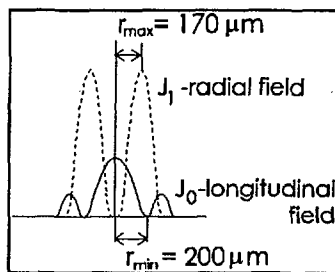


FIGURE 2. Electric field components in axicon-focused laser beam

To ensure efficient and monochromatic acceleration, the e-beam must be focused to a smaller radius than the width of the central lobe of the  $J_0$  Bessel pattern. For a 20-mrad Cherenkov angle, this lobe has a FWHM of  $\sim 200 \mu\text{m}$ . The first zero at the  $J_0$  Bessel distribution also occurs at a radius of  $200 \mu\text{m}$ .

Design parameters for the first phase of the STELLA experiment when the 10-GW  $\text{CO}_2$  laser beam will be used are summarized in Table 1. This table also includes results of simulations which are discussed in Section 3. During the second phase of the experiment, which will start after the ATF  $\text{CO}_2$  laser is upgraded to  $\sim 1$  TW peak power [5], 100-MeV monochromatic acceleration will be attempted.

### 3. MODEL PREDICTIONS

An integrated model of the STELLA experiment has been developed which combines existing IFEL and ICA codes, and utilizes a ray-tracing method along with the TRANSPORT code for simulating the electron trajectory through the focusing triplet. For a given wiggler configuration (i.e., spacing and magnetic field strength), e-beam energy, and laser wavelength, the optimum bunching distance for the IFEL is controlled by the amount of energy modulation imparted by the laser beam. Our analysis shows that a wiggler length of 0.47 m and uniform period of 3.3 cm enables suitable bunching performance over an input energy range of 40-65 MeV. The laser driver requirements are quite modest. For an  $\sim 2$ -m bunching distance, the laser power scales approximately as  $5 \text{ MW}(E/50 \text{ MeV})$ , where  $E$  is the energy of the e-beam in MeV. The initial energy spread must be much less than the induced energy spread, which needs to be approximately  $\Delta\gamma/\gamma = 1.2\%(E/50 \text{ MeV})$ .

Figure 3 shows the e-beam energy-phase diagrams calculated for an incoming emittance  $\varepsilon_n = 0.5$  mm-mrad and intrinsic energy spread of  $\Delta\gamma/\gamma = 0.15\%$ . The e-beam enters the IFEL uniformly distributed over phase and longitudinal space [Fig.3(a)]. At the exit of the IFEL the e-beam has a sinusoidal energy modulation of 1.2% ( $\pm 0.3$  MeV) [Fig.3(b)] and very little bunching has occurred yet. At the end of the drift region just before the entrance to the ICA cell, the more energetic electrons catch up with the slow ones resulting in the formation of a microbunch [Fig.3(c),(d)]. The FWHM of the bunch is  $0.63 \mu\text{m}$ . Some bunch smearing caused by the emittance, initial energy spread, and path length difference through the focusing triplet between the IFEL and the ICA cell can be seen. Indeed, electrons leaving the IFEL wiggler will take different paths as they are focused by the quadrupole magnets into the ICA cell. This results in bunch smearing that is illustrated by Fig. 4 assuming more conservative numbers for the normalized emittance  $\varepsilon_n$  and the intrinsic energy spread  $\Delta\gamma/\gamma$  than those entered in Table 1. We see that to avoid significant bunch smearing we should choose  $\varepsilon_n < 2$  mm-mrad and  $\Delta\gamma/\gamma < 0.25\%$  FWHM. Fortunately, an e-beam with such parameters is routinely produced by the ATF linac.

The results of Monte-Carlo computer simulations for short electron bunch acceleration in the ICA cell induced by the 10-GW laser pulse are illustrated in Fig.5. Figure 5(a),(b) show the e-beam expansion due to e-beam focusing into the gas cell, emittance, and gas and window scattering. From Fig. 5(c) we see how the amount of energy gain depends upon the radial position of the electrons within the e-beam profile. Electrons farther out from the center do not experience the peak laser field and, therefore, do not gain or lose the maximum possible amount of energy. However, most of the electrons are still grouped in a fairly tight bunch and gain up to 10 MeV energy. Over the 6.5-cm interaction distance this corresponds to  $>150$  MeV/m acceleration gradient for only 10-GW laser power. The FWHM width of the accelerated electron energy peak shown in Fig. 5(d) is 2.2 MeV and contains  $\sim 50\%$  of all the electrons.

The ATF  $\text{CO}_2$  laser is presently being upgraded to  $\sim 1$  TW peak power. Before presenting simulations for the STELLA performance for the high-power situation, the following comments need to be made.

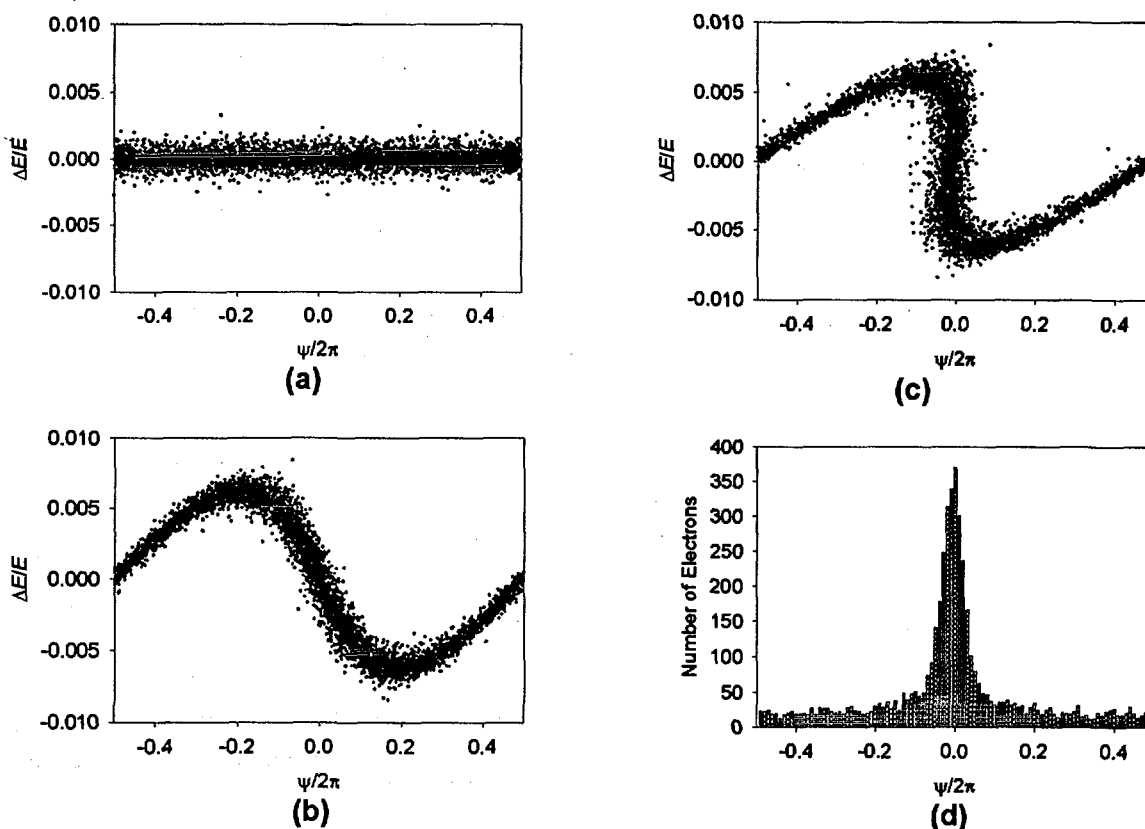


**FIGURE 3.** Simulations of electron beam bunching at  $\Delta E/E=1.2\%$  energy modulation in IFEL wiggler: a) initial uniform energy distribution; b) energy modulation at the wiggler exit; c) energy distribution at the entrance to the ICA cell; d) longitudinal density distribution in which 50% of the electrons are bunched into FWHM=0.63  $\mu\text{m}$ .

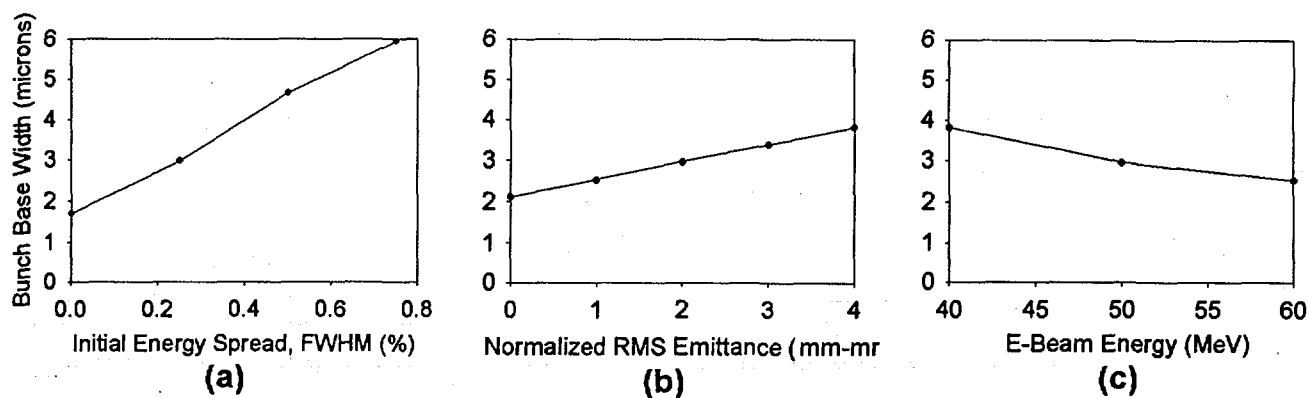


**FIGURE 4.** Micro-bunch smearing dependence upon the e-beam parameters: a) effect of the initial energy spread @  $\varepsilon_n=2$  mm-mrad,  $E=50$  MeV; b) effect of initial emittance @  $\Delta\gamma/\gamma=0.25\%$  FWHM,  $E=50$  MeV; c) effect of input electron energy @  $\varepsilon_n=2$  mm-mrad,  $\Delta\gamma/\gamma=0.25\%$  FWHM

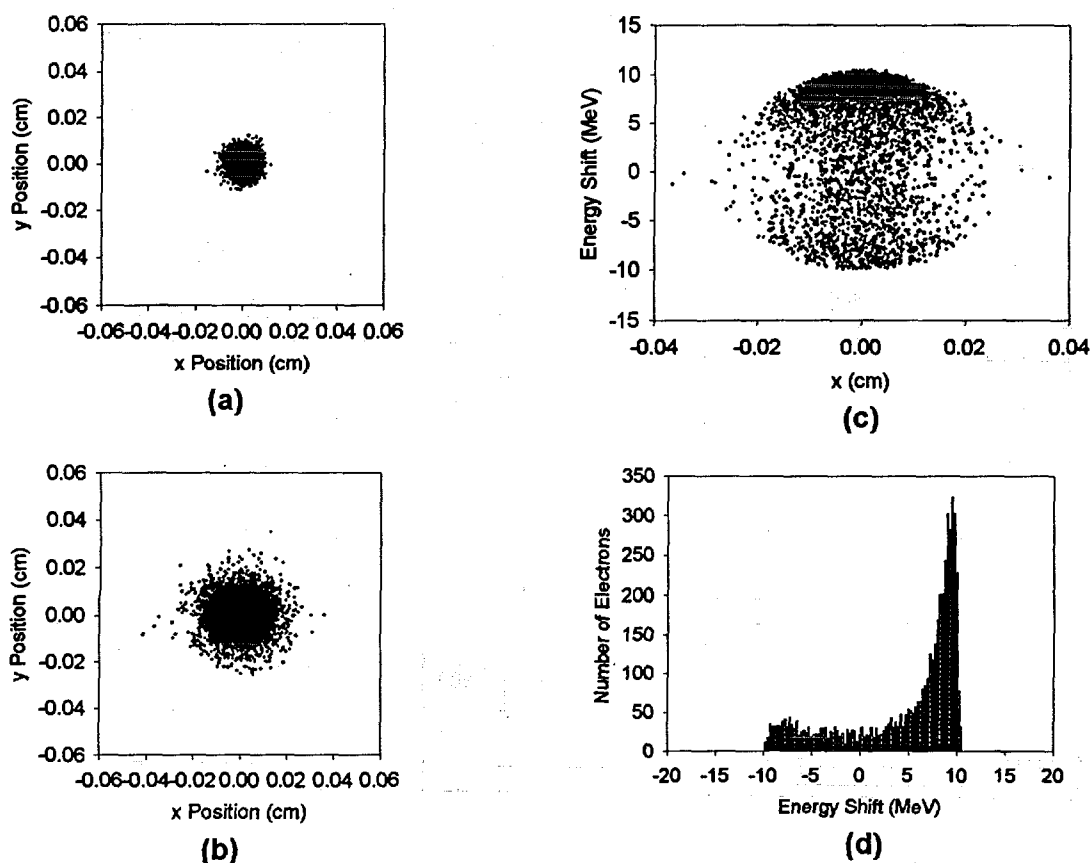


FIGURE 5. Simulations for electron bunch [see Fig.2(d)] acceleration in ICA cell at  $P_L=10$  GW: a) e-beam spot size at axicon; b) e-beam spot size exiting ICA interaction cell; c) radial energy distribution; d) electron energy spectrum

For relatively low- $\gamma$  e-beams such as the ATF, significant phase slippage occurs within the interaction region at high laser powers. A possible way to compensate for this effect is to introduce a curved wavefront to the axicon-focused laser beam which causes the laser beam to intersect the e-beam along the interaction region at different angles.

Second, at high laser power the issue of gas breakdown becomes more important. For Gaussian shaped laser pulses the upper limit to the maximum acceleration gradient is calculated to be  $\sim 650$  MeV/m.

Third, to handle the high peak power the laser beam size on the axicon must be increased. For a 1-TW laser beam (i.e., 3 J in 3 ps) and a  $5\text{-J/cm}^2$  damage fluence, this gives a minimum laser beam diameter on the axicon of 9 mm. For a 20-mrad Cherenkov angle and 1-mm diameter annulus hole, this yields an interaction length of 19.4 cm. For these conditions the maximum acceleration gradient is again  $\sim 650$  MeV/m. Hence, this 1-TW design is consistent with regard to avoiding optical damage and gas breakdown.

An energy gain of  $\sim 125$  MeV for a 50-MeV e-beam is predicted (see Fig.6). The energy spread of the accelerated bunch is just 6 MeV FWHM. The length of the microbunch is  $<1$   $\mu\text{m}$ . For this simulation we selected the laser and electron bunch phasing not to be at the maximum energy gain, but at the point where partial laser focusing begins to occur. This focusing effect can be clearly seen in the beam profile plot after

the interaction [Fig.5(b)]. Figure 5(c) also shows that most of the accelerated electrons are confined within the central portion of the beam. Thus, this 1-TW example shows the promise of >100-MeV net energy gains with well-controlled e-beam monochromaticity and emittance. The overall performance should improve by using a curved axicon. This capability will be added to the STELLA simulation program.

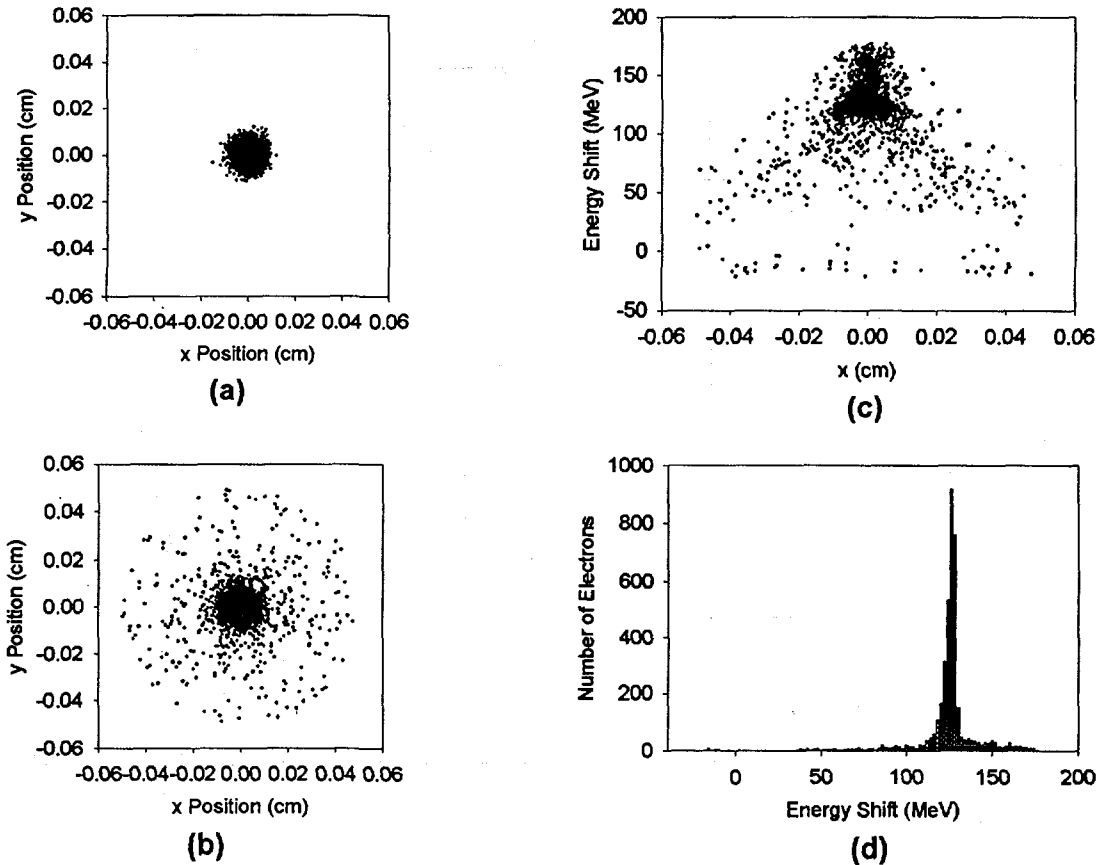


FIGURE 6. Simulations for electron bunch [see Fig.2(d)] acceleration over 19.4-cm ICA interaction length at  $P_L=1$  TW: a) e-beam spot size at axicon; b) e-beam spot size exiting ICA interaction cell (shows focusing); c) radial energy distribution (shows focusing); d) electron spectrum

#### REFERENCES

1. W.D. Kimura, et al. *Phys. Rev. Lett.*, **74**, 546 (1995).
2. A. van Steenbergen, et al., *Phys. Rev. Lett.*, **77**, 2690 (1996).
3. J.R. Fontana & R.H. Pantell, *J. Appl. Phys.*, **54**, 4285 (1983)
4. Y. Liu, et al., "Experimental Observation of IFEL Micro-Bunching Using Coherent Transition Radiation", *Particle Accelerator Conference, Vancouver, Canada, May 12-16, 1997*, to be published.
5. I.V. Pogorelsky, et al., "The First Terawatt Picosecond CO<sub>2</sub> Laser for Advanced Accelerator Study at the Brookhaven ATF", *Proceedings of 7<sup>th</sup> Advanced Accelerator Concepts Workshop, Lake Tahoe, CA, October 12-18, 1996*, to be published.

### 3. Simulation of Intense Laser - Dense Matter Interactions - X ray production and Laser absorption -

*Yutaka UESHIMA, Yasuaki KISHIMOTO, Akira SASAKI, Yasuhiko SENTOKU\*  
and Toshiki TAJIMA\*\**

*Kansai Research Establishment, Japan Atomic Energy Research Institute,  
2-6 Mii-mimami, Neyagawa, Osaka 562, Japan*

*\*Institute of Laser Engineering, University of Osaka, 2-6 Yamadaoka,  
Suita 565, Japan*

*\*\* also Fusion Studies, University of Texas at Austin, Austin, Texas 78712 U.S.A.*

#### ABSTRACT

The development of short-pulse ultra high intensity lasers will enable us to generate short-pulse intense soft and hard X-rays. Acceleration of an electron in laser field generates intense illuminated located radiation, Larmor radiation, around KeV at  $10^{18}$  W/cm<sup>2</sup> with 100TW and 1 $\mu$ m wave length laser. The Coulomb interaction between rest ions and relativistic electron generates broad energy radiation, bremsstrahlung emission, over MeV at  $10^{18}$  W/cm<sup>2</sup> with the same condition. These intense radiations come in short pulses of the same order as that of the irradiated laser. The generated intense X-rays, Larmor and bremsstrahlung radiation, can be applied to sources of short pulse X-ray, excitation source of inner-shell X-ray laser, positron production and nuclear excitation, etc.

**Keywords:** short-pulse ultra high intensity laser, Larmor radiation, bremsstrahlung emission, short-pulse intense X-ray, inner-shell X-ray laser

#### 1. INTRODUCTION

The development of short-pulse ultra high intensity lasers has opened new regime in the study of laser - plasma interaction. Recently, there has been a great deal of research devoted to generation higher harmonics and X-ray by ultra high intensity lasers. For example, D. von der Linde et al. [1] reported that the 15th higher harmonics was generated by CO<sub>2</sub> laser at  $10^{17}$  W/cm<sup>2</sup> with dielectric and metallic solid surface; J. J. Macklin et al. [2] observed that Ne gas excited by Ti: sapphire laser at  $10^{15}$  W/cm<sup>2</sup> generated harmonics up to the 109th order; P. Gibbon [3] investigated that the 60th harmonics reflected from solid-density plasma surface at  $I\lambda^2 > 10^{19}$  W/cm<sup>2</sup> with power efficiencies  $> 10^{-6}$ ; T. D. Donnelly et al. [4] observed that short-pulse high intensity laser (825nm,  $10^{15}$  W/cm<sup>2</sup>) interaction with Ar clusters were produced a higher harmonics and intensity as compared with monomer gases; S. Kato et al. [5] estimated with the use of a dynamical form factor

for a dense plasma that higher harmonics was generated by an oscillating current due to intense laser field.; S. Huller et al. [6] indicated that higher harmonics dependent on lattice period was generated with crystal targets; J. D. Kmetec et al. [7] reported that hard-X-ray was generated forward with metal in the experiments; B. N. Chichkov et al. [8] evaluated relativistic momentum distribution function for electron under the intense laser and bremsstrahlung emission from calculated momentum distribution function.

This proceeding reported the generation of intense-X-ray radiation by short-pulse ultra high intensity interaction with dense matters. Mainly, the following 2 type radiation processes are paid attention. The first is Larmor radiation from acceleration of an electron by intense laser field. The radiation has a character that its energy spectra is located around KeV at  $10^{20}$  W/cm<sup>2</sup> with 1 $\mu$ m laser wave length. The second is bremsstrahlung emission from the Coulomb interaction between rest ions and relativistic electron by intense laser field. The emission has broad energy spectra over MeV at  $10^{20}$  W/cm<sup>2</sup> with 1 $\mu$ m laser wave length. These intense radiations are short pulse length of the same order as that of the irradiated laser. The generated intense X-rays, Larmor and bremsstrahlung radiation, will be applied for source of short pulse X-ray, excitation source of inner-shell X-ray laser, positron production and nucleus excitation, etc.

In JAERI's laser system, it was achieved that the pulse time was less than 20 femtosecond and the peak power was more stronger than 10TW with 880nm laser wave length. Until this year, the peak power will reach 100TW. When the focused spot size of laser is 10  $\mu$ m, the laser intensity achieves  $10^{21}$  W/cm<sup>2</sup>. The interaction of this laser with electrons has interesting matters as follows. Under the action of a short pulse laser, there is not enough time to thermalize the electrons. This means that the electrons are very cool and laser - plasma interaction is very pure, in other words, all kind of phenomena are independent of temperature of electron. The pure interaction may also produce collective motion of electrons and then many kinds of phenomena with the electrons are coherent. At ultra high intensities, motion of an electron becomes relativistic. The electron quivers and drifts in the polarization and the propagation of the laser directions with the same order as photon speed. Since a orbit of the electron forms closed 8-figure in the drift frame, the motion of the electron is called for the 8-figure motion. This longitudinal acceleration in the propagation of the laser direction makes intensity of Larmor radiation higher than that for non-relativistic quivering motion. Enhancement of intensity and blue shift of wave length for Larmor and bremsstrahlung radiations are caused by Doppler effect from the relativistic drift velocity.

## 2. 8-FIGURE MOTION & CHARACTERISTIC PARAMETERS

As described before the section, laser - plasma interaction is very pure in the ultra intense laser. From the fact, the number of characteristic parameters is reduced. The non-dimensional laser strength parameter is as follows:

$$a_0 \equiv \frac{eE_0}{m_e c \omega_L}, \quad (1)$$

where  $e$ ,  $m_e$ ,  $c$ ,  $E_0$  and  $\omega_L$  represent elemental charge, rest mass of an electron, speed of light, maximum strength of electric field and frequency of laser, respectively. This non-dimensional parameter  $a_0$  can be regarded as the gained momentum of electron normalized by  $m_e c$  during a period of laser. Accordingly, for  $a_0 > 1$ , motion of the electron becomes relativistic. In terms of the laser intensity  $I$ , the quantity  $a_0$  is given by

$$a_0 = 0.85 \left( \frac{\lambda_L}{1 \mu\text{m}} \right) \left( \frac{I}{10^{18} \text{ W/cm}^2} \right)^{\frac{1}{2}}, \quad (2)$$

where  $\lambda_L$  represents wave length of laser. From Eq.(2), Highly relativistic electron motion requires laser intensities greater than  $10^{18} \text{ W/cm}^2$  for wavelength of  $\lambda_L \sim 1 \mu\text{m}$ . As described before the section, such intensities are now available enough from JAERI's laser system and  $a_0 \sim 100$  may be reached.

Next, we consider the motion of an electron, initially at rest, in a relativistic plane monochromatic linearly polarized electromagnetic (EM) wave propagating along the x axis[10]. Selecting the direction of the electric field  $\mathbf{E} = E_0 \cos \xi \mathbf{e}_z$  as the z axis, where  $\xi \equiv \omega_L t - 2\pi x / \lambda_L$ , and  $\mathbf{e}_i$  represents a unit vector in the  $i$  direction, the position  $\mathbf{r}$ , momentum  $\mathbf{p}$  and relativistic mass factor  $\gamma$  of the electron are then described as follows:

$$\frac{\mathbf{r}}{\lambda_L} = \frac{a_0^2}{4} \left\{ \xi - \frac{\sin 2\xi}{4\pi} \right\} \mathbf{e}_x + \frac{a_0}{2\pi} \cos \xi \mathbf{e}_y, \quad (3)$$

$$\frac{\mathbf{p}}{m_e c} = \frac{a_0^2}{4} \{1 - \cos 2\xi\} \mathbf{e}_x - a_0 \sin \xi \mathbf{e}_z, \quad \gamma = \sqrt{1 + \left( \frac{\mathbf{p}}{m_e c} \right)^2} \quad (4)$$

The quivering motion is called for 8-figure motion. The characteristic values are derived from these formula as follows:

$$\begin{aligned} \frac{z_0}{\lambda_L} &= \frac{a_0}{2\pi}, \quad \frac{p_{z0}}{m_e c} = a_0, \quad \frac{v_{xd}}{c} = \frac{1}{1 + 4a_0^{-2}}, \\ \gamma &= 1 + \frac{a_0^2}{2} \quad \text{and} \quad T = 1 + \frac{a_0^2}{4} T_{a_0=0} \end{aligned} \quad (5)$$

where  $z_0$ ,  $p_{z0}$ ,  $v_{xd}$  and  $T$  represent the position and max. momentum in the z direction, drift speed

in the x direction and a period of acceleration in the laboratory frame. The quivering length and max. momentum in the z direction is proportional to  $a_0$ . The drift speed in the x direction is almost the same as light speed for  $a_0 \gg 1$ , so that the angle between laser propagation and quivering direction is  $\tan\theta = 2/a_0$ . For example, the drift speed and  $\gamma$  become  $v_{xd} = 0.9975c$  and  $\gamma = 201$  for  $a_0 = 20$ . Accordingly, a period of acceleration becomes long in the laboratory frame, as is well-known in conventional accelerators.

### 3. LARMOR RADIATION & BREMSSTRAHLUNG EMISSION

It is well-known that an accelerated electron emits electromagnetic wave. In the non-relativistic regime, the power of radiation  $P$  can be calculated from famous Larmor's formula. In the case of the relativistic motion, Larmor's formula is extended in cgs units as follows:

$$P = \frac{2}{3} \frac{e^2}{c} \gamma^6 \left[ \dot{\boldsymbol{\beta}}^2 - (\boldsymbol{\beta} \times \dot{\boldsymbol{\beta}})^2 \right], \quad \dot{\boldsymbol{\beta}} = \frac{\dot{\mathbf{P}}}{\gamma m_e c} - \frac{\gamma \boldsymbol{\beta} (\dot{\mathbf{P}} \cdot \boldsymbol{\beta})}{m_e c \{1 + (\gamma \boldsymbol{\beta})^2\}} \quad (6)$$

where  $\boldsymbol{\beta}$  and  $\dot{\boldsymbol{\beta}}$  represent velocity and acceleration of the electron. Note that radiation power is a Lorentz invariant quantity, although its angular spectra distribution is not invariant. The angular spectra distribution of radiation power is calculated from Fourier transform of Lienard-Wiechert potential.

$$\frac{d^2 P}{d\omega d\Omega} = \frac{e^2}{4\pi^2 c} \left| \int_0^T \frac{\mathbf{n} \times [(\mathbf{n} - \boldsymbol{\beta}) \times \dot{\boldsymbol{\beta}}]}{(1 - \boldsymbol{\beta} \cdot \mathbf{n})} e^{i\omega(t - \mathbf{n} \cdot \mathbf{r})} dt \right|^2 / T(1 - \bar{\boldsymbol{\beta}} \cdot \mathbf{n}) \quad (7)$$

where  $\mathbf{n}$  and  $\bar{\boldsymbol{\beta}}$  represent a unit direction vector for observation and time-averaged velocity normalized by light speed. The denominator in Eq. (7) is continuing duration of illumination to the  $\mathbf{n}$  direction.

The radiation power averaged over an acceleration period of the electron can be calculated from Eq. (6). The radiation generated by EM waves is called for Larmor radiation or Thomson scattering. In the case of electron motion induced by circular polarized EM wave, that is synchrotron motion, the radiation power is proportional to  $a_0^4$ .

$$P [W/cm^3] = 1.81 \times 10^{15} a_0^2 (a_0^2 + 1) \left( \frac{1 \mu\text{m}}{\lambda_L} \right)^2 \left( \frac{n_e}{10^{21} \text{cm}^{-3}} \right), \quad (8)$$

where  $n_e$  represents number density of electron. However, the motion is induced only by adiabatic pulse raise, namely long pulse, and the motion may be broken by other dynamical processes, for example ponderomotive force. Next, consider the case of 8-figure motion for an electron induced by plane EM wave. The radiation power averaged over an acceleration period of the electron calculated from Eq. (6) with using Eq. (3, 4) in Sec. 2 is proportional to  $a_0^2$ , namely intensity.

$$P [W/cm^3] = 0.91 \times 10^{15} a_0^2 \frac{a_0^2 + 8}{2a_0^2 + 8} \left( \frac{1 \mu\text{m}}{\lambda_L} \right)^2 \left( \frac{n_e}{10^{21} \text{cm}^{-3}} \right), \quad (9)$$

The reason why this radiation power is smaller than that of the circularly polarized EM wave that the electron drifts in the direction of laser propagation and a period to pass through laser pulse becomes long. Due to this drift motion, the radiation power becomes  $a_0^2$  times large nearby the laser propagation direction. The angular spectra distribution of radiation power is calculated from Eq. (7). To change the power in the unit volume  $P [W/cm^3]$  into that in the unit surface area  $P' [W/cm^2]$ , Eq. (7) should be multiplied by the propagation length of the laser,  $cT$ . It is found that the angular distribution concentrates around the quivering direction,  $\tan\theta = 2/a_0$ , in the angle range of  $a_0^{-4}$  and the irradiated intensity and emitted photon energy are respectively proportional to  $a_0^8$  and  $a_0^3$  in the case of single particle motion. At  $a_0=20$ ,  $\lambda_L=0.88\mu\text{m}$  and  $n_e = 10^{21} \text{cm}^{-3}$ ,  $\sim 1\text{KeV}$  photons is irradiated about  $10^{18} \text{W/cm}^2$  at peak power. This high energy-intensity irradiation source is opened wide and new regime in the study and application. For example, the generated intense X-ray will be applied to source of short pulse X-ray, pumping source of inner-shell X-ray laser, etc.

When an electron is accelerated by the Coulomb force from an ion, the another radiation is generated. This radiation is called for bremsstrahlung emission. In the non-relativistic regime, the power of radiation is estimated by calculating acceleration of an electron from ions with using Eq. (6). Adopting ballistic orbit approximation, the power is then found to be proportional to  $a_0$ . In the case of the relativistic motion, the radiation power should be estimated with concerning quantum-photon effect, Compton scattering. In Born's approximation, the power is proportional to  $a_0^4$ . In the limit of large  $a_0$ , the radiation power per unit volume is approximated,

$$P [W/cm^3] \sim 2 \times 10^{13} a_0^2 \ln \left( \frac{a_0^2}{2} \right) \left( \frac{1 \mu\text{m}}{\lambda_L} \right)^2 \left( \frac{Z}{10} \right)^2 \left( \frac{n_e}{10^{21} \text{cm}^{-3}} \right) \left( \frac{n_i}{10^{20} \text{cm}^{-3}} \right), \quad (10)$$

where  $Z$  and  $n_i$  represent charge number and number density of ion, respectively. In the same as Larmor radiation, the radiation power becomes  $a_0^2$  times large nearby the laser propagation direction. The emitted photon energy spreads widely over MeV, which is proportional to logarithm of a reciprocal of photon energy. The angular distribution concentrates around the quivering direction in the angle range of  $a_0^{-4}$ . As a result, the irradiated intensity and maximum emitted photon energy are respectively proportional to  $a_0^{10}$  and  $a_0^2$  in the case of single particle motion. At  $a_0=20$ ,

$\lambda_L=0.88\mu\text{m}$  and  $Z=10$ ,  $n_e = 10^{21}\text{ cm}^{-3}$ ,  $\sim 100\text{MeV}$  photons are generated about  $10^{18}\text{ W/cm}^2$  at peak power. This high energy-intensity irradiation source is opened wide and new regime in the study and application. For example, the generated intense hard X-ray will be applied to source of short pulse hard X-ray, positron production and nucleus excitation, etc.

#### 4. CONCLUSION and REMARKS

Larmor radiation around KeV at  $10^{18}\text{ W/cm}^2$  is generated by interaction between dense plasma,  $n_e = 10^{21}\text{ cm}^{-3}$ , and intense laser around  $10^{21}\text{ W/cm}^2$  with  $1\mu\text{m}$  laser wave length. The generated intense X-ray will be applied for source of short pulse X-ray, pumping source of inner-shell X-ray laser. Bremsstrahlung emission over MeV at  $10^{18}\text{ W/cm}^2$  is also generated in the same condition. The intense hard X-ray can be applied to sources of short pulse X-ray, positron production and nucleus excitation, etc. It was also observed that short-pulse high intensity laser interaction with clusters absorbed laser energy and produced intense higher harmonics as compared with plasma and metal. These intense radiations may be opened new regime in the study.

#### 5. ACKNOWLEDGMENTS

The authors would like to thank H. Ohno and T. Arisawa for their interest and encouragement throughout this work.

#### REFERENCES

- (1) D. von der Linde et al., Phys. Rev. A. **52**, 52 (1995).
- (2) J. J. Macklin et al., Phys. Rev. Lett. **70**, 766 (1993).
- (3) P. Gibbon, Phys. Rev. Lett. **76**, 50 (1996).
- (4) T. D. Donnelly et al., Phys. Rev. Lett. **76**, 2472 (1996).
- (5) S. Kato et al., J. Phys. Soc. Jpn. **66**, 388 (1997).
- (6) S. Huller and J. Meyer-ter-Vehn, Phys. Rev. A. **48**, 3906 (1993).
- (7) J. D. Kmetec et al., Phys. Rev. Lett. **68**, 1527 (1992).
- (8) B. N. Chichkov et al., Phys. Rev. A. **46**, 4512 (1992).

## 4 . Pondermotive absorption of a short intense laser pulse in a non-uniform plasma

A.A. Andreev, K.Yu. Platonov, K.A.Tanaka\*

*Institute for Laser Physics, SC "Vavilov State Optical Institute"  
12, Birzhevaya line, St Petersburg 199034, Russia*

*\*Fac. of Engineering & ILE, Osaka University,  
2-6 Yamada-oka, Suita, Osaka 565, Japan*

### ABSTRACT

An analytical description of the pondermotive absorption mechanism at a short high intense laser pulse interaction with a strong inhomogeneous plasma is presented. The optimal conditions for the maximum of resonance absorption of laser pulse interaction with non-uniform plasma at normal incidence are founded.

**Keywords:** Short laser pulse, Inhomogeneous plasma, Resonant absorption

### INTRODUCTION

Significant amount of papers, both theoretical and experimental [1] are devoted in the last years to investigations of a process a short powerful laser pulse interaction with a dense plasma. The intensity of radiation, achieved in experiments at the moment reaches  $10^{19}\text{W/cm}^2$ . A movement of plasma in fields of such intensity gets essentially non-linear relativistic character.

The analytical consideration of laser pulse absorption in such situation rather difficult, therefore is used numerical simulations (PIC, Vlasov-codes) [2,5]. Whereas the analytical results have greater presentation, open physical mechanisms of occurring processes and serve the tests for the computer programs. In the present work the analytical decisions of non-linear relativistic hydrodynamic equations for plasma are considered.

There is shown, that at weak non-linearity the resonant absorption arises even at normal incidence of an electromagnetic wave on spatially non-uniform plasma. Absorption coefficient has the big rise in comparison with a linear case. This result coexist qualitatively with the fact of a weak dependence of absorption from an angle of incidence at high laser intensity [3].

### SYSTEM OF THE BASIC EQUATIONS

For the description of a plasma movement in strong laser fields we shall use one dimensional system of the hydrodynamic equations, including speed of an ordered movement superior thermal speed. The given approximation corresponds to a limit of normal skin-effect (SIB [4]).

The law of conservation of a perpendicular component of an initial pulse allows to reduce this system to two equations for longitudinal and perpendicular fields:

$$\frac{\partial^2 A}{\partial \xi^2} - \frac{\omega^2}{\omega_p^2} \frac{\partial^2 A}{\partial \tau^2} = \left( \eta(\xi) + \frac{\partial E}{\partial \xi} \right) A \sqrt{\frac{1-v^2}{1+A^2}} \quad (1)$$

$$\frac{\omega}{\omega_p} \frac{\partial}{\partial \tau} \sqrt{\frac{1+A^2}{1-v^2}} v = E - \frac{\partial}{\partial \xi} \sqrt{\frac{1+A^2}{1-v^2}}; v = -\frac{\omega}{\omega_p} \frac{\frac{\partial E}{\partial \tau}}{\eta(\xi) + \frac{\partial E}{\partial \xi}}$$

In (1) are entered following undimensional variables:  $A$  - vector potential of a perpendicular field in terms of  $mc^2/e$ ,  $E$  - strength of a longitudinal field in terms of  $m\omega_p/e$ ,  $\xi = \omega_p z/c$  - undimensional co-ordinate,  $\tau = \omega t$  - undimensional time,  $\omega_p$  - plasma frequency in depth of plasma,  $\eta(\xi)$  - plasma density (normalised per unit of in depth of plasma),  $\omega$  - frequency of an incident electromagnetic wave. We shall consider weak non-linearity ( $A^2 \ll A$ ), displaying the solution (1) in a number on degrees  $A$ . This approximation limits intensity of an incident radiation to intensity  $10^{18}$  W/cm<sup>2</sup>. Result of decomposition (1) looks like:

$$\frac{\partial^2 A^{(0)}}{\partial \xi^2} - \frac{\omega^2}{\omega_p^2} \frac{\partial^2 A^{(0)}}{\partial \tau^2} = \eta(\xi) A^{(0)}; E^{(0)} = 0 \quad (2)$$

$$\frac{\partial^2 E^{(1)}}{\partial \tau^2} + \frac{\omega_p^2}{\omega^2} \eta(\xi) E^{(1)} = \frac{\omega_p^2}{\omega^2} \eta(\xi) \frac{\partial A^{(0)2}}{\partial \xi} 2$$

For linear polarisation of a incident wave a pondermotive force depends on time. Then the solution of zero approximation of system (2) has the following form:

$$A^{(0)} = A(\xi) e_y \cos(\tau), \eta(\xi) \neq 0; \xi > 0$$

$$A^{(0)} = \left[ A(0) \cos(\omega \xi / \omega_p) + \frac{\omega_p}{\omega} A'(0) \sin(\omega \xi / \omega_p) \right] e_y \cos(\tau); \xi < 0 \quad (3)$$

Where  $A'(0)$  - derivative  $A(\xi)$  at  $\xi=0$ . In (3) it means, that  $\eta(\xi)$  is nonzero in area  $\xi > 0$ . The function  $A(\xi)$  depends on a specific structure of concentration. The further calculations will be made for any  $A(\xi)$ , and the example of absorption coefficient for exponential of growing concentration is resulted in the following paragraph.

The averaged Poynting vector of a laser wave, appropriate to a field (3) is determined by  $A(0)$  and  $A'(0)$ :

$$\langle \gamma \rangle = \frac{\omega^2}{32\pi c} (A^2(0) + \omega_p^2 A'^2(0) / \omega^2) \quad (4)$$

The solution of the equation of the first approximation for a longitudinal field  $E$  at a given right part in view of a resonance looks as follows:

$$E^{(1)}(\xi, \tau) = \frac{1}{4} \frac{\partial}{\partial \xi} A^2(\xi) \left[ 1 + \frac{\omega_p^2 \eta(\xi) / \omega^2}{\omega_p^2 \eta(\xi) / \omega^2 - 4} (\cos(2\tau) - \cos(\omega_p \sqrt{\eta(\xi)} \tau / \omega)) \right] \quad (5)$$

In a point  $\eta(\xi^*) = 4\omega^2 / \omega_p^2$  the field  $E^{(1)}$  linearly accrues in due course, that corresponds to a resonance between pondermotive force and plasma wave. Energy of a longitudinal field per unit of the area of plasma

$$W = \frac{m^2 c^2 \omega_p}{8\pi e^2} \int E^{(1)2} d\xi \quad (6)$$

Calculated with the help of presentation of  $\delta$ -function

$$\lim_{\tau \rightarrow \infty} \frac{\sin^2 \alpha\tau}{\pi\tau\alpha^2} = \delta(\alpha)$$

Also linearly grows in due course:

$$W = \frac{m^2 c^3 \omega\tau}{2^7 e^2} \left[ \frac{\partial A^2}{\partial \xi^*} \right]^2 \left[ \frac{\partial \sqrt{\eta(\xi)}}{\partial \xi^*} \right]^{-1} \quad (7)$$

By dividing absorbed power on Pointing vector of laser wave we shall receive required absorption coefficient  $\zeta$

$$\zeta = \pi A^2(\xi^*) \left[ \frac{\partial A(\xi^*)}{\partial \xi^*} \right]^2 \left[ (A^2(0) + A'^2(0)) \frac{\partial \sqrt{\eta(\xi^*)}}{\partial \xi^*} \right]^{-1} \quad (8)$$

So, the received expression determines absorption coefficient at normal incidence of an electromagnetic wave on non-uniform plasma through the decision of the equation of zero approximation for vector potential. A condition of applicability (8) is: electron thermal speed less then its hydrodynamic speed, or amplitude of vector potential it imposes a condition  $1 \gg A^2 \gg v_T \omega_p / c\omega$ . Remember, that the case of normal skin effect is realised when  $v_T / c \ll \omega / \omega_p$ .

### Absorption coefficient in plasma with exponential growing density

The function  $A(\xi)$  manages to be constructed analytically for a limited set of structures  $\eta(\xi)$ . One of variants is  $\eta(\xi) = \exp(\alpha\xi)$ , where  $\alpha = c/L\omega_p$  - undimensional scale of plasma in-homogeneity. The solution (2), aspiring to zero at large  $\xi$  looks like

$$A(\xi) = -2A_0 (2\Omega sh(2\pi\Omega/\alpha) / \pi\alpha)^{1/2} K_{2i\Omega/\alpha} (2 \exp(\alpha\xi/2) / \alpha) \quad (9)$$

In (9) for  $\Omega$  is the relation  $\omega/\omega_p$ ,  $K(\xi)$  - function McDonald,  $A$  - amplitude of a laser wave is designated at  $\xi \rightarrow -\infty$ . Doing further account according to the above-stated technique, we shall receive the following result for absorption coefficient:

$$\zeta = \frac{64}{\pi} A_0^2 x^3 \operatorname{sh}^2(2\pi x) K_{2ix}^2(4x) K_{2ix}^2(4x) ; x = \omega L / c \quad (10)$$

The stroke in (10) designates derivative of function McDonald. We shall carry out research of absorption coefficient. We shall note, that as well as in case of incident at some angle the resonant absorption does not depend on density of plasma  $\omega_p$ . At small in-homogeneity scales  $L$  ( $x \ll 1$ )

$$\zeta = 16\pi A_0^2 x^3 \ln^2(1/2x) \quad (11)$$

We shall remind, that at inclined incident for small  $x$ ,  $\zeta = 2\pi x \sin^2\theta / \cos\theta$ . At large  $x$ , asymptotic (10) looks as follows:

$$\zeta = 4\pi A_0^2 x \exp(-(16 - 4\pi)x)$$

The maximum  $\zeta = 0.38A_0^2$  absorption coefficient reaches at  $x_{\max} = 0.26$ , it means that at in-homogeneity scales about length of a wave, as well as in case of inclined incident. We compare resonant absorption to other channels of absorption. In uncollisional plasma this is Landau damping on separate electrons (SIB [4]):

$$\zeta^{SIB} = 8\sqrt{2/\pi} \frac{v_T^3 \omega_p^2}{c^3 \omega^2} ; 0 < L < c/\omega_p \quad (12)$$

At large  $L$ ,  $\zeta^{SIB}$  exponentially decreases with increase  $L$ . Thus, at sufficient intensity of a laser wave  $A_0^2 > v_T \omega_p / c\omega$  in spatially non-uniform plasma ( $L > c/\omega_p$ ) the resonant absorption is dominant, and absorption coefficient reaches tens of percents. We shall note, that at some angle of incidence the account of the members proportional  $A$  in the equations also results in additional absorption, connected to generation of the second harmonic in reflected radiation and presence of the second resonant point. But at inclined incidence these effects give only amendment to standard linear transformation.

## THE CONCLUSION

Considered effect allows qualitatively to interpret results of numerical simulations, according to which at  $A < 1$  dependence of factor of absorption on an angle of incidence becomes weak, as inclusion of the pondermotive mechanism of absorption.

## REFERENCES

1. Luther-Davies B., et al. Laser Phys. 1991 v.1 p. 325.  
Mourou G., Umstadter D. Phys. of Fluids B4, (1992), p.2315.
2. Wilks S.C. Phys.Fluids B 5 (7), (1993), p. 2603.
3. Ruhl H., Mulser P. Phys.Let.A 205 (1995), p. 388.
4. Briang Yang T.-Y., et. al, Phys. Plasmas v.2, (1995) p.3146.
5. Kruer W. Phys. of Fluids (1987), p.1278.

## 5. Integrated Code Development for Studying Laser Driven Plasmas

Hideaki TAKABE, Hideo NAGATOMO, Atsusi SUNAHARA,  
Naofumi OHNISHI, Syuji NARUO, and Kunioki MIMA

*Institute of Laser Engineering, Osaka University*  
*Suita, Osaka 565 Japan*  
E-mail: takabe@ile.osaka-u.ac.jp

### ABSTRACT

Present status and plan for developing an integrated implosion code are briefly explained by focusing on motivation, numerical scheme and issues to be developed more. Highly nonlinear stage of Rayleigh-Taylor instability of ablation front by laser irradiation has been simulated so as to be compared with model experiments. Improvement in transport and rezoning/remapping algorithms in ILESTA code is described.

**Keywords:** laser fusion, implosion, integrated code, 2-D ALE code, rezoning, Rayleigh-Taylor instability

### 1. INTRODUCTION

Recently much attention is focused on the topics of physics in complex phenomena. The study of complex systems requires a large scale computing and is roughly classified into two categories: (1) Elementary process of a system with huge number of freedom. (2) Phenomena stemming from strong coupling of a variety of different physics.

In case of category (1), the basic equations are simple, but because of nonlinearity in the equations a complex phenomena are seen. As a subject belonging to this category, we can enumerate, for example, fluid turbulence, galaxy formation, multi-electron atomic structure, and so on. In case of the fluid turbulence, it is essential to treat a system in which small and large scale vortices co-exist. With increase of the Reynolds number, the ratio of the scale between the largest and smallest vortices increases; consequently, a large scale computing is necessary to directly simulate the turbulence. In the category (1), the key words are nonlinearity, non-locality, many-body, non-equilibrium, etc.

On the other hand, the category (2) includes fusion, astrophysics, aerodynamics, meteorology, and so on. In this case, we have to treat the phenomena stemming from the coupling of many of different physics. It can be said that this is the physics of combined system. It has become possible to study the combined physics with a dramatic progress of computational ability after the start with ENIAC of 51 years ago[1]. It has become to be recognized that the computer simulation is an essential method in researching physics. This is the third method additive to the traditional methods, theory and experiment. The computer science is getting to be essential in modern science.

In laser fusion, a micro-pellet called target is explosively squeezed to 1/30 - 1/50 of its initial radius and high density and high temperature fuel plasma is produced in the central region. The physics controlling such phenomena is complex, where the compressible

hydrodynamics coupled with electron heat conduction, x-ray radiation transport plays a key role. In laser implosion, it is difficult to analyze the experimental data without a help of computer simulations, because a micro-target is imploded to a radius of several tens micron in an extremely short time of a few 100 ps. Therefore, simulation codes have been developed from the beginning of the research in order to reproduce the whole physical scenario of implosion[2]. We call such code for laser fusion an "integrated implosion code". The entitled research purpose is to analyze experimental data and do research planning by developing the integrated code systematically. In this paper, we briefly show the outlook of our integrated implosion code and the present status of its development.

## 2. INTEGRATED IMPLOSION CODE

In studying the physics of a complex system, four elements are necessary to promote the research. Two are experimental ones, namely, "synthetic experiment" and "model experiment". The implosion experiment is a synthetic one and a variety of model experiments are necessary to clarify the physics controlling the implosion phenomena. The other two are theoretical ones, "theoretical models" and "integrated code". The theoretical models checked with corresponding model experiments should be installed in the integrated code to analyze experimental data and design fusion targets. The integrated code is the essence of the computer science and its development has become possible with the dramatic progress of high-speed computers.

Let me try to describe the definition of the integrated implosion code. It should satisfy the following conditions.

- (1)The code should be a multi-dimensional hydrodynamic code to be able to simulate the whole scenario of the physics in laser driven fusion from laser absorption to implosion and fusion burn.
- (2)All the physics thought to be important should be included in the code.
- (3)The appropriateness of the physics models and the accuracy of the numerical scheme should be checked by comparing with experiments.
- (4)The code should be highly reliable so as to be used for the purpose of "numerical high gain experiment (NHGX)".

The readers may have an impression that the item (2) is reckless. What is important is to judge which should be modeled and which should be abandoned. To do so, a good sense of physics may be required. The spirit of the item (4) stands on the same base as the numerical wind tunnel (NWT)[3] and numerical Tokamak[4]. It is well known that the NWT has been replaced of the experiment with a wind tunnel for designing aerodynamics of aircraft. In the early stage of an aircraft design, NWT is very efficient from an economical point of view, because we can reduce the number of candidates for prototype in a real wind tunnel experiment. Recently, it has become possible to control the turbulence with a sophisticated design of wing surface[3]. The numerical Tokamak is a big challenge because we are required to bridge huge scale (difference) in temporal and spatial dimensions from tiny eddies to the whole machine, for example[4]. The long time scale transport should be solved consistently with a short time scale instability phenomena.

The third example is numerical astrophysics. The astrophysics is very resemble to physics of laser fusion and laboratory astrophysics is proposed to study a variety of hydrodynamic, radiation, atomic, and relativistic plasmas by use of intense lasers[5]. The

astrophysical phenomena are synthetic and model experiments are required to make astrophysics precise science. By developing and checking codes for astrophysics by comparing with model experiments, we can promote the numerical astrophysics.

### 3. BASIC EQUATIONS

The basic equations governing the laser implosion process are one-fluid, two-temperature fluid equations. In addition, for example, non-ideal equation of state (EOS), and radiation transport with non-LTE spectral opacity affect the fluid dynamics. The central part of the equations are

$$\frac{d\rho}{dt} = -\rho \nabla \mathbf{u} \quad (1)$$

$$\rho \frac{d\mathbf{u}}{dt} = -\nabla(P_i + P_e) \quad (2)$$

$$\rho \frac{d\varepsilon_i}{dt} = -P_i \nabla \mathbf{u} - \nabla \mathbf{q}_i + Q_{ei} + S_\alpha^i \quad (3)$$

$$\rho \frac{d\varepsilon_e}{dt} = -P_e \nabla \mathbf{u} - \nabla \mathbf{q}_e - Q_{ei} + S_L + S_r + S_\alpha^e \quad (4)$$

$$\frac{1}{c} \frac{\partial I^\nu}{\partial t} + \boldsymbol{\Omega} \cdot \nabla I^\nu = \eta^\nu - \chi^\nu I^\nu \quad (5)$$

$$\frac{\partial}{\partial t} \phi^\alpha + \mathbf{v} \cdot \nabla \phi^\alpha = S_{DT} + \left( \frac{\partial \phi^\alpha}{\partial t} \right)_{coll} \quad (6)$$

$$\mathbf{v}_g \cdot \nabla I_L^k = -\nu_{abs} I_L^k \quad (7)$$

In Eqs. (3) and (4),  $Q_{ei}$  is the temperature relaxation term,  $S_\alpha^{i,e}$  are the alpha particle heating terms for the ions and electrons respectively,  $S_L$  is the laser heating term,  $S_r$  is the radiation heating/cooling term, and  $\varepsilon_i$  and  $\varepsilon_e$  are the ion and electron internal energies which should be modeled so as to describe from the solid to plasma states including Fermi degeneracy[6]. Radiation transport is governed by Eq. (5), where  $\eta_\nu$  and  $\kappa_\nu$  are emissivity and opacity. In case when high or medium Z materials are used as target composite, the calculation of  $\eta_\nu$  and  $\kappa_\nu$  becomes complex[7]. Equation (6) is for the alpha particle transport based on the numerical scheme described in Ref. [8]. Equation (7) represents the ray-tracing of laser beamlets with the classical absorption coefficient[9]. In Eqs. (3) and (4), the electron and ion heat fluxes of  $\mathbf{q}_e$  and  $\mathbf{q}_i$  are taken from Ref. [10]. More details are given in Ref. [11].

#### 4. NUMERICAL METHODS

Equations (1) - (4) are solved with finite difference method in the Lagrangian frame. The details of the method are described in Ref. [11] for one-dimensional case. Since the integrated code should be at least two dimensional, more sophisticated numerics are required especially relating to transport algorithm and rezoning/remapping algorithms.

The Lagrangian scheme in which the numerical mesh moves with fluid elements is more convenient compared to the Eulerian scheme because of the following reasons. In laser plasmas, the density and temperature varies over many order of magnitude, for example, across the ablation front. A thin shell is imploded with high in-flight aspect ratio of more than 100. A high radius convergence ( $C_R = 30 - 40$ ) implosion should be simulated. In addition, a target consisting of different material layers with different EOS, atomic state, opacity etc should be simulated. In some case, rate equation for determining ionization state distribution should be solved for each fluid element by coupling with fluid dynamics.

In employing the Lagrangian scheme, following numerical difficulties should be solved. Since the numerical mesh structure is distorted, for example, by shear flow due to hydrodynamic instabilities, a rezoning of mesh is necessary to continue the calculations. In this case, the rezoning should be designed so as to keep the merit of Lagrangian scheme. In addition, a remapping scheme should be developed so that the physical quantities such as density, momentums, energy densities are re-defined precisely from those in the old mesh to in the new mesh zones. Numerical diffusion and overshooting well-known in numerical method in solving a convective term should be reduced. Since the Lagrangian mesh becomes non-orthogonal structure, the transport algorithm becomes complicated even for the case of diffusion-type transport.

##### 4.1 Transport Algorithm

In order to explain the numerical algorithm for transport, we briefly explain the guideline in solving the following diffusion equation.

$$\rho C_v \frac{\partial}{\partial t} T = \nabla(\kappa \nabla T) \quad (8)$$

After volume integration of Eq. (8) over a mesh zone, it is solved with the fully implicit method. It is required to estimate the gradient of T in the Lagrangian mesh. In two dimensional (2-D) planer geometry,  $\partial T/\partial x$  and  $\partial T/\partial y$  can be given with the Lagrangian coordinate (X,Y) in the form;

$$\frac{\partial T}{\partial x} = \frac{1}{J} \left( \frac{\partial T}{\partial X} \frac{\partial y}{\partial Y} - \frac{\partial T}{\partial Y} \frac{\partial y}{\partial X} \right) \quad (9)$$

$$\frac{\partial T}{\partial y} = -\frac{1}{J} \left( \frac{\partial T}{\partial X} \frac{\partial x}{\partial Y} - \frac{\partial T}{\partial Y} \frac{\partial x}{\partial X} \right) \quad (10)$$

$$J = \left( \frac{\partial x}{\partial X} \frac{\partial y}{\partial Y} - \frac{\partial y}{\partial X} \frac{\partial x}{\partial Y} \right) \quad (11)$$

The total heat flux coming across the four boundaries as seen in Fig. 1 can be calculated by

expressing Eqs. (9) - (11) in the finite difference forms. Then, not only the quantities defined at the center of the zone, but also those at four grid points are also necessary. At the present time, we define them as the average of the surrounding four quantities. As the result, the total heat flux is given with nine quantities which are still unknown.

In order to reverse the matrix for such nine point transport scheme, ICCG scheme is usually used[12]. However, this method is not applicable to the present scheme and we use ILUBCG (Incomplete LU Biconjugate Gradient) scheme[13]. This is time consuming compared to ICCG, but can be extended to more general cases. We have checked the accuracy of the scheme in strongly distorted mesh cases and reasonable accuracy has been seen[13].

#### 4.2 Rezoning/Remapping

The orthogonality of the mesh structure can be maintained by solving a Poisson-type equation for new x and y grid coordinate  $\xi$  and  $\eta$ :

$$\frac{\partial^2 \xi}{\partial x^2} + \frac{\partial^2 \xi}{\partial y^2} = P(\xi, \eta), \quad \frac{\partial^2 \eta}{\partial x^2} + \frac{\partial^2 \eta}{\partial y^2} = Q(\xi, \eta) \quad (12)$$

where P and Q are called forcing terms. By controlling the definition of P and Q, we can assume many zones, for example, in the region with steep density gradient. In order to keep the displacement of the new grid point from the old one, a relaxation parameter is set to be small in solving Eq. (12) with the relaxation method.

We have two different rezoning/remapping schemes. One is done a few tens times over several thousand time steps, when the mesh distortion becomes very severe. This scheme has been used to study nonuniform ignition and burn simulations[14]. The other developed recently[15] is every-time-step rezoning/remapping scheme. The rezoning schemes are same, while the remapping schemes are completely different. In the latter case which we use in the present paper, the displacement of the grid from old to new at each time step is assumed to be much smaller than the grid distances. This corresponds to the Courant condition in solving the convection term in Eulerian scheme. In the remapping case, the physical quantities are convected from one to another adjacent zone because of move of the boundary by rezoning. Then, the convected quantities can be evaluated by various numerical methods developed in the past two decades.

In 2-D, we calculate the convected quantities one by one in x and y directions. The convected flux is calculated with FCT (Flux Collected Transport) scheme. As for the flux limiter in FCT, two types of limiter proposed by Boris et al and Zalesak are used[16]. The former is rather dissipative than the latter, although the former is numerically more stable. We have checked an appropriateness and accuracy of the present scheme by artificially moving the meshes from a strongly distorted case to a smoothed code[15].

## 5. SIMULATION OF EXPERIMENT

As mentioned previously, two different kind of experiments are necessary and have been done with Gekko XII laser. One is a model experiment. The Rayleigh-Taylor (R-T) instability of ablatively accelerating planer target has been studied intensively[16]. The other is the spherical implosion experiments. At the present time, the integrated code is not robust

enough to simulate whole of implosion process in 2-D and, therefore, comparison has been mainly done with 1-D code[17] or Eulerian code with 2-nd order Godunov scheme[18]. The implosion dynamics are well reproduced with 1-D code as seen in Fig. 2, where trajectories of x-ray streak image are compared. This indicates that energetics of implosion process is well modeled in 1-D code. However, the neutron yield, fuel temperature, and compressed core images are not reproduced. Most of these discrepancies appear to be explained in 2-D simulations with nonuniformity of relatively long wavelength[19].

The integrated code has been tested to study linear and nonlinear R-T instability of the ablation front. In Gekko XII experiments, a planer plastic target with corrugated surface on laser irradiation side is used to be accelerated with green light of square pulse. We show a typical simulation result. The target initial thickness is 16  $\mu\text{m}$  and a surface corrugation is 60  $\mu\text{m}$  in wavelength and 3  $\mu\text{m}$  in amplitude. Laser intensity is  $0.7 \times 10^{14} \text{ W/cm}^2$ . A half of one wavelength region is simulated with 180 numerical zones in the accelerating direction and 40 zones in the perpendicular direction. The pulse duration is 2 ns. In Fig. 3, the density contours and the mesh structure at 3.5 ns are shown. The target initial position is at 0  $\mu\text{m}$  in the scale shown in Fig. 3. As clear from Fig. 3, it is possible to simulate highly nonlinear stage with the present integrated code.

The comparison of linear growth rate and spike-bubble structure to corresponding experimental data is on going with a developed spectroscopic code to reproduce back-light and side-light images.

## 6. INTEGRATED CODES IN WORLD

The concept of the integrated code is not our original, but is natural trend from the spirit of computational science. As for the integrated implosion code, code development has started due to a necessity to promote laser fusion program.

In LLNL, an integrated code development started at the same time as laser fusion research started[1,20]. The most famous code is LASNEX code[1], which is one and two dimensional. Recently, more advanced and tractable code CALE2D has been developed and been used to analyze radiation driven hydrodynamic instabilities[22]. This code is also used to study EOS effect on R-T instabilities[23], because the code is user-friendly in modeling and modifying EOS. In addition, 3-D Lagrangian code HYDRA which came to appear a few years ago in papers is used for systematic study of implosion experiments as well as model experiments[24]. It could be possible to say that LLNL has come to the level that they can perform reliable experiments numerically without real experimentst.

In LANL, the LANL version of LASNEX has been developed and been used to study a target design of medium gain for NIF (National Ignition Facility)[25]. In the US, in addition, 2-D hydrodynamic code ORCHID[26] of LLE, University of Rochester, and FAST3D code[27] of NRL (Naval Research Lab.) have been used to analyze experimental data and to design targets.

## 7. DEVELOPMENT PLAN

We have been developing implosion codes to analyze the experimental data from Gekko lasers and design the ignition and high gain target. Such simulation will be a theoretical base to

perform a hydrodynamically equivalent plasma (HEP) experiment to clarify the most critical issue of hydrodynamic instability of implosion. We plan to extend the codes to the integrated code by installing additional physics models and improving numerical schemes. The codes to be used are Lagrangian codes, ILESTA-1D[11,28] and ILESTA-2D[14]. As the first step, we focus on the following four subjects to be installed in ILESTA-2D code.

(1)*Numerical algorithm of transports:* This has been developed by Ohnishi and has been briefly explained in Sec.4. This scheme will be also used to the multi-group radiation transport with variable Eddington factor scheme and multi-group alpha particle transport. With the radiation transport algorithm, the code will be applied to analyze experimental data of so-called direct/indirect hybrid scheme[29]. The hybrid scheme will use radiation smoothing to avoid an initial imprint of laser non-uniformity by coating high-Z material and form zone on a target surface. This is a good example to test 2-D radiation transport and the code will be used to optimize the target and laser conditions.

(2)*Rezoning/Remapping algorithm:* This has been developed by Nagatomo and briefly explained in Sec. 4. Most of the algorithm has been already developed, while a remapping scheme for physical quantities defined at a grid point should be improved. In near future, we plan to develop a hybrid scheme in which two different rezoning schemes explained in Sec. 4 are used in the same job to reduce numerical diffusion as less as possible and fit the mesh structure to a deforming plasma structure as similar as possible.

(3)*Spectroscopic diagnostic code:* This has been developed by Naruo and used to analyze R-T instability experiment and implosion experiments[30]. Only with the implosion code, we can not compare the numerical result with the experimental data directly. We have to approach to the experimental data. Since most of experiments are carried out with spectroscopic or back-lighting techniques, we have to develop a variety of codes to calculate the x-ray image and time history of hydrodynamics calculated with the integrated code. In case of the R-T experiment, the transmitted x-ray image should be Fourier transformed to see the generation of higher harmonics. In case of implosion experiments, fuel-doped argon line emissions of  $\text{Ly}^{\beta}$  and  $\text{He}^{\beta}$  are measured[31]. This data should be analyzed by use of non-LTE atomic model and multi-dimensional code. We use RATION[32] code to get spectral opacity and emissivity to do ray-tracing in 2-D simulation. The rate equation solver FLY[33] is also going to be installed in the present scheme.

(4)*Kinetic-diffusion hybrid transport scheme:* This is a big issue under progress by Sunahara. It has been pointed out that the kinetic effect is important to analyze the R-T experiment done even with moderate intensity[34]. The purpose is to develop a hybrid model of diffusive and kinetic transport for electrons and to install into the 2-D integrated code. At the present time, we still work for 1-D case and the hybrid model will be compared to the case with Fokker-Planck code.

At the second stage, we will apply the integrated code to analyze the implosion experiments from the very beginning of laser irradiation. The EOS package based on Thomas-Fermi model[6] should include an additional effect such as molecular dissociation[35]. Then, the code will be used to study stability and nonuniformity of implosion dynamics of high gain targets. Even with the implosion code, it is difficult to treat the mixing governed by the modes with spherical wavenumber of  $\ell$  from one to several hundreds because of limited number of meshes in the azimuthal direction. Some mixing model[36] should be developed to clarify the effect of mixing in the stagnation phase. This is much hard job compare to the case of NIF indirect target design. The most unstable mode has the spherical wavenumber  $\ell$  of roughly several tens[37] in NIF design, while the direct high gain has

$\ell$  of a few hundreds[38].

At the third stage, we have to consider to upgrade the code to include magnetic field. In the limit of pure central ignition, the implosion scenario is spherically symmetric and no need to include magnetic field. However, the fast ignition scheme[39] is thought to be a promising alternative to the central ignition after the technical accomplishment of ultra-intense lasers. In this case, an ultra-short pulse is irradiated at the edge of a compressed core and a strong magnetic field of Giga gauss range is expected to be generated[40]. Then, we have to include transport inhibition by generated magnetic field and the magneto hydrodynamics becomes important in analyzing and designing the fast ignition.

Finally, the integrated code should be upgraded to three dimension. In this case, complexity exists in transport algorithm, while this does not require a new algorithm and the same scheme described in Sec. 4 will be extended. The development plan has been summarized in Fig.4. The integrated code can be developed by a good combination of researches who work for modeling of element physics and those who develop the integrated code by developing numerical scheme to install the models of element physics.

## 8. CONCLUSION

In order to study multi-dimensional hydrodynamic phenomena coupled with a variety of energy transports in high-energy-density plasmas produced by intense laser irradiation on a solid material, we have developed 2-D integrated code ILESTA-2D. A new transport algorithm has been developed to solve diffusion equations in distorted Lagrangian mesh structure. The rezoning/remapping algorithm is essential to continue 2-D simulation even after strong deformation of Lagrangian mesh. A new algorithm has been developed.

By installing these schemes into 2-D code, we have studied linear and nonlinear evolution of R-T instability in a planer plastic foil being accelerated by laser irradiation. Highly nonlinear stage with bubble and spike structure has been simulated. A spectroscopic code has been developed to post-process the 2-D simulation results. Back-lighting, side-lighting, and line emission spectroscopy can be simulated with this package. We have shown an expected plan to upgrade ILESTA to 3-D code after installing the kinetic effect of electron transport and magnetic effect.

Finally, it is important to ask ourselves whether by developing the integrated code, we can find a new physics. It is difficult to answer this question at the moment. We can, however, enumerate an example. When the heat transport becomes important and modifies the growth of R-T instability in the stagnation phase, it is not clear whether the growth is suppressed by the fire-polishing effect or the mixing is enhanced because of melting of cold spikes into hot fuel. We have to keep in mind this question in developing the integrated code and try to find some new phenomena which can appear only through couplings of a variety of physics elements.

## REFERENCES

- [1] A. E. Brenner, Phys. Today, October issue(1996) p.24.
- [2] T. A. Heppenheimer, "The man-made Sun" (An Omni Press, Boston, 1983) Chap. 5.
- [3] P. Moin and J. Kom, Scientific American, January issue (1997).
- [4] J. Glanz, Science 274, 1600-1002 (1996).
- [5] H. Takabe, "Laboratory astrophysics with intense and ultra-intense lasers", in the Proceedings of "Intn. Conf. Superstrong Fields in Plasmas", Varenna, Italy, Aug. 27 Sep. 2 (1997).
- [6] K. Takami and H. Takabe, Tech. Rep. Osaka Univ. **40**, 159 (1990); R. L. More et al, Phys. Fluids **31**, 3059 (1988).
- [7] H. Takabe and K. Nishikawa, J. Quant. Spec. Rad. Transfer **51**, 379-395(1994).
- [8] E. G. Cormann et al, Nucl. Fusion **15**, 377(1975).
- [9] W. L. Kruer, "The Physics of Laser Plasma Interactions" (Addison-Wesley Pub., 1988).
- [10] S. I. Braginskii, in "Rev. Plasma Physics Vol.1" (Consultant Bureau, New York, 1965) p. 205.
- [11] H. Takabe, "Hydrodynamic Simulation Code for Laser Driven Implosion", to be published.
- [12] D. S. Kershaw, J. Comput. Phys. **26**, 43 (1978).
- [13] N. Ohonishi et al, in preparation.
- [14] H. Takabe and T. Ishii, Jpn. J. Appl. Phys. **32**, 5575-5580 (1993).
- [15] H. Nagatomo et al, to be published.
- [16] K. Shigemori et al, Phys. Rev. Lett. **78**, 250-253 (1997).
- [17] A. Sunahara et al, Jpn. J. Appl. Phys. **35**, 6265 (1996).
- [18] A. Sunahara et al, in preparation.
- [19] R. E. Kidder, "Laser Fusion : the first ten years 1962-1972", unpublished.
- [20] J. A. Harte et al, ICF Quarterly Report, LLNL, July - Sep. 1996 Vol. 6, No. 4. p. 150.
- [21] G. Dimonte et al, Phys. Rev. Lett. **74**, 4855-4858 (1995).
- [22] D. H. Kalantar et al, in the 6-th Int. Wksp on "Physics of Compressible Turbulent Mixing", Marseille, France, June 18 - 21, 1997.
- [23] M. M. Marinak et al, Phys. Plasmas **3**, 2070-2076 (1996).
- [24] W. J. Krauser et al, Phys. Plasmas **3**, 2084 (1996).
- [25] R. L. McCrory and C. P. Verdon, in "Inertial Confinement Fusion", ed. by A. Caruso (Editrice Compositori, Bologna, 1989) pp.83-124.
- [26] R. J. Taylor et al, Phys. Rev. Lett. **76**, 1643-1646 (1996).
- [27] H. Takabe et al, Phys. Fluids **31**, 2884-2893 (1988).
- [28] H. Nishimura, private communication.
- [29] S. Naruo et al, in preparation.
- [30] Y. Ochi et al, to be published.
- [31] R. W. Lee, "Users Manual for RATION", LLNL Report, January 1990.
- [32] R. W. Lee, J. Quant. Spect. Rad. Transfer **56**, 535 (1996).
- [33] M. Honda and K. Mima, submitted to Phys. Rev. Lett. (1997).
- [34] L. B. Da Silva et al, Phys. Rev. Lett. (1997).
- [35] S. W. Haan, Phys. Rev. A **39**, 5812-5825 (1989).
- [36] C. J. Keane et al, J. Quant. Spec. Rad. Transfer **54**, 207-220 (1995).
- [37] H. Takabe et al, in the Proceeding of IAEA TCM on "Drivers and Ignition Facilities for Inertial Fusion", March 10-14, Osaka (1997).
- [38] M. Tabak et al, Phys. Plasmas **1**, 1626 (1994).
- [39] S. C. Wilks et al, Phys. Rev. Lett. **69** 1383 (1992).
- [40]

**FIGURE CAPTIONS**

- Fig. 1** The heat flow into the zone (X,Y) is the sum of fluxes 1 - 4. These fluxes are described with surrounding nine quantities. The quantities Q's at the four corner grid points are approximated by Q's.
- Fig. 2** The radius-time diagram of DD gas-filled plastic shell implosion. The solid circles with error bars are from the x-ray streak image of Gekko XII experiment, while the open circles are from ILESTA-1D code. Energetics is well reproduced with 1-D code.
- Fig. 3** Highly nonlinear stage of Rayleigh-Taylor instability of ablatively accelerating plastic foil. The left shows the density contours and the right shows numerical mesh structure. The target is roughly accelerated by 100  $\mu\text{m}$  during 3.5 ns.
- Fig. 4** Expected plan for developing the integrated implosion code. The code development consists of two parts; one is basic research as to physics elements or models, and the other is code integration by installing the accomplishment through the former activity.

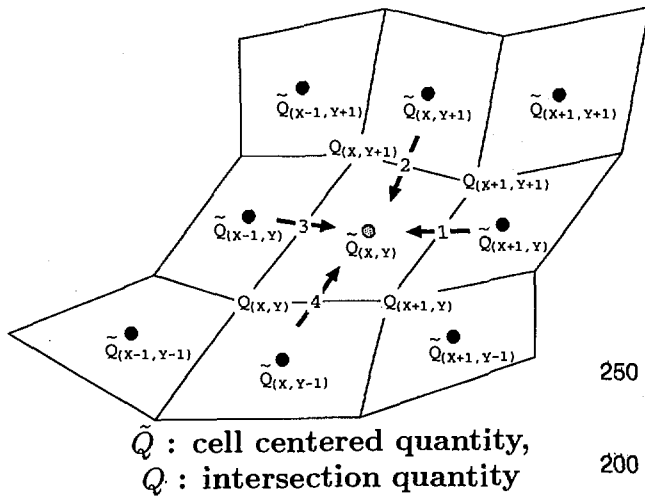


**Fig. 1**

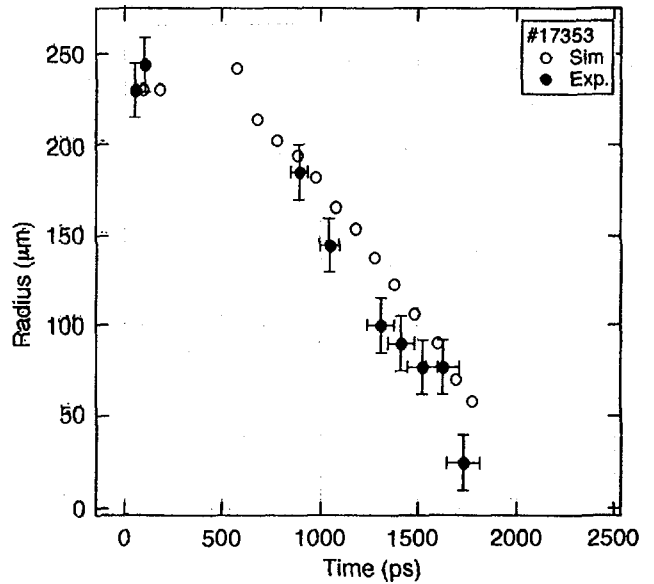


**Fig. 2**

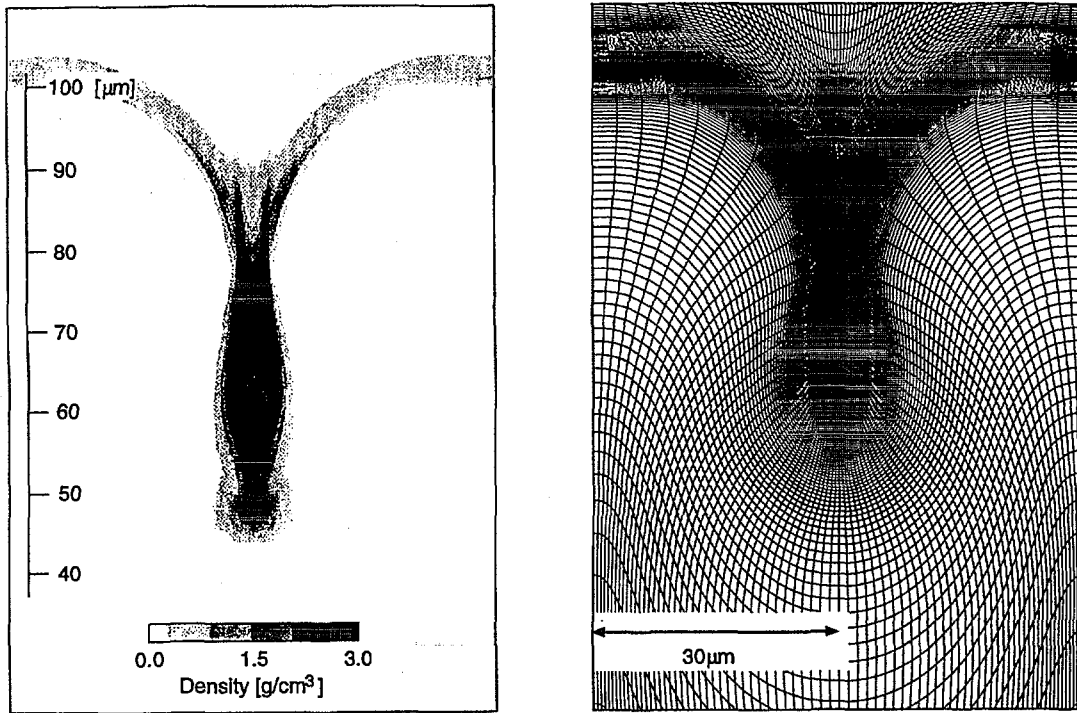


Fig. 3

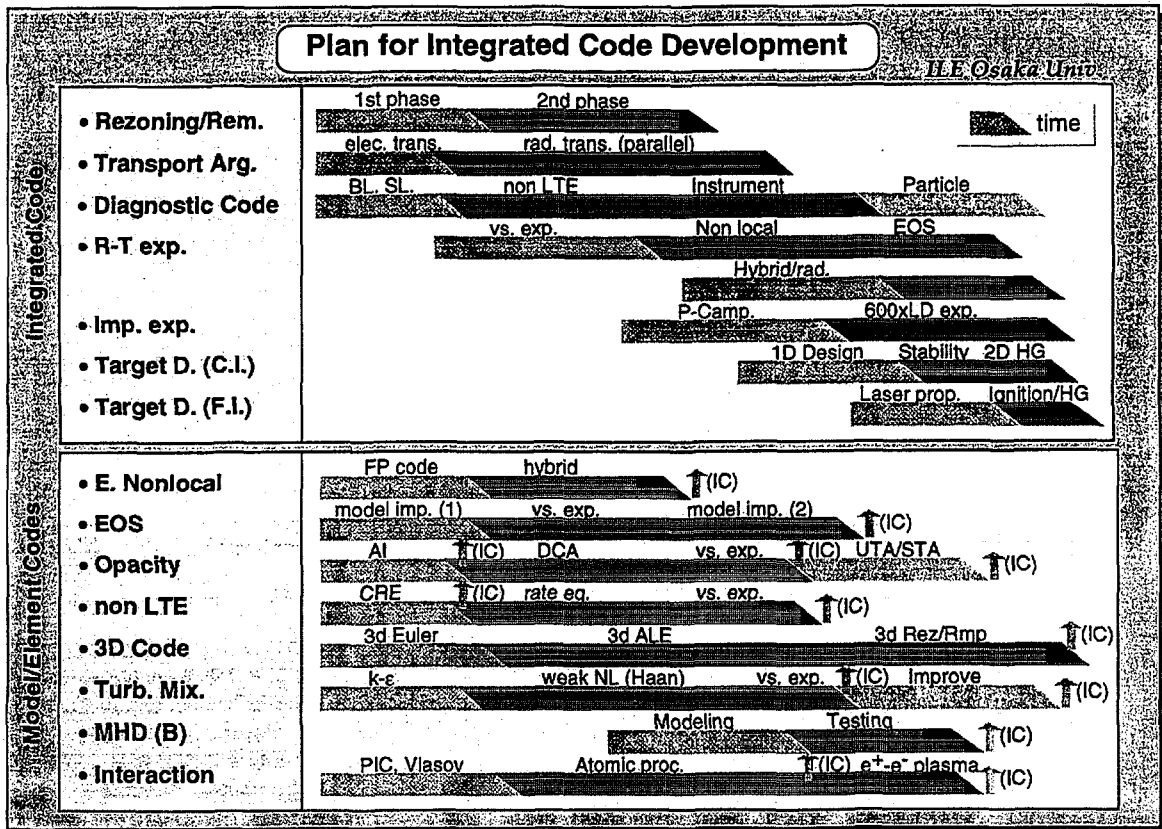


Fig. 4

## 6 . 3d Particle Simulations on Ultra Short Laser Interaction

Katsunobu NISHIHARA, Takashi OKAMOTO and Hidekazu YASUI

*Institute of Laser Engineering, Osaka University  
Suita, Osaka 565, Japan*

### ABSTRACT

Two topics related to ultra short laser interaction with matter, linear and nonlinear high frequency conductivity of a solid density hydrogen plasma and anisotropic self-focusing of an intense laser in an overdense plasma, have been investigated with the use of 3-d particle codes. Frequency dependence of linear conductivity in a dense plasma is obtained, which shows anomalous conductivity near plasma frequency. Since nonlinear conductivity decreases with  $v_0^{-3}$ , where  $v_0$  is a quivering velocity, an optimum amplitude exists leading to a maximum electron heating. Anisotropic self-focusing of a linear polarized intense laser is observed in an overdense plasma.

**Keywords:** electric conductivity, self focusing, dense plasma, ultra short pulse.

### 1. INTRODUCTION

An ultra short laser pulse may interact directly with a solid density plasma, if its pulse duration,  $\tau_L$ , is very short so that plasma expansion length,  $c_s \tau_L$ , is shorter than the skin depth  $c/\omega_{pe}$ , where  $c$ ,  $c_s$  and  $\omega_{pe}$  is light speed, sound speed and electron plasma frequency, respectively. This is quite different from a long pulse case of pulse duration longer than picosecond, in which a laser light can not penetrate over the critical density. Other feature of the ultra short laser interaction is that electrons and ions are not in a thermal equilibrium, since pulse duration is longer than the electron-ion energy relaxation time. Thus the ion coupling constant,  $\Gamma \equiv Z^2 e^2 / a k_B T_i$ , may still be greater than one, where  $a$ ,  $T_i$  and  $Z$  are an ion sphere radius ( $4\pi a^3/3 = n_i^{-1}$ ), ion temperature and ion ionization state, respectively. Both ion-ion correlation and electron shielding then play important roles to reduce high frequency conductivity. When a quivering velocity,  $v_0 = eE_0/m\omega_0$ , is greater than electron thermal speed, the conductivity depends on a laser intensity, since electron-ion scattering is determined by the quivering velocity instead of thermal speed.

In this paper we have studied these features of intense ultra-short laser interaction with the use of a 3-d strongly coupled plasma particle code "SCOPE" [1]. The code calculates particle dynamics determined by Coulomb forces among individual particles. In the force calculation, quantum diffraction and quantum symmetry are effectively introduced [2].

Recently, self focusing and filamentation of an intense laser beam have been investigated intensively related to laser acceleration and fast ignitor in ICF [3-5]. Most of previous works are laser interaction in an underdense plasma. In this paper we deal with the self-focusing of an intense laser in an overdense plasma with the use of 3-d PIC. Anisotropic self-focusing is observed in simulations.

### 2. LINEAR AND NONLINEAR HIGH FREQUENCY CONDUCTIVITY IN SOLID DENSITY HYDROGEN PLASMA

We used 500 electrons and 500 ions in a periodic cubic system. A two component plasma can be characterized by two parameters, the ion coupling constant and the electron degeneracy parameter,  $k_B T_e / \epsilon_{F0}$ , where  $\epsilon_{F0}$  is the Fermi energy at zero temperature. For a solid density hydrogen with an initial temperature of 1eV and 13.6eV, the ion coupling constant is of the order of 1 to 10, and the degeneracy parameter is greater than one for 13.6eV. The parameter used are summarized in Table 1.

Table 1 Physical parameters of solid density hydrogen plasma

density ( $\text{cm}^{-3}$ )	ion temp. (ev)	ele. temp (ev)	ion coupling const.	degeneracy parameter
$5 \times 10^{22}$	13.6	13.6	0.629	2.75
$5 \times 10^{22}$	1	13.6	8.55	2.75

Since electrons are heated very rapidly by laser electric field, but not ions, the ion-ion correlation and electron shielding becomes important. Observed ion-ion pair correlation functions without an external electric field are shown in Fig.1 for the temperatures of 1eV and 13.6eV. It is clearly seen that there is a strong ion-ion correlation, which reduces the high frequency conductivity. When an external electric field oscillating with a frequency  $\omega_0/\omega_{pe}=0.423$  is applied, rapid electron heating is shown in Fig. 2 at  $\omega_0 t \sim 9.5$  and with an quivering velocity of  $v_0/v_{te0}=2.9$ , where  $v_{te0}$  is an initial electron thermal speed.

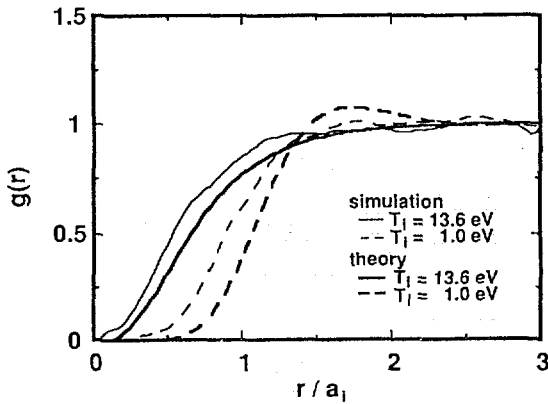


Fig. 1 Ion-ion pair distribution functions obtained by simulation (thin lines) and theory (thick lines) for ion temperature of 13eV (solid lines) and 1eV (dotted lines). Distance is normalized by ion sphere radius. Theory assumes uniform electron background.

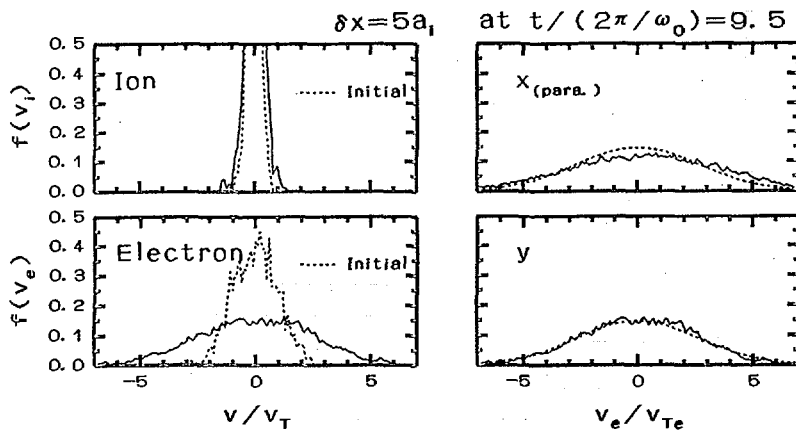


Fig. 2 Electron and ion velocity distribution functions, dotted lines represent initial values and solid lines at  $\omega_0 t=9.5$ . Isotropic electron velocity distribution is achieved.

Linear high frequency conductivity can be calculated by taking the Fourier transform of the autocorrelation of electron current. The complex high frequency conductivity is shown in Fig.3. The real part of the observed conductivity agrees well with analytical values [6] except in the frequency range of  $\omega_0 \sim \omega_{pe} \sim 2\omega_{pe}$ . The theory takes the ion-ion correlation into account through the ion formfactor and the electron shielding through the linear dielectric response function. However the collective response of a plasma is not considered in the theory. The discrepancy between the simulation results and the theory beyond the plasma frequency may be due to the collective response of the plasma. The large peak of the conductivity around  $\omega_0 \sim$

$0.2\omega_{pe}$  indicates that a laser with the wavelength of  $1\mu\text{m}$  gives high absorption rate at least for a plasma with the parameters used.

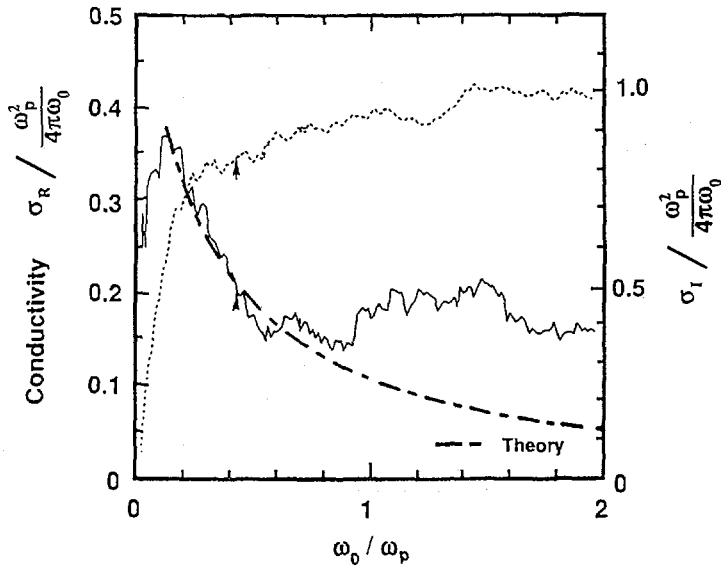


Fig. 3 Linear electric conductivity as functions of frequency. Solid line is real part and thin dotted line imaginary part. Dashed line is analytical values [6].

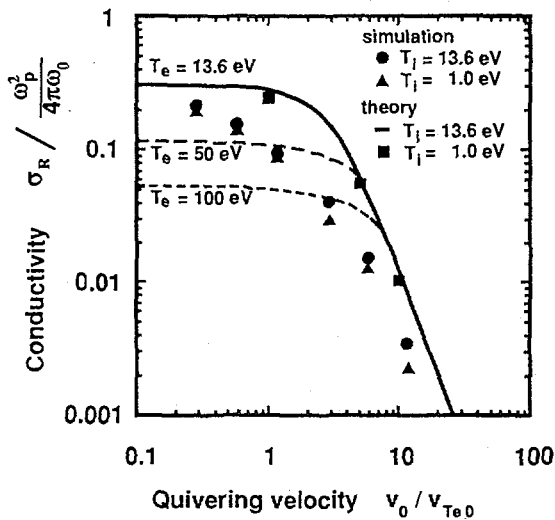


Fig. 4 Nonlinear conductivity as function of quivering velocity for initial temperatures of 1 and 13 eV. Lines represent theoretical values [6].

The nonlinear conductivity is estimated by observing directly oscillating current induced by an external electric field oscillating at the frequency of  $\omega_0/\omega_{pe}=0.423$  which corresponds to wavelength of  $0.353\mu\text{m}$ . The results are shown in Fig.4 with the theoretical values. They agree fairly well. The difference between them in the low intensity region is mainly due to rapid electron heating in the simulation. However, it is still difficult to explain the difference of the factor of 2 in the high intensity region. The nonlinear conductivity decreases with  $v_0^{-3}$  as expected, because electron-ion collision frequency is determined by the quivering velocity and proportional to  $v_0^{-3}$ .

### 3. ANISOTROPIC SELF-FOCUSING OF INTENSE LASER IN OVERDENSE PLASMA

We consider a slab plasma of which dimension is  $1.28\lambda \times 5.14\lambda \times 5.14\lambda$ , where  $\lambda$  is a laser wavelength in a vacuum. Linear polarized laser light is irradiated normal to the plasma in the x-direction. The electric field is in y direction. The vacuum regions are located in both sides of the plasma with a length of  $1.93\lambda$ . Numbers of particles and meshes are 5,268,480 for both electrons

and ions and  $128^3$ . The spatial profile of the laser is a Gaussian with  $3\lambda$  FWHM, and the temporal profile is given by a Gaussian with  $2\lambda/c$  FWHM and a flat profile follows the peak. The plasma density and the amplitude of the laser are chosen to be  $n_e/n_c=1.75$  and  $a=eE_0/m_e\omega c=2$ , respectively. Thus for the peak intensity  $\gamma_0=2.25$ , the plasma becomes transparent because of the relativistic mass effect, but not transparent for the time averaged intensity,  $\langle\gamma\rangle=1.68$ .

Spatial profiles of the magnetic field of the electromagnetic wave and the electron density are shown in Fig.5 and 6 at  $50 w_0 t$ . The magnetic field and electron density are normalized by that of the incident laser light and the critical density, respectively. As shown in Fig.5, the laser light penetrates into the overdense plasma with self-focusing. Anisotropic self-focus is clearly seen, namely the width in the magnetic field direction(z) is much narrower than that in the electric field direction y. Density holes are also anisotropic. DC magnetic field of the order of 100MGauss is generated in the plasma. The x component of the current and the magnitude of the DC magnetic field is plotted in Fig.7, which is measured at the point c in Figs. 5 and 6. Both the current and magnetic field have complex structures, elliptic shape in the center surrounded by many banana shapes. Physical mechanisms which cause these structures are not well understood yet. However the stronger self-focusing of a laser light is observed in the direction of the magnetic field of the laser light.

Even if a uniform laser light is impinged onto a plasma, anisotropic filamentation occurs in the direction of the magnetic field of the incident laser light as shown in Fig.8. The size of the filaments is the order of the wavelength of the laser light.

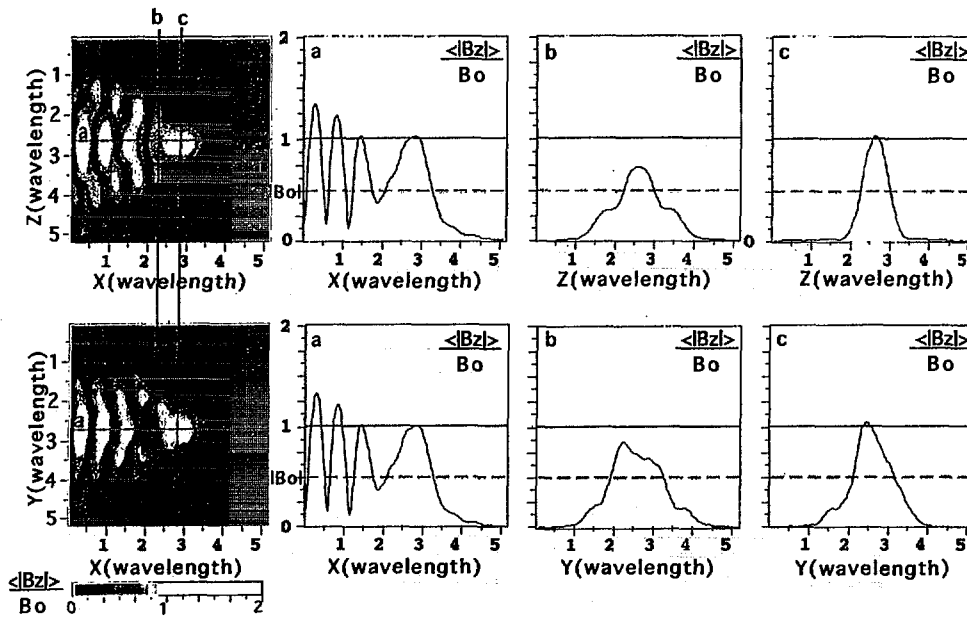


Fig. 5 Spatial profiles of magnetic field of electromagnetic wave in x-z plane (above) and x-y plane (bottom) for linear polarized wave ( $E_y, B_z$ ). Magnetic field is normalized by its incident value. a, b, and c represents profiles along the lines indicated in left figures.

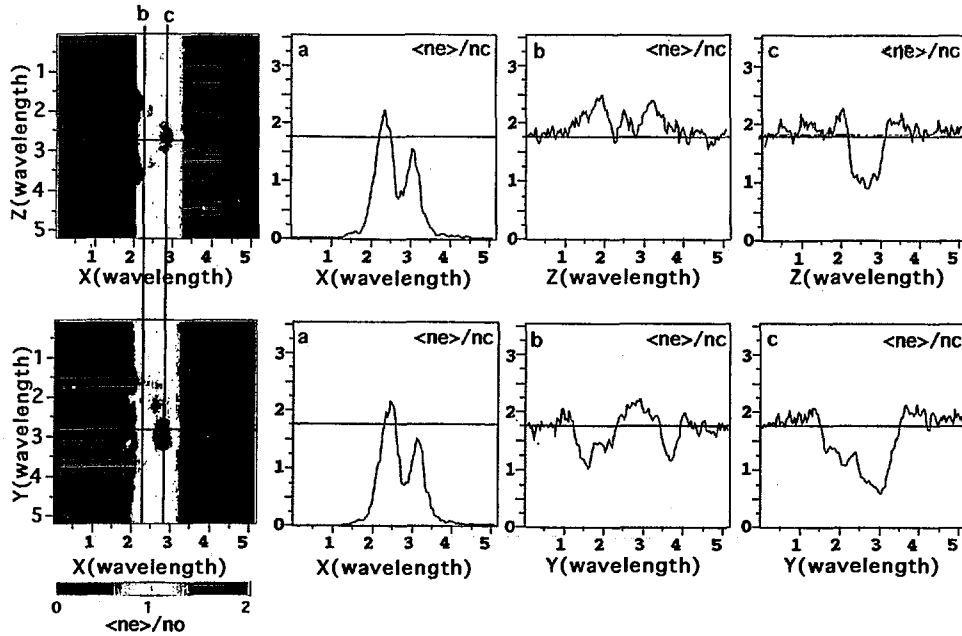


Fig. 6 Spatial profiles of electron density normalized by the critical density in x-z plane (above) and x-y plane (bottom). a, b, and c are the same in Fig. 5.

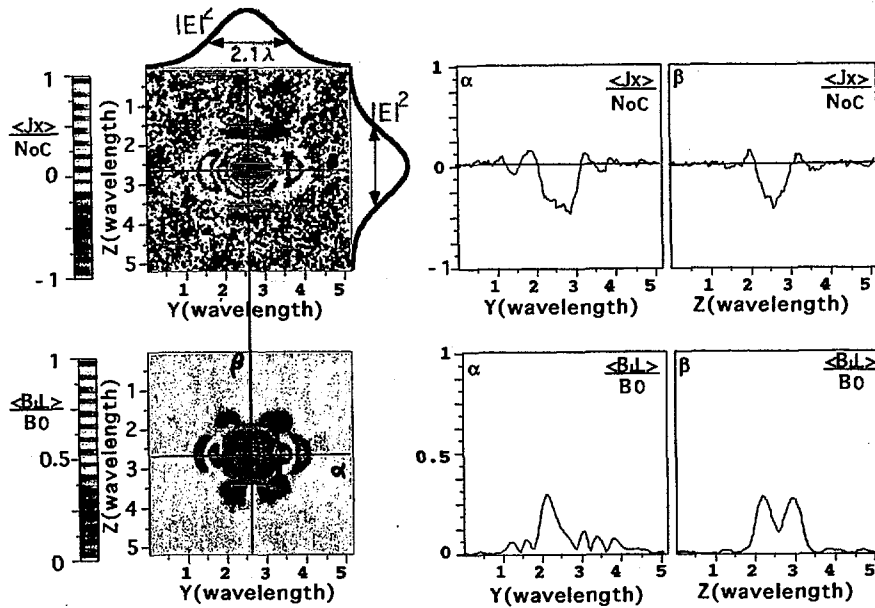


Fig. 7 Spatial distributions of current density (top) normalized by  $en_0c$  and y-component of DC magnetic field (bottom) normalized by magnetic field of the incident electromagnetic field in y-z plane at  $x/\lambda=2.8$  corresponding to the point c in Fig.5 and 6.  $\alpha$  and  $\beta$  represents the values along the lines  $\alpha$  and  $\beta$  in the left figures.

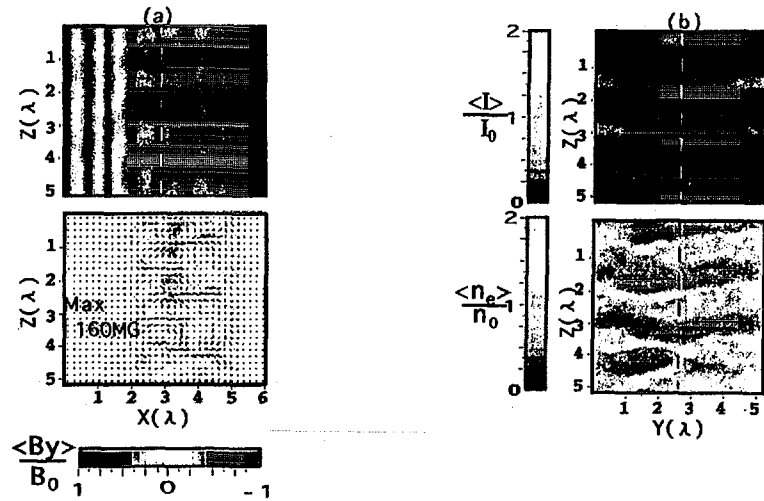


Fig. 8 (a) Spatial profile of magnetic field of electromagnetic wave ( $B_z$ ) (top) and y component of DC magnetic field (color) and current distribution (arrow) in x-z plane at the center.  
 (b) Spatial profiles of x-component of current (top) and electron density (bottom) in y-z plane at  $x/\lambda=2.93$  for uniform laser irradiation.

#### 4. CONCLUSION

Linear and nonlinear high frequency conductivities are obtained for a solid density hydrogen plasma, in which both the ion-ion correlation and electron shielding play important roles. The results indicate that there is an optimum laser wavelength and intensity resulting in high absorption efficiency.

Strong anisotropy of laser self-focusing is observed in an overdense plasma, although its physical mechanism still remains to be investigated in future.

#### REFERENCES

- [1] K. Nishihara, *Kakuyugo Kenkyu* 66, 253 (1991).
- [2] H. Furukawa and K. Nishihara, *Phys. Rev. A* 42, 3532 (1990)
- [3] A. Pakhov and I. Meyer-ter-vehn, *Phys. Rev. Lett*, 76, 3975 (1996).
- [4] G. A. Askaryan and S. V. Bulanov, *JETP Lett.* 60, 250 (1994).
- [5] M. Tabak et al, *Phys. Plasma* 1, 1626 (1994).
- [6] S. Kato et al, *Phys. Rev. A* 43, 5560 (1991).

## 7. Ultra fast atomic process in X-ray emission by inner-shell ionization

Kengo Moribayashi, Akira Sasaki, and T.Tajima<sup>†</sup>

*Advanced Photon Research Center, Kansai Research Establish, Japan Atomic Energy Research Institute, 25-1, Mii-minami-cho, Neyagawa-shi, 572, Osaka, Japan*

<sup>†</sup> *also at Fusion Studies, University of Texas at Austin, Austin, Texas 78712*

### ABSTRACT

An ultra-fast atomic process together with X-ray emission by inner-shell ionization using high intensity ( $10^{18}\text{W}/\text{cm}^2$ ) short pulse (20fs) X-ray is studied. A new class of experiment is proposed and a useful pumping source is suggested. In this method, it is found that the gain value of X-ray laser amounts to larger than 1000(1/cm) with use of the density of  $10^{22}/\text{cm}^3$  of carbon atom. Electron impact ionization effect and initial density effect as well as intensity of pumping source effect are also discussed.

**Keywords:** ultra fast atomic process, inner-shell ionization, high intensity short pulse X-ray emission, X-ray laser, carbon atom.

### 1. INTRODUCTION

An inner-shell ionization process of atoms is thought to be one of the useful method for emission of X-ray laser[1-4]. Furthermore, in the process, there are some interesting physical phenomena and applications such like (1)application of ultra-short pulse X-ray pumping source[5-9], (2)ultra-fast atomic process, and (3)interaction between high intensity short pulse X-ray and atoms as well as (4)the application to X-ray laser. Nevertheless, there are no experiment as far as we know. Further, only a small number of recent theoretical research[3, 4] exists.

The method was suggested by Duguay and Rentzepis[1] in the first place. Recently, by Kapteyn[3] and Moon *et.al.*[4], the gain value of X-ray laser amounts to about  $10\text{cm}^{-1}$  for the "water window" region with Ne atom and carbon atom, respectively. They used the density of smaller than  $10^{20}(1/\text{cm}^3)$  by about  $10^{16}\text{W}/\text{cm}^2$  in 50fs pumping source. We can get the gain value of larger than 1000/cm with use of density of  $10^{22}(1/\text{cm}^3)$  and ultra-fast atomic process by  $10^{18}\text{W}/\text{cm}^2$  in 20fs pumping source. Recently, Ueshima *et.al.*[9] have generated short pulse high intensity X-ray emission theoretically by Larmor radiation resulting from the interaction between ultra short pulse laser and plasma. In this method, it is possible to make X-ray emission with the intensity of  $10^{18}\text{W}/\text{cm}^2$  in 20fs pulse.

In this paper, we will demonstrate the ultra-fast atomic process in X-ray emission by inner-shell ionization with the use of the high intensity of  $10^{18}\text{W}/\text{cm}^2$  in short pulse of 20fs pumping

source. We take carbon atom with density of  $10^{22}\text{cm}^{-3}$  as sample. Further, we also solve the lasing condition, propose a new class of experiment, and suggest a useful pumping source.

## 2. ATOMIC PROCESSES

Fig.1 shows the atomic process of the carbon atom in X-ray emission by inner-shell ionization. The photo-ionization and the electron impact ionization cross sections ( $\sigma^P$  and  $\sigma^e$ ) are derived from the data or the empirical formula in Refs.[10] and [11], respectively. Here, the electrons and their energies are assumed to be ejected through ionization processes and the photon energy minus ionization energy, respectively. Then, the photo ionization rate ( $R^P$ ) and the electron impact ionization rate ( $R^e$ ) are given by

$$R^P = \frac{I\sigma^P}{h\nu_I} \quad \text{and} \quad R^e = \langle v_e\sigma^e \rangle n_e, \quad (1)$$

respectively, where  $I$ ,  $h\nu$ ,  $n_e$  are intensity of pumping source, photon energy, electron density, respectively. The energy levels, radiative transition probability ( $A_r$ ), and auto-ionization rate ( $A_a$ ) are calculated by Cowan's code[12, 13]. Then, the inner-shell ionization energy and ionization energy to the ground state of  $\text{C}^+$  from the ground state of C atom are about 300eV and 10eV, respectively. Further, the  $A_r$  and  $A_a$  values are about  $3 \times 10^{12}/\text{s}$  and  $10^{14}/\text{s}$ , respectively.

In order to get the gain value given by

$$\text{gain} = 2.7 \times 10^{-2} \phi_i g_{low} \left( \frac{N_{up}}{g_{up}} - \frac{N_{low}}{g_{low}} \right) f_{ul}, \quad (2)$$

following rate equations must be solved:

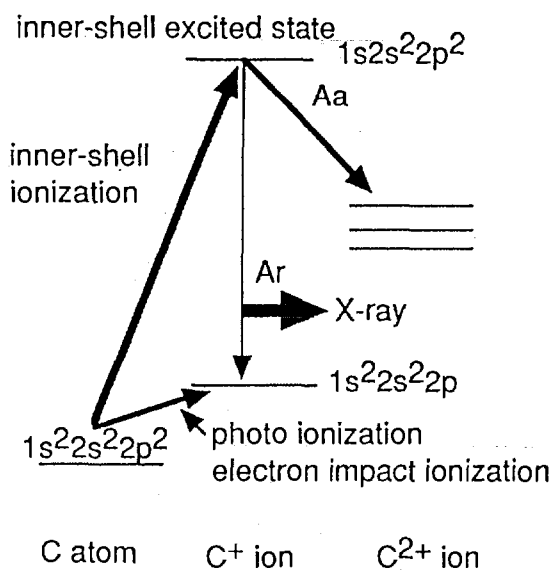


Fig.1 Atomic process in X-ray emission by inner-shell ionization.

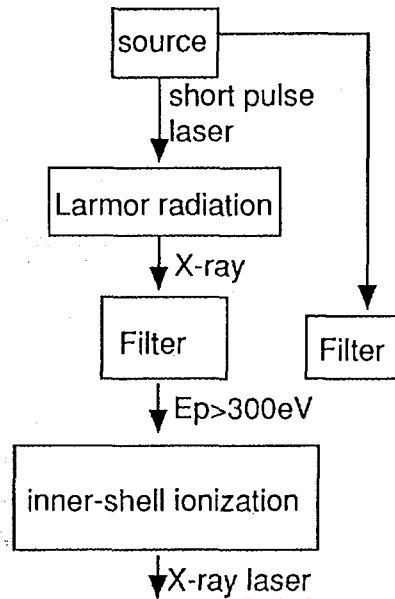


Fig.2 Our proposal of class of experiment

$$\dot{N}_0 = -(R_{up}^P + R_{low}^P + R_{low}^e)N_0, \quad \dot{N}_{up} = R_{up}^P N_0 - (A_r + A_a)N_{up}, \quad \dot{N}_{low} = (R_{low}^P + R_{low}^e)N_0 + A_r N_{up}, \quad (3)$$

where  $\phi_i$ ,  $N_0$ ,  $N_{up(low)}$ ,  $g_{up(low)}$ ,  $f_{ul}$  are the Doppler or Voigt broadening, population of C atom, populations of upper (lower) state, statistical weight of upper (lower) state, oscillator strength, respectively. The  $N_0$ ,  $N_{up}$ ,  $N_{low}$  values can be solved analytically:

$$N_0 = N_{00}e^{-R_{up}^P t}, \quad N_{up} = \frac{R_{up}^P N_{00}}{R_{up}^P - A_a}(e^{-A_a t} - e^{-R_{up}^P t}),$$

$$N_{low} = R_{up}^P N_{00}^2 < v_e \sigma^e > \frac{1}{R_{up}^P - A_a} \left\{ \frac{1}{R_{up}^P + A_a} (1 - e^{-(R_{up}^P + A_a)t}) - \frac{1}{2R_{up}^P} (1 - e^{-2R_{up}^P t}) \right\}, \quad (4)$$

where  $N_{00}$  is the  $N_0$  value at  $t=0$ . Here we consider only the fast processes, then the slow processes such like the radiative transition process can be ignored, further the  $n_e$  value can equal to the  $N_{up}$  value approximately.

### 3. PROPOSAL OF NEW CLASS OF EXPERIMENT AND SUGGESTION OF USEFUL PUMPING SOURCE

As is seen from eqs.(2) and (4), the  $R^P$  and  $R^e$  values in eq.(1) must be decreased to make  $N_{low}$  value smaller, that is, gain value larger.

In the photo-ionization cross sections of carbon atom[10], the low energy component with photon energy ( $E_p$ )  $\leq 300\text{eV}$  gives the contribution only to the ionization to the lower state. Therefore, we propose that the lower energy component should be cut and only the high photon energy component should be used.

The  $n_e$  value is almost in proportional to  $t$  and the electron impact ionization rate coefficient  $< v_e \sigma^e >$  is in inverse proportional to  $v_e$ . Therefore, the interaction time and the  $v_e$  value should be shorter and faster, respectively. To reduce the interaction time, we propose the use of high intensity short pulse pumping source because it can make all the initial C atom ionize in a moment. On the other hand, as far as the velocity is concerned, we have no idea of increasing the velocity now.

The pumping source should be high intensity short pulse X-ray as mentioned just now. In the pulse duration time of 20fs, the  $R^P$  value is requested larger than  $5 \times 10^{13}/\text{s}$  for ionizing all the atom during this duration time. Since the inner-shell photo-ionization cross section at the photon energy  $E_p$  of 1keV is  $4 \times 10^{-20}\text{cm}^2$ , we suggest the intensity of larger than  $2 \times 10^{17}\text{W}/\text{cm}^2$  to the the most useful pumping source.

Fig.2 shows our proposal of a class of the experiment. Firstly, by Larmor radiation resulting from short pulse laser with the intensity of  $\sim 10^{20}\text{W}/\text{cm}^2$ , short pulse ( $\sim 20\text{fs}$ ) high intensity ( $I \sim 10^{18}\text{W}/\text{cm}^2$ ) X-ray emits[9]. Then, with use of a filter, X-ray with  $E_p \geq 300\text{eV}$  can be selected. Lastly, as soon as this X-ray interacts with the C atom solid, the X-ray laser by inner-shell ionization method will be generated. We should use another filter in order to avoid the interaction between the short pulse laser and the solid carbon atom because it may destroy the inner-shell excited state by optical field ionization.

4. RESULTS AND DISCUSSIONS

For  $I=10^{15} \sim 10^{18} \text{ W/cm}^2$  and  $E_p=400\text{eV} \sim 1\text{keV}$ , the gain value in Eq.(2) and populations of the carbon atom, the upper and lower state are calculated. Then, the electron impact ionization effect and the initial atom density effect are discussed.

Figs.3(a) and (b) show the gain values at  $E_p=600\text{eV}$  and  $N_{00}=10^{22}/\text{cm}^3$  as a function of time without and with electron impact ionization effect, respectively. In both cases, the gain values become larger as the intensity value increases, however, a different feature for the duration time of the large gain value is seen. Namely, the duration times are more than 20fs without it and about 1fs with it, respectively. This means that the electron impact ionization plays an important role at high density.

At  $I \geq 10^{16} \text{ W/cm}^2$ , the maximum of the gain value is more than 10/cm. We found that the  $I \geq 10^{16} \text{ W/cm}^2$  values are the lasing condition. It should be noted that the gain value is more than 1000/cm at  $I = 10^{18} \text{ W/cm}^2$ .

In Fig.3(b), only the duration time with  $I=10^{18} \text{ W/cm}^2$  is longer than those with  $I \leq 10^{17} \text{ W/cm}^2$  which are almost the same among them. The reason why the difference exists is seen from Fig.4(a) and Fig.4(b), which show the populations of the carbon atom, the upper state, and lower state for  $I=10^{17}$  and  $10^{18} \text{ W/cm}^2$ , respectively. In the case of  $I=10^{18} \text{ W/cm}^2$  (Fig.4(b)), the populations of the upper state and those of the carbon atom increases and

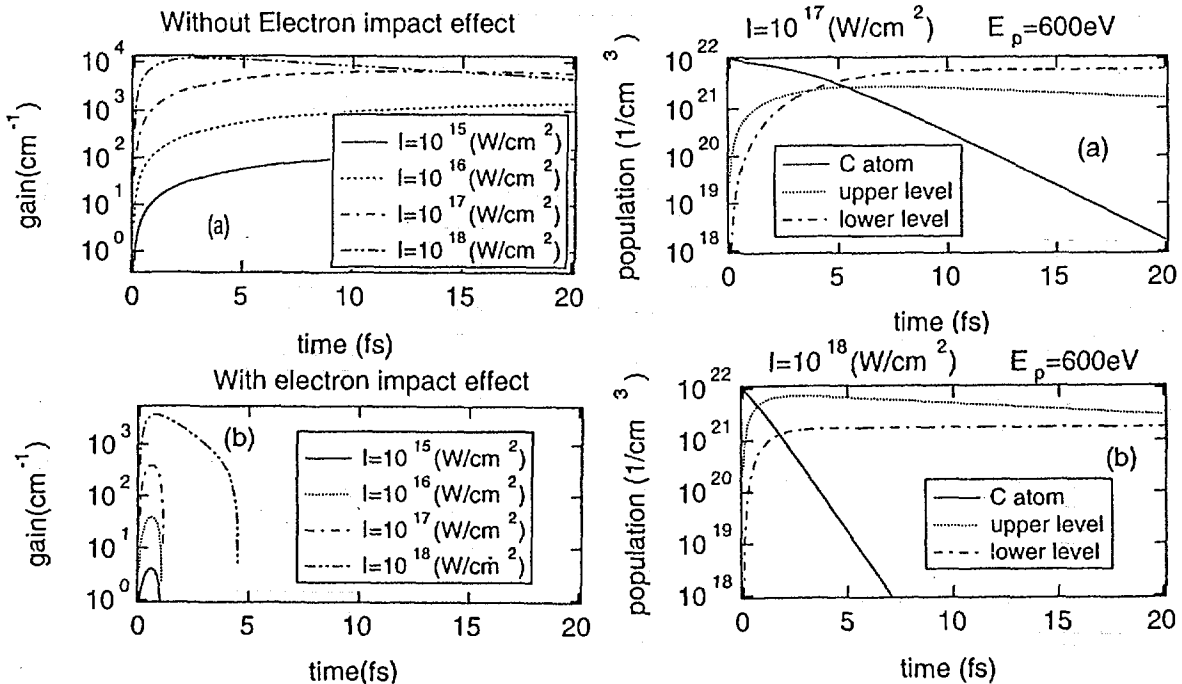


Fig.3 gain (1/cm) vs. time(fs). (a) without and (b) with electron impact ionization.

Fig.4 Population (1/cm<sup>3</sup>) vs. time (fs) (a)  $I=10^{17}$  and (b)  $I=10^{18} \text{ W/cm}^2$ .

decreases very rapidly, respectively. As a result, there is little time for the ionization process from the C atom to the lower state by electron impact. On the other hand, in the case of  $10^{17}\text{W/cm}^2$ (Fig.4(a)), all the populations change slower. Therefore, enough time for electron impact ionization exists. Further, the population of the upper state decreases because of autoionization and radiative transition processes, on the other hand, that of lower state converges soon. Therefore, the duration time can not be long even in the case of  $10^{18}\text{W/cm}^2$  high intensity.

Fig.5 shows the same as Fig.3(b) for the  $v_e$  value of the light velocity. You can see the larger gain values continue for longer time than those in Fig.3(b) though we can have no good idea for the increase of the velocity. This may be key to succeeding the method and our problem to be solved.

Fig.6 shows the same as Fig.3(b) for  $I = 10^{17}\text{W/cm}^2$  and  $N_{00}=10^{19} \sim 10^{22}/\text{cm}^3$ . At lower  $N_{00}$  value, longer duration time is seen. However, the gain value decreases as the  $N_{00}$  value becomes larger. We can also choose the best density for the request of the experiment.

### 5. SUMMARY

With use of the high intensity ( $\sim 10^{18}\text{W/cm}^2$ ) short pulse ( $\sim 20\text{fs}$ ) X-ray, we can treat the ultra fast atomic process. This is connected to the X-ray laser with the gain value of more than 1000/cm. We also propose the new experimental class and suggest the useful pumping source. Further, we discuss the electron impact ionization effect and the effect of the atom density on the X-ray laser.

In this paper, only the carbon atom is treated. However, we can choose the best atom for the request of experiment after the pumping source is decided.

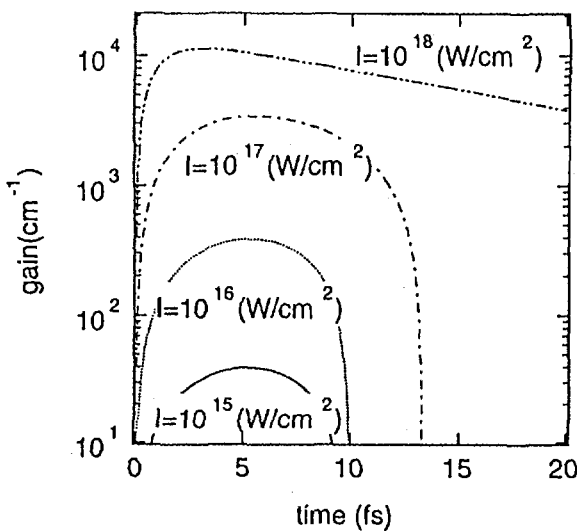


Fig.5 The same as Fig.2(b) for the electron velocity of the light one.

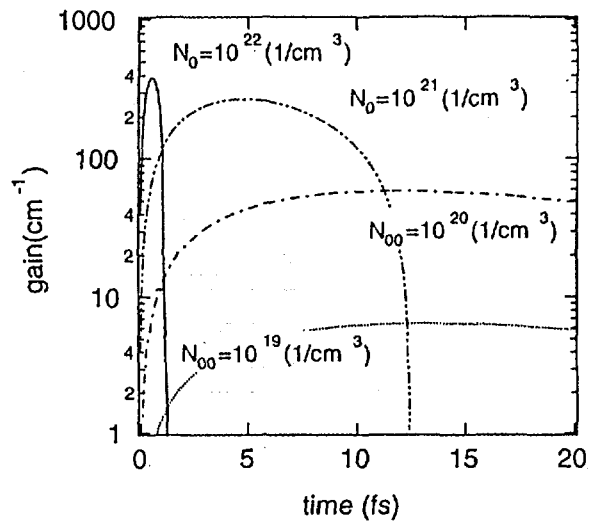


Fig.6 gain vs. time for  $I=10^{17}\text{W/cm}^2$  and  $N_{00}=10^{19} \sim 10^{22}(\text{1/cm}^3)$

## ACKNOWLEDGMENT

We wish to thank Drs. T. Kato(NIFS) and Y. Ueshima for their useful discussions. Cowan' code is employed for the calculations of the energy level, the radiative transition probability, and autoionization rate.

## References

- [1] M.A.Duguay and M.Rentzepis, *Appl.Phys.Lett.*, **10**, 350(1967).
- [2] T.S. Axelrod, *Phys.Rev.A*, **13**, 376(1976).
- [3] H.C.Kapteyn, *Applied Optics*, **31**, 4391(1992).
- [4] S.J.Moon, D.C.Eder, and G.L. Strobel, *AIP Conference Proceedings*, **332**, 262(1994).
- [5] P.Gibbon, *Phys.Rev.Lett.*, **76**, 50(1996).
- [6] J.J. Macklin, J.D. Kmetec, and C.L. Gordon, *Phys.Rev.Lett.*, **70**, 766(1993).
- [7] T.D. Donnelly, T.Ditmire, K.Neuman, M.D. Perry, and R.W. Falcone, *Phys.Rev.Lett.*, **76**, 2472(1996).
- [8] J.D.Kmetec, C.L. Gordon III, J.J. Macklin, B.E. Lemoff, G.S.Brown, and S.E.Harris, *Phys.Rev.Lett.*, **68**, 1527(1992).
- [9] Y.Ueshima, Y.Kishimoto, A.Sasaki, Y.Sentoku, and T. Tajima, this proceeding.
- [10] J.J.Yeh and I.Lindau, *Atomic data and Nucl. data tables*, **32**, 1(1985).
- [11] W.Lotz, *Z.Phys.*, **232**, 101(1970).
- [12] R.D. Cowan, *J.Opt.Soc.Am.*, **58**, 808(1968).
- [13] R.D. Cowan, "The theory of atomic structure and spectra", University of California Press, 1981.

## 8 . Stimulated Raman Backscattering at High Laser Intensities

Milos M. ŠKORIĆ<sup>\*</sup>, Toshiki TAJIMA, Akira SASAKI,  
Aleksandra MALUCKOV<sup>\*\*</sup> and Moma JOVANOVIĆ<sup>\*\*</sup>

*Advanced Photon Research Center, Kansai Research Establishment  
Japan Atomic Energy Research Institute, Osaka, 572, Japan*

*\*Vinča Institute of Nuclear Sciences, POB 522,  
11001 Belgrade, Yugoslavia*

*\*\*Faculty of Philosophy, Department of Physics  
University of Niš, 18000 Niš, Yugoslavia*

### ABSTRACT

Signatures of Stimulated Raman backscattering of a short-pulse high-intensity laser interacting with an underdense plasma are discussed. We introduce a nonlinear three-wave interaction model that accounts for laser pump depletion and relativistic detuning. A mechanism is revealed based on a generic route to chaos, that predicts a progressive increase of the backscatter complexity with a growing laser intensity. Importance of kinetic effects is outlined and demonstrated in fluid-hybrid and particle simulations. As an application, we show that spectral anomalies of the backscatter, predicted by the above model, are consistent with recent sub-picosecond, high-intensity laser gas-target measurements at Livermore and elsewhere. Finally, a recently proposed scheme for generation of ultra-short, low-prepulse laser pulses by Raman backscattering in a thin foil target, is shown.

**Keywords:** Laser Plasma, X-Ray Lasers, Stimulated Raman Scattering, Anomalous Absorption

### 1. INTRODUCTION

A large amount of research on short-pulse laser driven plasmas in gas targets /1-11/ has been motivated by interest in novel recombination and collisionally excited x-ray lasers /1-5/. In recombination schemes in order to achieve shorter XUV wavelength, high laser intensities are needed to produce ions of higher ionization potential, while higher plasma density and very low electron temperatures are required to achieve high gain. Generally taken, short wavelength-248 nm and short-pulse ~100 fs lasers are expected to be favorable /3-7/. Moreover, Lemoff et al. demonstrated a new class of XUV lasers in which intense circularly polarized fs-laser pulse is used to tunnel ionize a gaseous target with simultaneous collisional excitation by hot electrons /6/. More recently, anomalous x-ray emissions in the sub-ps laser interaction with dense gas targets were reported. It was Crane et al. of Livermore, first to point out /6/ the interrelation between anomalous x- emissions from Ne plasmas and anomalous signatures of stimulated Raman backscattering /1,2/. In this paper, we intend to clarify

signatures of stimulated Raman backscattering (SRBS) related to sub-ps high-intensity laser underdense plasma experiments /12-14/. Based on a generic model /8-9/ of SRBS we believe to be able to offer an interpretation of spectral anomalies reported at Livermore and Rutherford, and more recently elsewhere /4-9/. As a further application, the novel ultrashort –laser pulse generation scheme by SRBS in a thin foil target is proposed /15-16/. Results are demonstrated by hybrid-fluid as well as particle simulations /13,14/.

## 2. COUPLED MODE MODEL

Stimulated Raman Backscattering (SRBS) in a plasma is a paradigm of a three-wave parametric process whereby a strong incident laser light (0-pump) decays into an electron plasma wave (2) and backscattered light (1) downshifted in frequency /1,2/. This process obeys a resonant matching condition for wave frequencies and wavenumbers, in a form :

$$\omega_0 = \omega_1 + \omega_2 \quad , \quad k_0 = -k_1 + k_2$$

The standard model of SRBS described by both linear and nonlinear parametric theory is well established predicting threshold /instability growth rates and steady-state reflectivity saturation /1,2/.

It was only recently, that a generic route to complex saturated Raman regimes was revealed by some of these authors, in a form of a quasi-periodic transition to chaos via intermittent route /8,9/. Depending on control parameters (laser intensity, plasma length, etc.), Raman reflectivity signatures span from the steady-state, to coherent temporal pulsations, temporal intermittency and chaos. A comprehension of SRBS complexity and its parameter dependence has allowed possible explanation of puzzling spectral anomalies recently observed in short high-intensity laser interaction with gas targets /3-7/. Although based on a fluid approximation, the model was qualitatively confirmed in particle simulations. /12,13/.

We consider a coupled three-wave interaction (3WI) model of SRBS. In one-dimensional case, which is of major importance, the linear parametric Raman backscatter growth rate is given by

$$\gamma \approx \beta_0 \alpha^{1/2} / 2(1 - \alpha)^{1/2} \omega_0 \quad ; \quad \alpha \equiv \omega_{pe} / \omega_0 = \sqrt{n_0 / n_{cr}}$$

is the ratio between the electron plasma frequency and the frequency of the laser light. In a bounded, uniform, completely ionized plasma, the spatio-temporal evolution of coupled waves is governed by the following set of partial differential equations

$$\dot{a}_0 + V_0 a_0' = -a_1 a_2 \quad (1)$$

$$\dot{a}_1 - V_1 a_1' = a_0 a_2^* \quad (2)$$

$$\dot{a}_2 + V_2 a_2' + \Gamma a_2 + i\sigma |a_2|^2 a_2 = \beta_0^2 a_0 a_1^* \quad (3)$$

Where the dot and the prime sign designate partial temporal and spatial derivatives, respectively; given in normalized coordinates :

$$\tau = \omega_0 t, \quad \xi = x/L \quad ; \quad \text{where } a_j(\xi, \tau)$$

Are normalized, slowly varying complex amplitudes of a pump (0), backscattered wave (1) and plasma wave density (2), respectively. Matching conditions for frequency and wave numbers are assumed; each wave satisfying its linear dispersion relation. The group velocities of the waves are:

$$V_0 = c^2 k_0 / \omega_0^2 L, \quad V_1 = c^2 k_1 / \omega_0 \omega_1 L, \quad V_2 = 3v_T^2 k_2 / \omega_0 \omega_{pe} L,$$

With a plasma wave linear damping rate given by  $\Gamma$ . Damping of the light waves is neglected.

The quantity  $\beta_0$  is a relative laser pump strength, i.e. the ratio between the electron quiver velocity in the laser light and the speed of light in vacuum. :

$$v_{osc} [m/s] = 0.256 \sqrt{I} \lambda_0, \quad \text{where } I \text{ is in } W/cm^2, \text{ and } \lambda_0 \text{ is in microns.}$$

An important feature of the system is the self-modal cubic term in the plasma wave equation (3).

It appears as a nonlinear shift due to relativistic frequency detuning of a large amplitude plasma wave. We solve the system (1-3) in space-time for standard initial and boundary conditions. In the steady-state, for zero phase shift, the system predicts well known elliptic-function solutions, together with a set of (Manley-Rowe) conserved quantities /2/. However, with a nonzero phase shift ( $\sigma > 0$ ), for finite boundary conditions, invariants are broken. A violation of the steady-state condition, thus points to a nonstationary Raman saturation. A time-only version of (1-3) was studied in detail, and it was shown to exhibit bifurcation to a low-dimensional chaos under restricted conditions. Indeed, in early works on particle acceleration, transition to incoherency due to multicascading of scattered waves was readily predicted /10,11/. The spatially extended model is of more physical significance and have recently revealed rich complexity related to low-dimensional as well as spatio-temporal chaos. For completeness, we briefly review, with details available, elsewhere /8,9/. For a low pump intensity, bellow the threshold for absolute SRBS, the system (1-3) attains the steady-state (fixed point) with reflectivity saturated at a noise level /2/. Beyond the threshold Hopf bifurcation saturates to a single-periodic (limit-cycle) state. Reflectivity displays weak periodic modulations around the maximum, limited by a pump depletion, according to the Manley-Rowe relation. Another Hopf bifurcation brings a second frequency leading to a 2-torus dynamics with strong quasi-periodic pulsations. Further pump increase leads to a collapse of a torus to transit a nonlinear coherent state to a deterministic chaos. The subsequent evolution first exhibits a low-dimensional intermittency to finally result in a fully developed spatio-temporal chaos /8-9/, in a fluid model (1-3) of SRBS. Chaotic dynamics is related to plasma wave breaking followed at a kinetic level, by strong nonlinear electron acceleration /1,3,13/. In turn, hot electrons tend to Landau-damp freshly driven plasma waves to suppress instability and limit the level of a kinetic SRBS complexity to be observed. To perform studies in this direction we have recently introduced particle and hybrid- 3WI simulations.

### 3. ANOMALOUS SPECTRAL SIGNATURES

We chose to simulate conditions relevant to recent short-pulse high-intensity laser plasma experiments, to study anomalous Raman signatures, in particular, complex spectral properties. According to Livermore experiments /5-6/, deep modulations on backscatter spectra have been observed at variety of densities and intensities. Major spectral features are the large frequency extent, the irreproducibility and the broadening mainly to the blue side of standard Raman. More recent data further relate hot electron generation and x-ray emission to Raman anomalies /6,7/. To emulate some of the kinetic effects missed by the fluid 3WI model (1-3), we introduce a hybrid scheme by including effects of electron acceleration in breaking plasma waves and subsequent Landau damping on hot electrons . Assuming that plasma wave energy is transferred to suprathermal electrons we numerically solve hot electron balance equation together with 3WI set (1-3). In turn, hot electrons suppress SRBS through Landau damping-  $\Gamma$  term in (3). We further add simple transport equation to model bulk heating via partial thermalization of hot electrons. Typical simulation results for a Gaussian pulse are presented in figures 1 and 2. Anomalies, such a temporal pulsations, bursting and incoherence that result in modulated broadened blue shifted spectra are obtained. We find a consistency with recent experimental findings. Blue shift is explained to be due to a relativistic drop of plasma frequency in a large plasma wave, with a backscatter blue shifting to maintain in a resonance with a laser pump.

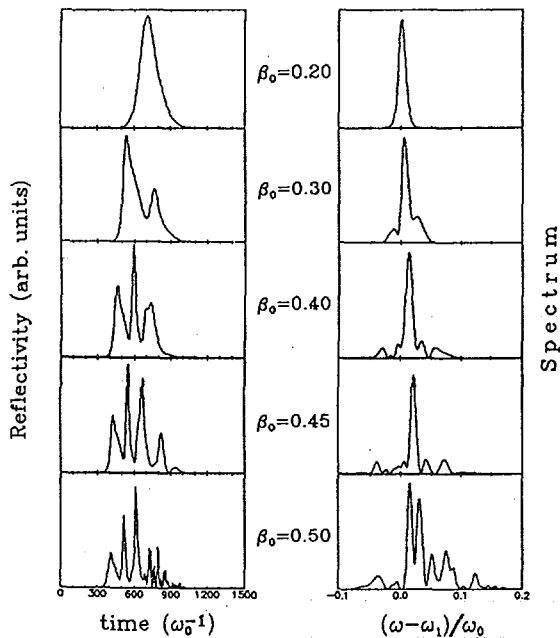


Fig. 1

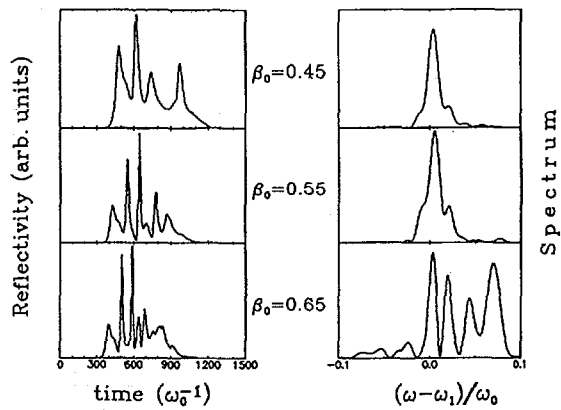


Fig. 2

FIGURE 1: Backward SRS reflectivity vs. time and frequency spectrum for a plasma layer ( $n_0 = 0.01n_{cr}$ ,  $T_e = 1keV$ ,  $L = 100c/\omega_0$ ) by different values of short (600 fs) laser pulse intensities  $\beta_0$ .

FIGURE 2: Reflectivity and spectrum for the parameters of Fig. 1, except length:  $L = 500c/\omega_0$ .

#### 4. FS LASER -PULSE GENERATION

Chirped-pulse (CPA) has become a standard technique for damage-free amplification of sub-ps laser pulses to terawatt levels and beyond. Such laser systems offer promise as convenient tools for investigation of high field phenomena, particle acceleration and generation of ultra-fast x-ray radiation. At a frontier of FS-science, sub-10 fs laser oscillators readily exist, however amplification of sub-20 fs pulses to energies greater than 0.1 mJ is difficult to achieve. Further, we discuss a method for the generation of ultra-fast fs-range pulses recently proposed /16/. The scheme is based on a SRBS in a very thin foil target. In an underdense exploding foil plasma, beyond the threshold for absolute Raman instability it was shown that reflectivity can saturate via strong quasi-periodic coherent pulsations /9/. By a proper choice of plasma parameters one can produce a low-prepulse, ultra-short backscatter pulse shorter than 10 laser periods, i.e. in the 10 fs range. In that way, one can possibly master an inexpensive and flexible method for proliferation of fs-range energetic laser pulses by using ps-scale laser drivers, commonly available. To illustrate we show particle simulation results /13/ in figure 3. After initial development, reflectivity pulsations are quickly suppressed due to intense plasma heating. We plot a diagram to find a scaling of a pulse length on intensity and plasma parameters (figure 4).

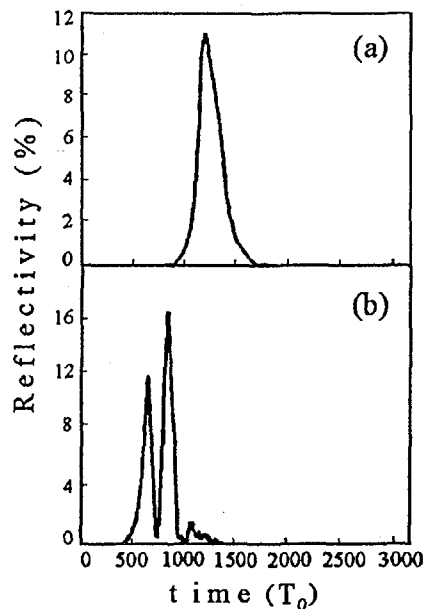


FIGURE 3. PIC simulation reflectivity versus time for two different pump intensities  $\beta_0$ : a) 0.02, b) 0.03. For the fundamental wavelength  $1.06 \mu\text{m}$ , the pulse lengths are estimated to approximately 1 ps and 0.5 ps, respectively. Plasma is underdense:  $n_0 = 0.1n_{cr}$ ,  $T_e = 0.5\text{keV}$  and  $L = 16\lambda_0$ .

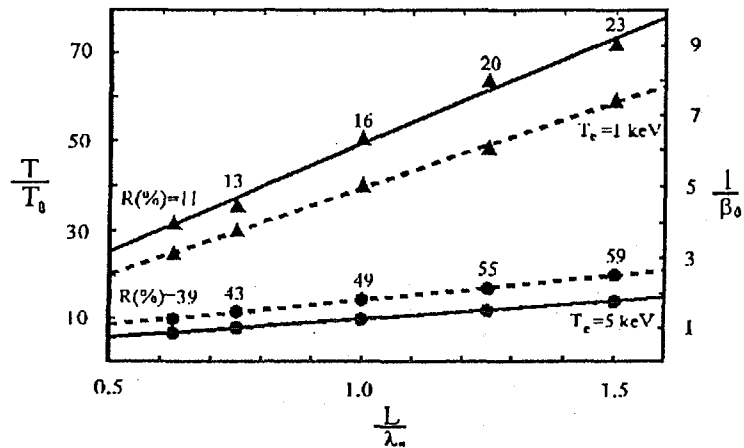


FIGURE 4. Pulse length  $T/T_0$  (full line) and laser intensity  $\beta_0$  (broken line) versus plasma foil thickness  $L$  with corresponding peak reflectivity for plasma temperatures of 1 keV (triangles) and 5 keV (dots). Plasma is underdense ( $n_0 = 0.1n_{cr}$ );  $\lambda_0$  and  $T_0$  are the laser wavelength and period, respectively.

## 5. ACKNOWLEDGEMENTS

Discussions and encouragement by Professor H. Takuma, Dr T. Arisawa, Professor K. Mima and Dr Y. Kishimoto are gratefully acknowledged. One of us (M.M.Š) was a JAERI Guest scientist at the Advanced Photon Research Center. The hospitality of Kansai Research Establishment is appreciated.

## 6. REFERENCES

1. W.L. Kruer, **The Physics of Laser Plasma Interactions** (Addison-Wesley, 1988)
2. D.W. Forslund, J.M. Kindel and E. Lindman, *Phys. Fluids* **18**, 1002 (1975)
3. S.C. Wilks et al., *Physics of Plasmas* **2**, 274 (1995)
4. C.J. Joshi and P.B. Corkum, *Phys. Today* **48**, 36 (1995); see *Science* **271**, 25 (1995)
5. C. Coverdale et al. *BAPS* **40**, 1663 (1995); *Plasma Phys. Repts* **22**, 617 (1996)
6. J.K. Crane et al., *J. Opt. Soc. Am.* **B13**, 89 (1996); *ibid.*, B.E. Lemoff et al
7. A.A. Offenberger et al. *Laser and Particle Beams* **13**, 19 (1995) ( and to appear)
8. M.M. Škorič and M.S. Jovanović, in **Laser Interaction and Related Plasma Phenomena**, Vol. 11, ed. G. Miley (AIP, N.Y., 1994); *ibid.*, Vol. 12, p.363, (AIP, 1996)
9. M.M. Škorič et al., *Phys. Rev.* **E53**, 4056 (1996); *Europhys. Lett.* **34**, 1 (1996)
10. T. Tajima and J.M. Dawson, *Phys. Rev. Lett.* **43**, 267 (1979);
11. T. Tajima, *Laser and Particle Beams* **3**, 351 (1985)
12. K-C. Tzeng, W.B. Mori and C.D. Decker, *Phys. Rev. Lett.* **76**, 3332 (1996)
13. S. Miyamoto, K. Mima, M.M. Škorič, M.S. Jovanović, *J. Phys. Soc. Japan* (to appear)
14. M.M. Škorič, A. Maluckov, A. Sasaki, T. Tajima and K. Tani, JAERI-Memo (1997)
15. M.D. Perry and G. Morou, *Science* **264**, 917 (1994); also, in *STA Today* (4/97)
16. K. Mima, M.M. Škorič et al. in **Laser Interaction and Related Plasma Phenomena**, Vol. 14, eds. E.M. Campbell and G.M. Miley (AIP, N.Y., 1997, to appear)

## 9. Plasma Simulation with the Differential Algebraic Cubic Interpolated Propagation Scheme

Takayuki UTSUMI

Advanced Photon Research Center, Kansai Research Establish,  
Japan Atomic Energy Research Institute  
Tokai-mura, Naka-gun, Ibaraki-ken 319-11, Japan

### ABSTRACT

A computer code based on the Differential Algebraic Cubic Interpolated Propagation scheme has been developed for the numerical solution of the Boltzmann equation for a one-dimensional plasma with immobile ions. The scheme advects the distribution function and its first derivatives in the phase space for one time step by using a numerical integration method for ordinary differential equations, and reconstructs the profile in phase space by using a cubic polynomial within a grid cell. The method gives stable and accurate results, and is efficient. It is successfully applied to a number of equations; the Vlasov equation, the Boltzmann equation with the Fokker-Planck or the Bhatnagar-Gross-Krook (BGK) collision term and the relativistic Vlasov equation. The method can be generalized in a straightforward way to treat cases such as problems with nonperiodic boundary conditions and higher dimensional problems.

**Keywords:** Boltzmann equation, Vlasov equation, Differential Algebraic CIP scheme

### 1 INTRODUCTION

In the analysis of nonlinear oscillations and instabilities of plasmas, numerical calculation plays an important role. Many numerical techniques have been proposed in recent years such as particle simulation [8], Fourier-Hermite transform [1], Fourier-Fourier transform [5], finite element [12], and splitting methods [4]. For the elucidation of nonlinear plasma phenomenon in super strong electromagnetic fields generated by ultra high peak and ultra short pulse lasers, the development of the high-precision and efficient numerical techniques have been continually desired.

In the meantime, the cubic interpolated propagation (CIP) scheme introduced by Yabe *et al.* [9] is a low diffusion and stable method, and is a universal solver for hyperbolic equations. The CIP scheme has been successfully applied to various complex fluid flow problems [11, 10], covering both compressible and incompressible flow, such as shock wave generation, laser-induced evaporation, and elastic-plastic flow. The basic idea is that a physical quantity within a grid cell is approximated by a cubic polynomial, of which coefficients are determined by the physical quantity and its spatial first order derivatives at each grid point. Here, the physical quantity obeys a governing equation and the equations for its spatial first order derivatives are derived by taking spatial derivatives of the master equation for the sake of consistency. These equations are

split into two phases; the nonadvection and advection phase. The equations for the advection phase are the free stream equation containing the convection terms and those for the nonadvection phase contain other dynamical terms and compression terms. For each time step, after the nonadvection phase is solved via a finite-difference approach, the quantities at each grid point are determined by interpolating profiles. Viewing the CIP scheme from the Lagrangian point of view, the nonadvection phase represents dynamics along characteristics and the advection phase reconstructs profiles on the grid points. Based on this idea, we propose the differential algebraic CIP (DA-CIP) scheme [6], in which the trajectory equations are solved explicitly and the dynamics along each stream line are solved with a numerical integration method for ordinary differential equations (ODEs) like the Runge-Kutta (RK) integration method. All the quantities appearing during derivative evaluation are estimated by using cubic polynomials. Then the DA-CIP scheme can attain higher order accuracy and avoid finite-difference operation. Furthermore, these integration methods are local in the sense that the time evolution for each grid point depends only on the local information around it, so they conform to parallel computation based on the Single Instruction Multiple Data (SIMD) model.

The Boltzmann equation is the advection equation in phase space and one of hyperbolic equations, the DA-CIP scheme might be expected to be directly applicable. Though many modern schemes has been derived from various points of view and are applicable only for specific purposes, we show in this paper that the DA-CIP scheme is a robust and efficient numerical method with a wide range of applicability.

In Section 2, we briefly describe the governing equations to be treated in this paper and the DA-CIP scheme. In Section 3, some numerical results are shown; for the Vlasov equation, the Boltzmann equation with the Fokker-Planck or the Bhatnagar-Gross-Krook (BGK) collision term and the relativistic Vlasov equation. The conclusions are given in Section 4.

## 2 GOVERNING EQUATIONS AND NUMERICAL PROCEDURE

The system we solve here is the single species one-dimensional electron (charge  $-e$ , mass  $m$ ) plasma with periodic boundary conditions. The physics of the non-relativistic unmagnetized electron plasma is described by the Boltzmann equation,

$$\frac{\partial f}{\partial t} + v \frac{\partial f}{\partial x} - E_x \frac{\partial f}{\partial v} = \left( \frac{\partial f}{\partial t} \right)_c, \quad (1)$$

where  $f = f(x, v, t)$  is the electron distribution function and  $\left( \frac{\partial f}{\partial t} \right)_c$  is the collision term. For collisionless plasma,  $\left( \frac{\partial f}{\partial t} \right)_c = 0$ , (1) is called as Vlasov equation. Supplemented by Poisson equation for electrostatic field  $E_x = E_x(x, t)$ ,

$$\frac{\partial E_x}{\partial x} = 1 - \int_{-\infty}^{\infty} f dv. \quad (2)$$

Lengths are measured in units of the Debye length  $\lambda_D = (kT/4\pi n_0 e^2)^{1/2}$ , times in units of the inverse plasma frequency  $\omega_p^{-1} = (4\pi n_0 e^2/m)^{-1/2}$ , velocities in units of the thermal velocity  $v_T = \lambda_D \omega_p$ , where  $n_0$  is the average number density of ions providing a uniform neutralizing

background.  $E_x = E_x(x, t)$  and  $f = f(x, v, t)$  are the dimensionless electric field and distribution function, respectively.

The above defined system is also extended, replacing the independent variable  $v$  with the momentum  $p_x$ , to the relativistic electromagnetic electron plasma as

$$\frac{\partial f}{\partial t} + \frac{p_x}{\gamma} \frac{\partial f}{\partial x} - (E_x + u_y B_z) \frac{\partial f}{\partial p_x} = 0, \quad (3)$$

with the relativistic factor  $\gamma = (1 + \mathbf{p}^2)^{1/2}$ , the quiver velocity  $u_y = u_y(x, t)$ , and magnetic field  $B_z = B_z(x, t)$ , assuming  $u_z = 0, B_x = B_y = 0, E_z = 0$ . The quiver velocity  $u_y$  satisfies  $\frac{\partial}{\partial t} u_y = -E_y$ . The longitudinal electrostatic field  $E_x$  obeys Poisson equation (2), and the transverse electromagnetic fields  $E_y, B_z$  obey Maxwell equations,  $\frac{\partial}{\partial t} B_z = -\frac{\partial}{\partial x} E_y, \frac{\partial}{\partial t} E_y = -\frac{\partial}{\partial x} B_z - J_y$ , where  $J_y = -u_y \int_{-\infty}^{\infty} f dp_x$  is the current density in y-direction. The units used in this system are  $\omega_p^{-1}$  for times,  $c\omega_p^{-1}$  for lengths,  $c$  for velocities, and  $mc$  for momenta, where  $c$  is the speed of light. The fields  $E_x$  or  $E_y$  are normalized to  $\omega_p mc/e$  and the field  $B_z$  to  $\omega_p m/e$ .

According to the general formulation of the DA-CIP scheme, the governing equations for the relativistic system are expressed as follows: (see [7] for the non-relativistic system)

$$\frac{Dx}{Dt} = p_x/\gamma \quad \frac{Dp_x}{Dt} = -(E_x + u_y B_z) \quad \frac{Df}{Dt} = 0 \quad (4)$$

supplemented by Poisson equation(2) and  $\frac{D}{Dt_0} u_y = -E_y, \frac{D}{Dt_{\pm}} E^{\pm} = -J_y$ , where  $E^{\pm} = (E_y \pm B_z)$ , and  $\frac{D}{Dt_0}, \frac{D}{Dt_{\pm}}$  are the differentiation along the characteristics  $x = const, x \mp t = const$ , respectively. The equations for the first derivatives of  $f, u_y, E_y, B_z$  in the phase space are obtained by taking derivatives of these equations. Then the numerical procedure of the DA-CIP scheme is as usually defined [7].

### 3 NUMERICAL RESULTS

In this section, several numerical results are described to demonstrate the accuracy and efficiency of the DA-CIP scheme for the collisionless plasma, the collisional plasma, and the relativistic collisionless plasma.

#### (a) the collisionless plasma simulation

The physics of the collisionless plasma is described by the Vlasov-Poisson equation ((1) without collision term and (2), and the results are shown elsewhere [7] for the well-understood problems; the recurrence effect for a free streaming distribution, linear Landau damping, strong nonlinear Landau damping, the two-stream instability, and the bump-on-tail instability.)

Here we only show the case for the evolution of a two-stream plasma to Bernstein-Greene-Kruskal (BGK) equilibria with the initial condition

$$f(x, v, 0) = \frac{\mu}{\sqrt{(2\pi)}} \frac{(2 - 2\xi)}{(3 - 2\xi)} \left(1 + \frac{v^2/2}{(1 - \xi)}\right) e^{(-v^2/2)} (1 + A_1 \cos(k_1 x) + A_2 \cos(k_2 x + \psi)), \quad (5)$$

where  $\mu = 1, \xi = 0.9, \psi = \pi/5, A_1 = 10^{-3}, A_2 = 10^{-6}, k_1 = 0.25,$  and  $k_1 = 0.5$ . Figure 1 shows that at first the two-hole structure appears at  $t \simeq 80$ , then two holes start coalescence due to the perturbation term  $A_2 \cos(k_2 x + \psi)$ , and finally one-hole BGK structure appears and persists

from  $t \simeq 240$ . In the other computer experiment setting  $A_2 = 0$ , the two holes do not merge and a two periodic BGK structure is observed.

(b) the collisional plasma simulation

Due to the notorious difficulty of solving the Boltzmann equation, some simplified collision models are introduced. Perhaps the most useful of these are the BGK model [2] and the simplified Fokker-Planck model [3]. These collision models are easily incorporated in the DA-CIP scheme by evaluating the collision terms on each characteristics in the Lagrange phase.

The collisional effects with the BGK model is examined for the bump-on-tail case. The collision term is  $(\frac{\partial f}{\partial t})_c = \nu(f_{eq} - f)$ , where  $\nu$  is the collision frequency and  $f_{eq}$  the local Maxwellian. The initial distribution function is chosen as

$$f(x, v, 0) = \frac{1}{\sqrt{(2\pi)}} (n_p e^{-v^2/2} + n_b (e^{-((v-V_0)/v_0)^2/2} + e^{-((v+V_0)/v_0)^2/2})) (1 + A \cos(kx)), \quad (6)$$

where  $n_p = 0.9$ ,  $n_b = 0.1$ ,  $V_0 = 4.5$ ,  $v_0 = 0.5$ ,  $A = 0.05$ , and  $k = 0.3$ . Figure 2 shows the evolution of the first mode of the electrostatic field. For collisionless case ( $\nu = 0$ ), the unstable mode grows exponentially until it saturates because of particle trapping. After saturation, the electric fields undergoes oscillations at the trapping frequency [7]. In Figure 2, however, we can see that more particles are detrapped and the oscillations are destroyed by increasing  $\nu$ .

Next, we investigated the collisional effects with a simplified Fokker-Planck model for the two beam instability case. The collision term is  $(\frac{\partial f}{\partial t})_c = \frac{\partial}{\partial v}(\beta v f + D \frac{\partial}{\partial v}(f\beta))$ , where  $\beta$  is the collision frequency and  $D$  a diffusion coefficient. In this task,  $\beta$  is taken to have the form  $\beta = \nu_0(3\bar{v}^2)^{3/2}/(2v^2 + \bar{v}^2)^{3/2}$ , corresponding to Coulomb collision, where  $\bar{x}$  means to take the average of  $x$ .  $D$  is given by  $D = \beta v^2/\bar{\beta}$  from the energy conservation condition. Figure 3 shows the results of the two-stream instability with the initial condition

$$f(x, v, 0) = (2\pi)^{-1/2} v^2 \exp(-v^2/2) (1 + A \cos(kx)), \quad (7)$$

where  $A = 0.05$ ,  $k = 0.5$ . The amplitude of the electrostatic field in Fig. 3 shows that the initial transients are little affected by collisions, whereas the following profiles are damped in amounts depending to  $\nu_0$ . The distribution function in Fig. 3 shows the two beams to coalesce filling up the valley.

(c) the relativistic collisionless plasma simulation

In the investigation of the laser-plasma accelerators, the particles at relativistically high energy should be considered. The physics of the relativistic collisionless plasma is described by (3). We solved the stimulated Raman scattering (SRS) case with the initial condition

$$f(x, p_x, 0) = ((1-\alpha)(2\pi T_1)^{-1/2} \exp(-p_x^2/2T_1) + \alpha C \exp(-(\gamma-1)/T_2)) (1 + A \cos(k_e x)), \quad (8)$$

where  $\alpha = 0.05$ ,  $T_1 = 15 keV/mc^2$ ,  $T_2 = 100 keV/mc^2$ ,  $A = 0.01$ ,  $k_e = 1.2$ , and  $C$  is a normalization constant. The initial pump electromagnetic wave is taken as

$$E_y = E_0 \cos(k_0 x) \quad B_z = \frac{k_0 E_0}{\omega_0} \cos(k_0 x) \quad (9)$$

where the wavenumber  $k_0$  is 2.4, the magnitude  $E_0$  is 0.32, and  $\omega_0 = (1 + k_0^2)^{1/2}$ , corresponding intensity is  $1.8 \times 10^{14} W/cm^2$  for a  $10.6 \mu m$   $CO_2$  laser. With these conditions, the Forward SRS

instability occurs involving three waves; the incident pump wave, a scattered electromagnetic wave, and an electron plasma wave.

Figure 4 shows the time history of the energy exchange between these three waves. The 3D surface representing distribution function in Fig.5 exhibits the acceleration of positive velocity particles.

## 4 Conclusions

In this work we have shown the DA-CIP scheme can be applied to solve the collisionless plasma, the collisional plasma, and the relativistic collisionless plasma that describes a plasma with a homogeneous background plasma of opposite charge. The DA-CIP code solved a number of initial value problems stably, accurately, and efficiently. In principle, the DA-CIP scheme can be extended to solve more complicated problems such as problems with nonperiodic spatial boundary conditions, two- and three-dimensional problems, and problems with external electromagnetic field.

## References

- [1] T. Armstrong and D. Montgomery. *Physics of Fluids*, 12(10):2094–2098, 1969.
- [2] P. Bhanagar, E. Gross, and M. Krook. *Physical Review*, 94:511, 1954.
- [3] S. Chandrasekhar. *Review of Modern Physics*, 15:1, 1943.
- [4] C. Z. Cheng and G. Knorr. *Journal of Computational Physics*, 22:330–351, 1976.
- [5] A. J. Klimas. *Journal of Computational Physics*, 50:270–306, 1983.
- [6] T. Utsumi. *CFD journal*, 4(2):225–238, 1995.
- [7] T. Utsumi, T. Kunugi, and J. Koga. *JAERI-memo*, 09-115, 1997.
- [8] S. Wollman and E. Ozizmir. *SIAM J. Numerical Analysis*, 33(4):1377–1409, 1996.
- [9] T. Yabe and T. Aoki. *Computer Physics Communications*, 66(3):219–232, 1991.
- [10] T. Yabe and *et al.* *Geophy. Res. Lett.*, 22:2429–2432, 1995.
- [11] T. Yabe and F. Xiao. *Nucl. Eng. and Design*, 155:45–53, 1995.
- [12] S. I. Zaki and L. R. T. Gardner. *Journal of Computational Physics*, 79:184–199, 1988.

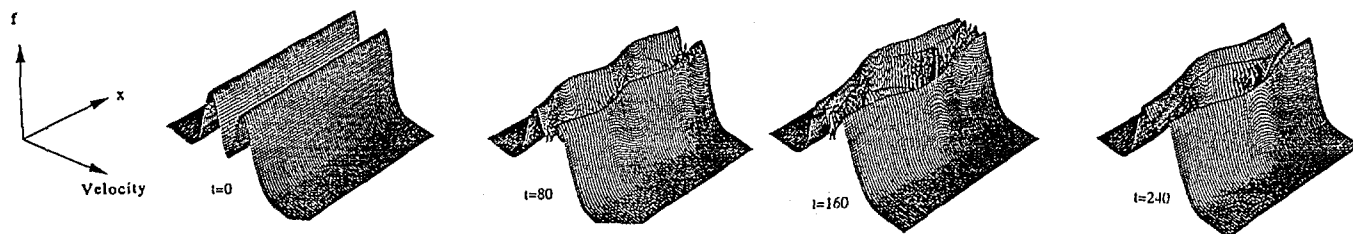


Figure 1. The over-view of the distribution function showing the appearance of two-hole structure and its subsequent coalescence in the two-stream instability.

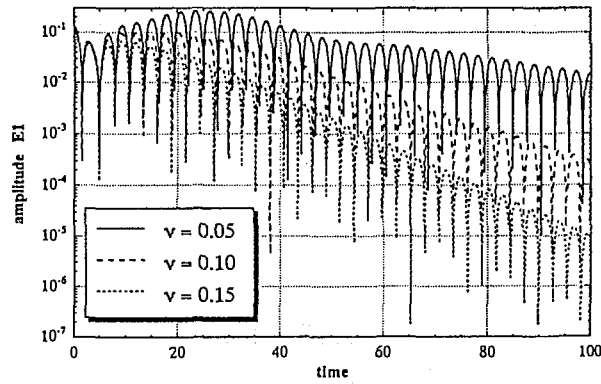


Figure 2. Evolution of the amplitude of the first electrostatic mode for the bump-on-tail instability with BGK collision term.

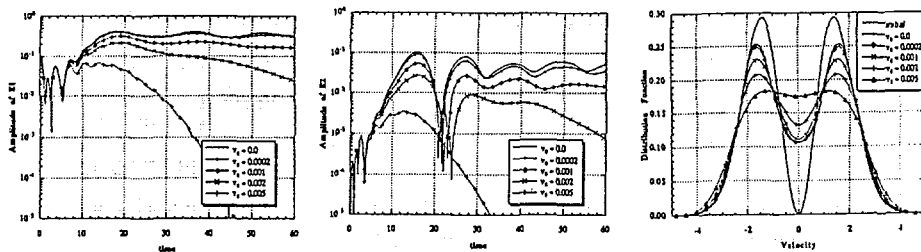
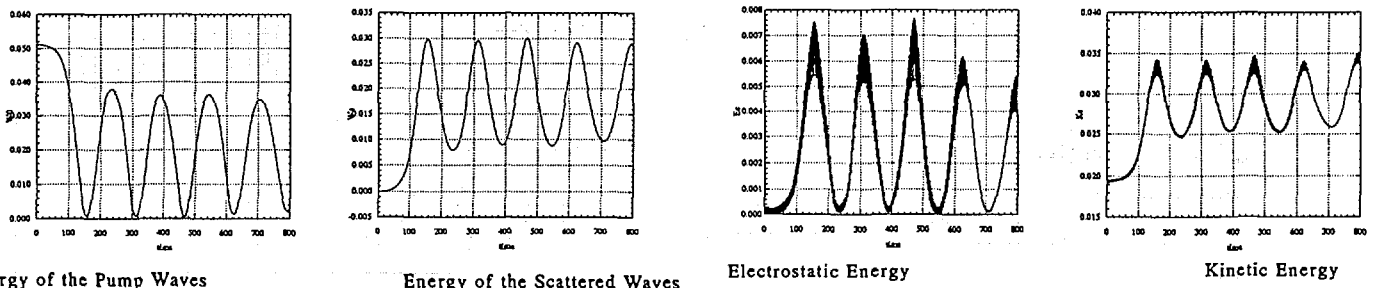


Figure 3. Two beam instability. Evolution of the amplitude of the first and second electrostatic mode, and the distribution function compared at  $t=0, 80$ .



Energy of the Pump Waves      Energy of the Scattered Waves      Electrostatic Energy      Kinetic Energy

Figure 4. Evolution of the energy of the pump wave, the energy of the scattered wave, the electrostatic energy and the kinetic energy for the forward SRS.

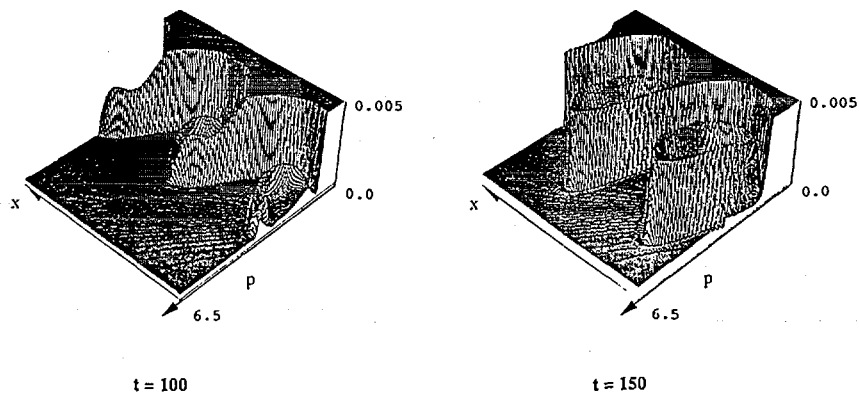


Figure 5. The 3D plot of the distribution function of the accelerated particles for the forward SRS.

## 10. Correlations in a Partially Degenerate Electron Plasma

Junzo CHIHARA

*Advanced Photon Research Center,  
Japan Atomic Energy Research Institute,  
Tokai, Ibaraki 319-11, Japan*

### ABSTRACT

The density-functional theory proves that an ion-electron mixture can be treated as a one-component liquid interacting only via a *pairwise* interaction in the evaluation of the ion-ion radial distribution function (RDF), and provides a set of integral equations: one is an integral equation for the ion-ion RDF and another for an effective ion-ion interaction, which depends on the ion-ion RDF. This formulation gives a set of integral equation to calculate plasma structures with combined use of the electron-electron correlations in a partially degenerate electron plasma. Therefore, it is important for this purpose to determine the electron-electron correlations at a arbitrary temperature. Here, they are calculated by the quantal version of the hypernetted chain (HNC) equation. On the basis of the jellium-vacancy model, the ionic and electronic structures of rubidium are calculated for the range from liquid metal to plasma states by increasing the temperature at the fixed density using the electron-correlation results.

**keywords:** degenerate electron plasma, ionization, atomic structure, radial distribution function, plasma, liquid metal

### 1 INTRODUCTION

In the standard theory, a liquid metal is treated as a one-component liquid interacting via a binary effective potential, which is determined by the pseudopotential formalism; a pseudopotential is introduced either by first-principles calculations or by adjusting parameters involved in model potentials to some experimental results. In this treatment, the ionic structure is determined independently of the electronic structure in a liquid metal. Therefore, this usual method to treat a liquid metal can not be extended to calculate the plasma structure, since we can not set up this kind of the pseudopotential for a plasma.

Previously, we have proposed a set of integral equations for radial distribution functions (RDF's) in an electron-ion mixture on the basis of the density functional (DF) theory in the quantal hypernetted (QHNC) approximation.<sup>1,2</sup> The QHNC equations are derived from exact expressions for the electron-ion and ion-ion RDF's in an electron-ion mixture: these exact expressions are only formal results derived from the DF theory. Already, we have applied this approach to liquid metallic hydrogen,<sup>1</sup> lithium,<sup>3</sup> sodium,<sup>4</sup> potassium<sup>5</sup> and aluminum<sup>6</sup> obtaining ion-ion structure factors in excellent agreements with experiments. Recently, we have performed a first-principles molecular dynamics based on the QHNC theory for alkali metals, and obtained structure factors, where a small deviation between experiment and the QHNC result disappears.<sup>7</sup>

In a plasma such as produced by the laser compression for example, the ionic valency  $Z_I$  and the electron-ion interaction  $v_{eI}(r)$  may vary over a wide range as its temperature and density change. As a consequence, it is significant in the treatment of plasmas that our method can calculate these quantities in a self-consistent manner using the atomic number of the system as

the only input data. A liquid metal can be considered as one kind of a high-density plasma. Therefore, it is important that the QHNC method has been successfully applied to liquid metals which have reliable experimental data. In order to treat plasmas including liquid-metal state, the electron-electron correlation must be calculated for temperatures from zero to arbitrary temperature. In this work, we show that the QHNC equation for the electron gas can provide the electron correlation at arbitrary temperature, with use of which we show to calculate plasma structures taking rubidium as an example by increasing the temperature at the fixed density of liquid-metal state.

## 2 QHNC METHOD

A liquid metal or a plasma can be modeled as a mixture of electrons and ions interacting through pair potentials  $v_{ij}(r)$  [ $i, j = e$  or  $I$ ]. Applying the DF theory to this electron-ion mixture model, the ion-ion and electron-ion RDF's  $g_{ii}(r)$  are exactly expressed in terms of direct correlation functions (DCF's)  $C_{ij}(r)$  and bridge functions  $B_{ii}(r)$  as follows:<sup>2</sup>

$$g_{ii}(r) = n_i^0(r|U_i^{\text{eff}})/n_i^i, \quad (1)$$

$$U_i^{\text{eff}}(r) \equiv v_{ii}(r) - \frac{1}{\beta} \sum_l \int C_{il}(|\mathbf{r} - \mathbf{r}'|) n_l^l [g_{ll}(r) - 1] d\mathbf{r}' - B_{ii}(r)/\beta. \quad (2)$$

Here,  $n_i^i$  is the number density and  $n_i^0(r|U_i^{\text{eff}})$  is the density distribution of the noninteracting system. It is shown from these expressions that the electron-ion mixture can be described as a one-component fluid interacting only via pairwise interaction  $v_{\text{eff}}(r)$ . That is, these expressions for  $g_{ii}(r)$  can be transformed into a set of exact integral equations for the one-component model of liquid metals: one is an usual integral equation for the DCF  $C(r)$  of a one-component fluid:

$$C(r) = \exp[-\beta v_{\text{eff}}(r) + \gamma(r) + B_{II}(r)] - 1 - \gamma(r), \quad (3)$$

with an interaction  $v_{\text{eff}}(r)$  and the other an equation for  $v_{\text{eff}}(r)$ , that is expressed in the form of an integral equation for the electron-ion DCF  $C_{eI}(r)$ :

$$\hat{B}C_{eI}(r) = n_e^0(r|v_{eI} - \Gamma_{eI}/\beta - B_{eI}/\beta)/n_e^e - 1 - \hat{B}\Gamma_{eI}(r), \quad (4)$$

since the effective interionic interaction  $v_{\text{eff}}(r)$  is given by

$$\beta v_{\text{eff}}(Q) \equiv \beta v_{II}(Q) - \frac{|C_{eI}(Q)|^2 n_e^e \chi_Q^0}{1 - n_e^e C_{ee}(Q) \chi_Q^0}, \quad (5)$$

where  $n_e^0(r|U_e^{\text{eff}})$  is determined by solving the wave equation for an electron under the external potential  $U_e^{\text{eff}}(r)$ . Here,  $\chi_Q^0$  is the density response function of the noninteracting electrons,  $n_e^e$  is the electron density,  $\hat{B}$  being an operator to represent some quantum effect and  $\gamma(r) \equiv \int C(|\mathbf{r} - \mathbf{r}'|) n_0^I [g_{II}(r') - 1] d\mathbf{r}'$ .

The QHNC equation can be obtained from Eqs. (3) and (4) by introducing the following five approximations:<sup>2</sup> (1)  $B_{eI} \simeq 0$  (the HNC approximation). (2) The bridge function  $B_{II}$  of the ion-electron mixture is approximated by that of one-component hard-sphere fluid (Modified HNC

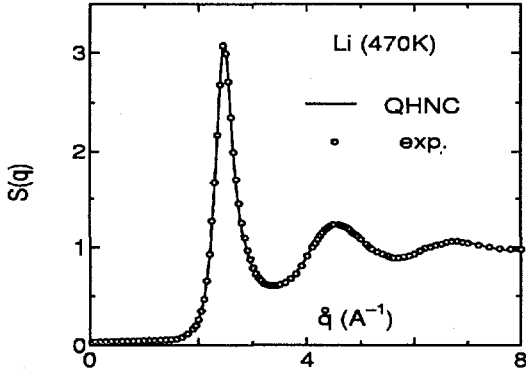


Figure 1: The ion-ion static structure factor  $S_{II}(Q)$  for liquid Li at temperature 470 K: solid curve, the QHNC result; o, experiment.<sup>10</sup>

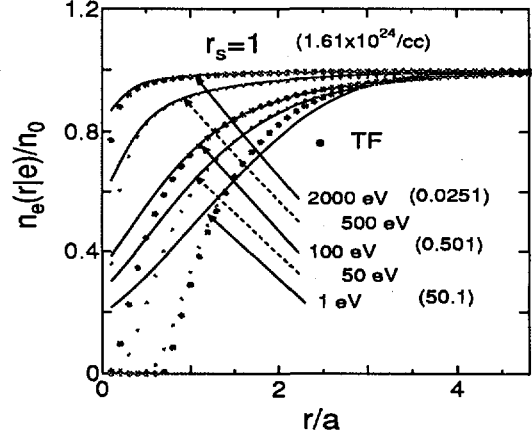


Figure 2: Electron-electron correlations at the density  $r_s = 1$  for temperatures from 1 eV to 2000 eV.

approximation<sup>8</sup>). (3)  $C_{ee}(Q) \simeq -\beta v_{ee}(Q)[1 - G^{iell}(Q)]$  in terms of the the local-field correction (LFC)  $G^{iell}(Q)$  of the jellium model. (4) An approximate  $v_{ei}(r)$  is obtained by treating a liquid metal as a nucleus-electron mixture<sup>9</sup> in the form:

$$v_{ei}(r) = -Z_A e^2 / r + \int v_{ee}(|\mathbf{r} - \mathbf{r}'|) n_e^b(r') d\mathbf{r}' + \mu_{XC}(n_e^b(r) + n_0^e) - \mu_{XC}(n_0^e), \quad (6)$$

where  $n_e^b(r)$  is the bound-electron distribution and  $\mu_{XC}(n)$  the exchange-correlation potential in the local-density approximation. (5)  $v_{II}(r)$  is taken as pure Coulombic.

Under these approximations, a set of integral equations can be solved to determine the electron-ion and ion-ion correlations together with the ionization and electron bound states. Figure 1 is an example calculated from this procedure: the structure factors of Li liquid. The full curve is the QHNC result, which exhibits an excellent agreement with experiment denoted by white circles. From this example, we can expect the QHNC method to give an accurate description of strongly coupled plasmas.

However, when we apply the QHNC method to plasmas, there occur the following problems: for liquid metal where the electron gas is treated in the absolute zero temperature, the LFC involved in the electron-electron DCF has been calculated by many persons. To treat a plasma, this electron-electron DCF must be evaluated at arbitrary temperature. The electron-density distribution under the external potential can be obtained by solving wave equation generally. However, at high temperature it is difficult to determine this density distribution from the wave equation, since it becomes nearly the classical Boltzmann factor:  $n_e^0(r|U_{eff}) = \sum_i f(\epsilon_i) |\psi_i(r)|^2 \Rightarrow n_0^e \exp[-\beta U_{eff}]$ . Here, we apply the QHNC equation to obtain the electron-electron DCF,

$$n_e(r|e) = n_e^0(r|U_{eff}) = \sum_i f(\epsilon_i) |\psi_i(r)|^2 \quad (7)$$

with

$$\beta U_{eff}(r) \equiv \beta v_{ee}(r) - \int C_{ee}(|\mathbf{r} - \mathbf{r}'|) [n_e(r'|e) - n_0] d\mathbf{r}', \quad (8)$$

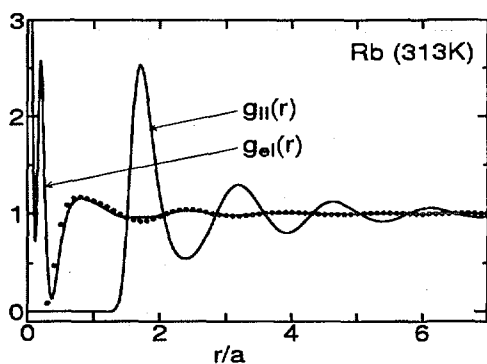


Figure 3: The electron-ion and ion-ion radial distribution functions for liquid Rb: solid curve, the QHNC result; •, the electron-ion RDF derived by the use of the Ashcroft potential.

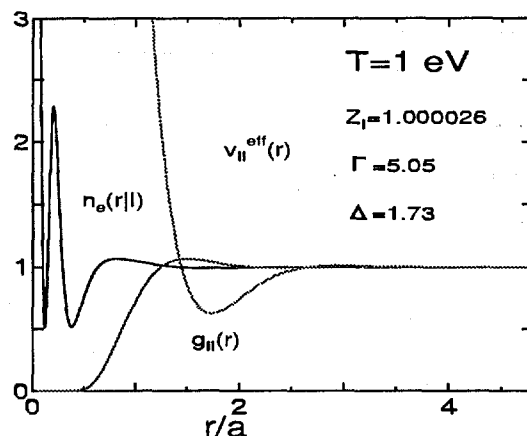


Figure 4: The electron-ion and ion-ion RDF's together with effective ion-ion interaction at temperature 1 eV.

which reduces to the well known HNC equation for classical electron gas in the high temperature limit. Here, the DCF for one-component system is defined by

$$n_0 C_{ee}(Q) = 1/\chi_Q^0 - 1/\chi_Q^{ee} = -\beta v_{ee}(Q)[1 - G(Q)]. \quad (9)$$

The Fourier transform of the density distribution yields the following bootstrap relation for  $C_{ee}(Q)$  with combined use of Eqs. (7) and (8):

$$\mathcal{F}_Q[n_e(r|e) - n_0] = 1/[1 - n_0^e C_{ee}(Q)\chi_Q^0] - 1. \quad (10)$$

The electron-electron correlation, that is, the electron density distribution around a fixed electron is shown in Fig.2 calculated for a partially degenerate electron plasma at the density  $1.61 \times 10^{24}/\text{cm}^3$  ( $r_s = 1$ ) varying the temperature from 1 eV to 2000 eV. Degeneracy is denoted by  $\Delta = E_F/kT_B$ , which is defined by Fermi energy over temperature. When the degeneracy is high such as temperature 1 eV, the Thomas-Fermi (TF) approximation denoted by full circles gives the density distribution quite different from that calculated by the wave equation. When the temperature is increased to 100 eV, the TF result becomes identical to that from the wave equation except near the origin. When the temperature approaches 2000 eV, the electron-electron correlation reduces to the classical one. From this calculation, we can obtain the electron-electron DCF, which determine plasma properties in terms of the LFC  $G(Q)$ .

As a first step, we don't perform a full self-consistent calculation as was done in liquid metals. Instead, in order to obtain the ion-core structure and the electron-ion correlation, we take the jellium-vacancy model, where the following three approximations are introduced in the electron-ion interaction:

$$\beta v_{eI}^{\text{eff}}(r) = \beta v_{eI}(r) - \int C_{ee} \delta n_{eI} dr' - \int C_{eI} \delta n_{II} dr'. \quad (11)$$

(1) The ion-ion RDF involved above is approximated by the step function:  $g_{II}(r) = \theta(r - R)$ , (2) the electron-ion DCF by pure coulomb force:  $C_{eI}(r) = -\beta v_{eI}^c(r)$ , and (3) the last approximation is replacement of the electron-electron DCF by that of the one-component plasma:  $C_{ee}(r) = C_{ee}^{\text{jell}}(r)$ . Then, a problem to determine the electron-ion RDF becomes identical with the problem

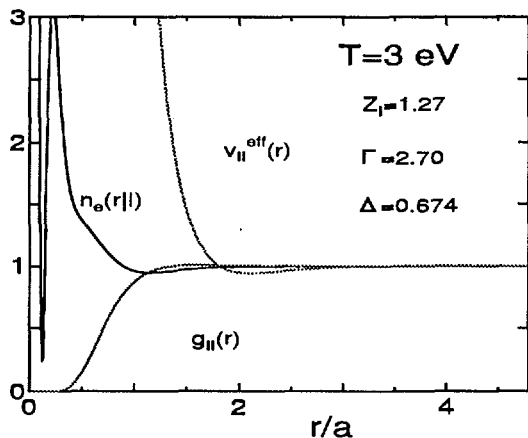


Figure 5: The electron-ion and ion-ion RDF's together with effective ion-ion interaction at temperature 3 eV.

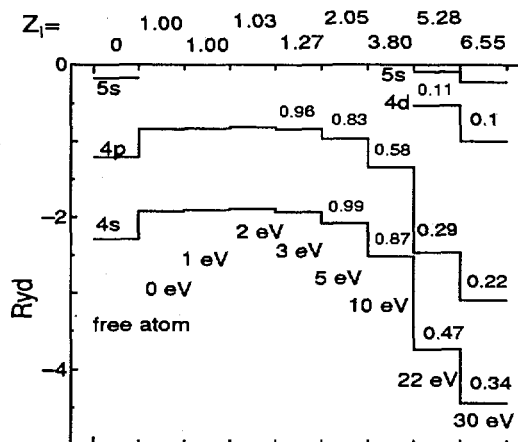


Figure 6: The temperature variation of outer bound levels in the Rb ion in a plasma. Numbers attached to bound levels denote the occupation numbers.

to determine the electron distribution around a fixed nucleus at the center of the spherical-vacancy in the jellium background. By solving these integral equations, we can obtain the electron-ion DCF, from which the ion-ion effective interaction is determined from the formula:

$$\beta v_{\text{eff}}(Q) \equiv \beta v_{\text{II}}(Q) - \frac{|C_{ei}(Q)|^2 n_0^e \chi_Q^0}{1 - n_0^e C_{ee}(Q) \chi_Q^0} \quad (12)$$

with the combined use of the electron-electron DCF. Here, we apply these equations to Rb at the fixed density of normal liquid metal: temperatures are varied from 0 to 30 eV in order to investigate how the liquid metal state changes into the plasma state.

The electron-ion RDF of Rb liquid is plotted in Fig. 3 along with the ion-ion RDF. The electron-ion RDF from the QHNC method has an inner-core structure which comes from the orthogonality of the free-electron wave function to core-electron wave functions. It should be noticed that the usual liquid metal theory yields the electron-ion RDF, which has no inner core structure as plotted by full circles: this cut off of inner core structure brings about simple treatment of liquid metals in the standard liquid metal theory. This clear distinction between inner- and core-structures is characteristic of a liquid metallic state and makes liquid metal theory simple. At the temperature 0.05 eV, the electron-ion RDF has clear distinct inner-core part and outer-core part. Even at temperature 1 eV as shown Fig. 4, this clear distinction remains to show characteristic of a liquid metal: the ionization also remains unity and the ion-ion effective interaction is almost same to that of liquid metal at the normal condition, although the ion-ion correlation becomes weak. Figure 5 shows that at the temperature 3 eV the distinction between inner- and outer-core parts are disappeared and the ionization becomes significant as 1.27. When temperature becomes 30 eV, the ionization becomes large like 6.55.

Figure 6 shows the temperature variation of the outer bound levels in plasma Rb at the fixed density of normal liquid metal. The 4s- and 4p-bound levels are plotted there corresponding to free atom, 0, 1, 2, 3, 5, 10, 22, 30 eV, respectively. As the temperature increases, the bound levels become deeper due to the decrease of bound-electron number, which makes the screening effect weak. At the temperature 22 and 30 eV, new bound levels, 5s and 4d, appear. The occupation number at each level is shown at each level line in Figure 6. The ionization

variation  $Z_I$  is shown in the top of Figure 6 as the temperature is increased.

### 3 DISCUSSION

Using the atomic number as the only input, we can determine ion-configuration and atomic structure by the QHNC method, and obtain results in excellent agreement with experiments for the case of liquid metals. It should be emphasized that in the QHNC formulation the inner electronic structures around a fixed nucleus, such as the electron-ion RDF in the core region and the bound-electron distribution  $n_b(r)$  of an ion in a liquid metal, are determined to be consistent with the outer structure, that is, the surrounding ion and electron configurations. Therefore, the QHNC method can be applied to a high density plasma, where a usual pseudopotential can not be constructed due to the fact the atomic structure in a highly compressed plasma state is quite different from that in the vacuum. The QHNC method has been applied to a dense plasma Rb by increasing the temperature from 0 to 30 eV at the fixed density of normal liquid metal. We have shown that the QHNC method produces a nonlinear pseudopotential applicable to plasma state. However, applicability of this method is limited to simple metallic system, where the bound electrons are clearly distinguished from the free electrons. Here, we used the Jellium-Vacancy model as the first step. In the next work, we are planning to determine the ionic structure, the electron-ion RDF using the self-consistent ion-ion RDF, as was done to treat liquid metals. The QHNC method can give the electron and ionic structures in a wide region of temperatures and densities ranging from liquid-metal to plasma states along with the atomic structure in a plasma.

### 4 REFERENCES

1. J. Chihara, *Phys. Rev. A* **33**, 2575 (1986).
2. J. Chihara, *J. Phys.: Condens. Matter* **3**, 8715 (1991);  
J. Chihara and M. Ishitobi, *Molecular Simulation* **12**, 187 (1994).
3. J. Chihara, *Phys. Rev. A* **40**, 4507 (1989).
4. M. Ishitobi and J. Chihara, *J. Phys.: Condens. Matter* **4**, 3679 (1992).
5. M. Ishitobi and J. Chihara, *J. Phys.: Condens. Matter* **5**, 4315 (1993).
6. J. Chihara and S. Kambayashi, *J. Phys.: Condens. Matter*, **6** 10221 (1994).
7. S. Kambayashi and J. Chihara, *Phys. Rev. E* **53**, 6253 (1996).
8. Y. Rosenfeld, *J. Stat. Phys.* **42**, 437 (1986).
9. J. Chihara, *J. Phys. C: Solid State Phys.* **18**, 3103 (1985).
10. H. Olbrich, H. Ruppertsberg and S. Steeb, *Z. Naturforsch.* **38A**, 1328 (1983).

## 11. Time-dependent H-like and He-like Al lines produced by ultra-short pulse laser

Takako Kato and Masatoshi Kato  
 Ronnie Shepherd\*, Bruce Young\*, Richard More\* and Al Osterheld\*,

National Institute for Fusion Science, Nagoya 464-01, Japan  
 \*V-Division, L-41, Lawrence Livermore National Laboratory, P.O. Box 808,  
 Livermore, CA 94550

### ABSTRACT

We have performed numerical modeling of time-resolved x-ray spectra from thin foil targets heated by the LLNL Ultra-short pulse (USP) laser. The targets were aluminum foils of thickness ranging from 250 Å to 1250 Å, heated with 120 fsec pulses of 400 nm light from the USP laser. The laser energy was approximately 0.2 Joules, focused to a 3 micron spot size for a peak intensity near  $2 \times 10^{19}$  W/cm<sup>2</sup>. Ly $\alpha$  and He $\alpha$  lines were recorded using a 900 fsec x-ray streak camera.

We calculate the effective ionization, recombination and emission rate coefficients including density effects for H-like and He-like aluminum ions using a collisional-radiative model. We calculate time-dependent ion abundances using these effective ionization and recombination rate coefficients. The time-dependent electron temperature and density used in the calculation are based on an analytical model for the hydrodynamic expansion of the target foils. During the laser pulse the target is ionized. After the laser heating stops, the plasma begins to recombine. Using the calculated time dependent ion abundances and the effective emission rate coefficients, we calculate the time dependent Ly $\alpha$  and He $\alpha$  lines. The calculations reproduce the main qualitative features of the experimental spectra.

**Keywords:** Ultra-short pulse laser, H and He-like Al spectra,  
 time evolution of X-ray, ionization, recombination

### 1. Introduction

The ultra-short pulse (USP) laser has been developed as a unique facility able to create small plasmas at a known high density, near the initial solid density, during the 100 - 200 fsec laser pulse. However it is difficult to make good measurements of x-ray spectra with corresponding time resolution.

The USP laser plasma can also be regarded as launching a precisely defined initial value problem. It makes a plasma with rather few degrees of freedom whose subsequent evolution can be measured and compared to theoretical calculations. In this paper we compare plasmas made from thin and thick Aluminum foils and try to understand the observed x-ray emission.

### 2. Measurement of H-like and He-like Al ion spectra

The time evolution of the H-like and He-like Al ion spectra has been measured for five different foils; 250 Å, 500 Å, 750 Å, 1000 Å and 1250 Å[1]. The time evolution of i) Ly $\alpha$  ( $1s - 2p$ ) line, ii) He $\alpha$  ( $1s^2 - 1s2p(^1P)$ ) together with intercombination ( $1s^2 - 1s2p(^3P)$ ) and satellite lines, and iii) He $\beta$  ( $1s^2 - 1s3p(^1P)$ ) line are measured. A more detailed description of this experiment is given in

Ref.1. In Fig.1 we show the time history of the intensity for Ly $\alpha$ , and He $\alpha$ . As seen from Fig. 1 the intensity decreases slowly for thin foil and rapidly for thick foil respectively. Especially for He $\alpha$  line, decay is very slow for 250, 500 and 750A foils.

### 3. Scaling of expansion for plasma parameters

In order to analyze the time behavior of lines we need the time evolution of the plasma parameters. We estimated the plasma parameters by the following scaling laws.

The foil with the thickness  $d_0$  is heated by USP laser and absorbs a constant energy assumed to be independent of  $d_0$ . For this reason,

$$T_0 d_0 = \text{constant} \quad (1)$$

where  $T_0$  is the initial electron temperature for this foil. The foil expands with velocity  $v_0$

$$v_0 = (\gamma k T_0 / m)^{1/2} \quad (2)$$

then at time  $t$  the plasma width  $d$  and the density  $\rho$  are:

$$d \sim 2v_0 t \quad (3)$$

$$\rho = (\rho_0 d_0 / d) = (\rho_0 d_0 / 2v_0 t) \propto d_0^{3/2} / t \quad (4)$$

where  $\rho_0$  is initial density of the foil. The electron temperature at time  $t$  cools through ideal-gas adiabatic expansion to

$$T_e = T_0 (\rho / \rho_0)^{2/3} = (T_0^{3/2} d_0 / 2v_0 t)^{2/3} = (m / \gamma k)^{1/3} (T_0 d_0 / 2t)^{2/3} \quad (5)$$

The electron temperature  $T_e$  is independent of  $d_0$  because  $T_0 d_0 = \text{constant}$ . However when the electron temperature is low, three body recombination raises temperature. We assume  $T_e = T_0 (\rho_0 / \rho)^{\gamma-1}$  as a general law of EOS for low  $T_e$ . We used  $\gamma = 1.366$  from QEOS which includes the heat released by three body recombination. These equations apply only for  $d \gg d_0$ . The exact formulae for  $n_e$  and  $T_e$  which are used in our calculation are given in ref.2.

As for the electron density,  $n_e$  decreases rapidly for thin foil and for thick foil  $n_e$  decreases slowly.

### 4. Numerical model for time evolution of the emission lines

#### i) Effective rate coefficients

In order to calculate the time dependent line emission we should solve time dependent rate equations with many levels. However because most of the excited states are considered in a quasi steady state, it is not necessary to solve the complete time dependent rate equations. We have derived the effective ionization  $S_{\text{eff}}$ , recombination  $a_{\text{eff}}$  and emission rate coefficients  $\epsilon$  assuming the quasi steady condition by solving a collisional radiative model (CRM) of H-like and He-like[3] Al ions. We use these rate coefficients to solve the rate equation and calculate the time dependent line intensities. The detailed description of these rate coefficients is given in Ref.[2].

The effective emission rate coefficients are defined as follows,

$$\epsilon^i(i, j) = n_z(i) A(i, j) / n_e \quad \text{for } n_z(1) = 1, n_{z+1}(1) = 0, \quad (6)$$

$$\epsilon^r(i, j) = n_z(i) A(i, j) / n_e \quad \text{for } n_z(1) = 0, n_{z+1}(1) = 1, \quad (7)$$

where  $A(i, j)$  is the radiative transition probability from the level  $i$  to the level  $j$ ,  $n_z(i)$

the population density of the level  $i$  of the ion with charge  $z$ . The emission rate coefficients in purely ionizing plasma  $\epsilon^i$  decrease at high density due to the excitation and ionization processes. On the contrary the emission rate coefficients in purely recombining plasma  $\epsilon^r$  increase for high densities at low temperatures. Therefore strong emission is expected in recombining phase at high densities.

## ii) Time variation of line intensities

The line emissivity per volume at time  $t$  is derived with the ion abundances and emission rate coefficients as follows,

$$\begin{aligned} I(z,t) &= n(z,t) n_e(t) \epsilon^i + n(z+1,t) n_e(t) \epsilon^r \\ &= n_e(t) \sum n(z,t) \epsilon \end{aligned} \quad (8)$$

where  $n(z)$  indicates the ion density of an ion with charge  $z$ . The detailed results for time dependent ion abundances are given in Ref.[2]. Here we define  $\epsilon$  as the effective emission rate coefficient including ion fraction at time  $t$ .

$$\epsilon = n(z,t) / \sum n(z,t) \epsilon^i + n(z+1,t) / \sum n(z,t) \epsilon^r \quad (9)$$

The observed line intensity from a uniform plasma is given by

$$F = \epsilon n_e S d_0 n_0 / 4\pi \quad (10)$$

where  $S$  is the surface area of the plasma. This equation means that the observed intensity is proportional to the initial foil thickness  $d_0$  and the quantity which varies with time is  $\epsilon$  and  $n_e$ .

The emission rate coefficient  $\epsilon$  at time  $t$  is derived with ion abundances and effective emission rate coefficients following the formula (9). The  $\text{He}\alpha$  emission has two peaks; one produced in the ionizing phase and the other in the recombining phase. The first peak is much larger than the second one due to the time variation of  $n_e$ . The contribution of excitation is dominant in the initial phase before  $10^{-13}$  s and that of recombination is dominant later. However since the first peak is produced in this early phase in a short period before 0.1ps, the measurement can not resolve the first peak clearly. The observed intensities given in Fig. 1 were measured by streak camera. The streak camera has a time resolution as well a time delay. We have assumed the Gaussian type of response of the streak camera with time delay of 5 ps and time resolution of 3 ps. The time history of the convoluted intensity is given in Fig. 2 for four different foils. The effective emission rate coefficients used in Eq.(8) are shown in Fig. 3.

## 5. Comparison with experiment and calculation

When we compare our calculation to the experimental results, the time behaviors of different thick foils agree qualitatively. The slopes in later phase agree quite well as compared in [2]. In the case of 1250A the agreement is very good in total. However the intensity in the early phase in our calculation is always larger than the measurement except 1250A.

Since we do not know the initial temperature  $T_0$  we guessed it from the time behaviour of the line. When we increase  $T_0$  H-like line intensity increases compared to He-like line intensity. Our calculation shows higher intensity for  $\text{Ly}\alpha$  than  $\text{He}\alpha$  although the experimental results show the contrary as shown in Figs. 1 and 3. However if we decrease  $T_0$  to reduce  $\text{Ly}\alpha$ , ions disappear rapidly due to the low temperature and then the  $\text{He}\alpha$  line in the recombining phase will decrease too rapidly compared to the experiment. We have an impression that  $T_e$  or  $n_e$  decays

more slowly than indicated by the scaling formula.

The observed peak intensity for different thickness are almost the same as shown in Fig. 1 although from Eq.(10) the intensity is expected proportional to  $d_0^2$ . This result might come from opacity because the opacity is estimated to be more than 2 even for He $\alpha$  line with 250A. We have briefly estimated the effect of the opacity in Ref.[2] and found that the discrepancy of Ly $\alpha$  and He $\alpha$  intensity ratio and the slow decay can not be solved by the opacity.

## 6. Summary and Discussions

Time evolution of line intensity of H-like and He-like Al ions are calculated using effective ionization, recombination and emission rate coefficients. The main qualitative feature of observed line intensity is rapid decay of intensity for thick foil and slower decay for thin foil emission. The slope of the intensity is mostly sensitive to density and/or temperature and the calculation reproduce this trend of the experiment. This agreement is a test of EOS in hydrodynamic expansion. The model for hydrodynamic expansion uses a non-ideal equation of state, including the large effect of recombination energy. This gives results which reproduce the main qualitative feature of the experiment. A model using ideal gas expansion disagrees strongly with the late-time behaviour of the emission.

The observed He $\alpha$  line intensity has a small dip at around 30 ps for 250 A and the intensity is almost constant after 35 ps. An ion is created, disappears by ionization in the initial phase and is produced again by recombination in the decay phase. The density of H-like ions reaches the minimum which corresponds to the ionization time at around 1 ps by our calculation. If we interpret the observed dip as the minimum of the H-like ion abundance between ionising and recombining phase, the values of electron density should be smaller by factor of 10. This could happen if there is a prepulse. However in our calculation when we reduced the initial value of  $n_e$  by factor of 10 in Eq.(4), the convoluted intensity ratio of the first peak to the second peak become more than 10 which is too large compared to the experimental value of a factor 2.

Intensity Ratio,  $I(\text{Ly}\alpha) / I(\text{He}\alpha)$ , is a factor of 5 larger in our calculation than in the measurement. Long duration of He $\alpha$  line for thin film indicate the recombination rate for H-like ion is slow. The time evolution of  $n_e$  and  $T_e$  might be slower decay than the scaling law for thin foils.

Local thermodynamic equilibrium (LTE) level  $n = (z^2 I_H / 3kT_e)^{1/2} \sim 2$  for 100 eV under the plasma condition of the short pulse laser. Therefore the levels  $n > 3$  is considered in LTE. In such a condition we have to include the excitation - ionization through autoionising states[4]. We also have to know the effect of the recombination through the autoionising states on the population density at low temperature[5].

## References

1. R. Shepherd et al, JQSRT, 1997
2. T. Kato et al, JQSRT, 1997
3. T. Fujimoto and T. Kato, Phys. Rev. A 30, 379 (1984)
4. T. Fujimoto and T. Kato, Phys. Rev. Lett., 48, 1022 (1982)
5. T. Kawachi and T. Fujimoto, Phys. Rev. E, No.2, 1836 (1997)

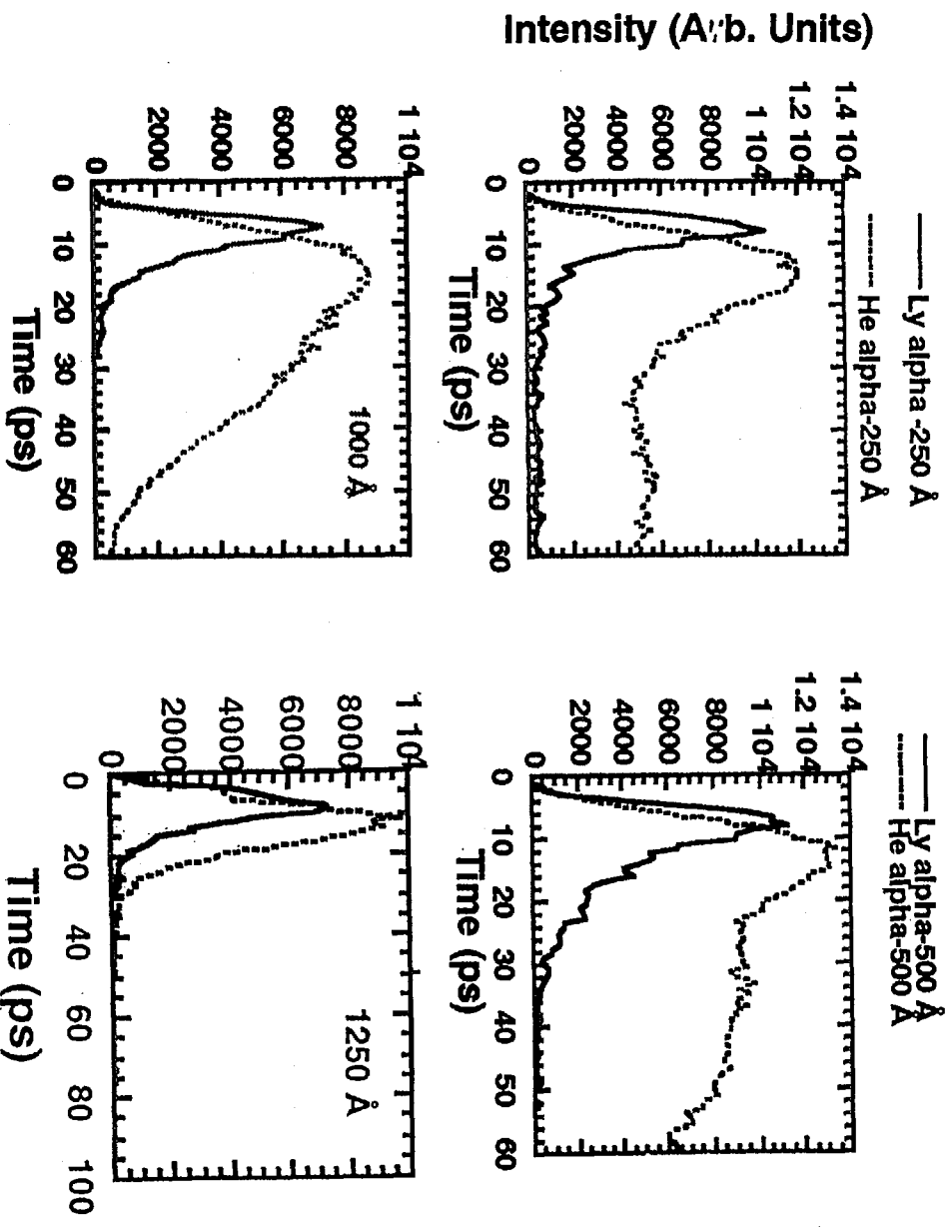
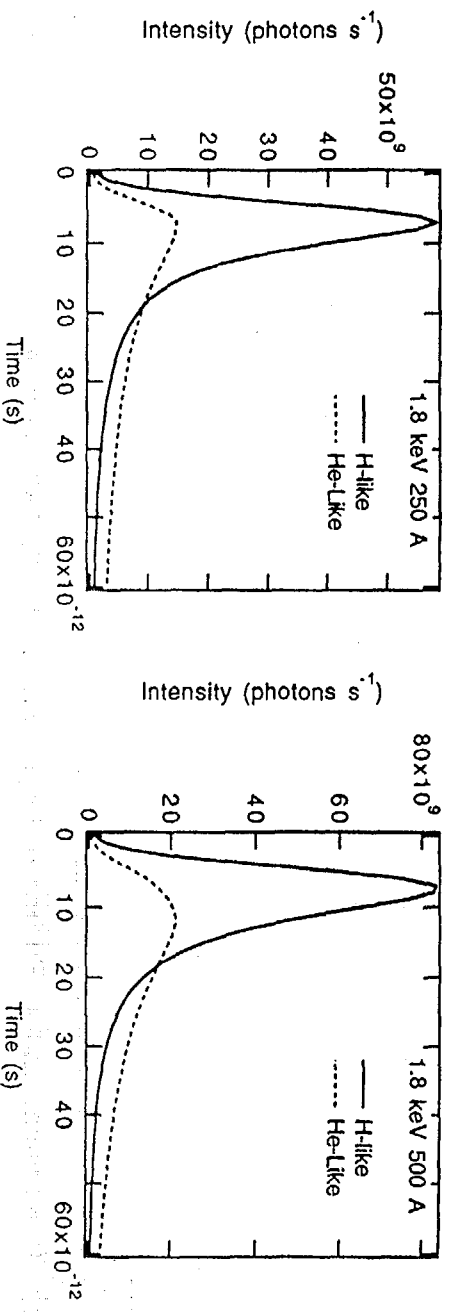


Fig.1 Observed time history of Ly $\alpha$  and He $\alpha$  for different foils.



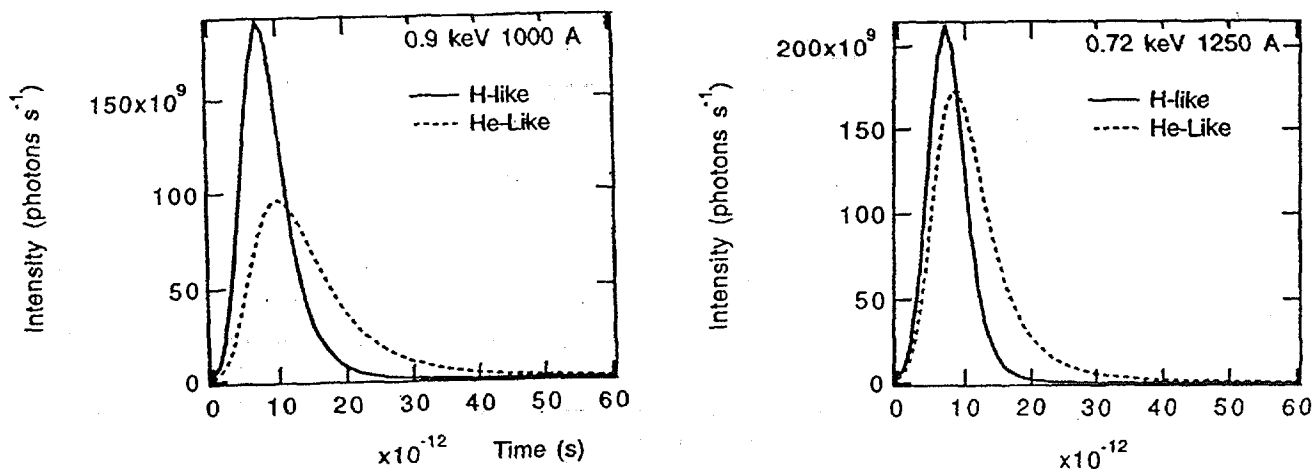


Fig.2 The convolute intensity with time resolution of streak camera as a function of time for Ly $\alpha$  and He $\alpha$  for different foils.

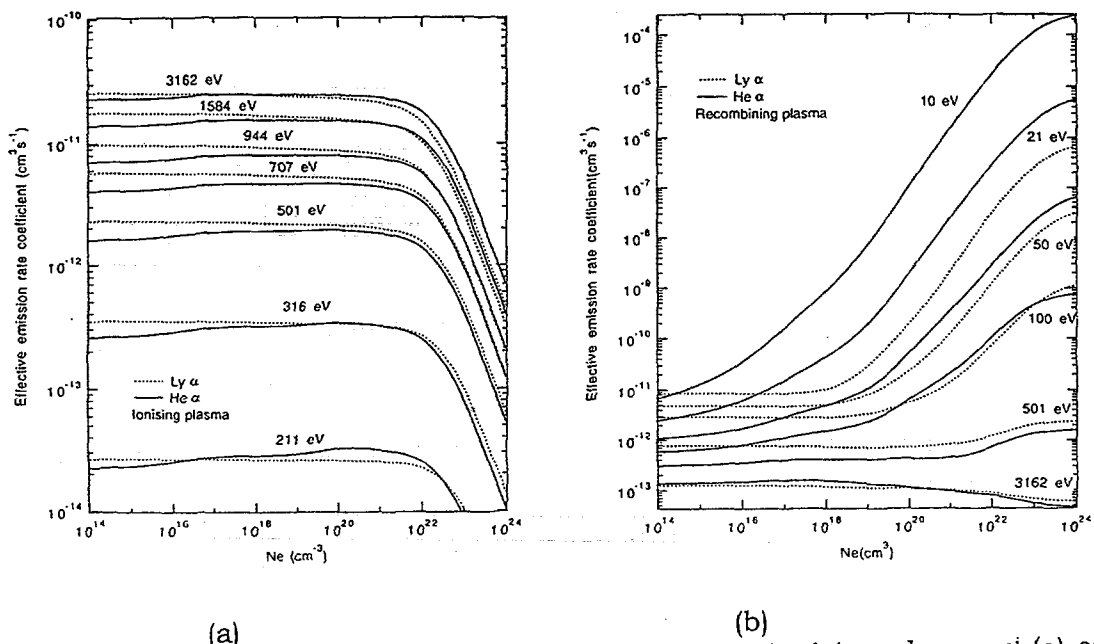


Fig.3. Effective emission rate coefficients for purely ionising plasma  $\epsilon^i$  (a) and for purely recombining plasma  $\epsilon^r$  (b) as a function of the electron density for different electron temperatures.

## 12. Theory and Simulation of Ultra-short Pulse Laser Interactions

Richard MORE, Rosemary WALLING, Dwight PRICE, Gary GUETHLEIN  
Rick STEWART, Steven LIBBY, Frank GRAZIANI and Joann LEVATIN

*Lawrence Livermore National Laboratory  
Livermore, California, USA, 94550*

### ABSTRACT

This paper describes recent Livermore work aimed at building computational tools to describe ultra-short pulse laser plasmas. We discuss calculations of laser absorption, atomic data for high-charge ions, and a new idea for linear-response treatment of non-equilibrium phenomena near LTE.

**Keywords:** Ultra-short Pulse, Laser Interaction, Optical Properties, Atomic Models, Non-LTE Atomic Kinetics

### INTRODUCTION

This paper will describe recent Livermore work aimed at building computational tools to describe ultra-short pulse laser plasmas. We will discuss calculation of optical phenomena, a semiclassical atomic model (SAM) for high-charge ions, and a new idea for linear-response theory of near-equilibrium non-LTE atomic dynamics.

### I. OPTICAL PHENOMENA

At the LLNL USP laser we have measured target absorption as a function of angle of incidence, laser intensity and polarization.<sup>(1)</sup> These experiments are performed with 120 fsec pulses at intensities ranging from  $10^{13}$  to  $10^{18}$  W/cm<sup>2</sup>. We also have begun to measure thin-foil transmission, a test of laser penetration through a thin overdense plasma, and we are using Fourier Interferometry to measure the phase-shift of probe pulses reflected with various time-delays. This data can accurately characterize the plasma expansion.

Because there is some surface expansion even during the 120 fsec heat pulse, our analysis includes a surface density profile, usually taken to be an exponential  $\rho = \rho_0 \exp(-x/L)$ , corresponding to an isothermal rarefaction. Because the target materials are heated to temperatures ranging from 1 eV to more than 100 eV, the material properties, especially the optical properties, are dramatically altered from those known for cold matter. We cannot necessarily predict these high-temperature optical properties and want to determine them from the experimental data.

We analyze laser-target interaction experiments using a simple code for solution of Maxwell equations in planar (1-D) geometry. The inputs to this code are the scale length  $L$  for the surface expansion profile, the solid-density optical

coefficients  $\epsilon_1^0$ ,  $\epsilon_2^0$ , the laser wavelength  $\lambda$ , the angle of incidence  $\theta$ , and the laser polarization (s or p).

The code uses a matrix-multiplication method to solve Maxwell equations for light interacting with the target. The optical coefficients are assumed to have the usual density-dependence,

$$[\epsilon_1 + i\epsilon_2 - 1] \propto \rho$$

so the code only requires the solid-density value  $\epsilon_1^0 + i\epsilon_2^0$ .

Output from the code includes s- and p-polarized absorption, phase shifts and transmission through thin targets. With appropriate choice of the input parameters, the code achieves excellent agreement with experiment.

For aluminum angle-dependent absorption experiments, we find surface expansions in the range 20 - 80 Å during the 120 fsec laser pulse, depending of course on the laser intensity. Absorption range from a few percent to about sixty percent.

Absorption by thin layers of  $\text{Al}_2\text{O}_3$  on aluminum substrates show remarkable temperature variation of the dielectric properties of the oxide (the experimental data-set includes data from eight layer thicknesses ranging from a few Angstroms to about 1 micron). At temperatures of a few eV the oxide is a very strongly absorbing medium.

Fourier interferometry probes of aluminum surface expansion yield expansion velocities  $\approx 28$  km/sec for a laser intensity near  $10^{15}$  W/cm<sup>2</sup>. The data analysis uses the Maxwell code to match both s- and p-polarized phase shifts with a single scale-length.

To interpret this FDI data, we have derived a general formula relating the expansion scale length to the plasma equation of state,

$$L = [d(\rho c_s)/d\rho] t \quad (1)$$

where  $L$  is the scale-length,  $\rho$  is the density,  $c_s$  is the isothermal sound speed, and  $t$  is the time of the probe-pulse. Equation (1), which assumes adiabatic expansion of a uniformly heated solid, is valid for any equation of state.

Continued development of the FDI technique offers several benefits: first, a way to measure the equation of state of hot dense plasmas, and second, a way to determine hydrodynamic expansion to remarkable precision (perhaps 5 %). For x-ray lasers based on flat targets, such hydrodynamic expansion controls the x-ray refraction which will limit the gain length, and for this reason we believe it will be very important to accurately understand and control the plasma hydrodynamics.

## II. SEMICLASSICAL ATOMIC MODEL

The semiclassical atomic model (SAM) is intended as a practical way to generate atomic data for hydrodynamic applications. SAM does not have the high precision required for spectroscopy, but it compensates for that by being rapid, flexible and more convenient than other approaches.

The basic idea is very simple. SAM imitates a quantum *jj*-coupled self-consistent field calculation of atomic structure but replaces the numerical calculation of wave-functions by the use of closed-form WKB wave-functions.

This is possible because of two technical advances: first, an accurate WKB solution of the Dirac equation<sup>(2)</sup>, and second, a method to compute matrix-elements between WKB functions<sup>(3)</sup>. The WKB functions are known in closed form for Coulomb potentials, and so we approximate the electrostatic potential in the general high-charge ion as a series of screened Coulomb potentials on radial shells defined by K-, L-, M-shell electrons. Then the screened charges are made consistent with the charge density given by the WKB wave-functions.

In quantum mechanics, the 3s electrons (for example) have their largest charge density in the M-shell region, but actually extend over a large radial range, sampling the potential in the K- and L-shell regions. The semiclassical rule is that an electron of quantum numbers  $n, l$  extends from a minimum radius set by  $l$  to a maximum radius set by  $n$ . Study of quantum wave-functions shows the semiclassical rule is reasonably accurate.

The SAM computer code is small, robust and reasonably accurate. The code itself is about fifteen pages of FORTRAN. It requires a few milliseconds per ion, averaged over the entire list of 4278 ions (nuclear charge  $Z = 1$  to 92, ion charge  $Q = 0$  to  $Z-1$ ). The code is robust because it converges for all 4278 ions without failing.

To test the accuracy we compare SAM with quantum atomic structure codes. For the ionization potentials of the 4278 ions, the overall average error is 7 %. However large percentage errors occur only for neutrals or low-charge ions which have small ionization potentials. For ions with charges greater than about 10+ the ionization potentials are always accurate to 1 or 2 %.

We have also compared one-electron eigenvalues from SAM with those generated by a relativistic quantum self-consistent field code (J. Scofield supplied the comparison data). Figure 1 shows one example of these comparisons. This comparison shows that SAM is able to reproduce the important features of x-ray spectra without achieving spectroscopic accuracy.

Today SAM describes an isolated atom (ion) and provides electron energies. Our plan is to extend the code first to radiative properties (line-strengths), then to include plasma density effects in a finite-temperature context, and finally to add collisional and autoionization processes to produce a non-LTE code.

The structure of the code permits use in either average-atom or detailed configuration modes, although the spectrum is always computed from *jj*-coupled one-

electron eigenvalues. This approximation neglects term splitting and configuration interaction and is most appropriate to high-Z ions. Because average-atom calculations are simpler we plan to implement that method first.

### III. TABULAR NON-LTE ATOMIC KINETICS

For all but the simplest atomic models, it requires very much computer time to perform detailed configuration NLTE calculations consistently coupled to hydrodynamic simulations. One new approach proposes using multiple effective temperatures and LTE opacities in order to imitate the main consequences of NLTE. (Busquet, (4)) However this is an intuitive model and we have no exact idea of its accuracy.

We propose to develop a systematic treatment of NLTE corrections to LTE behavior in high-density plasmas.

General thermodynamic principles apply to near-LTE plasmas and can give us important consistency checks. For plasmas maintained in a near-equilibrium steady state, the rule is that the rate of entropy production is minimized by the (NLTE) choice of ionic populations that compromise between between the temperatures of the different heat reservoirs (Prigogine theorem). For an ion in a hot plasma, these heat reservoirs are free electrons and photon frequency groups. If we examine the rate of entropy production near the steady state, we find symmetry relations (Onsager relations) that must be obeyed by any correct NLTE calculation. Finally, the fluctuation-dissipation theorem, gives a rigorous expression (Kubo relation) for the non-equilibrium linear-response function as an average over equilibrium populations and cross-sections.

Some obvious applications of a near-LTE non-LTE theory are to the interaction of x-ray lasers with a hot plasma target; emission from ions near the surface of a semi-infinite medium, as in strong shock waves or Marshak (heating) waves; and the typical opacity experiment performed by irradiating a foil sample confined in a laser-heated hohlraum. We also believe these methods will be useful for modeling high-density short-pulse laser target interactions, and even for planning experiments to produce plasmas for x-ray laser experiments.

For a near-LTE atom(ion), the linear-response matrix  $R_{\nu, \nu'}$  can be defined by

$$\int (\kappa_{\nu}^e - \kappa_{\nu}^a) B_{\nu} d\nu = \sum_{\nu'} R_{\nu, \nu'} [\Delta\nu \Delta\nu' \delta T_{\nu'}] / 4\pi \quad (2)$$

where  $\kappa_{\nu}^e$ ,  $\kappa_{\nu}^a$  are emission and absorption opacities,  $B_{\nu}$  is the black-body photon intensity spectrum,  $\Delta\nu$  and  $\Delta\nu'$  are photon frequency group widths, and  $\delta T_{\nu'}$  is the perturbation which causes the deviation from LTE, expressed as a change in radiation temperature which applies over a photon group  $\Delta\nu'$  centered at  $\nu'$ . The integral on the left runs over the frequency group  $\Delta\nu$  centered at  $\nu$ .

If the matrix  $R_{\nu, \nu'}$  is tabulated, we can use the local photon frequency distribution (in the form of photon group temperatures  $\delta T_{\nu}$ ) to calculate  $(\kappa_{\nu}^e - \kappa_{\nu}^a)$ .

Then together with the LTE opacities, which supply the sum  $\kappa_{\nu}^e + \kappa_{\nu}^a$ , we have the information required for radiation transport.

We have formulated atomic kinetics for near-LTE steady plasmas and find that the rate of entropy production is given by a quadratic form proportional to

$$dS/dt = \text{constant} * \Sigma_{\nu} \Sigma_{\nu'} R_{\nu, \nu'} \Delta \nu \Delta \nu' \delta T_{\nu} \delta T_{\nu'} \quad (3)$$

The atomic populations are those which minimize this quadratic form for fixed temperature perturbations  $\delta T_{\nu}$ . According to the Onsager relation, the response matrix  $R_{\nu, \nu'}$  must be symmetric

$$R_{\nu, \nu'} = R_{\nu', \nu} \quad (4)$$

This relation is actually a nontrivial general consistency test for non-LTE codes and calculations, and we plan to test whether it is obeyed by existing NLTE computer codes. Figure (2) gives a first test of Eq. (4), two scans through the matrix  $R_{\nu, \nu'}$  obtained from the screened hydrogenic average-atom model for an aluminum plasma at density .001 g/cm<sup>3</sup>, temperature 50 eV. The two scans approximately agree, so the screened hydrogenic model is approximately consistent with Eq. (4).

#### IV. SUMMARY AND CONCLUSIONS

We conclude with a list of useful tools (past, present and future) for ultra-short pulse laser interaction research.

##### Existing tools:

- One-dimensional Maxwell equation code for optical properties
- Inertial fusion code LASNEX (hydro accurate to perhaps 20%)
- X-ray laser design codes
- Atomic data sources (e.g., HULLAC code)

##### Tools in development today:

- Inline atomic/non-LTE models (SAM code, NLTE tables)
- Hydrodynamics validated to 5 % by USP laser experiments
- Advanced raytracing methods

##### Tools we will need in the future

- 2D, 3D Maxwell equation codes
- X-ray raytracing, x-ray laser interaction physics
- Heatflow validated by experiments
- Special atomic data for special x-ray lasers

As we develop these tools, it will be important that they work together, that the output from one code be compatible with the input to another. As we discuss our plans with the international community interested in short-pulse laser research, it

may be equally important that we find ways for the scientists of different laboratories to work together.

**Acknowledgement:**

The author is very grateful to Dr. Keiji Tani of the JAERI Kansai Research Establishment for assisting his participation in the Kyoto Workshop on ultrashort pulse ultrahigh power lasers.

Supported in part under the auspices of the U.S. Department of Energy by Lawrence Livermore National Laboratory under Contract No. W-7405-ENG-48.

**References:**

- (1.) D. Price, R. More, R. Walling, G. Guethlein, R. Shepherd, R. Stewart and W. White, Phys. Rev. Lett. **75**, 252 (1995).
- (2.) R. More, J.Q.S.R.T. **51**, 237 (1994).
- (3.) R. More and K. Warren, Annals of Physics **207**, 282 (1991).
- (4.) M. Busquet, Phys. Fluids **B5**, 4191 (1993).

**FIGURE CAPTIONS**

Figure 1.) One-electron eigenvalues for thorium ions at various ionization states calculated by a relativistic quantum self-consistent field theory and by the semiclassical atomic model (SAM) code. The author is grateful to Dr. J. Scofield for providing this comparison data.

Figure 2.) Scans of the linear-response matrix  $R_{\nu, \nu'}$  for an aluminum plasma at density  $.001 \text{ g/cm}^3$ , temperature 50 eV. One scan has varying  $\nu$  and the other has varying  $\nu'$ ; the results approximately agree. The lowest figure shows the two opacities (which are nearly equal for a very small perturbation) and indicates the perturbed photon group by a small box near 50 eV.

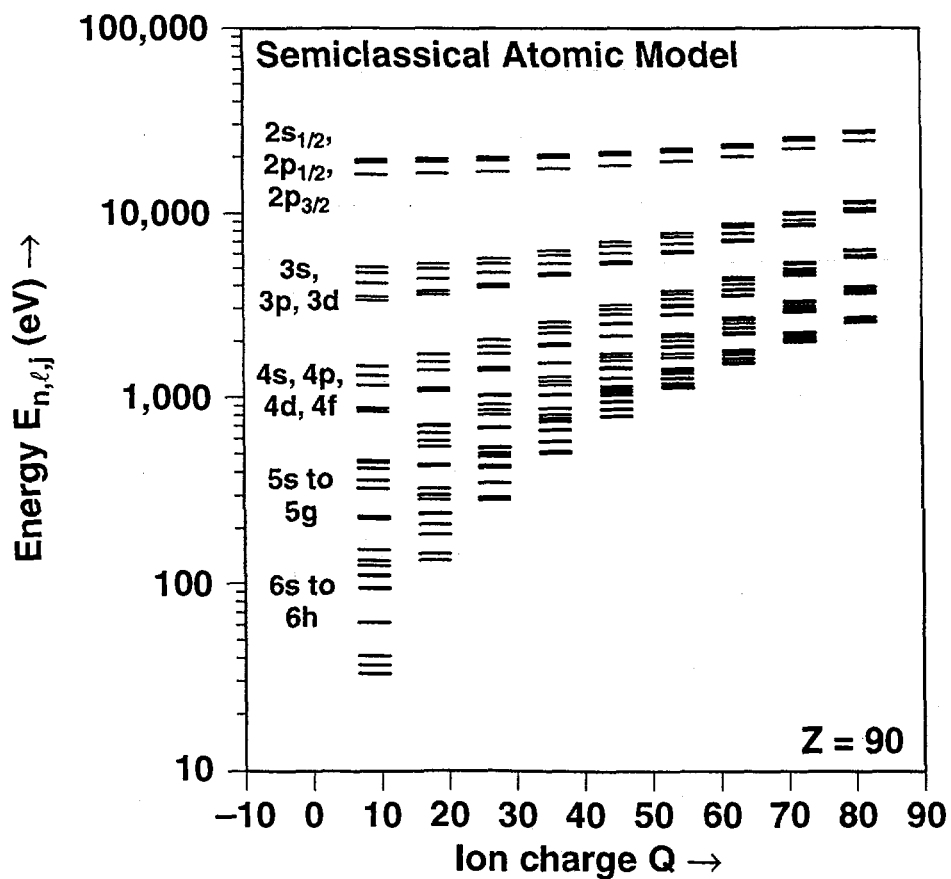
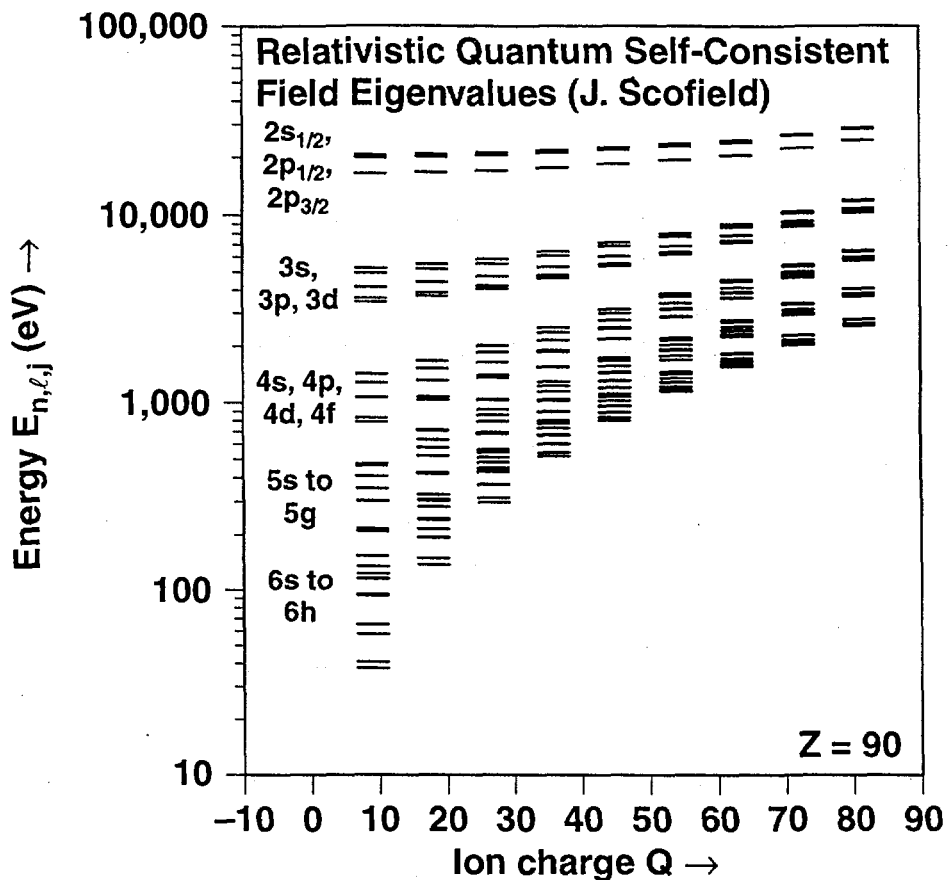


Figure 1.)

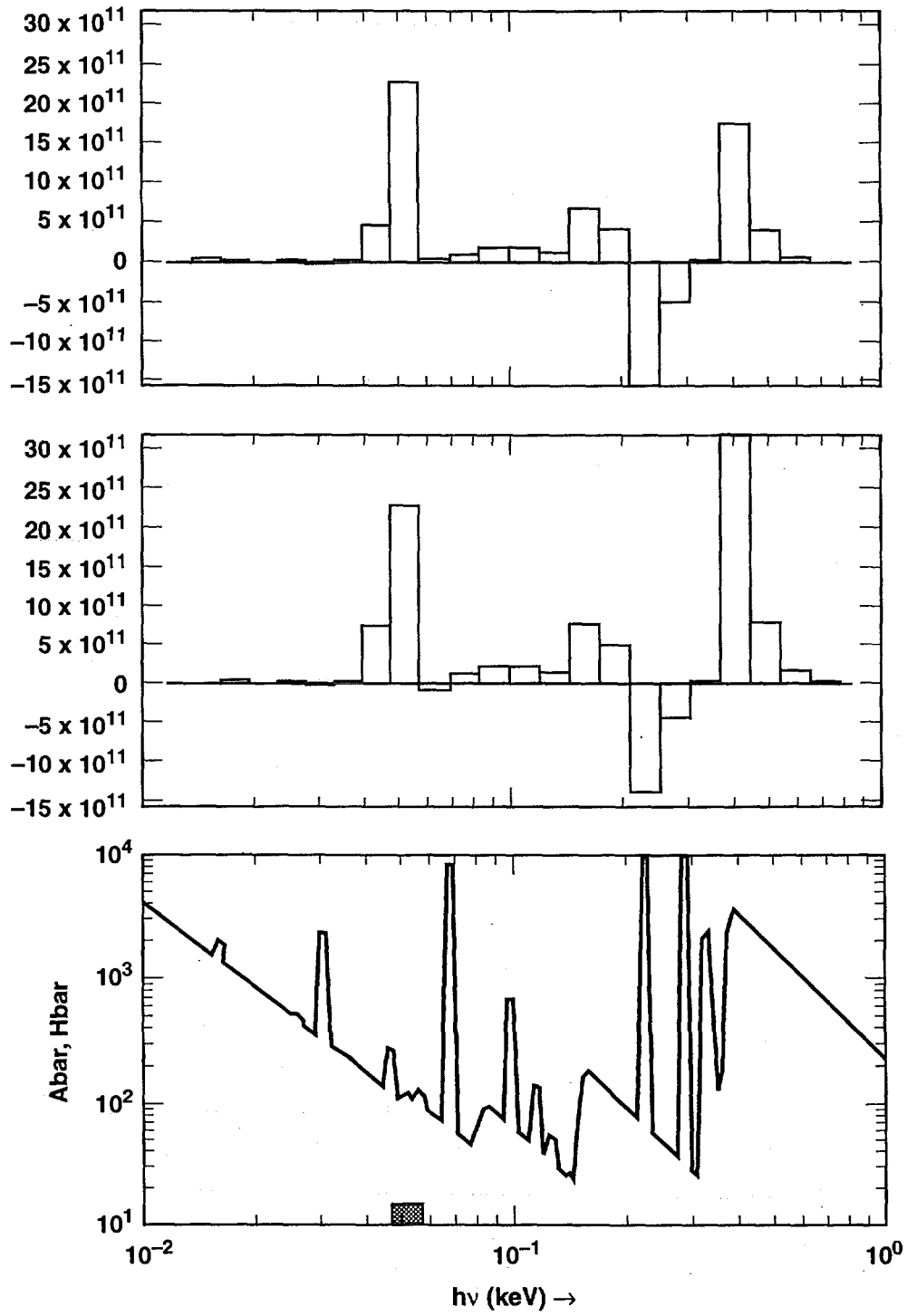


Figure 2.)

### 13. Modeling of collisional excited x-ray lasers using short pulse laser pumping

Akira Sasaki, Kengo Moribayashi, Takayuki Utsumi, and Toshiki Tajima

Advanced Photon Research Center, Kansai Research Establishment, Japan Atomic Energy Research Institute, 25-1 Mii-minami-cho, Neyagawa-shi, 572, Osaka, JAPAN

#### Abstract

A simple atomic kinetics model of electron collisional excited x-ray lasers has been developed. The model consists of a collisional radiative model using the average ion model (AIM) and a detailed term accounting (DTA) model of Ni-like Ta. An estimate of plasma condition to produce gain in Ni-like Ta ( $\lambda=44\text{\AA}$ ) is given. Use of the plasma confined in a cylinder is proposed to preform a uniform high density plasma from 1-D hydrodynamics calculations.

Keywords: x-ray laser, laser produced plasma, atomic kinetics

#### 1. INTRODUCTION

Development of efficient, short wavelength x-ray lasers have been pursued for many years. Especially, x-ray lasers in water window wavelength (20-40 $\text{\AA}$ ) are interested for biological purposes. Lasers in longer wavelength ( $\approx 130\text{\AA}$ ) will also be useful in lithography and material processing. Despite successful demonstration of gain up to Ni-like Ta and W[1], present collisional x-ray lasers require large pump energies. Reduction of the pump energy will make x-ray lasers much more useful for industrial and scientific applications. This can be possible by the use of short pulse pumping, after detailed understanding of the mechanism of lasing and optimization of experimental condition through intensive theoretical and numerical investigations.

In this paper, modeling of electron collisional excited lasers using Ni-like ions is presented. We have developed a simple atomic kinetics model of Ni-like Ta laser to determine temperature and density of the plasma required to produce gain. Preliminary target design has also been made using HYADES 1-D hydrodynamics code.

Soft x-ray gain is produced in  $4d(3/2, 5/2) J=1$  and  $4p(3/2, 3/2) J=0$ ,  $4p(1/2, 3/2) J=0$  transitions of Ni-like ions of high-Z elements. Two different schemes are proposed for efficient pumping. The OFI-collisional excitation scheme is proposed by Lemoff[2]. They irradiated Xe gas target by a circularly

polarized  $10^{18}$  W/cm<sup>2</sup>, 100fs laser pulse. Energetic electrons were created to ionize and excite Pd-like Xe ions. Gain in 417Å was demonstrated. The other method is the prepulse or multipulse technique. The weak prepulse preforms a plasma with an appropriate density. The subsequent intense mainpulse heats the plasma to excite the lasing level through electron collisional excitation, and to produce population inversion. Recently lasing has been reported from Ne-like Ti[3] to Ni-like Ag[4] and Sm[5] using this technique. Optimization of these methods using ultra short pulse laser as a pump source is interested toward achievement a compact water window laser.

## 2. MODELING OF ATOMIC KINETICS

A simplified energy level diagram of Ni-like Ta is shown in Figure 1[6]. The upper(4d) and lower(4p) configuration consist of 18 and 12 spectral terms. These excited configurations are about 2keV above the ground state, and energy spread of spectral terms belong to 4d configuration is 120eV. Total number of  $3d^9 4l$  levels is 54. The collisional excitation rate from the ground state to  $4d(3/2, 5/2)$   $J=1$  is exceptionally greater than to any other levels, therefore gain is expected for several transitions to 4p levels. Not only  $3d^9 nl$  levels but inner shell excited levels such as  $3s 4l$ ,  $3p^5 4l$  are below ionization limit and the energy levels are overlapped each other. We have to account for the population of detailed levels for calculation of soft x-ray gain.

For the calculation of soft x-ray gain, calculation of abundance of Ni-like ion is indispensable. To calculate ionization using the detailed term accounting(DTA) the model should include level structure of other ionization stages. In complex ions ionization and recombination take place through several channels. For example,  $3d^9 4l$  excited levels correspond to ionization limit of inner shell ( $3d^9 4s$ ) or double excited states of ( $3d^8 4l nl$ ) of Cu-like ion. Excitation Autoionization (EA) and Dielectronic Recombination (DR) processes may change ionization balance significantly. Inclusion of these detailed level structure make the atomic model huge. On the other hand the ionization balance is coupled to other groval plasma characteristics through hydrodynamics motion and radiative transfer. The model should be coupled with hydrodynamics or particle codes, development of simple approximated methods have practical importance. Therefore we have divided the model into two parts, a simple model to calculation of ionization balance and a detailed model of Ni-like Ta.

We have developed a collisional radiative model based on  $l$ -dependent average ion model (AIM) [7,8] to calculate ionization of the Ta plasma. Energy levels and rate coefficients are calculated using screened hydrogenic approximation, which gives most of ionization energies of Ta ions within 20% accuracy without detailed knowledge of atomic structure. In the AIM, instead of calculating populations of each level, average number of electrons in each  $nl$  shell is calculated. An advantage of the model is, in principle, this model includes effects of multiple excited levels and inner shell excited levels. On the other hand, ion abundance nor population of any specific level can not be inferred from the results of AIM except when the system is close to equilibrium state(LTE). Using this model, the

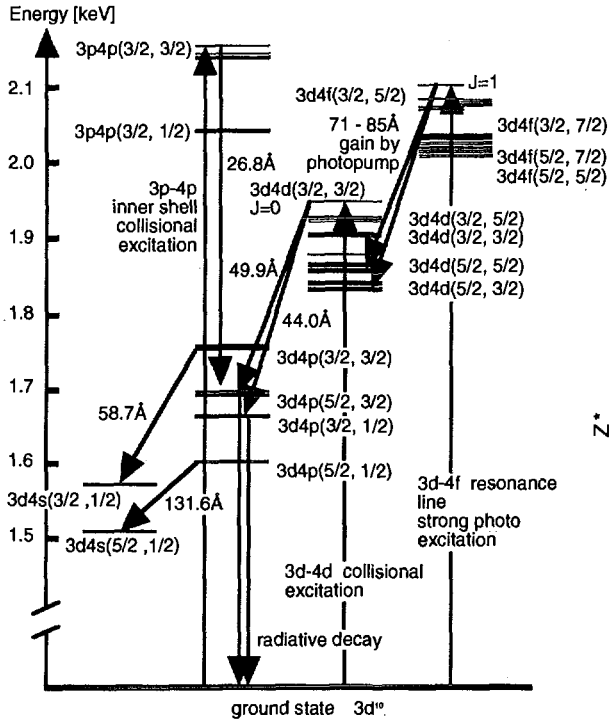


Figure 1 Energy level diagram of the Ni-like Ta laser.

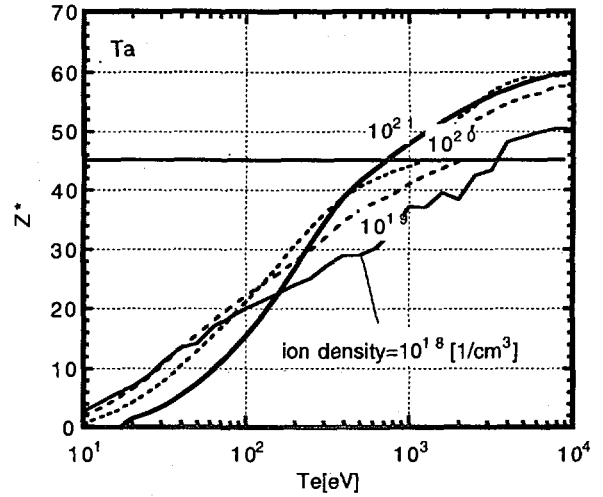


Figure 2 Temperature dependence of average charge of Ta.

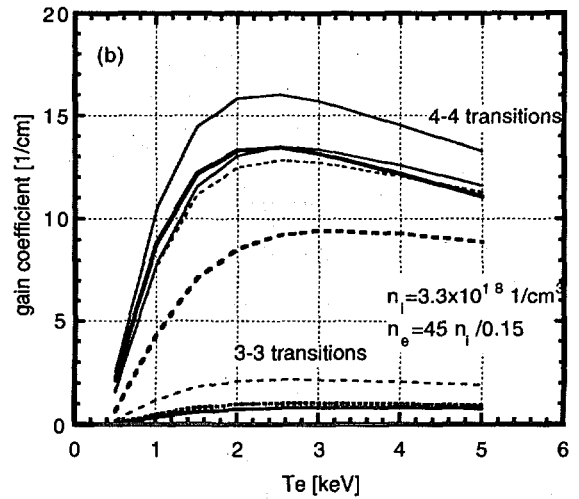
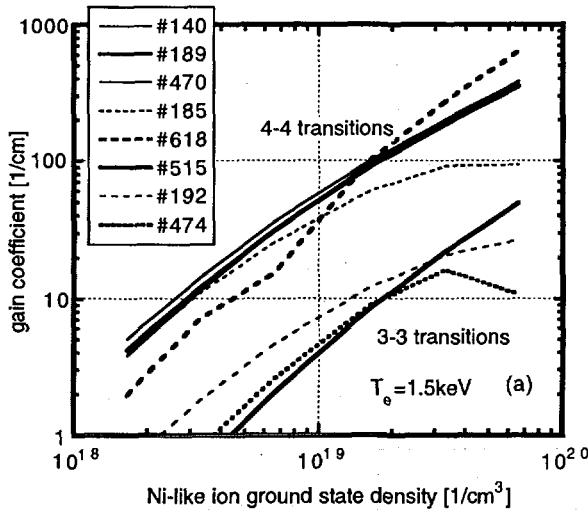


Figure 3 Density(a) and temperature(b) dependence of gain.

- #140 4d(3/2, 3/2) J=0 - 4p(3/2, 1/2) J=1, 44.0 Å
- #189 4d(3/2, 3/2) J=0 - 4p(5/2, 3/2) J=1, 49.9 Å
- #470 4p(3/2, 3/2) J=0 - 4s(3/2, 1/2) J=1, 58.7 Å
- #185 4d(5/2, 5/2) J=2 - 4p(5/2, 3/2) J=1, 74.5 Å
- #515 3d4f(5/2, 7/2) J=2 - 3p4f(3/2, 7/2) J=2, 28.6 Å
- #192 3d4p(3/2, 3/2) J=0 - 3p4p(5/2, 3/2) J=1, 26.8 Å
- #474 3p4s(3/2, 1/2) J=1 - 3s4s(1/2, 1/2) J=0, 23.3 Å

average charge of Ta plasma as functions of density and temperature as shown in Figure 2(a). For ion densities of  $10^{19}$  to  $10^{20}$   $1/\text{cm}^3$ , the temperature required to produce Ni-like ions ( $\text{Ta}^{45+}$ ) is found to be 1.0 - 1.5keV.

The steady state gain calculated using the atomic model of Ni-like Ta in Figure 1 is shown in Figure 3. In the figures, density of ground state of Ni-like ion is assumed to be 0.15 of ion density, and the average charge is assumed to be 45. Gain of more than 10  $1/\text{cm}$  is calculated in  $4d(3/2, 5/2)J=0 - 4p(3/2, 1/2)J=1$  transition for moderate densities which is consistent with experimental observations[1].

Using this model we can calculate gain for all transitions in Ni-like Ta. Positive gain is obtained for not only in the usual lasing transitions but between other  $4l$  levels and inner shell excited levels.  $4f$  levels are excited by strong photo pumping as well as electron collisions. The resonance transition probability from  $4f$  to ground state is large. However in the case of high densities the optical depth of this line could become large. Due to the effect of line trapping the population in  $4f$  levels could be increased to produce population inversion between  $4d-4f$ [9]. It is also found that some of the inner shell excited levels such as  $3p4p(3/2, 3/2) J=0$  are excited by strong electron collisions leading gain in 3-3 transitions. Emission from the inner shell transitions are observed in 2-2 transitions in Ne-like system and possibilities for lasing had been discussed[10]. Gain of 3-3 transitions in the present calculation is one order of magnitude smaller than usual 4-4 transitions, however the gain could be increased using transient pumping scheme with which very large gain in various 4-4 transitions had been observed. Wavelength of 3-3 transitions are almost 1/2 of 4-4 transitions as shown in Figure 4, and are inside the water window region with Nd ( $Z=60$ ). Requirement of large pump energies to obtain lasing in short wavelength with Ni-like ions might come from the fact that difficulty to obtain

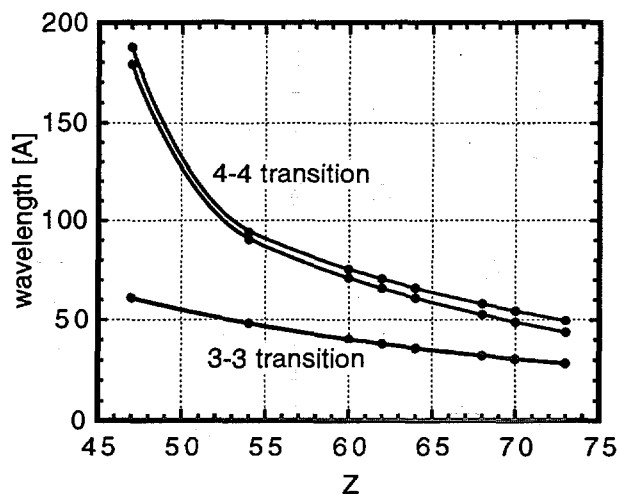


Figure 4 Wavelength scaling of 4-4 and 3-3 transitions of Ni-like ion.

high temperature to produce Ni-like ions of high-Z elements. If we made use of 3-3 transitions, water window laser would be obtained using smaller pump energies.

### 3. MODELING OF TARGET

In this section, methods to preform plasma with a sufficient density to produce gain of Ni-like collisional excited lasers are examined using a 1-D hydrodynamics code. Several schemes such as use of high pressure gas filled targets, foam targets, and use of plasma confined in a cavity are considered to be useful to produce a uniform, long scale length, sub-critical density plasma. We considered the plasma produced inside a cylinder target as schematically shown in Figure 5. In this scheme, firstly, a plasma production laser irradiates and ablates the inner surface of the cylinder. The ablated plasma converges to the center of the cylinder. Secondly, a short-pulse intense laser pulse is focused to the central region to heat the plasma to successively ionize the medium ions to Ni-like stage, and to excite them to lasing levels.

Density and temperature of the preformed plasma has been estimated using HYADES code as shown in Figure 5. Calculations were carried out for the laser intensity of  $10^{12}$ W/cm<sup>2</sup>, wavelength of 1.06 $\mu$ m, and pulse duration of 0.5ns. After 2ns from the beginning of the laser pulse, the plasma converged at center of the cylinder. At 5ns, the central region is filled with uniform plasma with a density of 0.1g/cm<sup>3</sup>.

### 4. SUMMARY

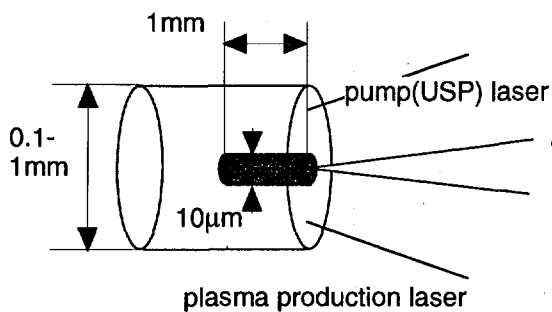


Figure 5 Schematic diagram of a plasma confined in a cylinder.

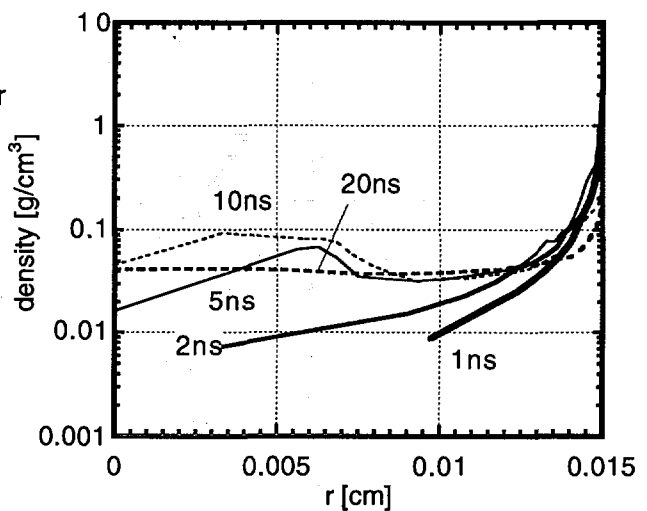


Figure 6 Density profile of the plasma confined in a cylinder.

Simple atomic kinetics and hydrodynamics calculations showed possibility to produce gain in Ni-like Ta by pumping a preform plasma confined in a cylinder. A detailed atomic model which can make more quantitative estimation of soft x-ray gain is under development. Application of the codes to transient pumping x-ray lasers using ultra short pulse laser pumping is projected to determine the optimum pulse duration and the minimum pump energy.

### References

1. B.J.MacGowan, S. Maxon, L.B.DaSilva, C.J.Keane, D.L.Mathews, A.L.Osterheld, J.H.Scofield, G.Shimkaveg, and G.F.Stone, *Phys. Rev. Lett.*, **65**, 420 (1990).
2. B.E.Lemoff, G.Y.Yin, C.L.Gordon III, C.P.J.Barty, and S.E.Harris, *Phys. Rev. Lett.*, **74**, 1574 (1995).
3. P.V.Nickles, V.N.shlyaptsev, M.Kalachnikov, M.Schnurer, I.Will and W.Sandner, *Phys. Rev. Lett.*, **78**, 2748(1997).
4. J. Zhang, A.G.MacPhee, J.Nilsen, J.Lin, T.W.Barbee, Jr., C.Danson, M.H.Key, C.L.S.Lewis, D. Neely, R.M.N.O'Rourke, G.J.Pert, R.Smith, G.J.Tallents, J.S.Wark, and E.Wolfrum, *Phys. Rev. Lett.*, **78**, 3856 (1997).
5. J. Zhang, A.G.MacPhee, J.Lin, E.Wolfrum, R.Smith, C.Danson, M.H.Key, C.L.S.Lewis, D.Neely, J.Nilsen, G.J.Pert, G.J.Tallents, and J.S.Wark, *Science*, **276**, 1097(1997).
6. A.L.Osterheld, private communication.
7. T. Nishikawa, M.Nakamura, H.Takabe, and K.Mima, *J. Plasma and Fusion Res.* 145, **66**(1992).
8. F.Perrot, *Phys. Scripta*, **39**, 332(1989).
9. J.Nilsen, H.Fiedorowicz, A.Bartnik, Y.Li, P.Lu, and E.E.Fill, *Opt. Lett.*, **21**, 408(1996).
10. G.D.Enright, D.M.Villeneuve, J.Dunn, H.A.Baldis, J.C.Kieffer, H.Pepin, M.Chaker, and P. R.Herman, *J. Opt. Soc. Am.*, **B8**, 2049 (1991).

## 14. Optical Properties of Cluster Plasma

Yasuaki KISHIMOTO<sup>†,††</sup>, Toshiki TAJIMA<sup>†,\*</sup>, Mike C. DOWNER<sup>\*</sup>

† Kansai Research Establishment,  
Advanced Photon Research Center

†† Naka Fusion Research Establishment  
Japan Atomic Energy Research Institute,  
Naka, Ibaraki, 311-01 Japan

\* Department of Physics, Institute for Fusion Studies  
University of Texas  
Austin, Texas 78712

### Abstract

It is shown that unlike a gas plasma or an electron plasma in a metal, an ionized clustered material ("cluster plasma") permits propagation below the plasma cut-off of electromagnetic (EM) waves whose phase velocity is close to but below the speed of light. This results from the excitation of a plasma oscillation mode (and/or polarization mode) through the cluster surface which does not exist in usual gaseous plasma. The existence of this new optical mode, *cluster mode*, is confirmed via numerical simulation.

Keyword : High Power Laser, Cluster Plasma, Surface Mode, Polarization Mode, X-Ray Generation, Stochastic Motion, Particle-In Cell Simulation,

## I Introduction

The properties of clustered materials have attracted interest for a long time (e.g. [1], [2]). Recently its interest has heightened, in part, due to the technical developments of nanotechnology and nanoparticles (e.g. [3], [4]) and, in part, due to irradiation of ultrashort femtosecond laser pulses (e.g. [5]-[8]). In particular, it is known that a clustered plasma can absorb a significant amount of laser energy through high power laser-cluster interaction and that highly ionized, very high temperature micro-plasmas are produced. Such a cluster plasma is found to emit a copious amount of intense X-ray than a comparable gas and/or uniform solid-like plasma [9] and, more recently, to eject ions with substantial kinetic energy (up to 1MeV) [10]. So far, although many interests are addressed to the high power nonlinear regime where the laser amplitude is high (i.e.  $a_0 \equiv eA/mc^2 \geq 1$ ) (e.g. [7], [11]-[12]), not only the above prominent features, but also fundamental optical properties, i.e. propagation and absorption in the linear regime have not been studied.

In this paper, we investigate the optical properties when a transverse electromagnetic (EM) field is irradiated onto cluster material and/or cluster plasma. In particular, we point out that the EM field can propagate in a cluster plasma below the plasma cutoff in the linear regime, showing the existence of a new optical branch. We found that this results from the excitation of plasma oscillation modes (and/or polarization modes) which are coupled with the transverse EM field through the existence of a cluster surface. We performed a numerical simulation of the laser-cluster interaction and confirmed that this prominent feature actually takes place.

In Sec.2, we derive the linear dispersion relation of the laser-cluster interaction and describe its properties. In Sec.3, we present our numerical simulation to confirm our theory. Concluding remarks are given in Sec.4.

## II Dispersion Relation of Laser-cluster Interaction

We here consider a fully ionized cluster plasma with the uniform electron density inside the cluster. Let  $p_c$  be the packing ratio, i.e. the ratio of the volume occupied by all the clusters to the entire volume. Since our interest is focused on short pulse laser irradiation, ions in the clusters are assumed to be immobile. A linearly  $p$ -polarized (in the  $y$ -direction) plane electromagnetic wave with frequency  $\omega$  propagating in the  $x$ -direction is irradiated onto this plasma. We assume that the wavelength of this electromagnetic wave  $\lambda = 2\pi/k$  is much greater than the (typical) cluster radius  $a$ , i.e.  $\lambda \gg a$ . The Maxwell equation is

$$\frac{\partial^2}{\partial x^2} E_y - \frac{1}{c^2} \frac{\partial^2}{\partial t^2} E_y = \frac{4\pi}{c^2} \frac{\partial}{\partial t} \langle J_y \rangle, \quad (1)$$

where  $E_y$  is the laser electric field oscillating with frequency  $\omega$ . The current density  $\langle J_y \rangle$  is averaged over the spatial wavelength of the electromagnetic wave and  $\langle J_y \rangle = -\langle n_e \rangle e \dot{y}$  where

$\dot{y} \equiv dy/dt$ , and  $\langle n_e \rangle$  is the average electron density and may be written as  $\langle n_e \rangle = p n_e$ , where  $n_e$  is the local electron density inside the clusters ( $n_e = Z n_i$ , where  $n_i$  is the immobile ionic density).

The dynamics of the electron displacement  $y$  is dictated by the electromagnetic field of course, but also now in a cluster, by the induced polarization within the cluster. In an ordinary plasma, polarization in the direction ( $y$ ) of the electric field of the EM wave does not happen, though polarization in the direction ( $x$ ) of the propagation of the EM wave can happen in the intense regime (and has been exploited for acceleration [13]). However, for a cluster this situation fundamentally changes due to the surface charge induced polarization in the  $y$ -direction. Because of this polarization, there arises a strong restoring force due to plasma electron space charge, which is not too different from the longitudinal plasma charge restoring force. The equation of motion of an electron in the  $y$ -direction is given by

$$\left( \frac{d^2}{dt^2} + \gamma \frac{d}{dt} + f \omega_p^2 \right) y = -\frac{e}{m} E_y(t) , \quad (2)$$

where  $\omega_p = (4\pi e^2 n_e / m)^{1/2}$  is the plasma frequency for the cluster density,  $f$  is a geometrical factor of order unity (unity for slab clusters), and  $\gamma$  denotes the damping rate of plasma oscillations, which may lead to wave absorption. The displacement  $y$  produces a polarization current  $\langle J_y \rangle$  and then Eq. (2) is coupled with Eq. (1), obtaining the dispersion relation of EM waves in a cluster plasma as

$$n^2(k, \omega) \equiv \frac{c^2 k^2}{\omega^2} = 1 - \frac{p \omega_p^2}{\omega^2 - f \omega_p^2 + i \gamma \omega} , \quad (3)$$

where  $n(k, \omega)$  is the index of refraction.

The dispersion relation of Eq. (3) is shown in Fig.1 both in  $(k, \omega)$  and  $(n, \omega)$  space and has one fundamental difference from that for a gaseous (or metallic) plasma, i.e. the term in the denominator of the second term on the right-hand side,  $-f \omega_p^2$ . This term arose from the transverse restoring force due to the space charge on the surface of the clusters. Because of the presence of this term, Eq. (3) now yields two branches in the dispersion relation and a new branch emerges that has a real frequency below the plasma cutoff as seen in Fig.1. By neglecting the damping term in Eq. (3), we obtain two roots in the small wavenumber regime as

$$\omega^2 \simeq (f + p) \omega_p^2 + \left( \frac{p/2}{f + p} \right) c^2 k^2 , \quad (4)$$

$$\omega^2 \simeq \left( \frac{f}{f + p} \right) c^2 k^2 , \quad (5)$$

and those in the large wavenumber regime as

$$\omega^2 \simeq c^2 k^2 + p \omega_p^2 , \quad (6)$$

$$\omega^2 \simeq f \omega_p^2 . \quad (7)$$

Here both Eqs. (4) and (6) are the upper branch and correspond to the well-known EM wave dispersion relation in the presence of a plasma, while both Eqs. (5) and (7) emerge as a new

lower branch. The most striking feature of this new branch is the emergence of a propagating EM wave below the plasma cutoff (in the present case  $\omega = \sqrt{f+p}\omega_p$ ). This branch has a phase velocity close to but less than the speed of light,  $v_{ph} = c/\sqrt{(1+p/f)}$ , and a resonance at  $\omega = \sqrt{f}\omega_p$ .

Although in the present derivation we considered phenomenological damping  $\gamma$ , no kinetic affect is included. However, it can be shown that this wave doesn't suffer from Landau damping in the low  $k$  regime (even though  $v_{ph} < c$ ), while it damps near the resonance similar to the mechanism of cyclotron damping [14]. This is because the restoring force due to clusters does not allow ballistic motion to yield the Landau pole  $(\omega - kv)^{-1}$ . This situation is similar to the Alfvén wave [15] in which the restoring force is magnetic tension, while the phase velocity is typically  $v_A \ll c$ . There is a narrow stop band between  $\sqrt{f}\omega_p < \omega < \sqrt{f+p}\omega_p$ . When the EM waves are injected onto the cluster plasma, the reflection coefficient  $R$  and also the transmission coefficient  $1 - R$  can be obtained in terms of the complex refractive index [ Eq. (3) ] by  $R(\omega) = |(n-1)/(n+1)|^2 = [(n_r-1)^2 + n_i^2] / [(n_r+1)^2 + n_i^2]$ , where  $n = n_r(\omega) + in_i(\omega)$ .

### III Simulation of Laser-Cluster Interaction

Here, we perform a 2D fully relativistic electromagnetic PIC simulation of laser-cluster interaction to confirm the theory we presented in Sec.2. The configuration of the simulation ( $0 \leq x \leq 1524$  and  $0 \leq y \leq 256$ ) is shown in Fig.2 (a), where the grid size is  $\Delta x = \Delta y = 1$  in normalized units. A cluster is modeled by a fully ionized constant density plasma column in the  $(x, y)$ -plane occupying an area of radius  $a$ . Such a cluster plasma is uniformly distributed in the region  $800 \leq x \leq 1200$  with a packing ratio of  $p \simeq 0.31(a = 10)$  as seen in Fig.2. Note that the ions are immobile and each electron is initially distributed in the same position as the ion. We assume that the  $p$ -polarized laser field which is spatially localized in the  $x$ -direction modeling an ultrashort pulse laser, but uniform in the  $y$ -direction as seen in Fig.2. The wavelength is  $\lambda = 45\pi$  so that the condition  $\lambda \gg a$  is satisfied. In the simulation, the cluster density is chosen to  $n_e/n_c \simeq 64$  ( $n_c \equiv m\omega^2/4\pi e^2$ : the cut-off density) and then the average electron density becomes  $\langle n_e \rangle/n_c \simeq 19.4$ . The electron skin depth inside the cluster is  $\delta_e \equiv \omega_p/c \simeq 2.8$ . Therefore, the cluster plasma is sufficiently below the cut-off density so that the laser field usually would not penetrate into a plasma with same average density. The normalized laser amplitude is given by  $a_0 \simeq 0.022$  to simulate the linear regime and the ratio of the electron thermal velocity  $v_e$  to the oscillation velocity  $v_{os}$  is  $v_e/v_{os} \simeq 0.2$ .

The field pattern of  $E_y$  at  $y = L_y/2$ , i.e.  $E_y(x, y = L_y/2)$ , is illustrated in Fig.3 (a)-(e) for different times together with the two dimensional one of  $E_y$ -field at  $t = 40$  which corresponds to Fig.3 (a). After the laser pulse hits the lefthand side boundary of the cluster ( $x \simeq 800$ ), although some part is reflected at the boundary, the laser pulse is found to penetrate into the cluster and to come out from the righthand side, clearly showing the optical branch described in

Sec.2. During the propagation in the cluster, the laser amplitude is found to decrease showing a strong damping as we discuss later. In order to confirm the theory that the transmission results from the polarization in the  $y$ -direction through the cluster surface, in Fig.4, we also show the result when a  $s$ -polarized laser pulse is irradiated in the same manner. As is clearly seen, the laser pulse is completely reflected at the LHS without transmission as occurred in the  $p$ -polarized case.

Figure 5 shows the time evolution of the electromagnetic energy in the system and kinetic energy of cluster electrons for the  $p$  and  $s$ -polarized case corresponding to Figs. (3) and (4). In the case of the  $p$ -polarized wave, a significant portion of the laser energy (about 60 %) is absorbed by the cluster electrons during the transmission. On the other hand, no absorption is observed in the case of the  $s$ -polarized wave. The dashed line in Fig.5 also shows the  $p$ -polarized case, but for smaller packing ratio ( $p_c \simeq 0.2$ ) keeping the average density ( $n_e$ ) constant. The absorption rate is reduced when the ratio  $a/\lambda$ , i.e. [cluster radius]/[laser wavelength] becomes small. This is considered as follows. When  $a \ll \lambda$ , there is no variation of the electric field strength in one cluster. Therefore, the polarization and the corresponding plasma oscillation are well defined because of the splitting of the time scale,  $\omega_p \gg c/2a \gg \omega$ . On the other hand, when  $a \leq \lambda$ , i.e. when the cluster size is not neglected compared with the laser wavelength, the plasma oscillation is affected by the propagation of the laser pulse because of the relation  $\omega_p > c/2a \geq \omega$  and the adiabaticity of the plasma oscillation relative to the laser propagation becomes worse. Then stochasticity of the electron motion is enhanced and as a result the absorption rate increases.

## IV Concluding Remarks

In this paper, we present a new optical mode, i.e. *cluster mode*, where a transverse EM field can propagate below the plasma cut-off frequency and this mode is confirmed via numerical simulation. This results from the excitation of a plasma oscillation mode (and/or polarization mode) through the cluster surface which does not exist in usual gaseous plasmas. Many applications can be derived from the properties of the new branch, because the phase velocity is smaller than the speed of light. We discuss these applications in a different paper. It is important to emphasize that the current theory is linear and that nonlinear physics should play an important role in the interaction between the cluster plasma and laser and will be a focus of future work. Furthermore, although we initially assume a fully ionized cluster plasma, the formation of a cluster plasma where the ionization process is taken into account is important. Also collisional processes will significantly affect the absorption process. This will be examined in future works.

## V Acknowledgments

We would like to acknowledge Mr. K. Nakagawa and Mr. H. Watanabe for supporting the simulation, and Prof. Takuma for fruitful discussion. The work was supported in part by the U.S. DOE.

## Reference

1. A. Kawabata and R. Kubo, J. Phys. Soc. Jpn. **21**, 1765 (1966).
2. R.H. Doremus, J. Chem. Phys. **40**, 2389 (1964).
3. H.W. Kroto, J.R. Heath, S.C. O'Brien, R.F. Curl, and R.E. Smalley, Nature **318**, 162 (1985).
4. M.F. Becker, J.R. Brock, and J.W. Keto, U.S. Patent #5, 585, 07.0 (1996).
5. A. McPherson, et.al. Phys. Rev. Lett. **72**, 1810 (1994)
6. T. Seidman, M. Ivanov, and P.B. Corkum, Phys. Rev. Lett. **75**, 2819 (1995).
7. T. Ditmire, T. Donnelly, R.W. Falcone, and M.D. Perry, Phys. Rev. Lett. **75**, 3122 (1995).
8. E. Snyder, S. Buzzza, and A. Castleman, Phys. Rev. Lett. **77**, 3347 (1996).
9. T. Donnelly, et. al, Phys. Rev. Lett. **76**, 2472 (1996).
10. T. Ditmire, J.W.G. Tisch, et. al. Nature **386**, 54 (1997).
11. M. Rosenberg and N.A. Krall, Phys. Plasmas **3**, 644 (1996).
12. S. Vladimirov and O. Ishihara, Phys. Plasmas **3**, 444 (1996).
13. T. Tajima and J.M. Dawson, Phys. Rev. Lett. **43**, 267 (1979).
14. S. Ichimaru, S., *Statistical Plasma Physics*, (Addison-Wesley, Reading, MA, 1992).
15. H. Alfvén, Nature **150**, 405 (1942).

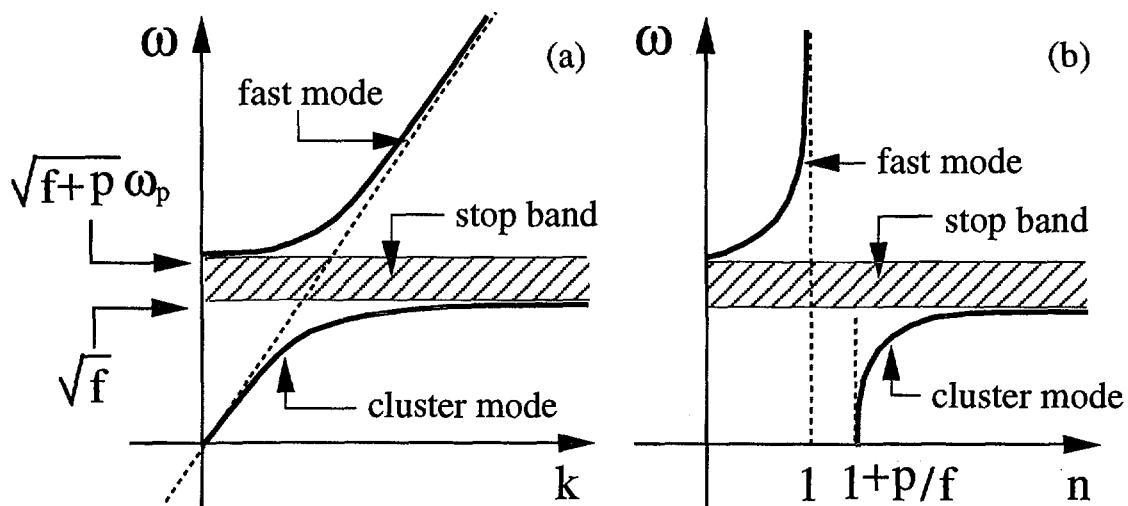


Fig. 1 Linear dispersion relation in the  $(k, \omega)$ -plane (a) and  $(n, \omega)$ -plane of a transverse electromagnetic field and cluster plasma interaction.  $n$  is the refractive index,  $p$  is the packing fraction, and  $f$  is the geometrical factor of order unity.

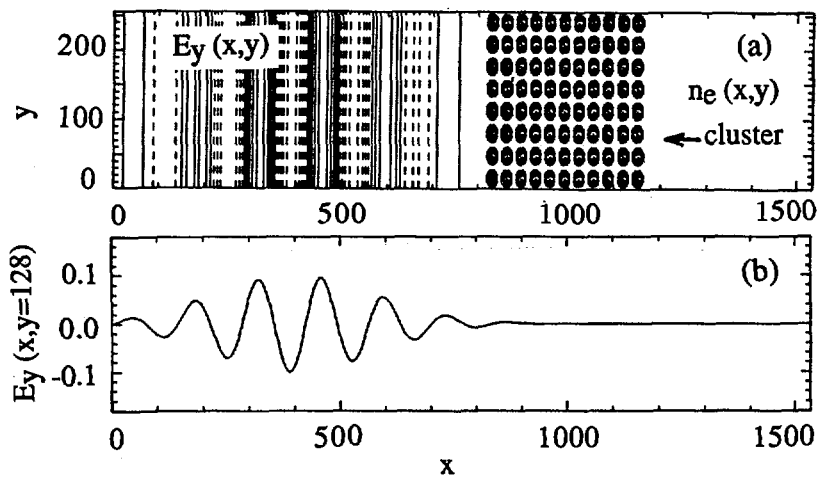


Fig. 2 Configuration of the simulation : (a) contour plot of the initial  $E_y$  field ( $p$ -polarized field) and density distribution of the clusters in the  $(x, y)$ -plane, (b) initial field pattern of  $E_y(x)$  at  $y(= L_y/2) = 128$ .

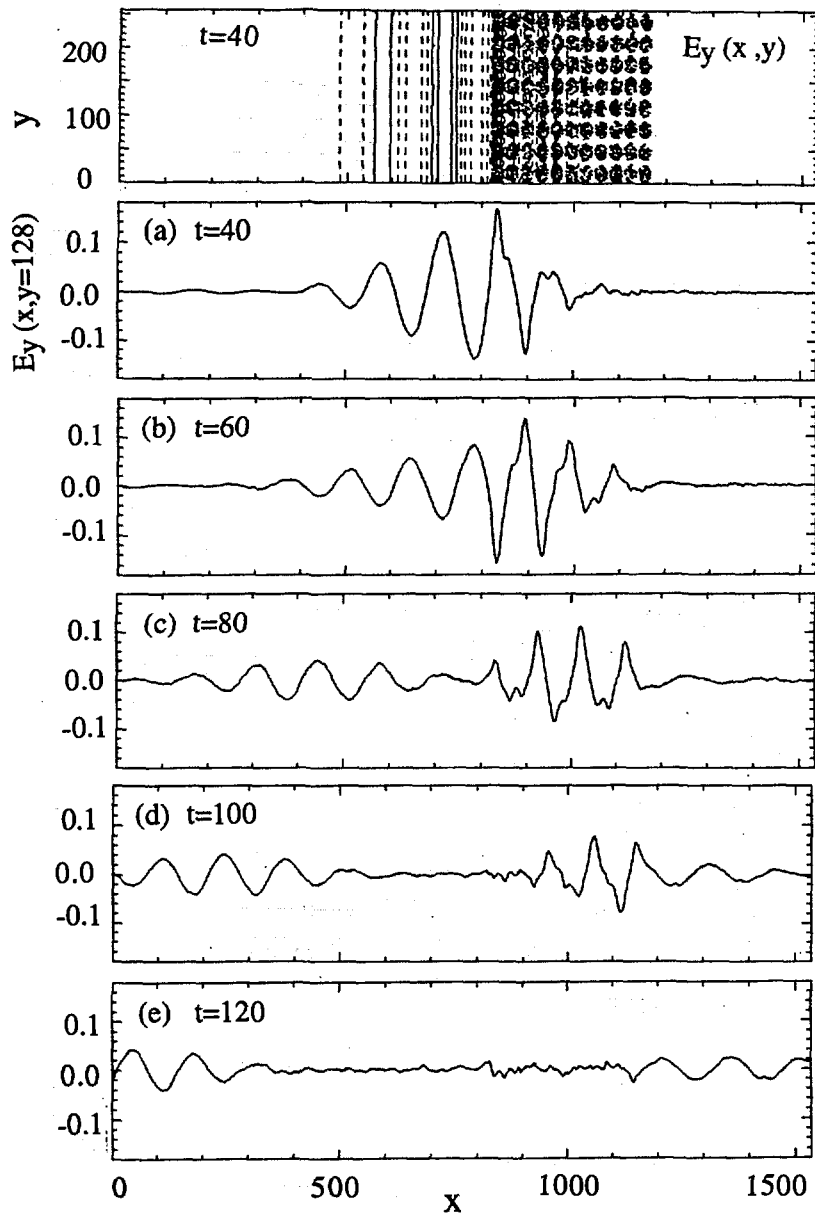


Fig. 3 Field pattern of  $E_y(x)$  at  $y = L_y/2$  for different time steps. Note that the time is normalized by  $\bar{\omega}_p^{-1}$  where  $\bar{\omega}_p$  is the plasma frequency averaged over the system.

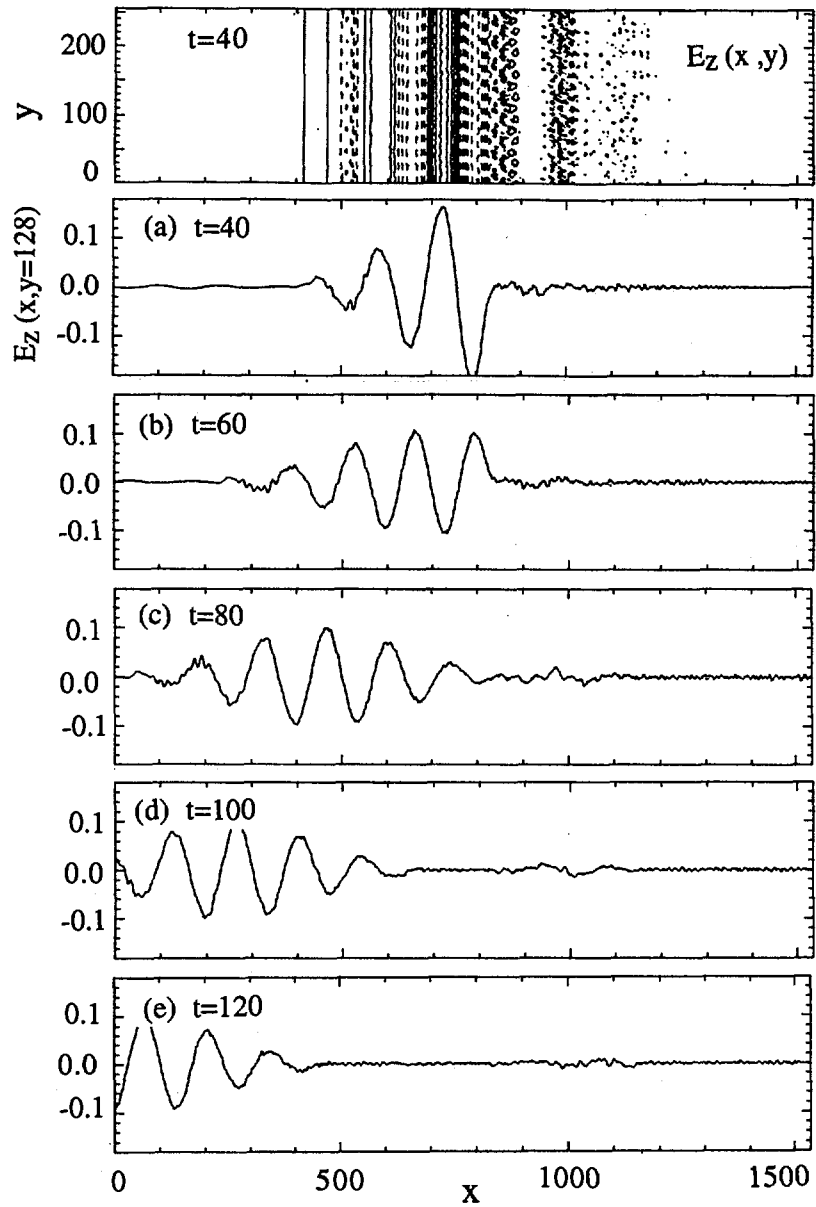


Fig. 4 Field pattern of the  $s$ -polarized field  $E_z(x)$  at  $y = L_y/2$  for different time steps.

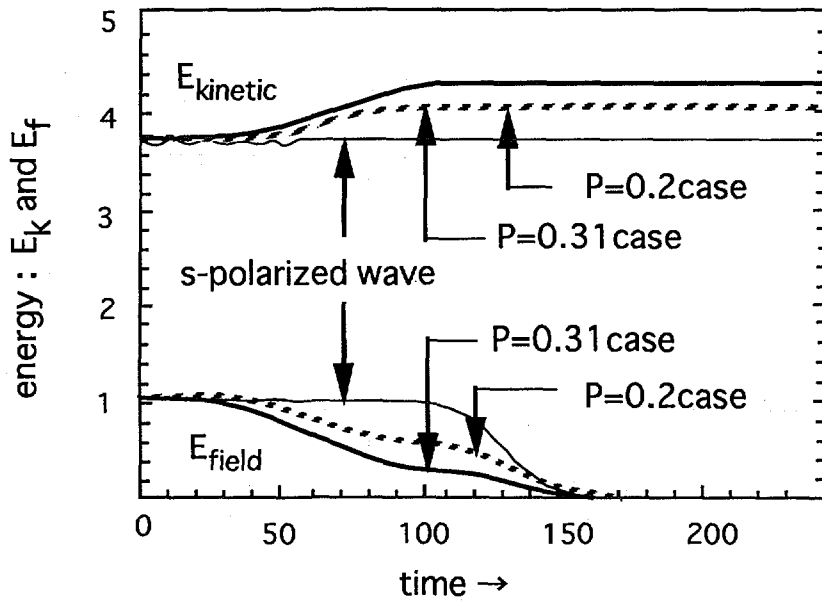


Fig. 5 Time evolution of the EM field energy and kinetic energy for the packing ratio of  $p_c \simeq 0.31$  and  $p_c \simeq 0.2$ . The s-polarized case is also shown by the solid thin line.

## 15. Array Processors Based on Gaussian Fraction-free Method

Shietung Peng\* , Igor Sedukhin<sup>+</sup> and Stanislav Sedukhin\*

<sup>\*</sup>)The University of Aizu, Fukushima 965-80, Japan

e-mail: {s-peng, sedukhin}@u-aizu.ac.jp

<sup>+</sup>)R&D Group, Hiwada Electronic Corp. Fukushima 969-13, Japan

### Abstract

*The design of algorithmic array processors for solving linear systems of equations using fraction-free Gaussian elimination method is presented. The design is based on a formal approach which constructs a family of planar array processors systematically. These array processors are synthesized and analyzed. It is shown that some array processors are optimal in the framework of linear allocation of computations and in terms of number of processing elements and computing time.*

**Keywords:** Linear systems, array processors, numerical algorithms, dependence analysis, systolic processing.

## 1 Introduction

Integer-preserving transformation is an effective technique in the areas like symbolic computation and the application areas where input values can be presented as integers and the results are required as ratios of integers [3]. Some mathematical software packages (like MATHEMATICA and MAPLE) use techniques of integer-preserving transformations simply because of its efficiency.

In the era of high-performance computing, the design of parallel algorithms and/or application-specific architectures which show high regularity in computations and communication is desired. Systolic/wavefront array processors design is one of candidates with great potential [5]. Traditionally, systolic/wavefront arrays were emphasized for its simplicity for VLSI implementation. However, in the recent study, it was shown that the design methodologies of systolic arrays can be applied elegantly to other models of parallel computations [4], e.g., array processors.

In this paper, an approach of systematic design/synthesis of systolic arrays [6, 7] is adapted. The fraction-free Gaussian elimination method for solving linear systems is used for developing the array processors. The systematic approach makes the algorithmic/architectural design of array processors more attractive.

## 2 Fraction-free Algorithm and Its Dependence Analysis

The formal specification of *fraction-free algorithm* [1] is presented below. Let a linear system of equations be given by  $\mathbf{AX}=\mathbf{B}$ , where  $\mathbf{A}=[a_{ij}]_{n \times n}$ ,  $1 \leq i, j \leq n$ , is a nonsingular matrix with determinant  $|A|$ ,  $\mathbf{X}=[x_{ij}]_{n \times (m-n)}$ ,  $1 \leq i \leq n$ ,  $1 \leq j \leq m-n$ , is a set of unknowns and  $\mathbf{B}=[b_{ij}]_{n \times (m-n)}$ ,  $1 \leq i \leq n$ ,  $n+1 \leq j \leq m$ , is an arbitrary right-hand side matrix. The reduction of extended  $[n \times m]$ -matrix  $\mathbf{A}^{(0)} = \mathbf{A} \oplus \mathbf{B}$  to diagonal form can be done by the recurrence formulas:

$$a_{00}^{(0)} = 1, a_{ij}^{(0)} = \begin{cases} a_{ij}, & 1 \leq i \leq n, 1 \leq j \leq n; \\ b_{ij}, & 1 \leq i \leq n, n+1 \leq j \leq m; \end{cases}$$

$$k = 1, 2, \dots, n, 1 \leq i \leq n, k+1 \leq j \leq m :$$

$$\begin{aligned}
 a_{ij}^{(k)} &= \begin{cases} a_{kj}^{(k-1)}, & \text{if } i = k; \\ \frac{1}{a_{k-1,k-1}^{(k-1)}} \begin{vmatrix} a_{kk}^{(k-1)} & a_{kj}^{(k-1)} \\ a_{ik}^{(k-1)} & a_{ij}^{(k-1)} \end{vmatrix}, & \text{otherwise.} \end{cases} \\
 a_{ii}^{(k)} &= a_{kk}^{(k)}, 1 \leq i \leq k-1;
 \end{aligned} \tag{1}$$

An initial algorithm can be derived directly from (1) using indexed, single-assignment format as follows:

```

a_{00}^{(0)} \leftarrow 1;
forall  $1 \leq i \leq n$  do
     $a_{ij}^{(0)} \leftarrow \begin{cases} a_{ij}, & 1 \leq j \leq n; \\ b_{ij}, & n+1 \leq j \leq m; \end{cases}$ 
k = 1 to  $n$  do
    begin
         $a_{kk}^{(k)} \leftarrow a_{kk}^{(k-1)};$ 
forall  $1 \leq i < n, k+1 \leq j \leq m$  do
         $a_{ij}^{(k)} \leftarrow \text{if } i = k \text{ then } a_{kj}^{(k-1)} \text{ else}$ 
         $(a_{kk}^{(k)} \cdot a_{ij}^{(k-1)} - a_{ik}^{(k-1)} \cdot a_{kj}^{(k-1)}) / a_{k-1,k-1}^{(k-1)};$ 
    end
1 \leq i \leq n, 1 \leq j \leq m-n do
     $x_{ij} = a_{i,n+j}^{(n+1)} = a_{i,n+j}^{(n)} / a_{nn}^{(n)};$ 
    
```

As it directly follows from (2), the *index or iteration space*  $\mathcal{I} = \mathbf{Z}^3$  of the initial algorithm consists of the index subsets of input, internal and output computations, i.e.  $\mathcal{P} = \mathcal{P}_{in} \cup \mathcal{P}_{int} \cup \mathcal{P}_{out}$ , where  $\mathcal{P}_{in} = \{(i, j, 0)^T \cup (0, 0, 0)^T \mid 1 \leq i \leq n, 1 \leq j \leq m\} \subseteq \mathbf{Z}^2$ ;  $\mathcal{P}_{int} = \{(i, j, k)^T \mid 1 \leq k \leq n, 1 \leq i \leq n, k+1 \leq j \leq m\} \subseteq \mathbf{Z}^3$ ;  $\mathcal{P}_{out} = \{(i, n+j, n+1)^T \mid 1 \leq i \leq n, 1 \leq j \leq m-n\} \subseteq \mathbf{Z}^2$ .

For this algorithm, local *data dependence graph* (DG) can be constructed in 3-dim index space  $\langle \vec{i}, \vec{j}, \vec{k} \rangle$ , representing the locations of the computations in the space (as the index points) and the data dependencies (as the arcs) between the computations of the algorithm. The local DG  $\Gamma_1$  of the algorithm (2) is shown in Fig. 1 for the case of  $n = 3$  and  $m = 6$ .

It can be shown that the *length*  $\mathcal{L}$  of the longest path is  $\mathcal{L}(p_{\min}, p_{\max}) = 4(n-1) + (m-n) = m + 3n - 4$ , where  $p_{\min} = (1, 1, 1)^T$  and  $p_{\max} = (1, m, n)^T$ . *Timing (step) function*  $\text{step}(p) : \mathcal{P}_{int} \rightarrow \mathbf{Z}_+$  which assigns a computational time step to each index point  $p \in \mathcal{P}_{int}$  can be defined as  $\text{step}(p) = |i-k| + |j-k| + 3k - 3$ . The spatial allocation of the set of computations is accomplished by an allocation function  $\text{place}(p) = \Lambda_\eta \cdot p$ , where  $\Lambda_\eta$  is a  $(2 \times 3)$ -matrix of the linear transformation corresponding to a *projection direction*  $\eta \in \ker \Lambda_\eta$  and which has the **rank**  $\Lambda_\eta = 2$ .

Along all possible projection directions which the cubic DG may be projected onto the plane, only those are *admissible* that keep local data dependencies between computations, and do not map any index points  $p, q \in \mathcal{P}_{int}$ , such that  $\text{step}(p) = \text{step}(q)$ , onto the same PE.

The major problems concerning the initial algorithm and its DG are: (1) some data are transmitted along opposite edges in  $\vec{i}$  direction, thus prevent projections in this direction; (2) the arc-delays along  $\vec{k}$ -axis vary, thus complicate the control of computation/communication. To design optimal array processors, we present a new algorithm which eliminates the problems mentioned above using an innovative reindexing technique in the next section.

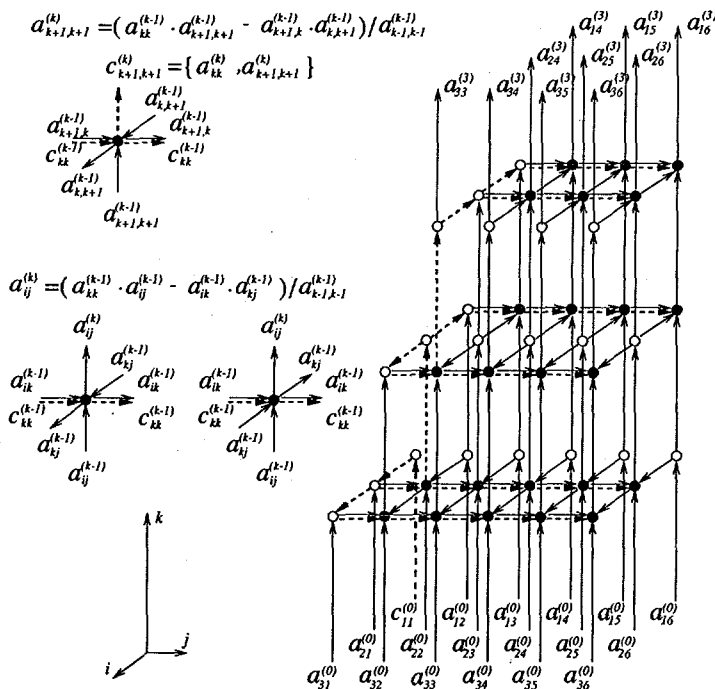


Figure 1: The data dependence graph of the initial algorithm.

### 3 The Design of the Regular Algorithm

One way to resolve the irregularity problem of the initial algorithm (2) is to reindex the nodes in the DG. The reindexing is as follows: at the  $k$ -th iteration, we shift the  $k$ -th row,  $(a_{k,k+1}^{(k-1)}, \dots, a_{km}^{(k-1)})$ , to  $(n+k)$ -th row. Based on the above scheme we can rewrite the algorithm (2) in the following form (*affine recurrent equations* scripted as nested loops):

```

\input computations (initialization)
a_{00}^{(0)} ← 1;
forall 1 ≤ i ≤ n do
    a_{ij}^{(0)} ← { a_{ij}, 1 ≤ j ≤ n;
                  b_{ij}, n+1 ≤ j ≤ m;
\internal computations
for k = 1 ton do
    begin
        a_{kk}^{(k)} ← a_{kk}^{(k-1)};
        forall k < i ≤ n+k, k < j ≤ m do
            a_{ij}^{(k)} ← if i = n+k then a_{kj}^{(k-1)} else
                (a_{kk}^{(k)} · a_{ij}^{(k-1)} - a_{ik}^{(k-1)} · a_{kj}^{(k-1)}) / a_{k-1,k-1}^{(k-1)};
        end
\output computations
forall 1 ≤ i ≤ n, 1 ≤ j ≤ m-n do
    x_{ij} = a_{i+n,j+n}^{(n+1)} = a_{i+n,j+n}^{(n)} / a_{nn}^{(n)};
    
```

The localized regular DG  $\Gamma_2$  corresponding to the equations (3) is depicted on Fig. 2 for the

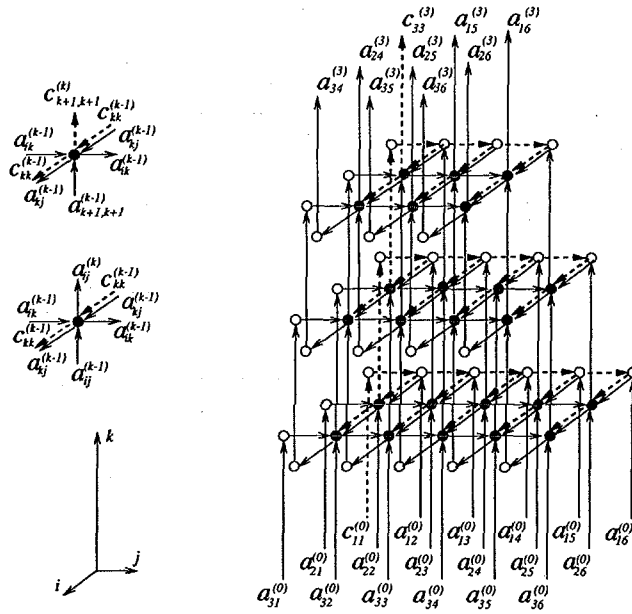


Figure 2: The data dependence graph of the regular algorithm.

case of  $n = 3, m = 6$ .

For the regular DG the *timing function*  $\text{step}(p)$  can be specified in the linear form as  $\text{step}(p) = \lambda \cdot p + \gamma$ . This function defines a set of hyperplanes orthogonal to the *schedule vector*  $\lambda$  on the index space of the algorithm. It is easy to show that the timing function of the *minimal form* for the regular DG is  $\text{step}(p) = i + j + k - 3$  for any  $p \in \mathcal{P}_{int}$ , taking into account that  $\text{step}(p_{min}) = 0$ , where  $p_{min} = (1, 1, 1)^T \in \mathcal{P}_{int}$ . Thus, the schedule vector  $\lambda$  is  $(1, 1, 1)$  and  $\gamma$  is  $-3$ . It can be proved that the *length of the longest path* in the regular DG is  $\mathcal{L}(p_{min}, p_{max}) = 3(n - 1) + m$ , where  $p_{max} = (2n, m, n) \in \mathcal{P}_{int}$ .

## 4 Optimal Array Processors

As mention before, the *timing* and *allocation functions* must guarantee that each PE executes at most one computation, which associated with any index point of DG, at any given time step. For the regular DG with a linear timing function this requires the condition  $\lambda \cdot \eta \neq 0$  to be held. According to [7] for the 3-dim DG of the regular algorithm there are 17 possible *projection directions* that keep the local communications and define systolic solutions. However, only 13 directions are admissible for the regular DG according to the above condition. It can be shown that the only solutions, generated by mapping the regular DG along the projection directions  $\eta_1 = (0, 1, 0)^T$  and  $\eta_2 = (1, 0, 0)^T$ , i.e. along  $\vec{j}$ -axis and  $\vec{i}$ -axis, are characterized in aggregate by the minimal numbers of PE's and I/O ports, and the number of delays. The array processor  $S_{(0,1,0)}$  is generated by mapping the regular DG along  $\vec{j}$  direction, i.e. along projection direction  $\eta_1 = (0, 1, 0)^T$ . This 2-dim rhombic array processor  $S_{(0,1,0)}$  (see Fig. 3 for the case of  $n = 3, m = 6$ ) consists of  $P_{(0,1,0)} = n(n - 1)$  orthogonally connected PEs,  $2n$  delay elements. Thus a size of array is independent of  $m$ . The initial matrix  $A^{(0)} = [a_{ij}^{(0)}]_{n \times m}$  is loaded into the array processor column by column. The total computation time for one task is  $T_{(0,1,0)}(1, n, m) = T_{min}(\Gamma_2) = 3(n - 1) + m$ . The data pipelining period is  $\alpha = |\lambda \cdot \eta_1| = 1$  and the block pipelining period is  $\beta = m + 1$ , i.e. the next task can be pushed into this array processor after  $m + 1$  time steps. The number of I/O ports is  $2n$ . Also it is

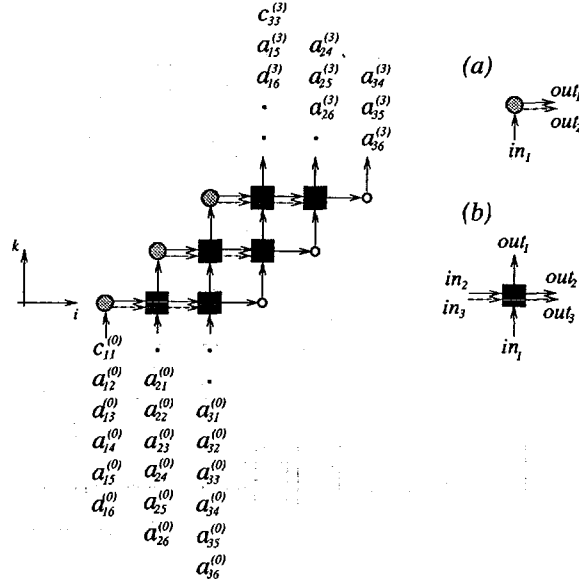


Figure 3: The array processor  $S_{(0,0,1)}$ .

evident that for  $l$  tasks the time of processing is  $T_{(0,1,0)}(l, n, m) = 3(n - 1) + l(m + 1) - 1$ .

Another optimal design can be obtained by mapping the regular DG along  $\vec{i}$  axis, i.e. along the projection direction  $\eta_2 = (1, 0, 0)^T$ . The corresponding systolic array processor and input/output data flows are shown in Fig. 4 for the case of  $n = 3$  and  $m = 6$ . The array uses  $P_{(1,0,0)} = n(2m - n - 1)/2$  processing elements  $PE_{j,k}$  (see Fig. 4 (a)),  $1 \leq k \leq n + 1, k + 1 \leq j \leq m$ , and  $n$  delay elements. It is not difficult to show that array processor  $S_{(1,0,0)}$  has smaller number of PEs than  $S_{(0,1,0)}$  and all other admissible projects if  $n < m < (3n - 1)/2 \approx 1.5n$ . The number of I/O ports in this design is  $2m - n$ . The initial expanded matrix  $\mathbf{A}_0 = [a_{ij}^{(0)}]_{n \times m}$  is loaded into array row by row. The total computation time is  $T_{(1,0,0)}(1, n, m) = T_{\min}(\Gamma_2) = 3(n - 1) + m$ . This array processor supports a noninterleaved block pipelining period of  $\beta = n$  and a data pipelining period of  $\alpha = |\lambda \cdot \eta_2| = 1$ , so successive computations can be repeated every  $n$  time steps.

## 5 Conclusion

In this paper, we show a systematic approach for designing array processors for solving linear systems using fraction-free Gaussian elimination method. The advantage of this approach is that the optimality of the proposed array processors can be verified systematically. The reindexing technique used in this paper is very powerful for refining the given algorithm so that it becomes suitable for the design of array processors.

There are some directions for further research. For example, to investigate the possibility of using non-linear scheduling for reducing number of PEs in optimal array processors generated by linear scheduling [2], and to implement the algorithm on high-performance parallel computers for performance evaluation, error analysis, and empirical study of scalability and benchmark are certainly worth of future work.

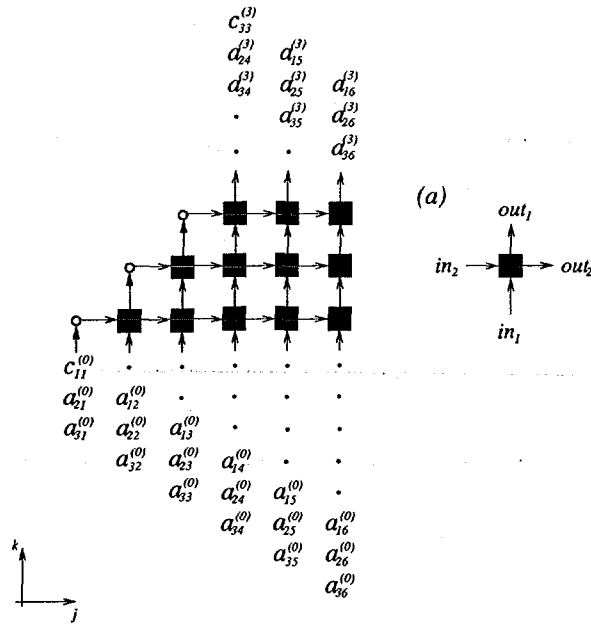


Figure 4: The array processor  $S_{(1,0,0)}$ .

## References

- [1] Bareis E.H. Sylvester Identity and Multistep Integer-Preserving Gaussian Elimination. *Mathematics of Computation*, No. 22, 1968, pp. 565–578.
- [2] Clauss Ph., Mongenet C., Perrin G.R. Synthesis of size-optimal toroidal arrays for the algebraic path problem. *Proc. of the International Workshop Algorithms and Parallel VLSI Architectures II*, France, June 3-6, 1991, Elsevier Publisher, 1992, pp. 199–210.
- [3] Fox L. *An Introduction to Numerical Linear Algebra*. Oxford University Press, New York, 1965.
- [4] Huang C.H., Lengauer Ch. The derivation of systolic implementations of programs. *Acta Informatica*. No. 24, 1987, pp. 595–632.
- [5] Kung S.Y. *VLSI Array Processors*. Prentice Hall, 1988.
- [6] Peng S., Sedukhin S. Array processor design for division-free linear system solving. *the Computer Journal*. Vol. 39, No. 8, 1996, pp. 713–722.
- [7] Sedukhin S.G., Sedukhin I.S. Systematic approach and software tool for systolic design. *Lecture Notes in Computer Science*, Number 854, Buchberger B. and Volkert J. eds., Springer-Verlag, 1994, pp. 172–183. (<http://gemini.u-aizu.ac.jp/HPCC/S4CAD/>)

## 16. Numerical Simulation of Extremely Chirped Pulse Formation with an Optical Fiber

Tamitake ITOH, Akihiko NISHIMURA, Kazuyoku TEI, Tohru MATOBA, Hiroshi TAKUMA  
JAERI, 2-4 Shirane, Tokai-mura, Naka-gun, Ibaraki-ken 319-11, Japan

Mikio YAMASHITA, Ryuji MORITA  
Department of Applied Physics, Hokkaido Univ., Kita-13, Nishi-8, Kitaku, Sapporo 060, Japan

### ABSTRACT

A nonlinear propagation code which used a symmetric split-step Fourier method as an algorithm was improved to simulate a propagation behavior of extremely chirped pulse in a long fiber. The performances of pulse propagation in noble gases cored hollow fibers and a pulse stretcher using a nonlinear and normal silicate fibers have been simulated by the code. The calculation results in the case of the hollow fiber are consistent with their experimental results. We estimated that this pulse stretcher could give a extremely chirped pulse whose spectral width was 84.2nm and temporal duration was 1.5ns.

Keywords: Chirped pulse, Nonlinear propagation, Symmetric split-step Fourier method,  
Pulse stretcher, Nonlinear fiber, Hollow fiber

### 1. INTRODUCTION

Chirped pulse amplification (CPA)<sup>1)</sup> has been widely applied to the high peak power laser systems to enable efficient energy extraction without optical damage from solid state gain media. The use of Ti:sapphire as a gain medium has produced wide variety of CPA laser systems. The output peak power is ranging from mJ to several J. The fs-mJ pulses easily undergo self phase modulation (SPM) in a hollow quartz fiber, giving broadened spectra, which make the pulses compressible down to the range of 10 fs<sup>2)</sup>. The high energy storage capacity, low quantum defect and long lifetime of excited-state are necessary for the gain media in order to make the systems compact and efficient. For this reason, Yb:glass is an attractive gain medium for the future CPA laser systems. Recently, an application of Yb:glass for CPA has been demonstrated<sup>3)</sup>. In this experiment, a silicate fiber was used to stretch a 100-fs pulse to 2-ns one before the amplification with a Yb:glass regenerative amplifier. This indicated that a silicate fiber stretcher was useful to obtain a extremely chirped pulses. However, further chirped pulses caused by SPM are required to cover the bandwidth of Yb:glass. A nonlinear fiber would meet this purpose. A numerical simulation for SPM coupled with dispersion calculation is necessary to estimate the characteristics of chirped pulse injection in a hollow fiber or a fiber stretcher. In this report, a calculation code improved to save CPU time and memory size successfully simulates the propagation in each fiber. The advantage of the use of a nonlinear fiber in pulse stretching is also demonstrated.

### 2. CALCULATION MODEL

Owing to a nonlinear refractive index, the refractive index of a fiber core varies with intensity of pulse. This effect induces an intensity-dependent phase modulation. As a result, the spectrum of the pulse from the fiber is broadened. The pulse duration also broadens in time domain, owing to the fiber



scale of arrangement variable is adopted to a pulse duration. As a pulse propagates farther, its duration becomes longer. Therefore, a time width should be extended in memory. By the use of super computers VPP300 and VPP500(FUJITSU) with vector processors, these calculations has been enable to be carried out.

### 3. CALCULATION RESULTS and DISCUSSION

#### 3.1 Simulation for a hollow fiber

As a first example, a propagation behavior in a hollow fiber are simulated. We also check our numerical method by comparing our calculation results with experimental results under the same conditions. The experimental data reported by Svelto et. al was used for the present simulation<sup>2)</sup>. The experimental setup is shown in Fig 2. An input pulse was focused into the fiber core and its output was collimated and compressed with the prism pairs. The fiber core was filled with noble gas at a high pressure. The output pulse was compressed to 10 fs. The input pulse duration was 140 fs and its peak power was several GW. Figs. 3 (a) and (b) show the experimental and calculated output spectra obtained with a fiber filled with krypton at 2-atm and a 1-GW input peak power. The vertical axis shows the normalized intensity. The horizontal axis shows the wavelength. The experimental and calculated spectral broadening are indicated by the arrows, and are almost the same. However the spectral structures showed a little difference. Though the calculated spectrum exhibited two main peaks and one small peak, but the experimental spectrum has only two peaks and the small was not observed. An initial chirp and a pulse asymmetry could explain the absence of the small peak in the experimental spectrum. Figs. 4 (a) and (b) show experimental and calculated output spectra obtained with a fiber filled with Argon at 4-atm and a 3.5-GW input peak power. The center wavelengths of the spectra are blue shifted by 10 nm in the both the cases. The experimental and calculated spectral structures are considerably different each other. The calculated spectrum has a large peak on the blue side, but the experimental one has a large peak on the red side. This difference also could be attributed to an initial chirp and a pulse asymmetry of input pulse. With these results, we think these calculation results are consistent with experiments.

#### 3.2 Simulation for a fiber stretcher

Spectral width of injected pulses should be wide enough in comparison with gain bandwidth of regenerative amplifiers. Over 60 nm spectrum width is necessary for Yb:glass CPA. However, it is difficult to generate such a broad spectrum at the wavelength of 1  $\mu$ m. For this reason, the fiber stretcher which consists of a short nonlinear fiber and a long silicate fiber is proposed(Fig. 5). Since the nonlinear refractive index of the nonlinear fiber is larger than that of the normal silicate fiber by several times, the nonlinear fiber can easily expand the spectrum of seed pulse from a mode-locked oscillator<sup>6)</sup>. The SPM effect disappears as the pulse width increases. In the silicate fiber, the broaden spectrum is chirped in time domain by the dispersion effect. Table 1 shows the comparison of a nonlinear fiber and a

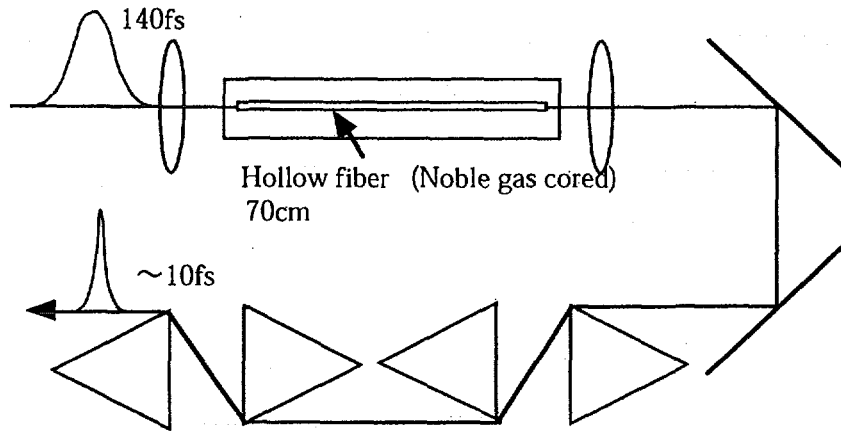


Fig 2. An illustration of pulse compression using a hollow fiber.

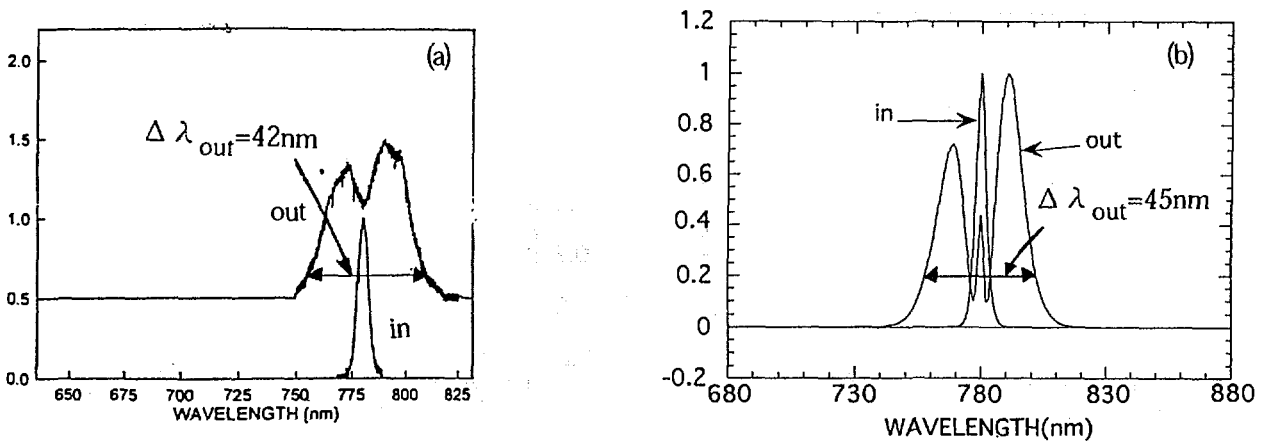


Fig 3. Output spectra from a krypton cored fiber with those of input pulse. (a) experimental and (b) calculated results. Fiber length 70cm, core diameter  $140\ \mu\text{m}$ , center wavelength 780nm, input pulse duration 140fs, input peak power 1GW,  $n_2\ 8.479 \times 10^{-26}\text{m}^2/\text{V}^2$  and pressure 2 atm.

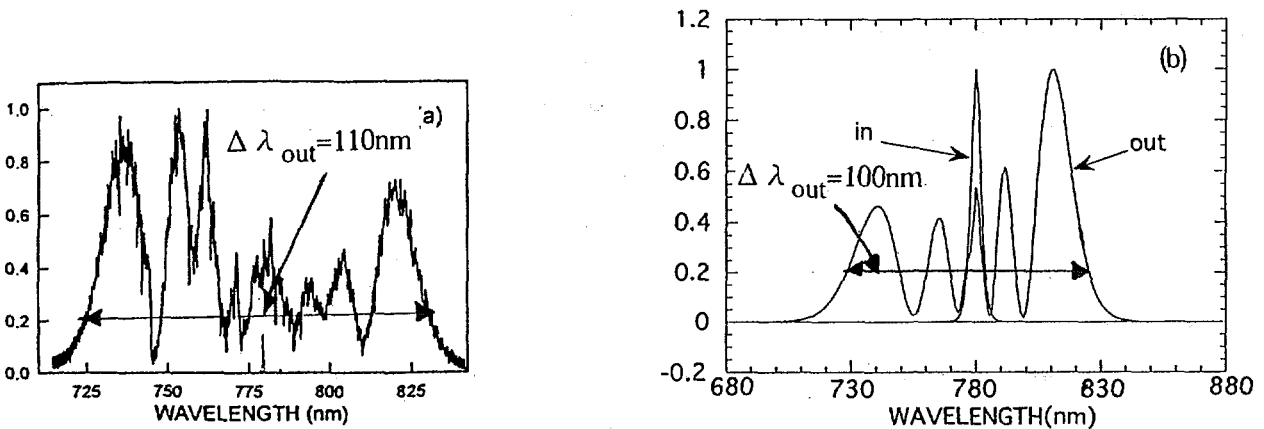


Fig 4. Output spectra from an argon cored fiber with those of input pulse. (a) experimental and (b) calculated results. Fiber length 70cm, core diameter  $140\ \mu\text{m}$ , center wavelength 780nm, input pulse duration 140fs, input peak power 3.5GW,  $n_2\ 5.977 \times 10^{-26}\text{m}^2/\text{V}^2$  and pressure 2 atm.

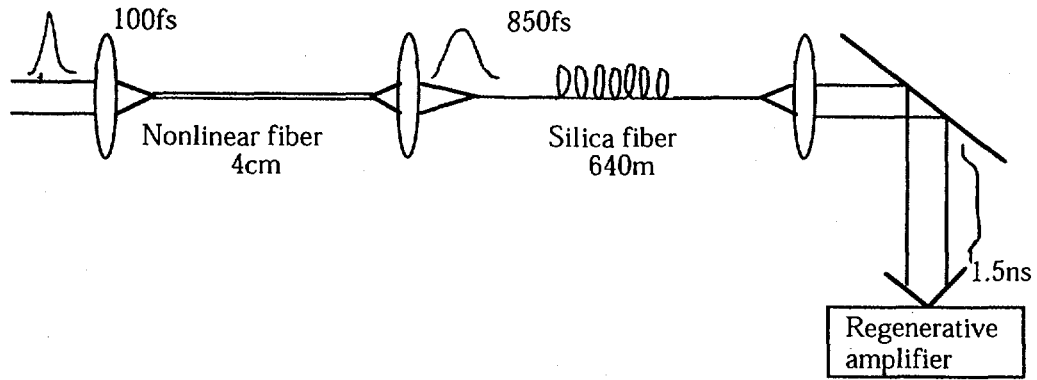


Fig 5. An illustration of pulse stretcher using nonlinear fiber.

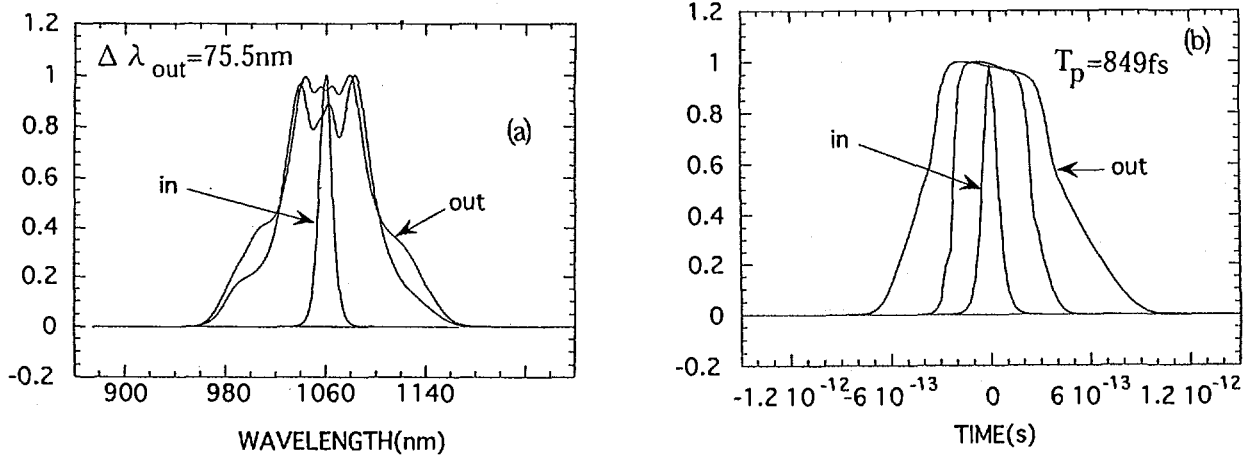


Fig 6. An output pulse from nonlinear fiber with those of the input pulse. (a) Spectrum shape and (b) temporal shape. Fiber length 4cm, core diameter  $4.5 \mu\text{m}$ , center wavelength 1060nm, input pulse duration 100fs, input peak power 10kW.

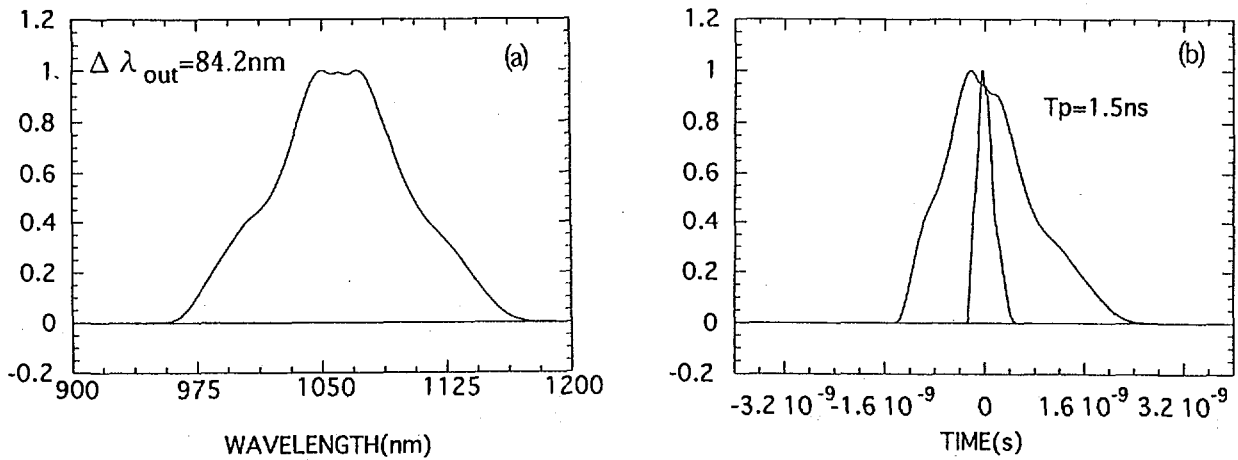


Fig 7. Output pulse from nonlinear fiber with those of the input pulse. (a) Spectrum shape and (b) temporal shape. Fiber length 640m, core diameter  $10 \mu\text{m}$ , center wavelength 1060nm, input pulse duration 850fs, input peak power 1.17kW.

silicate fiber. The peak power of seed pulse can be reduced for the sake of the nonlinear fiber section, which enable us to use a glass oscillator directly pumped with a laser diode<sup>7)</sup>. Here, the 100 fs pulse and 10 kW peak power at 1060 nm are used for the typical specification from this type of oscillator. The nonlinear refractive index of this nonlinear fiber core is 10 times larger than that of normal silicate fiber<sup>8)</sup>. However, no nonlinear fibers longer than several cm are commercially available. Figs. 6(a) and (b) show the calculation results obtained for the output pulses with the nonlinear fiber. The full width at half maximum of the output spectrum is 75.5 nm. It covers the gain band of a Yb:glass amplifier. The pulse is stretched to its duration of 850 fs, and is injected to normal silicate fiber. Figs. 7 (a) and (b) show the calculation results of a silica fiber output pulse. This calculation is carried out with the nonlinear fiber output pulse profile as show in Figs. 6. The pulse propagates 640 m through the silicate fiber. The SPM effect in the silicate fiber is negligibly small during the propagation of 640 m. The full width at half maximum of the output spectrum is 84.2 nm, and the pulse duration is stretched to 1.5 ns.

Table 1. Profiles of a lead-doped nonlinear fiber and a normal silicate fiber

Substance	$n_2$ ( $\text{m}^2/\text{V}^2$ )	Group velocity dispersion (1060nm) ( $\text{s}^2/\text{m}$ )	Material	Length
Nonlinear fiber	$1.196 \times 10^{-21}$	$1.279 \times 10^{-25}$	PbO doped Silica(75wt%)	Short
Silica fiber	$1.220 \times 10^{-22}$	$1.677 \times 10^{-26}$	Silica	Long

#### 4. SUMMARY

The performance of a pulse stretcher using a nonlinear and normal silicate fibers has been simulated by the symmetric split-step Fourier method. We adopted an increasing segment length for the decreasing nonlinear effects of the fiber during the propagation of the input pulse. At the same time, an increasing arrangement variable size was used for the increasing pulse duration to save CPU time and memory. We have demonstrated the spectral and temporal broadening of the input pulse after the propagation through hollow fibers. The results are in good accordance with the experimental data. We have simulated a pulse stretcher which consists of a nonlinear fiber and normal silicate fiber, and we showed the spectral broadening(8.2 nm  $\rightarrow$  84.2 nm) and the temporal broadening(100 fs  $\rightarrow$  1.5 ns).

#### ACKNOWLEDGMENTS

The authors would like to thank Dr. Hirokazu Kubota of Optical Soliton Communication Research Group, Nippon Telegraph and Telephone Corporation for valuable discussions.

REFERENCES

1. D. Strickland and Mourou, *Opt. Commun.*, 56, 219 (1985).
2. M. Nisoli, S. De Silvestri, and O. Svelto, *Appl. Phys. Lett.*, 60, 2793 (1996).
3. S. Biswal, F. Duron, J. Nees, G. Mourou and A. Nishimura, CThC1, Technical Digest CLEO '97(Baltimore) p.319 (1997).
4. R. Morota and M. Yamashita, *Opt. Lett.*, 19, 1459 (1994).
5. See for example, G. P. Agrawal, *Nonlinear Fiber Optics* (Academic Press, San Diego, 1989).
6. T. Itoh, R. Morita and M. Yamashita, *Jpn. J. Appl. Phys.*, 35, 1107 (1996)
7. J. Aus der Au, D. Kopf, F. Morier-Genoud, M. Moser, and U. Keller, *Opt. Lett.*, 22, 307 (1997).
8. T. Suemura, M. Ohtani, R. Morita, and M. Yamashita, FST'97 (1997. 2.13-14).
9. R. H. Stolen and C. Lin, *Phys. Rev.*, A 17, 1448 (1978).

## 17. Emerging Terawatt Picosecond CO<sub>2</sub> Laser Technology

I.V. Pogorelsky

*Accelerator Test Facility, Brookhaven National Laboratory, 725C, Upton, NY 11973, USA*

### ABSTRACT

The first terawatt picosecond (TWps) CO<sub>2</sub> laser is under construction at the BNL Accelerator Test Facility (ATF). TWps-CO<sub>2</sub> lasers, having an order of magnitude longer wavelength than the well-known table-top terawatt solid state lasers, offer new opportunities for strong-field physics research. For laser wakefield accelerators (LWFA) the advantage of the new class of lasers is due to a gain of two orders of magnitude in the ponderomotive potential. The large average power of CO<sub>2</sub> lasers is important for the generation of hard radiation through Compton back-scattering of the laser off energetic electron beams. We discuss applications of TWps-CO<sub>2</sub> lasers for LWFA modules of a tentative electron-positron collider, for  $\gamma$ - $\gamma$  (or  $\gamma$ -lepton) colliders, for a possible "table-top" source of high-intensity x-rays and gamma rays, and the generation of polarized positron beams.

### 1. NEW CLASS OF TERAWATT PICOSECOND LASERS

Table-top terawatt (T<sup>3</sup>) picosecond and subpicosecond solid state lasers are the sources of the most intense electromagnetic radiation and strongest electric and magnetic fields available for laboratory research. However, progress in the newly emerged strong-field physics applications, such as laser accelerators or laser synchrotron x-ray sources, to high repetition rate devices is impeded by the low average power of the T<sup>3</sup> lasers. This is due to the inherently low efficiency of the thermal diffusion cooling of the solid active elements. Much more efficient convection heat exchange may be implemented in the fast-flow gas lasers. The demonstrated high output energy and power of molecular and eximer lasers make them a rational complement to solid state laser technology. CO<sub>2</sub> lasers operating in the mid-IR spectral region ( $\lambda=10 \mu\text{m}$ ) deserve the most attention. This is not just because the absolute maximum average power has been demonstrated with these devices, but also due to favorable wavelength scaling of a number of light-matter interactions.

The relatively long nanosecond pulse duration of conventional CO<sub>2</sub> lasers is the prime reason why the potentials of CO<sub>2</sub> lasers have not been utilized so far in a full manner for high-energy physics research. Kilojoules of laser energy would be required to reach a terawatt peak power. This is still possible with CO<sub>2</sub> lasers, as it has been demonstrated previously. However, such lasers are very bulky and are not capable of high repetition rates. There is also a problem to deliver such a high laser energy to the interaction point without optics damage. And finally, the nanosecond pulses are incompatible with many of the strong-field physics processes which are typically localized in very short time and space intervals. Thus a picosecond and shorter pulse duration turns out to be a prerequisite for the successful use of lasers in advanced scientific applications.

A physical parameter that enables generation and amplification of picosecond laser pulses is the gain spectral bandwidth. In solid state lasers, radiation transitions in outer electron shells of active ions are broadened to 5-50 THz due to the perturbation action by the host matrix. Such a broad gain spectrum makes possible the generation of picosecond, and even femtosecond, laser pulses by the mode locking technique. Unlike a solid state, the spectral gain in the molecular gas discharge is periodically modulated by

the rotational structure. Due to the discrete spectrum, and for other physical and technical reasons, mode-locking techniques do not work for CO<sub>2</sub> lasers as well as for solid state lasers. However, alternative methods to produce picosecond and sub-picosecond CO<sub>2</sub> laser pulses have been developed. One of them is semiconductor optical switching. Using this method, subpicosecond CO<sub>2</sub> laser light slices has been demonstrated [1].

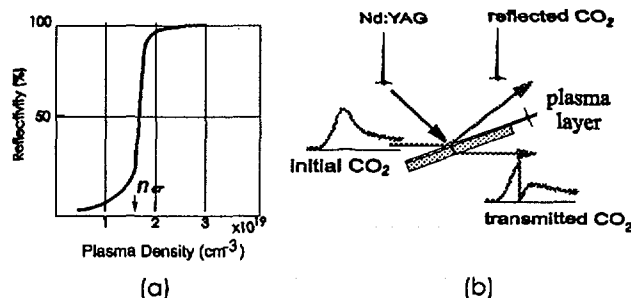


FIGURE 1. Principles of semiconductor optical switching:

a) reflectivity of Brewster Ge window versus surface free-electron density; b) transition reflection from semiconductor optical switch.

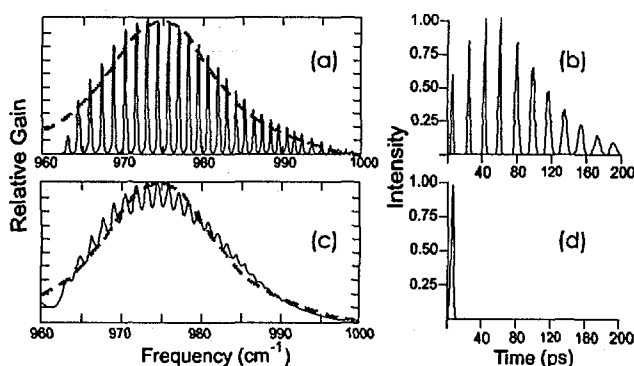


FIGURE 2. Picosecond CO<sub>2</sub> laser pulse amplification:

a) CO<sub>2</sub> gain spectrum at 1 atm (dashed line shows spectral envelope of 1 ps CO<sub>2</sub> pulse); b) 1 ps pulse splits into train after propagation through 1 atm laser amplifier (simulation); c) CO<sub>2</sub> gain spectrum at 10 atm matches 1 ps pulse; d) 1 ps pulse is amplified in 10 atm laser amplifier without distortions.

rotational line structure than with a regular CO<sub>2</sub> molecule. The theoretical limit to the pulse duration, defined by the total 1 THz bandwidth of the CO<sub>2</sub> vibrational band, is 0.5 ps. The 0.8 ps pulses have been demonstrated [3]. At that time they were produced in a several cubic centimeter discharge volume at a millijoule level, thus the peak power was still at a gigawatt level.

Illustrated in Fig. 1 by the example of the ATF laser system [2], the optical switching process works as follows. Nd:YAG pulse having photon energy above the band gap of germanium creates an electron-hole plasma in a surface layer. When the plasma reaches the critical density the refractive index becomes imaginary, and Ge, which is normally transparent to the 10- $\mu$ m radiation, immediately turns to a metal-like mirror. After the control pulse termination, the drop of reflection from the Ge has a characteristic time of diffusion of the free-carriers into the bulk material which is  $\sim 150$  ps. To define the trailing edge of the pulse thereby shortening it to a few picoseconds, the complement to reflection switching, transmission switching, is used for a second stage.

We know how to produce a short pulse. Now we need to amplify it. When a picosecond laser pulse propagates in a gas with a periodic modulated rotational spectrum, the nonuniform spectral gain modifies its spectral envelope; see Fig. 2(a,b). The intensity envelope, related to the spectrum by the inverse Fourier transform, will be correspondingly reshaped. The pulse will split into a train of pulses. The period in this train, 18 ps, corresponds to the frequency interval between the centers of rotational lines. Smoothing of the molecular spectrum via pressure broadening helps to minimize the laser pulse distortions; see Fig. 2(c,d).

An alternative way to achieve gain smoothing is to reduce the spectrum modulation period using an isotopic gas mixture CO<sub>2</sub><sup>16</sup>:CO<sup>16</sup>O<sup>18</sup>:CO<sub>2</sub><sup>18</sup>. Due to isotopic shifts, the combined spectrum has four times denser

To attain a terawatt peak power, a  $\sim 10$ -atm,  $\sim 10$ -l  $\text{CO}_2$  amplifier is required. To maintain a uniform discharge under such conditions, the following requirements should be satisfied: a) strong penetrating preionization, b)  $\sim 1$  MV voltage applied to the discharge, and c) the energy load of several kilojoules deposited in a relatively short,  $\leq 300$  ns, time interval. The first x-ray preionized laser with such parameters is under construction at the ATF. Fig.3 shows the principal optical diagram of the ATF TWps  $\text{CO}_2$  laser system.

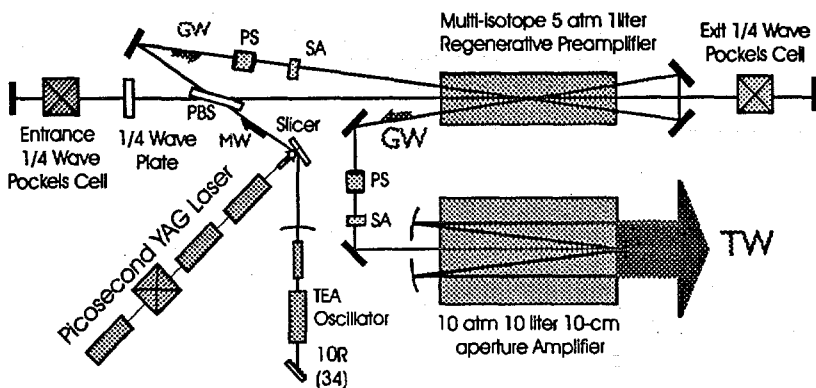


FIGURE 3. Optical diagram of the ATF TWps- $\text{CO}_2$  laser;  
PS - plasma filter; SA - saturable absorber; PBS - polarizing beam splitter

The 1 MW, 100 ns pulse produced by a 1-atm  $\text{CO}_2$  laser oscillator is sliced at a semiconductor switch controlled by the picosecond Nd:YAG laser. The high power will be attained via regenerative amplification and four additional passes through the preamplifier followed by three passes in the 10-atm, 10-l final amplifier with the beam expansion to its full 10-cm aperture.

This diagram looks relatively simple to anyone who

is familiar with the  $\text{T}^3$  laser designs. There is a principal physical reason for this. Because of the strong optical nonlinearity of solids, the high laser energy can not be extracted directly in a picosecond pulse. The relatively sophisticated chirping technique should be implemented. This technique requires diffraction stretchers and compressors of the laser pulse. As a result, the optical damage of diffraction gratings becomes the primary limiting factor for this technology. The gas medium of the  $\text{CO}_2$  laser is free from this limitation; thus a picosecond laser pulse may be amplified directly.

Table 1 serves to compare the main physical parameters of solid-state and  $\text{CO}_2$  lasers. Because of the broader gain bandwidth in the solid state lasers, as short as 10 fs laser pulses can be produced whereas the  $\text{CO}_2$  laser pulses are limited to  $\sim 1$  ps the shortest. However, such pulse duration is sufficient for the critical applications that we consider below.

A gain cross-section per ion or molecule is comparable for both types of lasers. About ten times higher concentration of active ions in solid matter than the  $\text{CO}_2$  molecules in a gas results in a ten times higher gain for solid state lasers. In addition, ten times higher photon energy makes the specific stored energy in solid state lasers about hundred times higher. However, the large volume of a gas laser makes the total stored energy per  $\text{CO}_2$  laser stage similar or higher than for a big-aperture slab solid state amplifier.

Because of the ease of the heat removal by fast gas exchange in the  $\text{CO}_2$  laser, it is potentially capable of high repetition rates that are difficult to attain with massive glass or crystal active elements. This will be important for future advanced particle accelerators. For example,  $\text{CO}_2$  laser pulses of  $\sim 1$  ps duration, 1 J energy, and 10 kHz repetition rate may be required to drive the  $e^{\pm} \Rightarrow \gamma$  converter of the future 5 TeV c.m. collider. Relatively compact  $\sim 10$  l discharge, high-pressure, fast-flow  $\text{CO}_2$  lasers operating at a  $\sim 100$  Hz repetition rate may approach this requirement when the energy stored in the laser medium is extracted by a train of pulses of 1 ps length each following at a  $\sim 1$  ns period. Such a regime looks not just feasible but also quite efficient, permitting extraction of a good portion of the stored  $\text{CO}_2$  laser energy. Overall electric efficiency of the laser may approach 20% as has been demonstrated for the long-pulse  $\text{CO}_2$

lasers pumped with the e-beam sustained discharge. An additional straightforward way to increase the efficient pulse repetition rate is recycling of the laser power in storage cavities [4].

## 2. TWps-CO<sub>2</sub> LASER APPLICATIONS IN HIGH ENERGY PHYSICS

### 2.1. Laser Wakefield Accelerators and e<sup>-</sup>e<sup>+</sup> Colliders

High-gradient laser acceleration is a fast advancing area of the high energy physics research. Among the known laser acceleration techniques, the LWFA method [5] is considered to be the most reliable approach. It is based on the ponderomotive charge separation and a relativistic wake formation when the propagating laser pulse duration is in resonance with the plasma oscillation. The amplitude of the accelerating field,  $E_a$ , due to the charge separation in a plasma wave reaches

TABLE 1.

Characteristics of Solid State and CO<sub>2</sub> Lasers

PARAMETER	Solid State	10-atm CO <sub>2</sub>
Bandwidth (THz)	5-50	1
Cross section ( $\times 10^{-20}$ cm <sup>2</sup> )	1-30	5
Gain (%/cm)	~50	3-4
Saturation energy (J/cm <sup>2</sup> )	1-20	0.5
Stored energy (J/cm <sup>3</sup> )	1	0.01
Active volume (cm <sup>3</sup> )	10-100	10,000
Maximum efficiency (%)	10	20
Average power (W)	10	10,000

$$E_a [V/cm] = \left( a^2 / \sqrt{1 + a^2} \right) \sqrt{n_e} [cm^{-3}], \quad (1)$$

where  $n_e$  is electron density in plasma, and  $a$  is the dimensionless laser vector-potential

$$a = eE_L / mc\omega = 0.3E_L [TV/m] \lambda [ \mu m ]. \quad (2)$$

From Eqs.(1) and (2) we see that a 10- $\mu$ m CO<sub>2</sub> laser is capable of producing an accelerating gradient at least 10 times higher than the 1- $\mu$ m laser of the same intensity. This is due to the stronger ponderomotive potential of plasma electrons oscillating in a lower-frequency electromagnetic field.

Using 1- $\mu$ m laser pulses of a shorter duration and at correspondingly higher plasma densities help to compensate for the low ponderomotive strength and attain high acceleration gradients. However, the maximum number of particles per bunch,  $N_e$ , at the limit when the bunch self-field

does not effect the plasma wake structure, drops proportionally to the plasma wavelength:  $N_e \propto \lambda_p \propto n_e^{-1/2}$ . This becomes especially important when we consider a prospective design of the LWFA stages for the future TeV e<sup>-</sup>e<sup>+</sup> collider [6] where the most critical characteristic, luminosity

$$\Lambda = N_e^2 f \zeta / 4\pi\sigma_{\perp}^2, \quad (3)$$

(where  $\zeta$  is a number of bunches per train,  $f$  is the linac repetition rate, and  $\sigma_{\perp}$  is the e-beam cross-section at the interaction point) is proportional to  $N_e^2$ .

Another potential advantage of using a longer period plasma wave is that it facilitates fitting of the electron bunch inside the small portion of the wake period thus ensuring the good beam quality (small energy spread and emittance). For example, at  $\tau_L=1$  ps and the resonance plasma wavelength  $\lambda_p=600$   $\mu$ m the desirable electron bunch duration is  $\tau_b \leq 200$  fs. Contemporary photocathode RF guns tend to approach these requirements. In particular  $\tau_b=370$  fs electron bunches of  $2.5 \times 10^8$  electrons,  $\Delta p/p=0.15\%$ , and  $\varepsilon_n=0.5$  mm.mrad have been demonstrated with the ATF photocathode RF gun [7].

Provided methods of plasma channel formation are available, compact (~1 m) LWFA of several GeV energy driven with the technically feasible ~50 TW lasers may become a reality. Staging of such accelerators permits the new generation of TeV-class e<sup>-</sup>e<sup>+</sup> colliders less than 1 km long.

### 2.2. Table-Top Laser Synchrotron Source

Synchrotrons equipped with wiggler magnets are the sources of x-ray fluxes at a level of 10<sup>18</sup> photon/sec. According to another approach to a relatively compact high-brightness x-ray generator called laser synchrotron source (LSS), the laser beam acts on relativistic electrons as an electromagnetic wiggler with a period 10<sup>4</sup>-10<sup>5</sup> times shorter than the magnetic undulator. Thus, LSS produces proportionally heavier photons than a conventional synchrotron source operating at the same e-beam energy. Similarly, LSS permits significant downsizing of the electron accelerator.

A combination of a high-gradient LWFA with LSS may open a route to table-top wakefield LSS operating in x-ray and gamma regions. Proof-of-principle table-top LSS may be realized at the ATF using the 5-TW CO<sub>2</sub> laser and a 5 MeV photocathode electron gun. The CO<sub>2</sub> laser beam is split into two beams that serve to drive both LWFA and LSS as is shown in Fig.4. PIC simulations predict 250 MeV acceleration when a 4 TW CO<sub>2</sub> laser beam is focused into the waveguide with parameters shown in Table 2 [8]. At the exit of the waveguide, electrons accelerated in the plasma wake field interact with the second CO<sub>2</sub> laser beam, generating an x-ray flux orders of magnitude above numbers obtained with conventional synchrotron light sources.

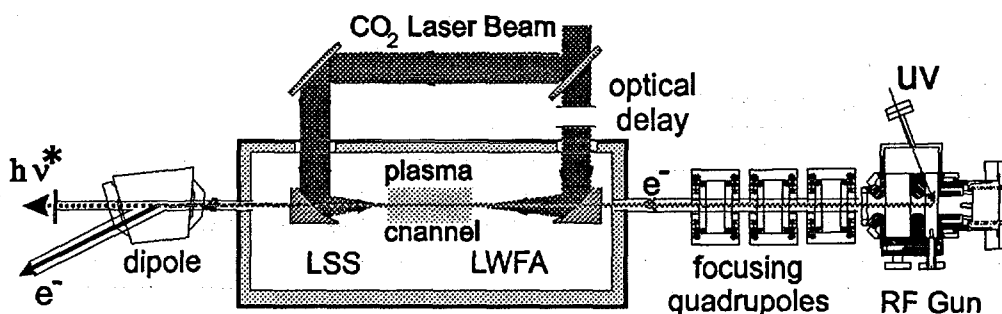


FIGURE 4. Table-top laser wakefield x-ray source

TABLE 2. Design Parameters for Table-Top LSS

LWFA	
Initial Electron Energy [MeV]	5
Bunch Charge [nC]	0.1
Bunch Duration FWHM [fs]	300
Laser Peak Power [TW]	4
Laser Pulse Duration [ps]	3
Plasma Density [cm <sup>-3</sup> ]	3.5×10 <sup>16</sup>
Channel Radius [μm]	60
Channel Length [cm]	4
Energy Gain [MeV]	250

LSS	
Laser Peak Power [TW]	1
Laser Pulse Duration [ps]	3
Laser Focus Radius [μm]	30
X-ray Photon Energy [keV]	470
Angular Spread [mrad]	0.1
Spectral Bandwidth [%]	0.2
X-ray Pulse Duration [fs]	300
X-ray Photons per Pulse	3×10 <sup>9</sup>
X-ray Peak Flux [photons/s]	10 <sup>22</sup>

### 2.3. Gamma and Positron sources for Linear Colliders

By Compton backscattering of the laser photons from the TeV electron beam, a high brightness TeV photon beam can be created. It opens an opportunity to study a variety of interaction processes by colliding  $e^-$ ,  $e^+$  and  $\gamma$  beams in any combination and at independently controlled polarization.

The expression for the maximum gamma photon energy for linear Compton backscattering is

$$\hbar\omega_\gamma = (x/x+1)E_e, \quad (4)$$

where  $E_e$  is the electron energy, and  $x = 4E_e\hbar\omega/m^2c^4$ . At  $x \gg 1$ , the Compton photon energy approaches the electron energy,  $\hbar\omega_\gamma \approx E_e$ . For CO<sub>2</sub> laser,  $x=1$  at  $E_e=0.5$  TeV. Thus, the long wavelength of the CO<sub>2</sub> laser used for the  $e^\pm \Rightarrow \gamma$  converter at  $E_e=2.5$  TeV does not degrade  $\omega_\gamma$  to compare with shorter wavelength lasers. Capable of high average power and delivering ten times more photons than solid state lasers of the similar energy, CO<sub>2</sub> lasers permit ultra-high intensity  $\gamma$ -sources.

The strong requirement to the laser wavelength is set by rescattering of gamma photons on the laser beam into pairs through the reaction  $\gamma + \lambda \Rightarrow e^- + e^+$ . This occurs when  $\omega\omega_\gamma > m^2c^4/\hbar^2$ . Based on this condition, the optimum laser wavelength is derived:  $\lambda[\mu\text{m}] = 4.2E_e[\text{TeV}]$ . Thus, for the 2.5 TeV collider the laser with  $\lambda=10.5 \mu\text{m}$  is the optimum choice.

Lasers may be used also in polarized positron sources for  $e^-e^+$  collider. Here, the backward Compton scattering serves as an intermediate process followed by pair production on a target. Polarization of the produced particles is controlled by the input laser beam. Picosecond CO<sub>2</sub> lasers have been selected as the optimum choice for the Japan Linear Collider [9]. Both applications described in this paragraph are illustrated by Fig.5.

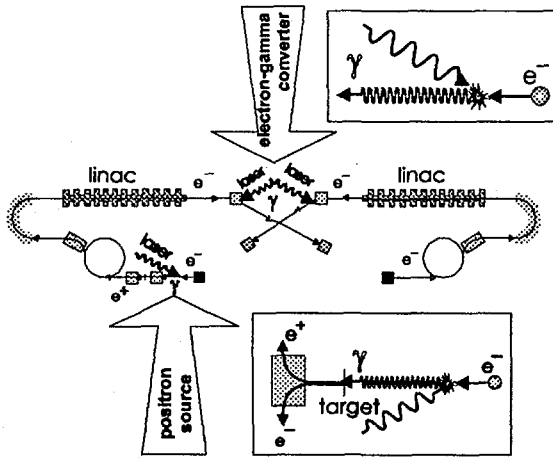


FIGURE 5.

Electron-gamma converter and polarized positron source for future electron-positron collider

### REFERENCES

1. C. Roland and P.B. Corkum, *J. Opt. Soc. Am.*, **B3**, 1625 (1986)
2. I.V. Pogorelsky, et al., "The First Terawatt Picosecond CO<sub>2</sub> Laser for Advanced Accelerator Study at the Brookhaven ATF", *Proceedings of 7<sup>th</sup> Advanced Accelerator Concepts Workshop*, Lake Tahoe, CA, October 12-18, 1996, to be published
3. P.B. Corkum, *IEEE J. Quant. Electron.*, **QE-21**, 216 (1985)
4. C.E. Clayton, N.A. Kurnit, D.D. Meyerhofer, *Nucl. Instr. & Methods Phys. Res.*, **A355**, 121 (1995)
5. T. Tajima & J.M. Dawson, *Phys. Rev. Lett.* **43**, 267 (1979)
6. I.V. Pogorelsky, "Prospects for Laser Wakefield Accelerators and Colliders Using CO<sub>2</sub> Laser Drivers", *Nucl. Instr. & Methods Phys. Res.*, **A**, to be published
7. X.J. Wang, X. Qui, and I. Ben-Zvi, *Phys. Rev. E*, **54**, R3121 (1996)
8. S.V. Bulanov, et al., *IEEE Trans. on Plasma Sci.*, **24**, 393 (1996)
9. T. Okugi, et al., *Jpn. J. Appl. Phys.* **35**, 3677 (1996)

## 18. Next Generation Chirped Pulse Amplification

John NEES, Subrat BISWAL, Gerard MOUROU

Univ. Michigan, Center for Ultrafast Optical Science, 2200 Bonisteel, 1006 IST, Ann Arbor, MI 48108, USA

Akihiko NISHIMURA, Hiroshi TAKUMA

Japan Atomic Energy Research Institute, 2-4 Shirane, Tokai-mura, Naka-gun, Ibaraki-ken 319-11, Japan

### ABSTRACT

The limiting factors of Chirped Pulse Amplification (CPA) are discussed and experimental results of CPA in Yb:glass regenerative amplifier are given. Scaling of Yb:glass to the petawatt level is briefly discussed.

### KEYWORDS

Ytterbium Glass, Chirped Pulse Amplification, Petawatt Lasers, High Energy Storage Density Laser Materials

### 1. Next Generation Chirped Pulse Amplification

Recent advances in high power lasers using Chirped Pulse Amplification (CPA) have generated a growing interest in studies of High-Field Science. This field supports research in high-harmonic generation, solid-density plasma physics, relativistic plasma dynamics, laser wakefield acceleration, and coherent control of chemical dynamics, as well as other subjects. One factor driving these topics is the fact that the technology for building table-top terawatt lasers is available to institutes and universities for an affordable price. Future high-power laser

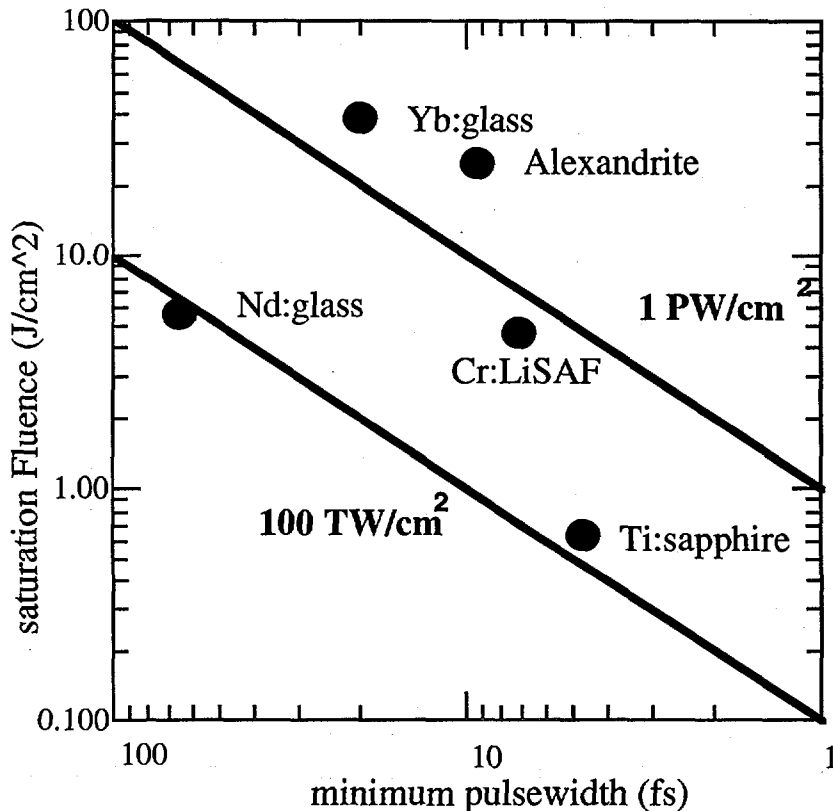


Figure 1. Theoretical peak power for various materials for operation at saturation fluence and assuming a minimum pulse duration inversely related to the emission bandwidth.

systems made for high-field studies will need to be based on new solid-state gain media with excellent energy storage capability and laser diode pumpability. In this paper we will attempt to establish a direction for the development of these sources in such a way that they will continue to be available to a broad range of researchers. The potential to scale these compact designs to achieve unprecedented intensities will also be discussed.

Using the technique of chirped pulse amplification (CPA) with solid-state laser materials high peak power laser systems have been reduced in size from the scale of a building to fit on an optical table. This advancement is a result of the reduction in pulse duration from the nanosecond to the subpicosecond range and a corresponding reduction of energy from the kilo joule level to well below a joule. To choose the best material for high field generation there are a number of parameters which must be considered; the saturation fluence of the gain material, which is a measure of the energy which can be extracted from the material; the gain-bandwidth, which provides a measure of the inverse of the pulse-width which may be obtained; and the fluorescence lifetime, which provides a measure of the maximum pump-pulse duration. In order to build a scalable system it is also necessary to choose a material with an absorption band compatible with high power laser diodes.

## 2. Theoretical Limits

The theoretical limit of peak power for a given aperture of gain material is given by the saturation fluence,  $h\nu/\sigma$ , divided by the minimum pulse duration,  $\tau_p$ . As shown in figure 1 peak powers in excess of  $1 \text{ PW/cm}^2$  could theoretically be extracted from Yb:glass.

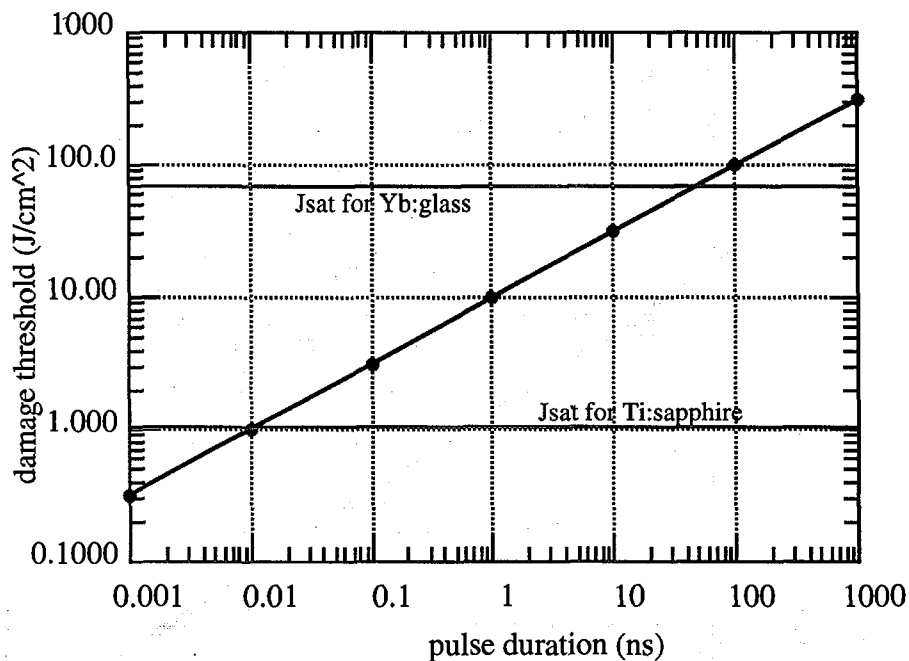


Figure 2. General scaling law for damage in laser materials. Saturation fluences for Ti:sapphire and Yb:QX are shown as guides.

## 3. Damage Threshold

This limit excludes the damage threshold of the laser material which scales as the inverse square-root of pulse duration in the picosecond and nanosecond regimes. It was in order to avoid nonlinear effects and damage at high intensities that CPA was developed. The level of optical fluence which induces damage may be approximated empirically by the relation  $J_{th} = 10 \text{ J/cm}^2 \times$

$(\tau_{\text{stretched}})^{1/2}$ , where  $J_{\text{th}}$  is the damage fluence threshold in  $\text{J}/\text{cm}^2$  and  $\tau_{\text{stretched}}$  is the pulse duration in ns. Stretching the ultrashort optical pulse to avoid the low damage threshold of femtosecond pulses, it is possible to efficiently extract energy at or near the saturation fluence of many solid-state materials. It is clear from figure 1 that Yb:glass is superior to other CPA candidates in its energy storage density and that its bandwidth is sufficient for operation the sub-100-femtosecond regime. In addition, the damage threshold scales inversely with the radius of the beam. This further increases the desirability of working with a small aperture system having high energy storage density.

#### 4. Yb:glass Characteristics

Another characteristic which makes Yb:glass especially well suited for advancement of lasers in High-Field Science is its long excited state lifetime. It is capable of integrating pump light over an interval of 2 ms. This is 600 times longer than Ti:sapphire. As a result the pump power requirements for Yb:glass are significantly lower than those of Ti:Sapphire. To date we have operated a diode pumped modelocked oscillator producing pulses as short as 60 fs and a diode-pumped Q-switched amplifier laser with 10  $\mu\text{J}$  output.

#### Spectral Characteristics of Yb:phosphate glass

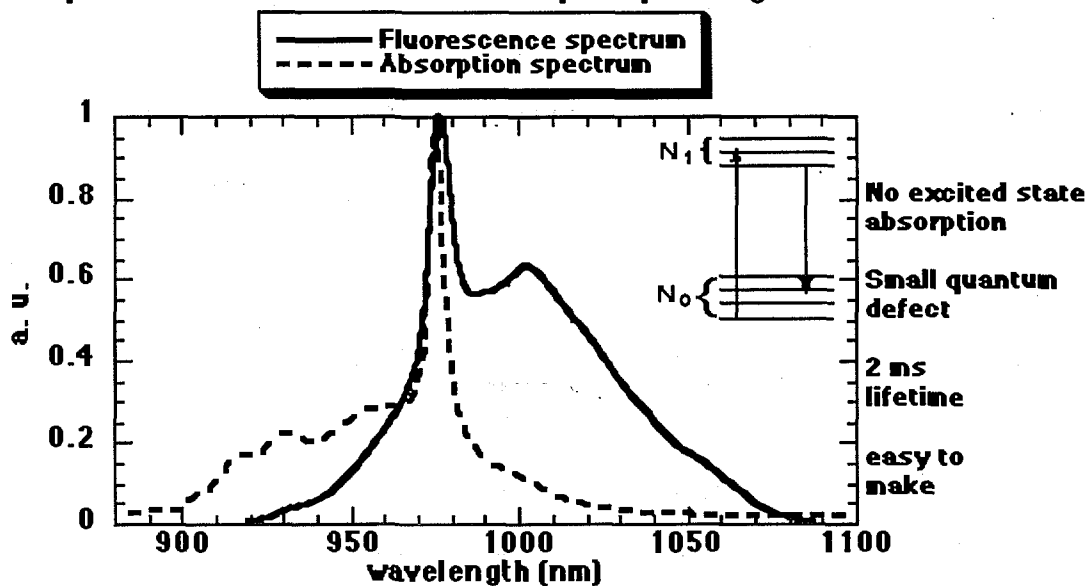


Figure 3 Absorption and emission curves for Kigre Yb:QX glass doped at 15% wt.

The features of Yb:glass (Kigre Yb:QX glass 15% by wt.  $\text{Yb}_2\text{O}_3$ ) including the emission and absorption spectra are shown in figure 3. Note the broad absorption and emission bands. The breadth of the absorption band from 920 to 965 nm is advantageous for diode pumping because it is much broader than the wavelength variation found in current laser diode manufacturing. Also the emission band in Yb:QX is near the absorption band so there is a low quantum defect of only 7 to 9%. The laser transition shown in the inset is quite simple allowing no excited state absorption and a long (2ms) excited-state lifetime.

The peak emission cross section of the Yb ion in this glass is  $0.6 \times 10^{-20} \text{ cm}^2$ , while other glasses may be found which have cross sections at 1.03 of  $1.3 \times 10^{-20} \text{ cm}^2$ . Saturation fluence at 1.03  $\mu\text{m}$  in Yb:QX is  $70 \text{ J}/\text{cm}^2$ . This poses a problem for the use of Yb at saturation fluence. To do so would require stretching the signal pulse to 50 ns. Rather than pressing to such a high energy density it is more useful to relax the extracted energy to an acceptable level near the

damage threshold for a pulse duration which may reasonably be achieved. Presently, 2 ns pulse may be obtained by using 22-cm gratings for stretching and compression. This sets the damage threshold near  $20 \text{ J/cm}^2$ . If the system is operated with a 50% safety margin a fluence of  $10 \text{ J/cm}^2$  is incident on the gain material. Though operation below the saturation fluence lowers the theoretical peak power per  $\text{cm}^2$  of aperture, the energy storage density and diode pumpability of Yb:glass still makes it the best material for new CPA systems.

### 5. Working Below Saturation Fluence

Efficient extraction of energy at a fluence much below the saturation fluence can also reduce the requirements for pump intensity. To efficiently extract energy stored in the laser gain material with out approaching the saturation fluence requires that the energy per  $\text{cm}^2$  stored be below the saturation energy. This in turn limits the laser to low gain operation with low losses. The low gain condition may be achieved by pumping with lower intensity. Hence, the pump intensity requirement is lowered.

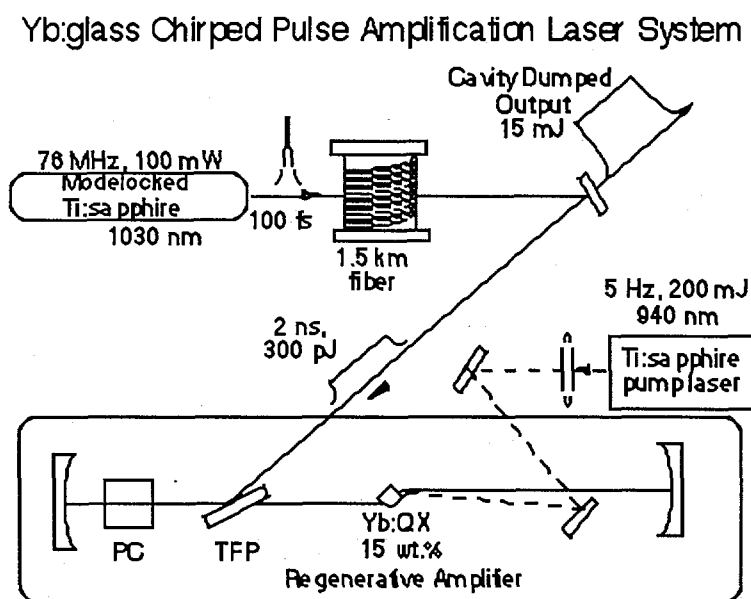


Figure 4 Experimental layout demonstrating CPA in Yb:QX glass. The blocks designated PC and TFP refer to the Pockels cell and thin film polarizer respectively.

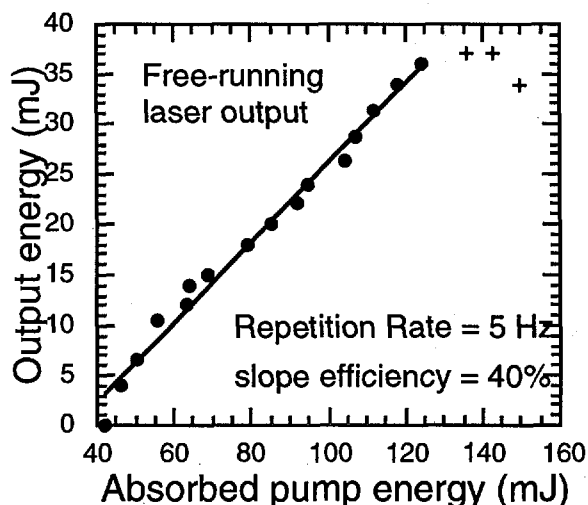


Figure 5 Output of the free-running Yb:QX amplifier without polarizer or Pockels cell in cavity .

## 6. Experimental Results

To test the capability of Yb: glass for CPA a flashlamp-pumped Ti:Sapphire laser was used to simulate a laser diode pump source. The experimental configuration is shown in figure 4. Removing the PC and the TFP and operating the Yb:QX laser as a free-running laser a slope efficiency of 40% was obtained with an efficiency of greater than 28% with respect to (w.r.t.) absorbed pump energy. When a TFP (8% per pass loss) and PC (1% per pass loss) were added the losses were increased to approximately 20% per round trip. In this configuration an efficiency of nearly 10% w.r.t. absorbed pump energy was obtained. Using the regenerative amplifier to amplify seed pulses from a modelocked source 8 nm bandwidth at 15 mJ was obtained without spectral filtering while 13 nm at 8 mJ was obtained with the use a thin intra-cavity etalon. These experiments operated with an absorbed pump fluence of about 50J/cm<sup>2</sup> and a signal fluence of about 7 J/cm<sup>2</sup>. By reducing the intra-cavity losses to 5% the efficiency should be increased to 20%.

## 7. Scalability

These results can be scaled by increasing the pump energy and the size of the gain aperture. As the gain aperture is scaled up the aperture of the remaining elements of the amplifier should also be increased. Extending amplification to the joule level it is expected that a 10 TW laser with 100 fs pulses can be obtained using a flashlamp-pumped Ti:sapphire laser. Scaling to the petawatt and beyond will require more energetic pump sources and a greater concentration on the control of dispersion to obtain a system with >40 J in 40 fs, operating at 20% efficiency w.r.t. absorbed pump energy (200 J). A petawatt laser based on this technology will require a gain-aperture only 3-cm in diameter and temporal pulse stretching of  $5 \times 10^4$  from 40 fs to 2 ns. A pump source of >200 J with a sub-ms pulse duration is also needed. While stacked laser diode pump configurations have demonstrated 35kW/cm<sup>2</sup> intensities at wavelengths compatible with the Yb:QX-based CPA laser a further discussion of these technologies is outside the scope of this paper.

## 8. Conclusion

We have reviewed the factors critical to producing diode-pumped table-top CPA systems with scalability beyond the petawatt level. Experiments using a flashlamp-pumped Ti:sapphire laser to simulate laser-diode pumping of Yb:QX glass have produced 15 mJ and 8 nm bandwidth and 8 mJ with 13 nm bandwidth. We conclude that Yb:glass is an excellent candidate for the new generation of diode-pumped table-top lasers and that it has the potential to scale into the petawatt range.

[1] D. Strickland and G. Mourou, Opt. Commun. 56, 219, 1985.

[2] S. Biswal, F. Duron, J. Nees, G. Mourou, A. Nishimura, "Ytterbium:glass CPA regenerative amplifier pumped by a free-running laser", CThC1 CLEO 1997, Baltimore, May 1997.

[3] S. Biswal, J. Nees, G. Mourou, A. Nishimura, "Efficient gain-switched operation of a highly-doped Yb:phosphate glass laser," OSA TOPS Vol. 10 Advanced Solid State Lasers, 1997, C. Pollack and W. Bosenberg, eds., 119-121.

## 19. Flashlamp Pumped Ti:sapphire Laser for Ytterbium Glass Chirped Pulse Amplification

Akihiko NISHIMURA, Akira OHZU, Akira SUGIYAMA, Yoichiro MARUYAMA  
Takashi ARISAWA, Hiroshi TAKUMA

Japan Atomic Energy Research Institute, 2-4 Shirane, Tokai-mura, Naka-gun, Ibaraki-ken 319-11, Japan

Edward ERICKSON

EEA, 634 W.Vista Hermosa Dr., Green Valley, AZ 85614, USA

Susumu OWADA, Sousuke SATOU

RASEL, 478 Nibukata-cho, Hachioji-shi, Tokyo 193, Japan

John NEES, Subrat BISWAL, Gerard MOUROU

Univ. Michigan, Center for Ultrafast Optical Science, 2200 Bonisteel, 1006 IST, Ann Arbor, MI 48108, USA

### ABSTRACT

A flashlamp pumped Ti:sapphire laser is designed for ytterbium glass chirped pulse amplification. A high quality Ti:sapphire rod and a high energy long pulse discharging power supply are key components. The primary step is to produce the output power of 10 J per pulse at 920 nm.

**KEYWORDS** Ti:sapphire, Flashlamp Pumping, Free Running, Ytterbium Glass, Chirped Pulse Amplification

Chirped Pulse Amplification (CPA) [1] is now widely used as a technique for extracting energy from solid-state laser material to achieve ultrahigh peak power. The CPA has been applied to demonstrate the range of Peta-watt of ps duration by Nd:glass amplifiers [2]. In the ultrashort pulse duration region of less than 20 fs, the peak power from a Ti:sapphire CPA laser system is now coming to 100 TW [3]. Such a high peak power laser can open the new research fields, such as laser wakefield generation, solid-density plasma studies, hard X-ray laser and  $\gamma$ -ray generation, which are called High Field Science.

Solid-state material having high saturation fluence, wide bandwidth and long upper state radiative lifetime is attractive as high peak power CPA. Ytterbium doped glass is a challenging material, having over 30 J/cm<sup>2</sup> high saturation fluence, 50 nm bandwidth and 2 ms upper state radiative lifetime. The long radiative lifetime makes it possible to pump Yb:glass directly by laser diodes. The laser diode pumped Yb:glass CPA laser should be very compact and efficient. For now, however, it is reasonable to use a flashlamp pumped free-running laser as a high energy pumping source due to the costly laser diodes. The authors have successfully demonstrated regenerative CPA of Yb:glass using the flashlamp pumped free running Ti:sapphire laser[4]. This laser made by ELIGHT having the output energy of 300 mJ/pulse at the wavelength of 920 nm was used. The output pulse energy of 15 mJ from the regenerative amplifier was achieved. For Yb:glass multipass amplifiers, higher output energy pulse of the free running pumping laser is required.

Flashlamp pumped Ti:sapphire lasers have attracted much attention. By Q-switching operation and frequency conversion, those can cover the wavelength ranging from IR to UV. Many technical innovations have been achieved, such as high quality Ti:sapphire rods, high speed switching power supplies, high efficiency pumping chambers, long lifetime flashlamps, and UV - visible fluorescence converters. Based on these innovations, the output energy 5.7 J /pulse at the wavelength of 800 nm has been achieved by free running operation [5]. The total efficiency up to 2 % has been obtained.

Our focus is directed towards the development of flashlamp pumped Ti:sapphire lasers for pumping the Yb:glass. High energy and long pulse operation are suitable for this purpose. Brown and Fisher have reported the 6.5 J output energy of 7  $\mu$ s at 800 nm, pumping a Ti:sapphire rod with cylindrically arranged six flashlamps [6]. Although the laser head and the power supply were not optimized for free running operation, the total efficiency of 0.5 % was obtained. The following laser system based on the previous work is capable to produce higher output energy and higher total efficiency for Yb:glass pumping[5].

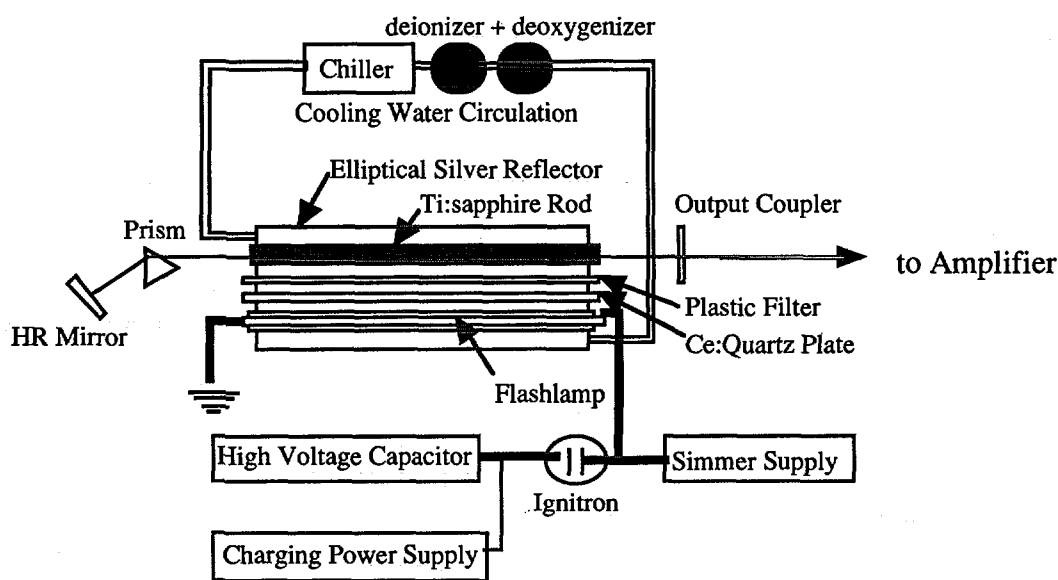


Figure 1 Schematic View of Flashlamp Pumped Ti:sapphire Laser System

### (1) Laser Head

A laser head has a single-elliptic pumping chamber made of a silver block. Ultraviolet cutting filters were placed between a flashlamp and a Ti:sapphire rod in the chamber. The flashlamp made by ILC Technology was 450 Torr Xenon filled type, having a double wall made of cerium doped quartz. The double wall of this lamp and the UV cutting filters can protect the Ti:sapphire rod from UV radiation. The pumping chamber was filled with deionized flowing water which can maintain the high reflectivity. Based on the Czochralski crystal growth technique, the Ti:sapphire rod of 190 mm length and 8 mm diameter doped at 0.1% has been fabricated by Union Carbide. The single pass loss at 920 nm less than 8% is

requested. Both faces of the rod have AR coated. A prism is placed in a laser cavity for wavelength selection for lasing at 920 nm for Yb:glass pumping.

## (2) Power Supply

A power supply consists of a master controller, a charging unit, simmer circuits, pulse forming networks and main discharging units. The flashlamp is conditioned prior to a main discharge by a simmer discharge. The plasma generated by the simmer discharge fills the inner bore of the flashlamp can stabilize the main discharge. An ignitron (mercury vapor switch) was used in the main discharging unit. The charging voltage of 5 - 10 kV can be varied continuously. In order to change the discharging duration, the capacitance of the main discharging unit is designed to be switchable. The energy of 810 J stored in a capacitor was successfully discharged through the ILC double wall flashlamp at 1 Hz repetition rate. The 140  $\mu$ s discharging duration at 10 % current on was obtained using a 65  $\mu$ F capacitor. The power supply has two sets of the main discharging units. Each unit drives an oscillator laser head and an amplifier laser head respectively.

The wide tunability of Ti:sapphire lasers can cover a broad absorption spectrum of Yb:glass ranging from 900 nm to 975 nm. The laser system which can produce the output energy of over 10 J /pulse at 920 nm is being assembled for the purpose of high energy Yb:glass CPA. To get much higher energy, it is expected to extend the explosion limit of flashlamps and to improve the direct bonding technique of Ti:sapphire crystals to fabricate a long uniform rod.

## Acknowledgment

The authors thank Dr. Milan Kokta of Union Carbide for helpful discussions about high quality Ti:sapphire rods.

## Reference

- [1] D.Strickland and G.Mourou, Opt. Commun., "Compression of amplified chirped optical pulses", 56, 219, 1985.
- [2] M.Perry, B.Stuart, G.Tietbohl, J.Miller, J.Britten, R.Boyd, M.Everett, S.Herman, H.Nguyen, H.Powell, B.Shore, "The petawatt laser and its application to inertial confinement fusion", CWI4 CLEO 1996, Anaheim, June 1996.
- [3] K.Yamakawa, M. Aoyama, T.Itoh, T.Matoba, H.Takuma, "Development of a repetitive ultrahigh peak power, ultrashort pulse Ti:sapphire laser system", TuE5 CLEO Pacific Rim, Makuhari, July 1997.
- [4] S.Biswal, F.Duron, J.Nees, G.Mourou, A.Nishimura, "Ytterbium:glass CPA regenerative amplifier pumped by a free-running laser", CThC1 CLEO 1997, Baltimore, May 1997.
- [5] E. Erickson, "State of the Art and Future Potential of the Flashlamp Pumped Ti:sapphire laser", TiS conference, Big Sky MT, August 1992.
- [6] A.Brown and C.Fisher, "A 6.5-J flashlamp-pumped Ti:Al<sub>2</sub>O<sub>3</sub> laser", IEEE J. Quantum Electron. 29, 2513, 1993.

## 20. Efficient Chirped-Pulse Amplification of Sub-20 fs Laser Pulses

Shinichi MATSUOKA and Koichi YAMAKAWA

*Advanced Photon Research Center, Kansai Research Establishment  
Japan Atomic Energy Research Institute  
2-4 Shirakata-Shirane, Tokai, Naka, Ibaraki, 319-11, Japan*

### ABSTRACT

We have developed a model for ultrabroadband and ultrashort pulse amplification including the effects of a pulse shaper for regenerative pulse shaping, gain narrowing and gain saturation in the amplifiers. Thin solid etalons are used to control both gain narrowing and gain saturation during amplification. This model has been used to design an optimized Ti:sapphire amplifier system for producing efficiently pulses of < 20-fs duration with approaching peak and average powers of 100 TW and 20 W.

**Keywords:** Chirped Pulse Amplification, Gain Narrowing, Gain Saturation, Regenerative Pulse Shaping

### 1. INTRODUCTION

Recently, there has been much interest in the development of high-peak-power, ultrashort pulse laser systems for investigations of high-field interaction and atomic physics [1]. Utilization of solid-state materials in conjunction with the technique of chirped pulse amplification (CPA) can produce high energy, ultrashort pulses [2-5]. The large gain bandwidth materials such as Ti:sapphire ( $\text{Ti:Al}_2\text{O}_3$ ) and Cr:LiSAF, which permits the capability of femtosecond pulse generation and amplification. In fact, Ti:sapphire has a largest gain bandwidth ( $\sim 230$  nm FWHM) which corresponds to the transform limited pulse duration of  $\sim 3$  fs [6]. However, in most terawatt Ti:sapphire CPA systems, a net gain of  $> 10^8$  is necessary to reach the desirable amplified pulse energy. Because of the frequency dependent gain profile, this amplification leads to gain narrowing of the pulse spectrum [7,8]. A reduction in gain bandwidth not only reduce the stretched pulse duration but also results in a longer pulse after compression.

The most recent evolution in ultrashort pulse CPA systems has been the utilization of regenerative pulse shaping to eliminate gain narrowing [9,10]. With this technique the pulse duration of the amplified, compressed pulses has been reduced by a factor of 2, reaching now 16 fs at a multiterawatt level [11]. This is conveniently accomplished in regenerative amplification schemes by placing a frequency dependent attenuator inside the amplifier cavity.

It is also desired to optimize the amplifier to achieve the highest possible output energy for a given pump energy. In principle, Ti:sapphire lasers can achieve extraction efficiencies that approach  $\sim 57\%$ ; most Ti:sapphire CPA systems, however, achieve only 10 - 30% efficiency. To achieve theoretical maximum quantum efficiency, one must operate the amplifier above the saturation fluence

of the laser materials [12]. While operating at these fluences, one also needs to maintain a low intensity in the amplifier, since the damage threshold of amplifier materials is  $\sim 5 \text{ GW/cm}^2$ . Dividing fluence by intensity, the pulse duration in the amplifier must be at least 300 ps for Ti:sapphire. Most Ti:sapphire CPA lasers use stretched pulse durations that are well below 300 ps and therefore are unable to operate at the high fluences necessary for efficient amplification.

Here we present our detailed analysis that govern the chirped-pulse amplification including the effects of a pulse shaper for regenerative pulse shaping, gain narrowing and gain saturation in the Ti:sapphire amplifiers in order to obtain the shortest compressed pulse, while simultaneously increasing the amplifier efficiencies.

## 2. MODEL FOR ULTRASHORT PULSE AMPLIFICATION

In our model we assume that 1) a gain medium is a homogeneously broadened two-level system, 2) an excited-state lifetime is much longer than the laser pulse duration, and 3) pump beam distributions and population inversion densities are uniform.

For a frequency chirped pulse, the emission cross-section,  $\sigma[\omega(t)]$ , is considered to be a function of instantaneous frequency  $\omega(t)$ . The basic equations for the pulse intensity,  $I(z,t)$ , and the population inversion,  $N(z,t)$ , can be written in the forms [13]

$$\frac{\partial I(z,t)}{\partial z} = \sigma[\omega(t)] \cdot N(z,t) \cdot I(z,t) \quad (1)$$

and

$$\frac{\partial N(z,t)}{\partial t} = -\frac{2^*}{\hbar \cdot \omega(t)} \cdot \sigma[\omega(t)] \cdot N(z,t) \cdot I(z,t), \quad (2)$$

where  $\hbar$  is Planck's constant, and  $2^*$  is a dimensionless population saturation factor with values between 1 (lower level empties out rapidly) and 2 (lower level bottlenecked). The total inverted population per amplifier area is defined as

$$N_{\text{tot}}(t) \equiv \int_0^L N(z,y) dz, \quad (3)$$

where  $L$  is the length of the amplifier. Equation (1) can be rearranged and integrated over the length of the amplifier and then be expressed in the form

$$I_{\text{out}}(t) = I_{\text{in}}(t) \cdot \exp\{\sigma[\omega(t)] \cdot N_{\text{tot}}(t)\}, \quad (4)$$

where  $I_{\text{in}}(t)$  and  $I_{\text{out}}(t)$  are the input and output intensities, respectively. Therefore the time-varying gain,  $G(t)$ , including gain narrowing and gain saturation at any instant within the pulse is given by

$$G(t) = \frac{I_{\text{out}}(t)}{I_{\text{in}}(t)} = \exp\{\sigma[\omega(t)] \cdot N_{\text{tot}}(t)\}. \quad (5)$$

Here gain narrowing is a function of the emission cross-section and gain saturation is a function of the population inversion. Equation (2) can also be integrated over the amplifier length and then rewritten,

using Equation (1), in the form

$$\begin{aligned} \frac{\partial N_{\text{tot}}(t)}{\partial t} &= -\frac{2^*}{\hbar\omega} [I_{\text{out}}(t) - I_{\text{in}}(t)] \\ &= -\frac{2^*}{\hbar \cdot \omega} \left\{ \exp \left\{ \sigma[\omega(t)] \cdot N_{\text{tot}}(t) \right\} - 1 \right\} I_{\text{in}}(t). \end{aligned} \quad (6)$$

Equation (6) can be solved numerically. Using the solved  $N_{\text{tot}}(t)$ , the instantaneous gain and the output intensity can also be obtained from Equations (5) and (6). The initial value of the population inversion is given by

$$N_{\text{tot}}(0) = \frac{\eta \cdot F_{\text{abs}}}{\hbar \cdot \omega_p}, \quad (7)$$

where  $\eta$  is the coupling efficiency,  $F_{\text{abs}}$  is the pump fluence absorbed by the amplifier crystal, and  $\omega_p$  is the pump frequency.

In the cases of the regenerative amplifier and the multi-pass amplifier, the input intensity,  $I_{\text{in}}^{(p)}(t)$ , and the output intensity,  $I_{\text{out}}^{(p)}(t)$ , per pass  $p$  in the amplifiers are related by

$$I_{\text{out}}^{(p)}(t) = I_{\text{in}}^{(p)}(t) \cdot G^{(p)}(t) \cdot T[\omega(t)] \cdot (1 - \text{Loss}), \quad (8)$$

where  $\text{Loss}$  is the loss coefficient per pass, and  $T[\omega(t)]$  is the frequency-dependent single-pass transmission function of the spectral filter for regenerative pulse shaping in the regenerative amplifier or unity for the multi-pass amplifier. We do not take into account wavelength-dependent reflectance and transmission of the optics in the amplifiers, since their bandwidths are relatively large. The input intensity and the population inversion for the next pass  $p+1$  are, respectively, given by

$$I_{\text{in}}^{(p+1)}(t) = I_{\text{out}}^{(p)}(t) \quad (9)$$

and

$$N_{\text{tot}}^{(p+1)}(0) = N_{\text{tot}}^{(p)}(\tau). \quad (10)$$

### 3. DESIGN AND OPTIMIZATION OF TI:SAPPHIRE AMPLIFIERS TOWARDS A 100 TW

We have recently developed a compact 2-stage Ti:sapphire amplifier system that has produced 16-fs 10-TW laser pulses at a 10-Hz repetition rate [11]. This system consists of a Ti:sapphire oscillator, a pulse expander, a regenerative amplifier, a 4-pass amplifier, and a pulse compressor. In the present system, the output of the four pass Ti:sapphire amplifier is then introduced into a final double-pass amplifier which is designed to produce >3 J of radiation. An optical layout of an upgraded 100 TW laser system is shown in Fig. 1. The output of the Ti:sapphire double-pass amplifier is passing through a spatial filter and then introduced into the final vacuum compressor.

We have modeled to optimize the performance of the double-pass amplifier using Equations (5) to (10) in order to obtain the largest bandwidth of the amplified pulses, while simultaneously extracting as much energy as possible. Calculated spectra after each amplifier are shown in Fig. 2.

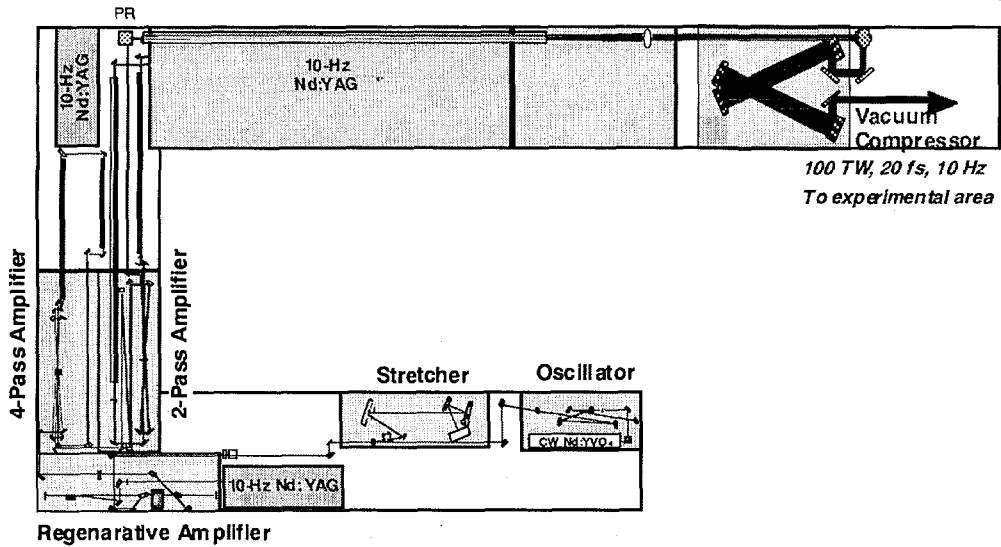


Fig. 1. JAERI 100 TW, 20fs, 10Hz Ti:sapphire laser system.

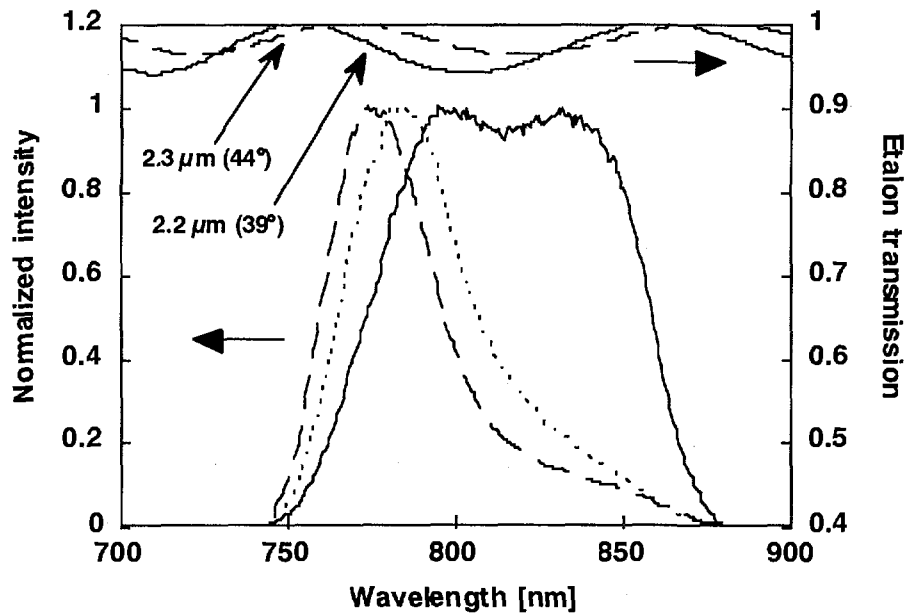


Fig. 2. Calculated spectra after a regenerative amplifier (dashed curve), a four-pass amplifier (dotted curve) and a double-pass amplifier (solid curve). Representative single-pass transmission curves for a 2.2 micron (solid curve) and a 2.3 micron (dashed curve) nitrocellulose etalon (angles of incidence 44 and 39 deg, respectively).

The spectrum after the pulse expander is used for the initial pulse to perform this calculation. Three amplifiers are pumped by 50 mJ, 700 mJ and 7 J of 532 nm radiation, respectively. Two solid etalons (thicknesses of 2.2  $\mu\text{m}$  and 2.3  $\mu\text{m}$ ) are used in transmission and is angle tuned so as to be off resonance around the peak of the gain profile of Ti:sapphire in the regenerative amplifier. In this

calculation, incidence angles of the two etalons are set to be  $39^\circ$  and  $44^\circ$ , respectively. It is clearly seen that it is not desirable to center the wavelength of the pulses at 800 nm in the regenerative and four-pass amplifier stages, since the effect of gain saturation causes the pulse spectrum to severely red-shift from the peak of the gain in the double-pass amplifier. In contrast, the broad amplified bandwidth at the high energy level can be obtained by positioning the input spectrum on the short wavelength side of the desired output. The bandwidth and output energy of the amplified pulse that we modeled are  $\sim 80$  nm and  $\sim 3.6$  J, respectively. In this case, a conversion efficiency of 532-nm pump light to 790-nm radiation is reached to over 90% of the theoretical maximum quantum efficiency. The calculated output energies and intensities after each amplifiers are also given in Table 1.

The duration of the transform limit, as calculated from the amplified spectrum after the double-pass amplifier is 17 fs as shown in Fig. 3. The energy of the compressed pulse is expected to be  $> 2$  J according to the measured diffraction efficiency of the pulse compression gratings, which implies a peak power for the laser pulse of  $> 100$  TW.

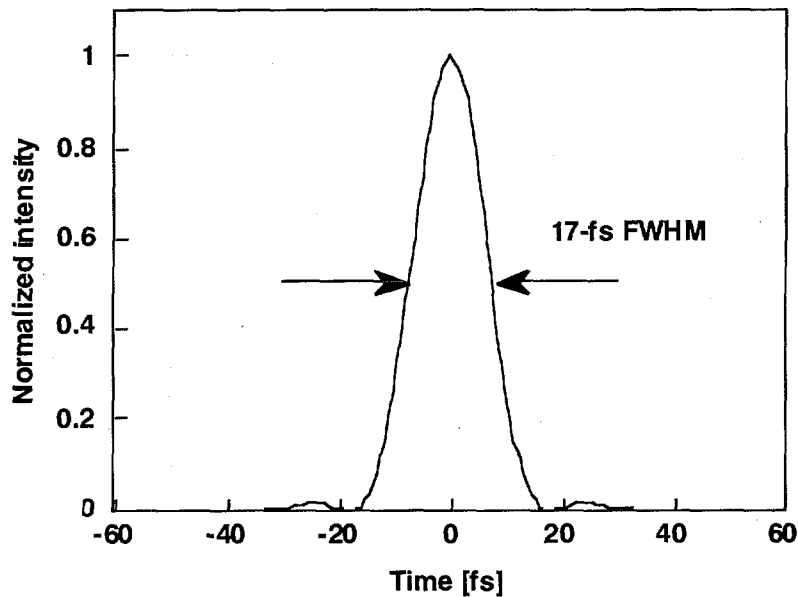


Fig. 3. Transform-limited pulse shape corresponding to the spectrum after the double-pass amplifier (FWHM 17fs).

Table 1. Calculated gains, energies and intensities after each amplifiers.

	Regenerative amplifier	4-pass amplifier	Double-pass amplifier
Gain	$\sim 10^7$	$\sim 40$	$\sim 10$
Output energy	$\sim 8$ mJ	$\sim 320$ mJ	$\sim 3.6$ J
Output intensity	$\sim 0.9$ GW/cm <sup>2</sup>	$\sim 2.9$ GW/cm <sup>2</sup>	$\sim 4.5$ GW/cm <sup>2</sup>

#### 4. CONCLUSION

In conclusion, we have developed a simple model for ultrabroadband and ultrashort pulse amplification including the effects of a pulse shaper for regenerative pulse shaping, gain narrowing and gain saturation in the Ti:sapphire amplifiers in order to obtain the shortest compressed pulse, while simultaneously increasing the amplifier efficiencies. This model has been used to design an optimized Ti:sapphire amplifier system for producing efficiently pulses of < 20-fs duration with approaching peak and average powers of 100 TW and 20 W.

#### 5. REFERENCES

1. M. D. Perry and G. Mourou, "Terawatt to Petawatt Subpicosecond Lasers," *Science*, vol. 264, pp. 917-924, 1994.
2. D. Strickland and G. Mourou, "Compression of amplified chirped optical pulses," *Opt. Commun.*, vol. 56, pp. 219-221, 1985.
3. K. Yamakawa, H. Shiraga, Y. Kato, and C. P. J. Barty, "Pre-pulse free 30-TW, 1-ps Nd:glass laser," *Opt. Lett.*, vol. 16, pp. 1593-1595, 1991.
4. B. C. Stuart, M. D. Perry, J. Miller, G. Tietbohl, S. Herman, J. A. Britten, C. Brown, D. Pennington, V. Yanovsky, and K. Wharton, "125-TW Ti:sapphire/Nd:glass laser system," *Opt. Lett.*, vol. 22, pp. 242-244, 1997.
5. J. D. Kmetec, J. J. Macklin, and J. F. Young, "0.5-TW, 125-fs Ti:sapphire laser," *Opt. Lett.*, vol. 16, pp. 1001-1003, 1991.
6. P. F. Moulton, "Spectroscopic and laser characteristics of Ti:Al<sub>2</sub>O<sub>3</sub>," *J. Opt. Soc. Amer. B*, vol 3, pp. 125-133, 1986.
7. F. G. Patterson and M. D. Perry, "Design and performance of a multiterawatt, subpicosecond neodymium:glass laser," *J. Opt. Soc. Amer. B*, vol 8, pp. 2384-2391, 1991.
8. J. Zhou, C. -P. Huang, M. M. Murnane, and H. C. Kapteyn, "Amplification of 26-fs, 2-TW pulses near the gain-narrowing limit in Ti:sapphire," *Opt. Lett.*, vol. 20, pp. 64-66, 1995
9. C. P. J. Barty, G. Korn, F. Raksi, C. Rose-Petruck, J. Squier, A. -C. Tien, K. R. Wilson, V. V. Yakovlev, and K. Yamakawa, "Regenerative pulse shaping and amplification of ultrabroadband optical pulses," *Opt. Lett.*, vol. 21, pp. 219-221, 1996.
10. K. Yamakawa, T. Guo, G. Korn, C. Le Blanc, F. Raksi, C. G. Rose-Petruck, J. A. Squier, V. V. Yakovlev, and C. P. J. Barty, "Techniques for controlling gain narrowing during ultrashort pulse amplification," *Proceedings of the SPIE - The International Society for Optical Engineering, "Generation, Amplification, and Measurement of Ultrashort Laser Pulses II"*, vol. 2701, pp. 198-208, 1996.
11. K. Yamakawa, M. Aoyama, S. Matsuoka, H. Takuma, C. P. J. Barty, and D. Fittinghoff, "Generation of 16 fs, 10 TW pulses at a 10 Hz repetition rate with efficient Ti:sapphire amplifiers," submitted to *Opt. Lett.*
12. L. M. Frantz and J. S. Nodvik, "Theory of Pulse Propagation in a Laser Amplifier," *J. Appl. Phys.*, vol, 34, pp. 2346-2349, 1963.
13. A. E. Siegman, *Lasers*. Mill Valley, CA: Univ. Sci., 1986, ch. 10.

## 21. Development of Laser Diode-Pumped High Average Power Solid-State Laser for the Pumping of Ti:sapphire CPA System

Yoichiro MARUYAMA, Kazuyoku TEI, Masaaki KATO, Yoshito NIWA,  
Sayaka HARAYAMA, Masaki OBA, Tohru MATOBA,  
Takashi ARISAWA and Hiroshi TAKUMA

*Advanced Photon Research Center  
Kansai Research Establishment  
Japan Atomic Energy Research Institute  
Shirakata, Tokai-mura, Naka-gun, Ibaraki-ken 319-11, Japan  
e-mail:maruyama@hikari.tokai.jaeri.go.jp*

### Abstract

Laser diode pumped all solid state, high repetition frequency (PRF) and high energy Nd:YAG laser using zigzag slab crystals has been developed for the pumping source of Ti:sapphire CPA system. The pumping laser installs two main amplifiers which compose ring type amplifier configuration. The maximum amplification gain of the amplifier system is 140 and the condition of saturated amplification is achieved with this high gain. The average power of fundamental laser radiation is 250 W at the PRF of 200 Hz and the pulse duration is around 20 ns. The average power of second harmonic is 105 W at the PRF of 170 Hz and the pulse duration is about 16 ns. The beam profile of the second harmonic is near top hat and will be suitable for the pumping of Ti:sapphire laser crystal. The wall plug efficiency of the laser is 2.0 %.

**Keywords:** Laser Diode, Nd:YAG, Zigzag Slab Crystal, Nonlinear Crystal, Master Oscillator Power Amplifier

### 1. INTRODUCTION

In Japan Atomic Energy Research Institute (JAERI), X-ray laser and laser acceleration driven by a high peak power laser has been studied. And as one of the high peak power lasers, development of high repetition rate Ti:sapphire CPA system has been carried out. Currently, a high average power Ti:sapphire CPA system has been pumped by A/O Q-switched solid state laser in which Nd:YAG, or Nd:YLF crystal is pumped by arc-lamp<sup>1,2,3</sup>). Although these solid state lasers can be operated at very high pulse repetition frequency between 1 kHz and 5 kHz, their pulse energy is limited to around 40 mJ because of the low energy of arc-lamp. Therefore, the peak power and average power of CPA system is also limited around 0.1TW and 5 W, respectively. Some effort has been carried out to produce higher average power with higher peak power. However, to achieve laser performance with ultra-high peak power at the PRF of kHz for above stated applications, the development of high energy and high PRF pumping laser is inevitable. Availability of high duty factor, high energy laser diode array leads to develop high repetition frequency, high energy solid state laser with high efficiency. And so far, high performance all solid state lasers have been developed<sup>4,5,6</sup>) for many applications such as precision machining, X-ray photolithography, LIDAR, illuminator, etc. However, for the pumping laser of CPA system, high spatial and temporal stability as well as high average power and high PRF are strongly required because the damage threshold of Ti:sapphire crystal is the same order as the saturation fluence. Therefore, we have been developing laser diode pumped all solid state laser for the Ti:sapphire CPA system<sup>7,8</sup>). In this paper, we report our present status of the development of laser diode pumped all solid state laser which consists of an oscillator, a preamplifier, two post amplifiers which compose ring type amplifier system, and image relay telescopes.

## 2. LASER DIODE PUMPED ND:YAG LASER SYSTEM

Figure 1 shows a schematic of laser diode pumped high repetition rate Nd:YAG laser. The laser has MOPA configuration and consists of an oscillator, a preamplifier, and two post amplifiers. All the laser heads install zigzag slab crystals in order to operate high repetition rate. And the both ends of the crystals are cut at near Brewster's angle to obtain highly polarized laser light. The master oscillator consists of a laser head, a Q-switch, cavity mirrors. Since the oscillator produces a multi-mode laser beam, there is a pinhole in the cavity to select TEM<sub>00</sub> mode laser beam. The laser crystal used is 3 x 3 x 83 mm slab crystal and pumped by a laser diode array with the peak

power of around 1kW. The pulse energy of the oscillator is around 10 mJ at the PRF of 200 Hz. Next to the output mirror, there is a Faraday isolator to prevent back reflection from the amplifier system. The preamplifier is a double-side pumped Nd:YAG laser amplifier. The size of the laser crystal is 3 x 6 x 83 mm and it is pumped by two 2 kW laser diode arrays. The laser pulse amplified in the preamplifier is around 30mJ. After the preamplifier, the laser beam is expanded to 5 x 20 mm using a cylindrical and a spherical beam expanders. In two post amplifier heads, slab laser crystals with the dimension of 6 x 20 x 125 mm are placed. One of the post amplifier is pumped from single-side of the crystal by a laser diode array with the peak power of 10 kW, shown in figure 2.

Another post amplifier is pumped by two laser diode arrays from double-side of the crystal. Each diode array consists of 8 diode sub-arrays and the maximum duty factor is around 20 %. The maximum stored energy is about 1 J for single-side pumped amplifier and 2 J for the double-side pumped amplifier. These two post amplifiers compose a ring type double-pass amplifier system connected each with three image

relay telescopes. The amplified laser beam is transferred to a second harmonic generator (SHG) with another image relay telescope. Before the SHG, the laser beam size is reduced by two cylindrical lenses. The size of the laser beam is around 10 x 6 mm. As a nonlinear crystal, a LBO crystal with the dimension of 10 x 8 x 15 mm is used. And the input energy fluence at the input surface of the LBO crystal is around 2 J/cm<sup>2</sup>. Thermal characteristics of KTP crystal is also studied because of its high conversion efficiency.

## 3. CHARACTERISTICS OF Nd:YAG LASER

Pulse duration is one of the important factors for the pumping of Ti:sapphire crystal. The

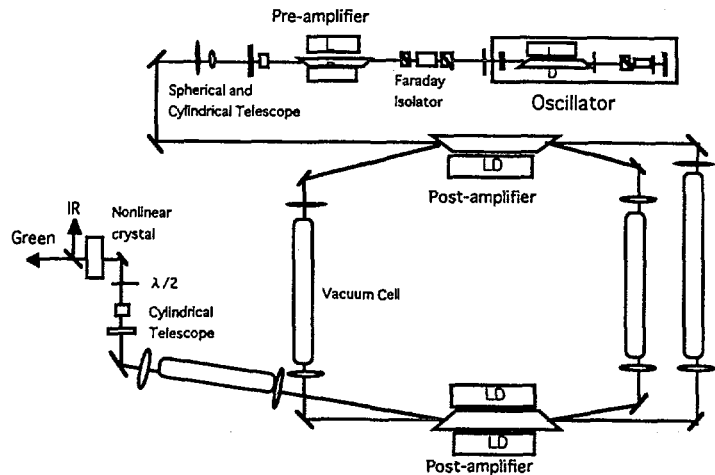
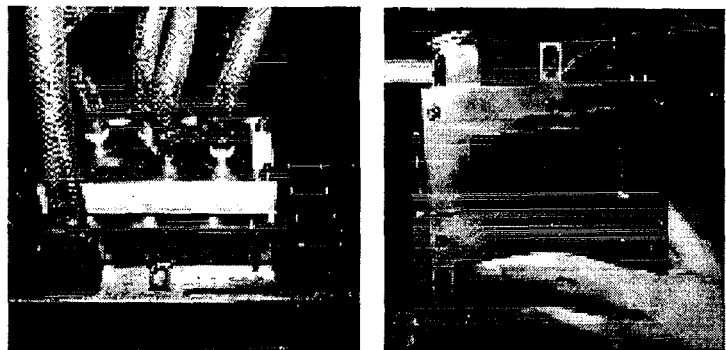


Fig.1 Schematic of high average power all solid state pumping laser



Amplifier module

Laser diode array

Fig.2 LD-pumped Nd:YAG amplifier module

pulse duration can be controlled by changing the cavity length of the oscillator or pumping power. By using former method, higher pulse energy with long pulse duration is expected. Figure 3 shows the pulse duration as a function of the cavity length. The squares and circles show the pulse duration and average power, respectively. With the cavity length of 30 cm, the pulse duration is around 20 ns and the pulse duration of 50 ns is obtained at the cavity length of 100 cm. The average output power is almost constant and is about 10 W. The triangles shows the pulse duration at 532 nm. The pulse duration at the cavity length of 30 cm is around 18 ns and that at the cavity length of 100 cm is around 40 ns. Therefore, the pulse duration at 532 nm can be controlled and the optimum pulse duration will be chosen for the pumping of Ti:sapphire CPA system.

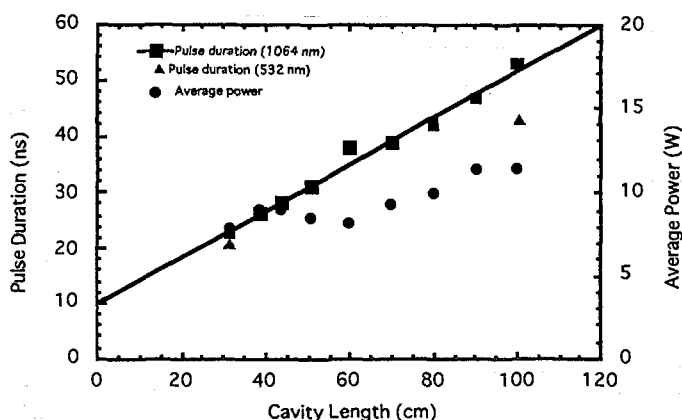


Fig.3 Pulse duration and average power of master oscillator as a function of cavity length

Figure 4 shows the pulse energy at 1064 nm as a function of laser diode drive current. The triangles represent the pulse energy with one post amplifier and the squares with two post amplifiers. The pulse repetition rate is 100 Hz. The output energy increases with laser diode drive current and 1.4 J at the drive current of 45 A and 1.2 J at 40 A are obtained, respectively. Since the preamplified pulse energy is 30 mJ, the double-pass amplification gain is about 13 with one post amplifier. The product of small signal gain ( $g_0$ ) and gain length ( $l$ ) is around 2.6. This low gain is due to that this post amplifier is pumped from single side of the crystal and has low stored energy. And with two post amplifiers, the gain for the ring type double-pass

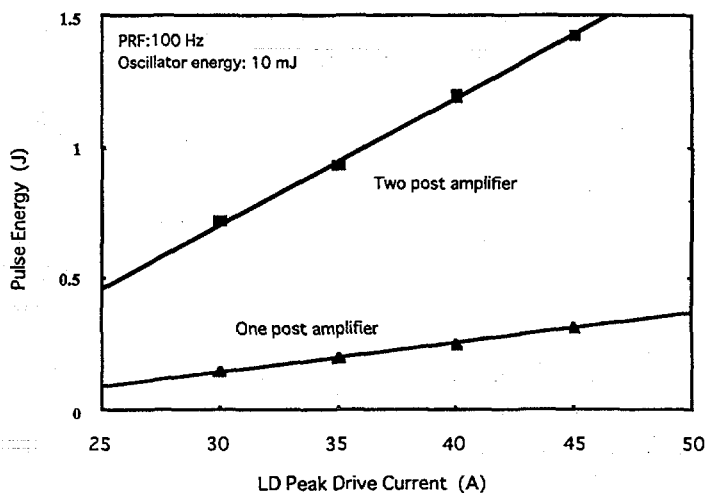


Fig.4 Fundamental output energy as a function of LD drive current at the PRF of 100 Hz

amplifier increases to 47. The  $g_0 l$  also increases and is 3.8. With this high amplification gain, the condition of saturation amplification is achieved. Figure 5 shows the average power at 532 nm and energy conversion efficiency as a function of fundamental power into the LBO crystal. The pulse repetition rate is 170 Hz and the laser diode array drive current 40 A. The pulse duration of the LD drive current is 250  $\mu$ s. The input fluence and the peak power are around 1.9 J/cm<sup>2</sup> and 98 MW/cm<sup>2</sup>, respectively. The average power increases linearly with fundamental power and is 105 W when the fundamental input power is 200W. The energy conversion efficiency is observed to decrease gradually with fundamental input power. This may be due to the heating of LBO crystal by the absorption of laser radiation. Figure 6 shows the pulse energy at 532 nm as a function of pulse repetition rate. The pulse energy at the pulse repetition rate

of 100 Hz is 0.64 J and 0.62 J at 170 Hz. The figure shows that the pulse energy is almost constant at the pulse repetition rate between 100 Hz and 170 Hz. This is due to the pulse energy of laser diode is also almost constant between wide pulse repetition rate. From the standpoint of Ti:sapphire crystal pumping, the intensity profile of green laser beam is important. Because if it has a hot spot with high peak power, the Ti:sapphire crystal will be damaged. Figure 7 shows the intensity profile of second harmonic at the PRF of 170 Hz. In this measurement, the image of the second harmonic is relayed to CCD camera by an image relay optics. The profile of green laser beam is nearly homogeneous and has near top hat. It is thought that the green laser beam is suitable for the pumping of Ti:sapphire crystal. Although some of the small peaks are observed, the peak power of these peaks are not so high. Therefore, Ti:sapphire crystal will not be damaged. In the future, a SBS reflector will be used to achieve more homogeneous laser beam. The efficiency of the pump laser is important from the stand point of realizing a compact pump laser system. Figure 8 shows the progress of wall plug efficiency and pulse energy. In 1993, the wall plug efficiency is around 1.3 % but in 1997 it becomes 2.0 %. The reason of this is the use of large amplifier with high amplification gain. At present, the small gain of the amplifier is nearly 4. therefore, the input laser pulse from the oscillator is amplified to high energy with first amplification. And in the second amplification in the ring system, the condition of the saturation amplification is achieved and as a result, the energy extraction efficiency increases. In this pump laser, one of the amplifier is pumped from one side of the crystal by a laser diode array. If it is also pumped from both sides, the stored

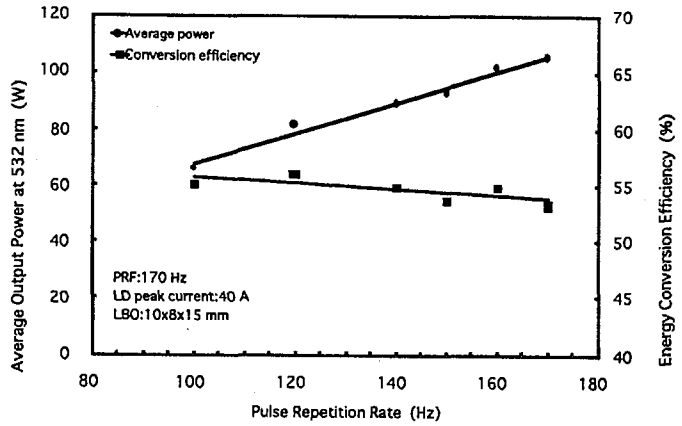


Fig.5 Average power at 532nm and energy conversion efficiency as a function of fundamental power

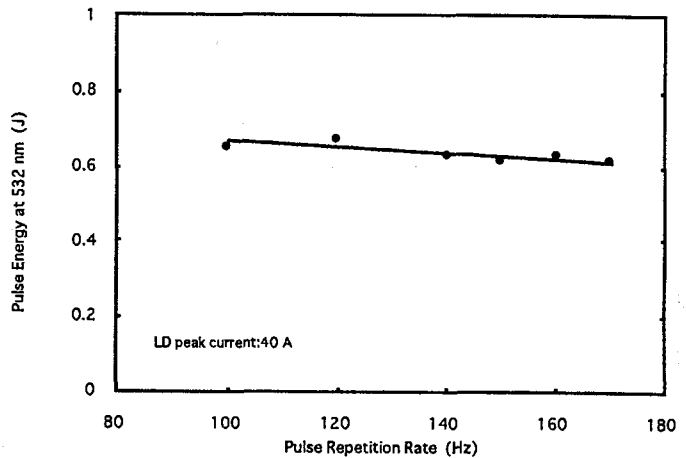


Fig.6 Pulse energy at 532nm as a function of pulse repetition rate

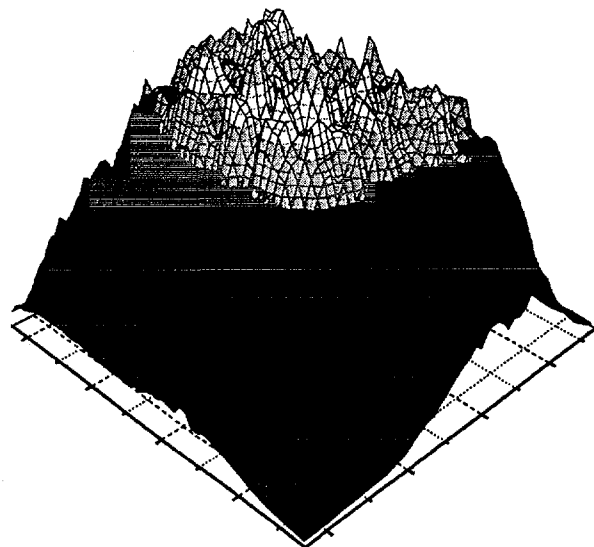


Fig.7 Intensity profile of green laser beam

energy will increase. Therefore, an amplification characteristics with two double-side pumped amplifier is studied. Measured and calculated pulse energy at 1064 nm is shown in figure 8 as a function of number of passes in amplifier at the pulse repetition rate of 170 Hz. In the measurement, some optical loss in 3rd and 4th amplification is observed and this is due to the reflection loss at the input surfaces of the amplifier which is near Brewster's angle. The calculation shows that if two post amplifiers are pumped from double-side of the crystals, the output energy will increase to about 1.9 J. The energy conversion efficiency is expected to be over 50 % for LBO and 60 %

for KTP. Therefore, it will be expected to have around 1 J in green if the two both sides pumped amplifier is used.

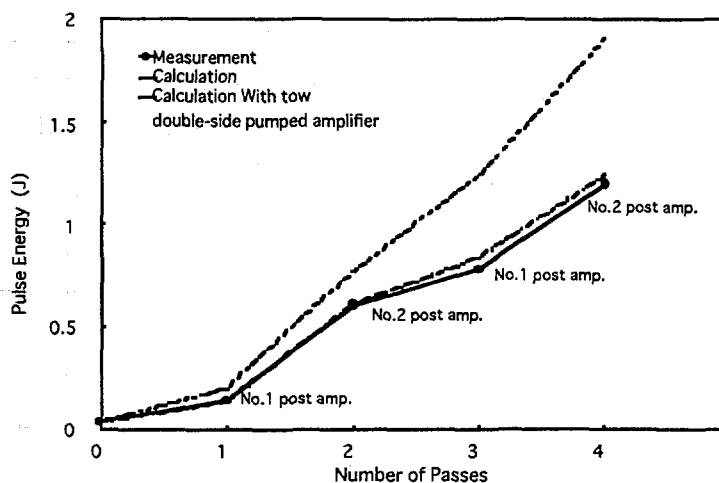


Fig.8 Measured and calculated pulse energy

#### 4. SUMMARY

We developed all solid state pumping laser for the pumping of high repetition rate Ti:sapphire CPA system. The pulse energy at 1064 nm is 1.25 J and the average power is 250 W at the repetition rate of 200 Hz. The pulse energy and average power at 532 nm are 0.62 J and 105 W at the pulse repetition rate of 170 Hz, respectively. The wall plug efficiency of the laser is 2.0%. It is shown by the calculation using Frantz-Nodvik equation that the pulse energy of around 1 J at 532 nm will be expected, if two double-side pumped amplifier is used.

#### REFERENCES

- 1) Q.Fu, F.Seier, "High average power kilohertz sub-100fs amplifier," in Technical digest of Conference of Lasers and Electro-Optics (Anaheim CA, 1996) paper CTul14
- 2) F.Salin, C.Le Blanc, C.Spielmann, et al, "kilohertz thermal eigen mode multipass-amplifier for high average power chirped pulse amplification," in Technical digest of Conference of Lasers and Electro-Optics (Baltimore Maryland, 1997) paper CMC2
- 3) S.Backus, C.G.Durfee III, M.Murnane, et al, "0.125 terawatt kilohertz laser system," in Technical digest of Conference of Lasers and Electro-Optics (Baltimore Maryland, 1997) paper CMC5
- 4) S.P.Velsko, C.A.Ebbers, B.Comaskey, G.F.Albrecht, et al, " 250Watt average power Electro-Optically Q-switched diode-pumped power oscillator," OSA Proceedings on Advanced Solid State Lasers, 20,308(1994)
- 5) J.J.Kasinski, R.L.Burnham, " Near diffraction limited output from a high power diode pumped laser via phase correction with aspheric diamond turned optics," in Technical digest of Advanced Solid State Lasers, (San Francisco, CA, 1996) paper FD5
- 6) R.St Pierre, G.Holleman, M.Valley, H.Injeyan, J.Berg, et al, " Active tracker laser (ATLAS)," OSA TOPS, 10,288(1997)
- 7) Y.Maruyama, M.Oba, M.Kato, T.Arisawa, "Characteristics of LD-pumped Nd:YAG green laser system," OSA TOPS, 1,369 (1996)
- 8) M.Oba, Y.Maruyama, M.Kato, T.Muramatu, T.Arisawa, " Laser Diode pumped high average power Nd:YAG green laser," in Technical digest of Conference of Lasers and Electro-Optics Europe (Hamburg Germany, 1996) paper CTh155

**22. Development of All Solid-State, High Average Power  
Ultra-Short Pulse Laser for X-ray Generation  
~ High Average Power CPA System  
and Wavefront Control of Ultra Short Laser Pulse ~**

Sayaka HARAYAMA, Katsuaki AKAOKA, Kazuyoku TEI,  
Masaaki KATO, Yoshito NIWA, Yoichiro MARUYAMA,  
Toru MATOBA, Takashi ARISAWA, Hiroshi TAKUMA

Advanced Photon Research Center  
Kansai Establishment  
Japan Atomic Energy Research Institute  
Tokai, Ibaraki 319-11 Japan  
E-mail : sayaka@hikari.tokai.jaeri.go.jp

**ABSTRACT**

We developed a prototype CPA laser system which is pumped by a all solid-state Nd:YAG laser. In a preliminary experiment, the output energy of 52mJ before compression was obtained when the pumping-energy was 250mJ. To compensate the wavefront distortion, an adaptive optics has been developed. By using this wavefront control system, the laser beam with the distortion of  $0.15 \lambda$  was obtained.

**Keywords** : Ultra short pulse laser, High peak power laser, LD-pumped laser, Chirped Pulse Amplification (CPA), Multi-pass amplification, Adaptive optics, Wavefront compensation

**1. Introduction**

An ultra high peak power laser with high repetition rate using Chirped Pulse Amplification (CPA) is very attractive light source for the development of X-ray laser, laser induced high energy particle acceleration, and for many other applications such as high field physics, laser processing, etc. But in the conventional high peak power CPA system, the repetition rate has been restricted up to 10Hz because the pumping laser is pumped by flashlamps. Recently, a high repetition rate CPA system has come into discussion and arc-lamp pumped, high repetition rate Nd:YAG and Nd:YLF have been used as pumping light source<sup>1,2,3</sup>). Although these pumping lasers are able to operate at kHz repetition rate region, the average power and peak power of the CPA system are limited because of the low pulse energy of the pumping laser. Therefore, to obtain high average power and high peak power in a Ti:sapphire CPA system, it is inevitable to develop a high repetition rate and high energy pumping laser.

In order to realize high repetition rate, high average power, and ultra high peak power laser, dispersion compensation is essentially important. The higher the peak power is, the higher order dispersion has to be taken into consideration. And the thermal load into the laser crystal

becomes more important with increasing the average power. Realization of laser beam of high quality and stability by compensating the thermal load in the laser crystals is indispensable for the above stated applications, because high thermal load causes the thermal lens effect as well as inhomogeneous diffraction index distribution resulting in the dispersion errors which makes the ultra short pulse width broader leading to the reduction of the peak power considerably.

In JAERI, to construct a high repetition rate, high average power CPA system, we have been developing LD-pumped Nd:YAG green laser<sup>4)</sup> and the wavefront control system.

## 2. CPA system

Our prototype Ti:sapphire CPA system is prepared to obtain design data for a higher average power CPA laser system. The schematic is shown in Fig.1. The CPA laser system consists of an ultra short pulse oscillator, a stretcher, a regenerative amplifier with a pockels cell, a 2-pass pre-amplifier, a 4-pass post-amplifier, a compressor, and a wavefront control systems.

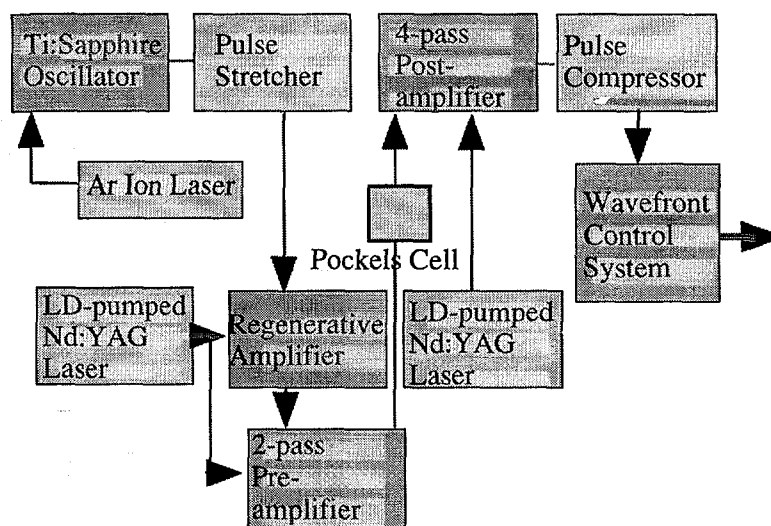


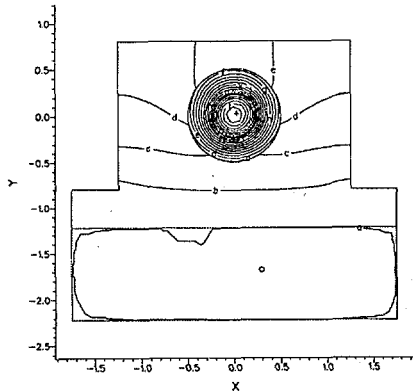
Fig.1 Schematic of Ti:sapphire CPA Laser System

The pulse duration of the oscillator is 100fsec and output power is 300mW at 100MHz when it is pumped by 5W CW green laser. Then the laser pulse is stretched to 100ps. The stretched pulse is amplified by the regenerative amplifier and 2-pass pre-amplifier. These regenerative and 2-pass pre-amplifier are pumped by a 2.5W LD-pumped Nd:YAG laser of which pulse duration is around 50ns. The green pump laser beam is divided into two, and one of which is used to pump regenerative amplifier and the other to pump 2-pass pre-amplifier. The output pulse energy of the regenerative amplifier is around 1mJ, and that of 2-pass pre-amplifier is about 3mJ. After the 2-pass amplifier, there is a second pockels cell to get a high contrast ratio. Then the laser pulse is introduced into 4-pass post-amplifier which is pumped by another LD-pumped Nd:YAG laser. After that, the laser pulse is compressed by a compressor. In order to compensate wavefront distortion, the wavefront control system is placed after the compressor.

In this CPA system, the 4-pass amplifier is pumped by a Nd:YAG laser with the maximum average power of 25W. Therefore, if the heat generated in the crystal can not be removed efficiently, the temperature of the crystal increases. As the result, some effects are caused such as thermal lensing, the shortening of the decay time of excited  $Ti^{+3}$  which results in a decrease of stored and output energy, etc. To avoid these effects, the crystal temperature has to be kept at near room temperature.

Fig.2 shows the calculated temperature distribution of the Ti:sapphire crystal and its

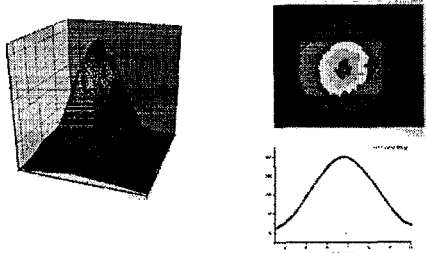
housing for the 4-pass amplifier when the input average power is 25W and the temperature of the cooling water is 18°C. It indicates the highest temperature in the crystal will be 30°C. Judging from this calculation, it is expected thermal effects caused by the pumping will be avoided by using this crystal housing when the input average power is up to 25W. The compressed pulse duration is shown in Fig.3. This measurement is done by optical delay back-ground free autocorrelation using second harmonic generation of KTP. The FWHM of the laser pulse is fit with



Pumping Power 25 W  
 Temperature of Cooling Medium 18° C  
 Highest Temperature in Crystal 30° C

**Fig.2 Temperature Distribution of Ti:sapphire Crystal by 25W Pump**

Profile of two pass amplifier output beam



Profile of four pass amplifier output beam

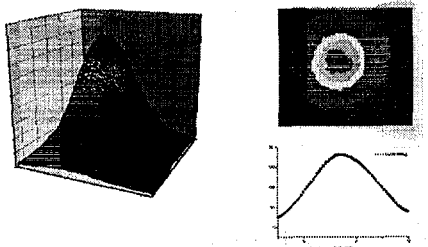


**Fig.5 Intensity Profiles of Pre-amp. and 4-pass amp. Output Beam**

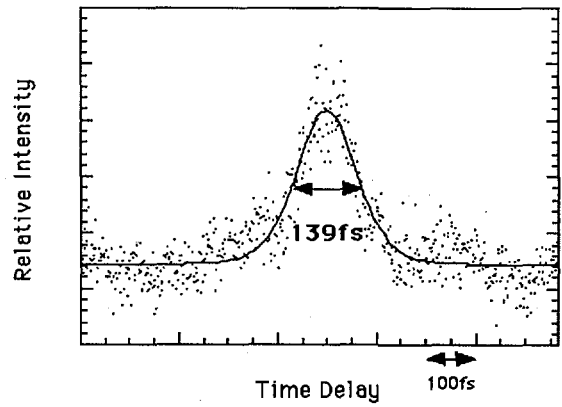


**Fig.3 Compressed Laser Pulse Duration**

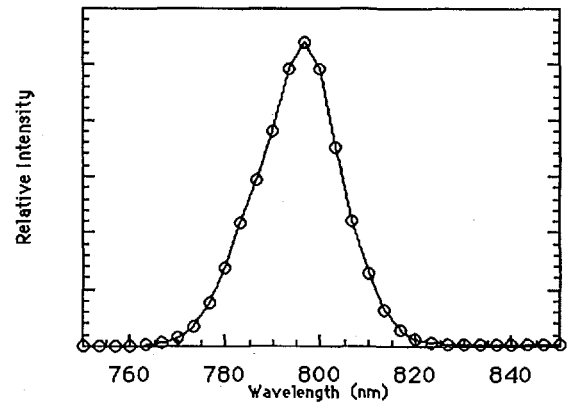


**Fig.4 Bandwidth of Laser Pulse**

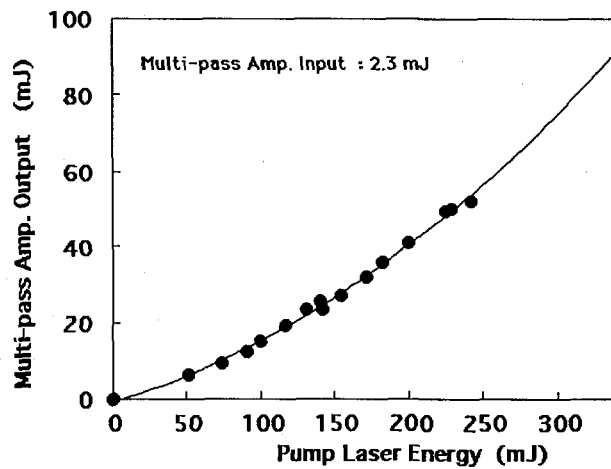


**Fig.6 Ti:sapphire CPA Laser Multi-pass Amplification Pumped by All Solid State Nd:YAG Laser**

square hyperbolic secant (Time bandwidth product is 0.315.) is 139fs. Fig.4 shows the bandwidth of the laser pulse. The FWHM of the bandwidth is about 20nm and the center wavelength is about 800nm. The intensity profiles of the output beam of 2-pass pre-amplifier and 4-pass post-amplifier are shown in Fig.5, both show good fits to Gaussian curves. Fig.6 shows the output energy of 4-pass amplifier as a function of pump pulse energy. The input energy into the amplifier is 3mJ. The output energy is 52mJ before compression with the repetition rate of 10Hz when the pumping energy is 250mJ. Our pumping laser is now operated at 200Hz, we intend to increase the repetition rate from now on.

Now, 100W green laser has been realized in JAERI, then much higher pulse energy and higher peak power can be expected by a CPA system. However, if it is pumped by the 100W laser beam, the temperature of the crystal will increase. So, thermal characteristic of the Ti:sapphire has been studied by using a heat code. Fig.7 illustrates the calculated temperature distributions when a crystal is pumped by the average power of

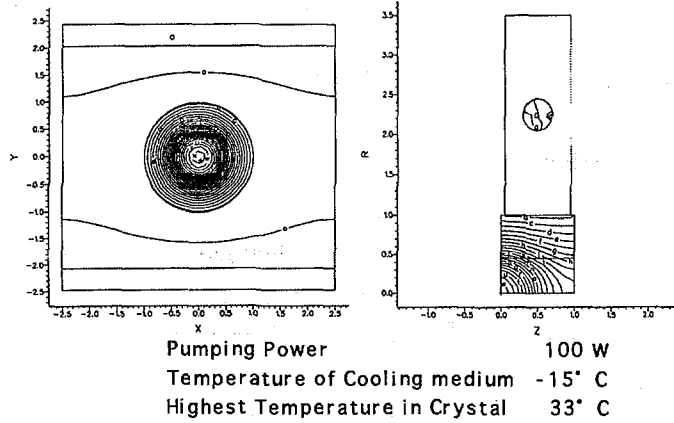


Fig.7 Temperature Distribution of Ti:sapphire Crystal by 100W Pump

100W. The cooling medium flows on upper and lower sides of the crystal. The temperature distribution shows a good symmetry. This calculation shows that highest temperature in the crystal will be 33 °C when the temperature of the cooling medium is -15 °C. Using this crystal as a second 4-pass amplifier, the average power of 20W will be obtained. And the peak power will be expected to increase to around 2TW level when the pulse duration is 100fs.

### 3. Wavefront Control System

Fig.8 shows a schematic of the wavefront control system. The system consists of a Shack-Hartmann type wavefront sensor, a control computer, a diagnostic computer, and a deformable mirror. A part of the laser beam from the CPA system is sampled by a beam splitter, and the wavefront is measured by the Shack-Hartmann type wavefront sensor<sup>5)</sup>. The conjugate surface on the deformable mirror is made by the

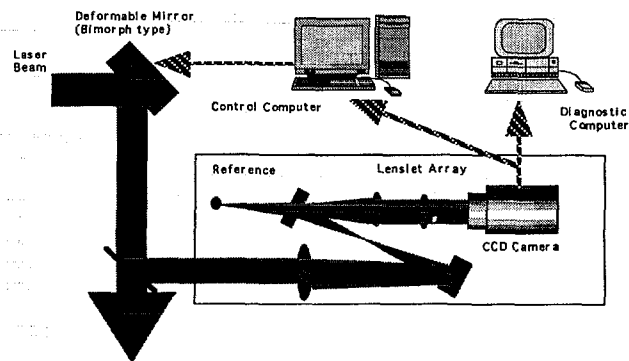


Fig.8 Schematic of Wavefront Control System

computer. Fig.9 illustrates the schematic of the Shack-Hartmann type sensor. The sensor includes the array of stacked lenslets of 32 x 32, a CCD camera, and a point light source. Each lenslet focuses the laser beam onto the CCD camera and a point light source generates a plane wavefront as a reference. Then the local tilt of wavefront can be calculated from the difference

between centroids of the reference beam and the measured laser beam.

A Bimorph-type mirror is made of two thin plates of piezoelectric material stuck together, and the two plates are oppositely poled. Then, when a voltage is applied, the piezoelectric effect leads to an opposite variation of the transverse length of the two plates; this results in bending the mirror. The Bimorph-type mirror has much less electrodes than a Stacked Array-type mirror with piezoelectric actuators, then the processing time by computer becomes shorter<sup>6,7)</sup>. The deformable mirror has 13 electrodes as shown in Fig.10, which is operated in 13.5Hz. The control computer makes the deformable mirror a proper shape according to the conjugate wavefront of the measured one. The input beam is expanded by lenses to fill the clear aperture of the mirror. Aberrations of these lenses are canceled because the reference beam and the laser beam propagate through the same optical path.

Fig.11 shows the results of the measurements. The wavefronts in (a) and (b) shown by the optical path difference (OPD). Root Mean Square of OPD is improved from  $0.78 \lambda$  ( $0.62 \mu\text{m}$ ) without wavefront control to  $0.15 \lambda$  ( $0.12 \mu\text{m}$ ) during the control. ( $\lambda = 800 \mu\text{m}$ ) And the peak value of Point Spread Function (PSF ; calculated far-field pattern) increases from 10 to 62 with control shown in (c) and (d). Judging from these results, the laser beam after the compressor is about 6 times brighter in its far-field with wavefront control. Fig.12 shows the

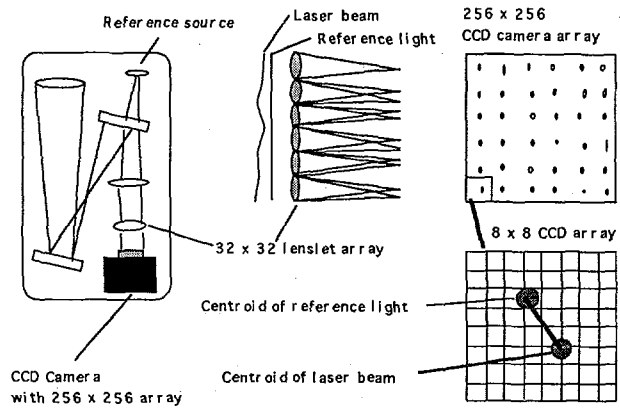


Fig.9 Shack-Hartmann Type Wavefront Sensor

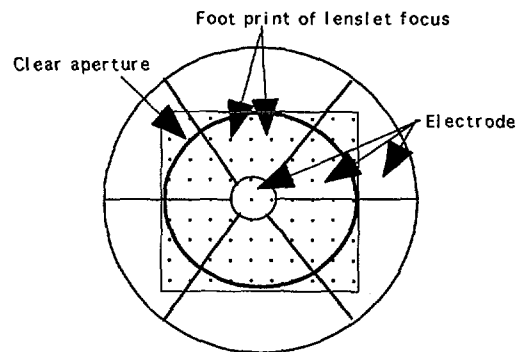


Fig.10 Schematic of Bimorph-type Deformable Mirror

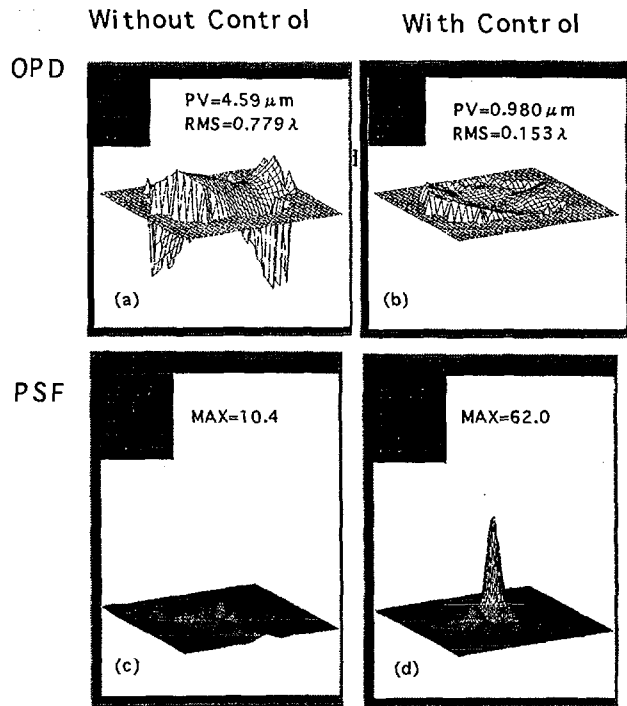


Fig.11 Correction of Wavefront Distortion

wavefront distortion in Root Mean Square with control and without wavefront control as a function of time. Without control, the wavefront distortion of  $0.6 \mu\text{m}$  is observed. However, the distortion is reduced less than  $0.2 \mu\text{m}$  with control.

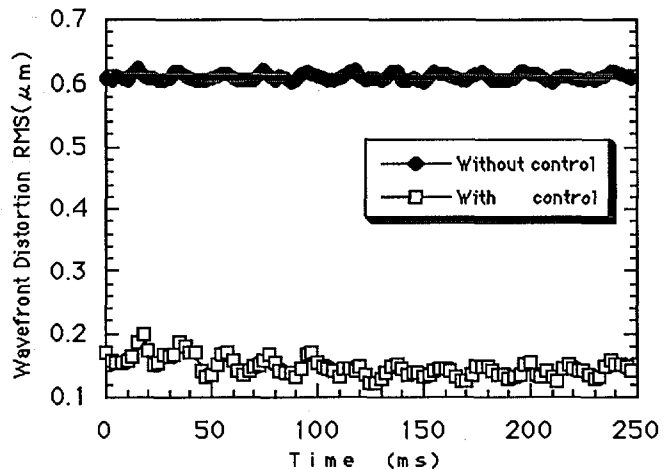


Fig.12 Wavefront Distortion with and without Control

### 5. Summary

In Summary, the prototype all solid-state high average power Ti:sapphire CPA system was constructed and the preliminary preliminary measurement has been studied at a low repetition rate. The output average of 52mJ was obtained by the pumping energy of 250 mJ.

The performance at high repetition rate will be measured from now on.

And by using the adaptive optics to compensate the wavefront distortion of the CPA system, the laser beam of high quality with the distortion of  $0.15 \lambda$  was obtained.

Our calculation shows if one more 4-pass post amplifier is installed, it will be able to increase the peak power to TW level and the average power of 20W.

### References

- 1) Sterling Backus, Charles G.Durfee III, Margaret Murnane, Henry Kapteyn, "0.125 terawatt kilohertz laser system," in Technical Digest of CLEO'97 (Baltimore MD), CMC5
- 2) Q.Fu, F.Sier, "High-average-power kilohertz sub-100-fs amplifier," in Technical Digest of CLEO'96 (Anaheim CA), CtuL14
- 3) F.Salin, C.Le Blanc, C.Spielmann, J.Squier, V.V.Yakovlev, C.P.J.Barty, "Kilohertz thermal eigenmode multipass amplifier for high-average-power chirped-pulse amplification," in Technical Digest of CLEO'97 (Baltimore MD), CMC2
- 4) Y.Maruyama, M.Ohba, M.Kato, T.Arisawa, "Characteristics of LD-Pumped Nd:YAG Laser System," OSA TOPS on Advanced Solid-State Lasers, 369-372, Vol.1 (1996)
- 5) K.Akaoka, Y.Maruyama, T.Arisawa, "Development of wavefront control system using deformable mirror for solid state lasers," in Proceedings of Solid State Lasers 6 (San Jose CA), 55-61 (1997)
- 6) J-P.Gaffard, J.P.Gex, P.Gosselin, P.Jagourel, "A Stacked Array Mirrors and Bimorph Mirrors Comparison," in Proceedings of Conference on Wave Propagation in Turbulent Media and Adaptive Optics, National Astronomical Observatory (Tokyo Japan), 235-240 (1993)
- 7) P.Gosselin, P.Jagourel, J.Peysson, "Objective Comparisons between Stacked Array Mirrors and Bimorph Mirrors," in Proceedings of Conference on Wave Propagation in Turbulent Media and Adaptive Optics, National Astronomical Observatory (Tokyo Japan), 241-250 (1993)

## 23. 80-W cw TEM<sub>00</sub> IR beam generation by use of a laser-diode-side-pumped Nd:YAG rod laser

Susumu Konno, Shuichi Fujikawa, and Koji Yasui

Advanced Technology R&D Center

Mitsubishi Electric Corporation

8-1-1 Tsukaguchi, Amagasaki 661, Japan

E-mail: konno@lap.crl.melco.co.jp

Phone: 81-6-497-7110

Fax: 81-6-497-7288

### Abstract

We have demonstrated high-efficient and high-power operation of a diode-side-pumped Nd:YAG rod laser. The laser has a simple and scalable configuration consisting of a diffusive pumping reflector and an advanced cavity configuration for polarization-dependent bifocusing compensation.

### 1. Introduction

Compact, electrically-efficient, scalable, and high brightness IR beam sources are desired for various applications in material processing and frequency conversion. Diode-pumped solid-state lasers are promising approaches satisfying these requirements. Diode-pumping could reduce the size and weight of the system, and could increase the electrical-to-optical conversion efficiency, reliability, and lifetime.

Several tens W of TEM<sub>00</sub> IR beams have been generated by using end-pumping configuration,<sup>1</sup> or side-pumping configuration with fiber-coupled diodes<sup>2,3</sup> and zigzag slab laser geometry.<sup>4</sup> However, in the end-pumping configuration, further enhancement of the output power is limited by the thermal fracture of the laser material.<sup>5</sup> In the side-pumping configuration, fiber-coupled diodes or slab-shaped laser material are relatively expensive and could reduce the overall system efficiency.

In this paper, we report a scalable and efficient approach for high-power multi transverse mode and  $TEM_{00}$  mode IR beam generation of a diode-side-pumped Nd:YAG laser. The laser has a diffusive-close-coupled side pumping configuration that we name CIDER (Close-Coupled Internal Diffusive Exciting Reflector)<sup>6,7,8</sup> with an advanced cavity configuration, we name HIPER(High-Brightness Polarization-dependence Erased Resonator).<sup>9</sup>

## 2. Experimental setup

Figure 1 shows the schematic drawings of the pumping configuration and the resonator configuration.

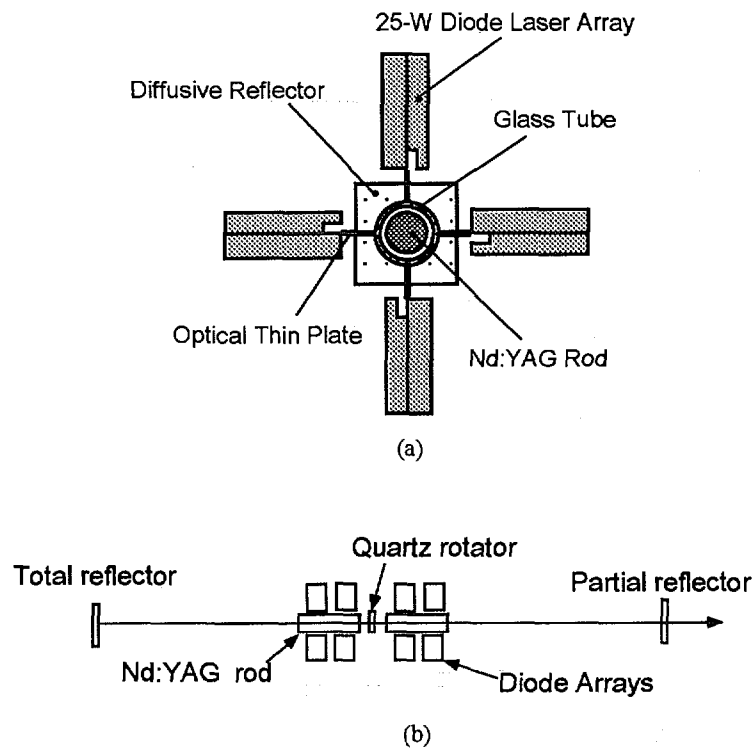


Fig.1. Schematic drawing of the (a) pumping module, and (b) resonator configuration.

Each pump head consists of eight 1cm long linear diode-arrays (808nm wavelength) and a Nd:YAG rod (4 mm in diameter, 70 mm in length, 0.6 % in Nd doping) that is surrounded by a flow tube and diffusive reflectors. Diode arrays are located symmetrically around the rod. Without any focusing elements or optical alignments, more than 97% of the diode power is coupled into the diffusive reflector through a thin plate by total internal reflection. Each diode beam is absorbed

into the laser rod both directly and also after multiple-reflection on the reflector. Detailed description of the pumping configuration is previously reported<sup>8</sup>. The IR operation was performed with a symmetrical 1.1m convex-convex resonator ( $R = 200$  mm,  $T=11\%$ ) for  $TEM_{00}$  mode operation and a 0.3m concave-concave ( $R=2m, T=8\%$ ) short cavity for low-brightness operation. A  $90^\circ$ -polarization-rotation quartz rotator is placed between two uniformly pumped Nd:YAG rods for polarization-dependent bifocusing compensation.

As described in Fig.4, the technical point of this resonator configuration is to cancel out the bifocusing of the two polarization directions ( $\phi$ -polarization and  $r$ -polarization). The focal length variation within the rod cross section could significantly degrade the laser performance. Therefore, uniform pumping of the rods is required. Detailed description of the basic mechanism of this resonator configuration is described elsewhere<sup>9</sup>. We measured the output power with a calorimetric power meter and the beam quality by a Coherent's  $M^2$  meter.

### 3. Experimental results

Laser performance obtained with low-brightness operation ( $M^2=45$ ) was shown in Fig.2. The laser output power of 147W was obtained at 386W and 992W of diode pumping power and electrical input power for laser diodes, respectively.

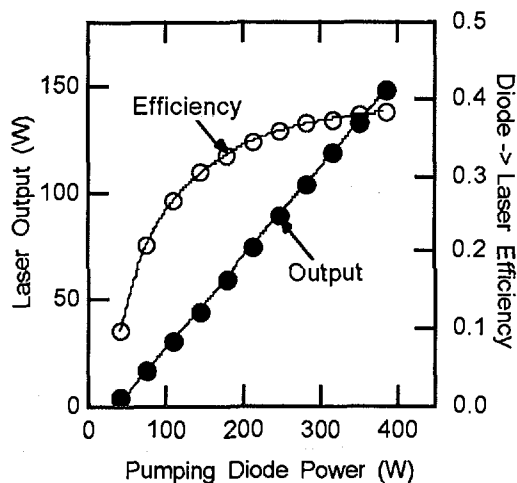


Fig.2(a)

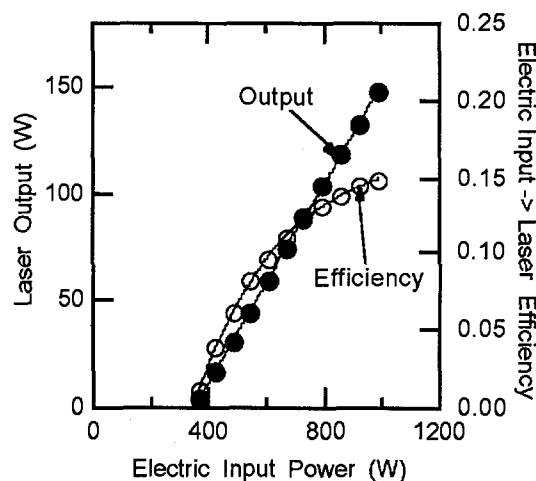


Fig.2(b)

Fig.2 Laser output (a) as a function of the total diode output power, (b) as a function of the electrical input power.

These values are corresponding to 38.1% of optical-to-optical conversion efficiency and 14.8% of electrical-to-optical conversion efficiency. To our knowledge, these values are the highest numbers for diode-side-pumped Nd:YAG lasers and the electrical -to-electrical conversion efficiency is comparable with that of CO<sub>2</sub> lasers.

Lasing performance of TEM<sub>00</sub> mode operation is shown in Fig.3 as a function of the total diode output power. To show the effect of bifocusing compensation, we also showed laser performance obtained without bifocusing compensation, thus without a quartz rotator between the rods. The highest TEM<sub>00</sub> output power of 80W was generated at 386 W of total diode output power with the beam quality of M<sup>2</sup>=1.1. Although the M<sup>2</sup> changed slightly between 1.1-1.7, the beam profile was always Gaussian. While, without the bifocusing compensation, the beam quality degraded to M<sup>2</sup>~3. and the highest output power decreased by 19 %. The temporal stability of the output power was also improved by introducing the bifocusing compensation. With bifocusing compensation, the average power remained stable with less than 1% fluctuation, while, without bifocusing compensation, the output power instability was more than 3%.

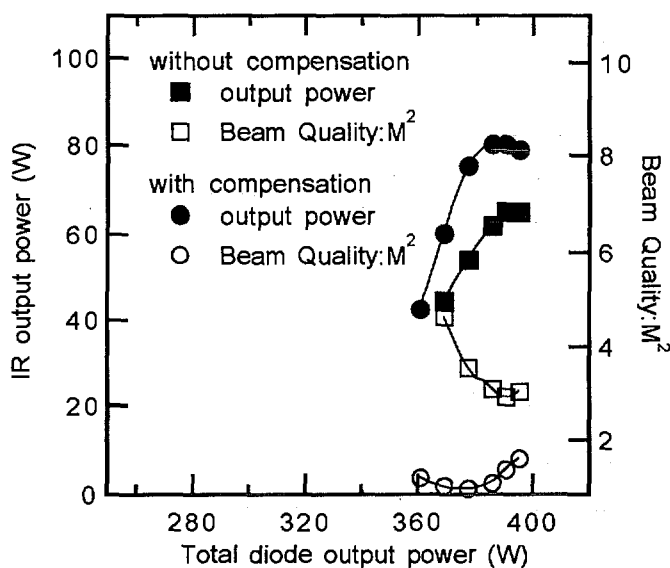


Fig.3. IR cw output power and beam quality as a function of the total diode output power obtained with and without bifocusing compensation.

Figure 4 shows the stability zone calculation of the resonator for  $TEM_{00}$  mode operation with and without bifocusing compensation. When a quartz rotator was placed between the Nd:YAG rods, thus with bifocusing compensation, the beam diameter at the rod was almost identical for both polarization directions (r-polarization and  $\phi$ -polarization), as shown in Fig. 4 (a). While, without a quartz rotator, thus without bifocusing compensation, stability zone separates for both polarization directions, as shown in Fig. 4 (b). This separations leads to inefficient and unstable operation.

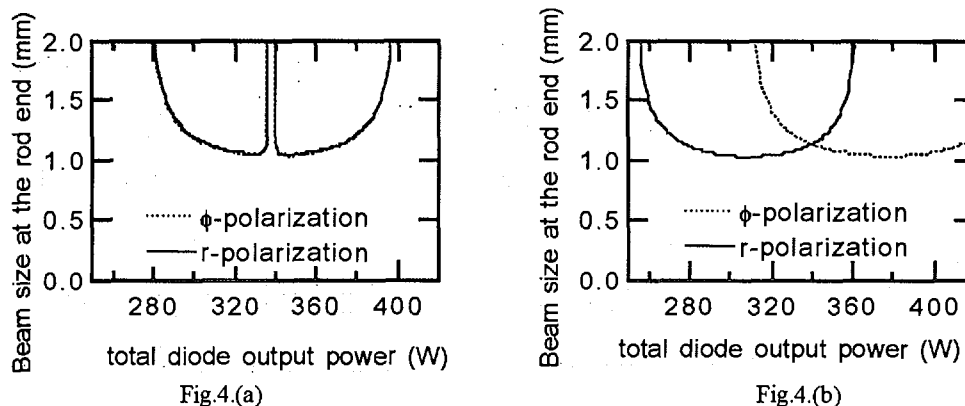


Fig.4. Stability zone calculation (a)with bifocusing compensation and (b) without bifocusing compensation.

This calculation is based on non-lasing thermal loading of the Nd: YAG rod. Therefore, the experimentally observed operation zone is slightly offset toward higher pumping region as shown in Fig. 3.

#### 4. Summary

We have reported efficient and high power IR operation. In  $TEM_{00}$  mode operation, 80-W IR beam was obtained with 20.7 % of the optical-to-optical and 8.06 % of the electrical-to-optical conversion efficiency. In addition, 147W of multi-transverse-mode IR beam was extracted with 38.1 and 14.8% of optical-to-optical and electrical-to-optical conversion efficiency, respectively. These values were obtained with diode-side-pumped Nd: YAG lasers by using the combination of a diffusive close-coupled pumping module and the bifocusing compensation. Since, the

configuration is simple and scalable, we believe further enhancement of the output power should be possible by increasing the pumping power.

The authors thank K. Yoshizawa, S. Yagi, and M. Tanaka for supporting and encouraging our research.

### References

- <sup>1</sup>S. C. Tidwell, J. F. Seamans, and M. S. Bowers, *Opt. Lett.* **18**, 116 (1993).
- <sup>2</sup>D. Golla, M. Bode, S. Knoke, W. Schöne, and A. Tünnermann, *Opt. Lett.* **21**, 210 (1996).
- <sup>3</sup>D. Golla, S. Knoke, W. Shöne, M. Bode, A. Tünnermann, and H. Welling, *Proc. SPIE* **2700**, 314 (1996).
- <sup>4</sup>R. J. Shine, Jr., A. J. Alfrey, and R. L. Byer, *Opt. Lett.* **20**, 459 (1995).
- <sup>5</sup>Steve C. Tidwell, Jonathan. F. Seamans, Mark S. Bowers, and Anada K. Cousins, *IEEE J. Quantum Electron.* **28**, 997 (1992).
- <sup>6</sup>T. Kojima, and K. Yasui, *Post Deadline papers CLEO/Pacific Rim.*, PD2.2 (1995).
- <sup>7</sup>T. Kojima and K. Yasui, *Appl. Opt.* **36**, 4981 (1997).
- <sup>8</sup>S. Fujikawa, T. Kojima, and K. Yasui, to be published in *IEEE J. Selected Topics Quantum Electron.* vol.3, No.1 February 1997
- <sup>9</sup>K. Yasui, *Appl. Opt.* **35**, 2566 (1996).
- <sup>10</sup>S. Konno, S. Fujikawa, and K. Yasui, *Appl. Phys. Lett.* **70**, 2650, (1997)

## 24. Reliability of Czochralski-grown $\beta$ -BaB<sub>2</sub>O<sub>4</sub>(BBO) Devices

Nobuhiko Umezu, Tatsuo Fukui, Tsutomu Okamoto,  
Hiroyuki Wada, Kouichi Tatsuki, Kenji Kondo  
and Shigeo Kubota

Kubota Optoelectronics Laboratory, Research Center, Sony Corporation  
6-7-35, Kitashinagawa, Shinagawa-ku, Tokyo 141, Japan

### Abstract

We have achieved more than 1000 hours-operation in 266 nm-continuous wave (CW), 100 mW-generation of all-solid-state-UV laser system using Czochralski (Cz)-grown  $\beta$ -BaB<sub>2</sub>O<sub>4</sub>(BBO) crystal devices. Absorption of the Cz-grown crystal for e-ray at 266 nm was improved to 1%/cm, which is one-third lower than that of the crystal grown by top seeded solution growth(TSSG) method. Degradation rate of 266 nm generation, using 7 kHz repetition rate laser diode pumped Q switched Nd: YAG laser as a fundamental light source, was one order of magnitude lower than that of TSSG-crystal. Surface roughness of the crystal was better than 0.3 rms.-nm. HfO<sub>2</sub> film with extremely high adhesion was deposited on the surfaces using reactive low voltage ion plating method. Our devices can be put to practical use in areas of photolithography, micro fabrication, material processing and ultra high density optical disk mastering.

**Keywords:** All-solid-State CW UV laser, Czochralski, BBO, Top Seeded Solution Growth, Laser Scanning Tomography, Photolithography,

### 1. Introduction

We have developed an all-solid state 266 nm CW UV laser system using an external frequency conversion cavity with a nonlinear optical device [1, 2]. As far as we know, there has been no report on long-term reliability in such a laser system. Recently, we have achieved long-term reliability of the system using a Cz-grown BBO device in CW operation. This results from the improvement of surface roughness of BBO and durability of optical coating on the surfaces as well as reduction of bulk optical loss. In this paper, we report the crystal quality, fabrication processes and reliability of our system.

## 2. Crystal Growth

We adopted the Czochralski method, because Czochralski grown crystals have a higher damage threshold than TSSG-crystals [3]. Refining the Cz-growing method reported by Itoh et al [4], we obtained BBO crystals 2" in diameter and 1" in length. Actual growth time was only about 8 hours. Except for damage threshold data [5], few data were available. For example, data on internal scattering and optical loss are not available. These data are important for designing and fabricating optical devices. We compared BBO crystals grown by these two different growth techniques.

### 2.1 Evaluation of Crystal quality

#### 2.1.1 Laser Scanning Tomography

The quality of these two crystals was evaluated using laser scanning tomography [6]. As shown in Fig. 1, no extreme scatters could be observed in Cz-crystal but many scattering sources were observed in a TSSG-crystal, mostly impurities and dislocations decorated by impurities taken into the crystal from the flux. This difference is supported by the result of Inductively Coupled Plasma -Atomic Emission Spectrometry (ICP-AES) measurement that the concentration of impurities in the Cz-BBO was less than that in the TSSG-BBO.

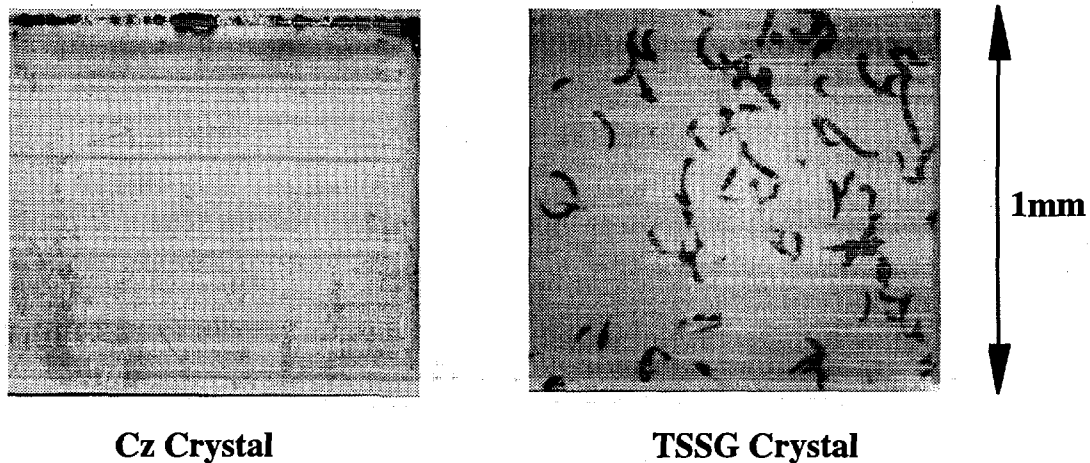


Fig.1 Internal scattering observed using laser scattering tomography

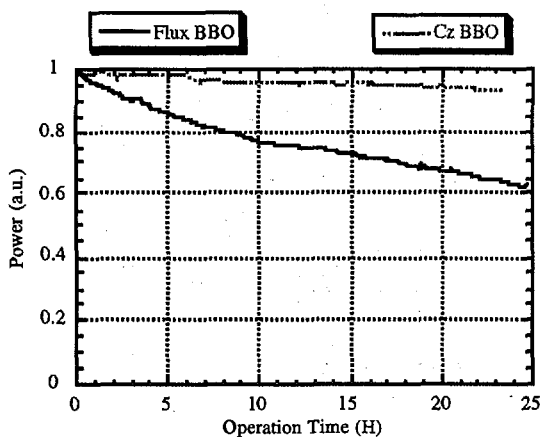
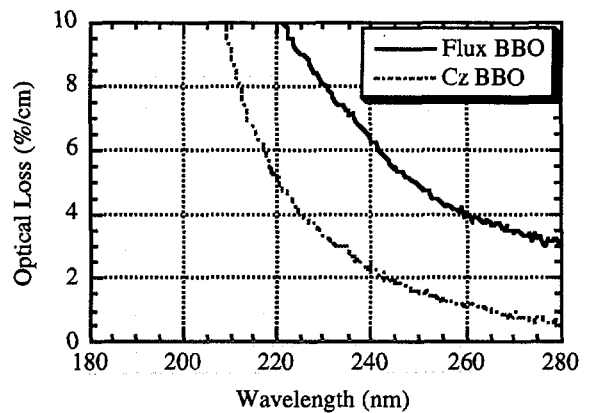
### 2.1.2 UV absorption

We also measured the UV transparency of these crystals, shown as Fig. 2. The optical loss of the Cz-crystal was a few times lower than the TSSG-crystal. We think that this comes from scattering and absorption of impurities. Better transparency of Cz-BBO is needed for good UV devices.

### 2.1.3 Evaluation of crystal quality using high-repetition-rate Q-switched Nd:YAG laser.

We evaluated the crystal quality using 266 nm UV generation system of laser diode pumped high-repetition-rate Q-switched Nd:YAG laser [1]. The 1064 nm fundamental light was frequency-converted using lithium triborate (LBO) and BBO stage. The average power of this system was about 2.6 W @ 532 nm and 0.8 W @ 266 nm. High repetition-rate-pulsed laser light causes optical damage, hence the UV generating power degrade. We select low degradation rate device samples of the bulk crystal. Our typical Cz-BBO showed a 0.1 %/H degradation rate, which was better by almost one order of magnitude than two pieces of TSSG-BBO supplied by outside vendors, shown as Fig. 3. We think this suggests a correlation between degradation rate in pulsed operation and UV absorption. The best in-house BBO shows a 0.05 %/H degradation rate, as is shown in Fig. 3.

Fig.2 Optical loss in e-ray polarization. The optical loss of Cz-crystal was a few times better than TSSG-crystal.



Degradation rate :

$$\Delta = \frac{1}{P(0)} \frac{dP(t)}{dt}$$

Cz : 0.1 %/hour  
 Flux : 1.5 %/hour  
 (Linear approximation)

Fig. 3 Degradation rate in the pulsed operation.

### 3. Process

Our device fabrication process is shown Table 1. The most important procedures in this sequence are optical polishing and coating the surfaces .

#### 3.1 Optical polishing

The fabrication of BBO has been thought to be difficult , because of a little deliquescence and a weak cleavage parallel to the c-plane of BBO. In general, the surface scattering loss is proportional to the square of rms. roughness and the inverse square of wavelength , so we had to make a better optical surface for the purpose of devices operating in the UV range than in the VIS and NIR range . We have not only employed a very precise polishing machine and high-quality polishing materials , but also optimized the polishing conditions . We achieved a 0.3 nm rms. roughness super optical surface. We were careful to avoid water and/or moisture from the polished BBO surface during cleaning and drying process.

#### 3.2 Anti-reflection (AR) coating

We successfully coated BBO crystal surfaces which have a small amount of deliquescence.  $\text{HfO}_2$  and  $\text{MgF}_2$  were deposited on the surfaces.  $\text{HfO}_2$  was deposited using Balzers BAP 800 reactive-low-voltage ion plating system [7]. The film deposited by ion plating had little spectral shift and little reflection change under the hot and humid atmosphere.  $\text{MgF}_2$  was deposited using the standard electron beam process. The coating provides less than 0.2 %-total optical loss in a cavity at 532 nm wavelength and has good durability for 900 kW/cm<sup>2</sup> at 532 nm and for 270 W/cm<sup>2</sup> at 266 nm in our system. Optical coating on the BBO crystal surfaces have the function not only as an AR coating but also as a protective layer from a trace of moisture in the air.

<b>Cutting</b>	<b>X-ray Laue Pattern</b>
<b>Direction Correction</b>	<b>Accuracy <math>\pm 0.1</math> deg</b>
<b>Inspection Polishing</b>	<b>rms. Roughness 0.7 nm</b>
<b>Evaluating Bulk Crystal</b>	<b>Homogeneity , Transparency</b>
<b>Dicing to Devices</b>	<b>Accuracy <math>\pm 0.1</math> mm</b>
<b>Polishing</b>	<b>rms. Roughness 0.3 nm</b>
<b>Cleaning and Drying</b>	<b>Water Free</b>
<b>Optical Coating</b>	<b>AR Coating , Ion Plating</b>
<b>Inspection</b>	<b>Outlook , UV Degradation</b>

Table 1 Fabrication process

### 4. Long-term reliability in CW generation

We evaluated 266 nm output power and cavity loss for incident green power. Figure 4 shows a schematic of the BBO evaluation system. The cavity is put into a container, from which all grease is removed. Nitrogen gas is flowed into the container to purge outgas. Long-term reliability data is shown in Fig. 5. 266 nm output power was very stable for over one thousand hours. No optical damage on the crystal surfaces could be found even using a microscope. After 1000 hours operation, 30 mW increasing of the input green power was needed to keep 266 nm output power at 100 mW. This means there was an the increase in the cavity loss for green power. The calculated cavity loss in this experiment is shown in Fig. 6. Total cavity loss for green power was calculated using incident green power into the external resonant BBO cavity and power converted to 266 nm. In this system, it is difficult for green light to be coupled with the cavity, when the cavity loss is more than 0.7%. Considering this value as a criterion , an additional 1000 hours might be expected. Some samples show much small increasing rate of cavity loss. We are measuring these now.

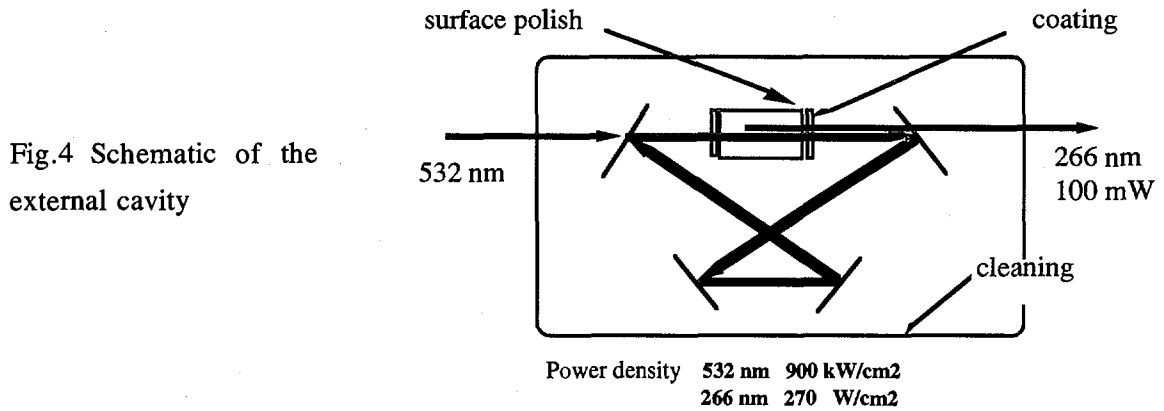


Fig.4 Schematic of the external cavity

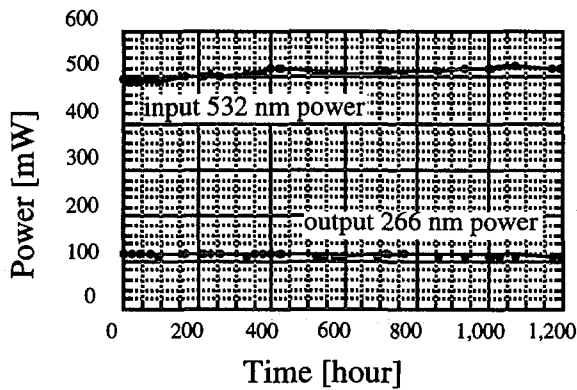


Fig. 5 100 mW, 1000 hours operation of the 266 nm CW laser

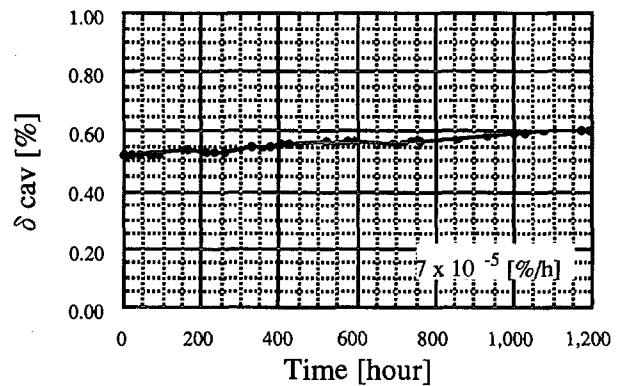


Fig. 6 Total cavity loss vs. operation time of UV generation.

## 5. Summary

We have refined a method of growing Cz-BBO which has low scattering and optical loss. The device fabrication technique and AR coating process suited for BBO have been improved. We operated BBO devices which generated 100 mW UV light for more than 1000 hours.

Hence, an all-solid-state-CW-UV laser system using Cz-grown BBO crystal devices is expected to find many applications.

## 7. References

- [1] M. Oka, L. Y. Liu, W. Wiechmann, Y. Taguchi, H. Wada, T. Okamoto, H. Suganuma and S. Kubota, Proc. SPIE 2700, (1996) 302
- [2] M. Oka, L. Y. Liu, W. Wiechmann, N. Eguchi, and S. Kubota, IEEE J. Sel. Top. in Quantum Electron. 1 (1995) 859
- [3] C. Chen, B. Wu, A. Jiang and G. You, Sci. Sinca (Ser.B) 28 (1985) 235
- [4] K. Itoh, F. Marumo, and Y. Kuwano, J. Crystal Growth 106 (1990) 728-731
- [5] D. Eimerl, L. Davis, and S. Velsko, J. Appl. Phys., 62 (1987) 1968-1983
- [6] Q. Tan, H. Mao, S. Lin, H. Chen, S. Lu, D. Tang, T. Ogawa, J. Crystal Growth 141 (1994) 393-398
- [7] A. J. Waldorf, J. A. Dobrowolski, B. T. Sullivan, and L. M. Plante, Appl. Opt. 32 (1993) 5583

APPENDIX

# Joint ICFA/JAERI-Kansai International Workshop '97

13th Advanced ICFA Beam Dynamics Workshop  
and 1st ICFA Novel and Advanced Accelerator Workshop :  
**the Second Generation Plasma Accelerators**

and

1st JAERI-Kansai International Workshop on  
**Ultrashort-Pulse Ultrahigh-Power Lasers**  
and Simulation for Laser-Plasma Interactions



Kyoto Research Park  
Kyoto, Japan

July 14-18, 1997

organized by

International Committee for Future Accelerators(ICFA)

hosted by

High Energy Accelerator Research Organization(KEK)

and

Japan Atomic Energy Research Institute(JAERI)

Joint ICFA/JAERI-Kansai International Workshop '97  
(July 14-18, Kyoto Research Park, Kyoto, Japan)

				Foyer	Restaurant "Bread Basket"	Science Hall	Room A	Room B	Room C	AV Room		
14-Jul	Registration	8:00 - 9:45	1:45	Registration coffee		(Chairman) K.Nakajima Welcome Address Y. Nishida C. Clayton  (Chairman) D.Umstädter H. Dewa M. Downer F. Amiranoff  (Chairman) W.Gai N.Barov A.M.Koudriavtsev R. Assmann P. Chen  (Chairman) Y.Kitagawa Working group introductory talks and organization						
		9:45 - 10:15	0:30									
	Joint Plenary session (Invited talks)	10:15 - 10:45	0:30									
		10:45 - 11:15	0:30	coffee								
		11:15 - 11:45	0:30									
		11:45 - 12:15	0:30									
		12:15 - 12:45	0:30									
		12:45 - 13:15	0:30									
		13:15 - 14:40	1:25	lunch								
		14:40 - 15:00	0:20									
	15:00 - 15:20	0:20										
	15:20 - 15:40	0:20										
15:40 - 16:00	0:20	coffee										
16:00 - 16:30	0:30											
Reception	18:00 - 20:00	1:30		Reception								
	20:00			Hotel bus								

				Foyer	Restaurant "Bread Basket"	Science Hall	Room A	Room B	Room C	AV Room
15-Jul	ICFA Working groups and JAERI workshop	8:30 - 9:00	0:30	coffee						
		9:00 - 10:30	1:30				ICFA WG-I	ICFA WG-II	ICFA WG-III	JAERI workshop
		10:30 - 11:00	0:30	coffee						
		11:00 - 12:30	1:30				ICFA WG-I	ICFA WG-II	ICFA WG-III	JAERI workshop
		12:30 - 14:00	1:30							
		14:00 - 15:30	1:30	coffee			ICFA WG-I	ICFA WG-II	ICFA WG-III	JAERI workshop
		15:30 - 16:00	0:30							
		16:00 - 17:30	1:30				ICFA WG-I	ICFA WG-II	ICFA WG-III	JAERI workshop
	18:00			Hotel bus						

				Foyer	Restaurant "Bread Basket"	Science Hall	Room A	Room B	Room C	AV Room	
16-Jul	ICFA Working groups and JAERI workshop	8:30 - 9:00	0:30	coffee							
		9:00 - 10:30	1:30				ICFA WG-I	ICFA WG-II	ICFA WG-III	JAERI workshop	
		10:30 - 11:00	0:30	coffee							
		11:00 - 12:30	1:30				ICFA WG-I	ICFA WG-II	ICFA WG-III	JAERI workshop	
	12:30 - 14:00	1:30									
	Joint Plenary session (Invited talks)	14:00 - 14:30	0:30				(Chairman) H.Takuma				
		14:30 - 15:00	0:30				C. Barty K. Yamakawa J.P. Chambaret				
		15:00 - 15:30	0:30	coffee							
		15:30 - 16:00	0:30								
		16:00 - 16:30	0:30								
16:30 - 17:00		0:30									
	17:00 - 17:30	0:30				G. Mourou T. Tajima					
	17:30 -										
										"Gion Festival Eve" Banquet	

				Foyer	Restaurant "Bread Basket"	Science Hall	Room A	Room B	Room C	AV Room
17-Jul		9:00 - 14:00	5:00							"Gion Festival"
	ICFA Working groups and JAERI workshop	14:00 - 15:30	1:30				ICFA WG-I	ICFA WG-II	ICFA WG-III	JAERI workshop
		15:30 - 16:00	0:30	coffee						
		16:00 - 18:05	2:05				ICFA WG-I	ICFA WG-II	ICFA WG-III	JAERI workshop
	18:30			Hotel bus						

				Foyer	Restaurant "Bread Basket"	Science Hall	Room A	Room B	Room C	AV Room
18-Jul	Joint Plenary session	8:30 - 9:00	0:30	coffee						(Chairman) K.Hirata
		9:00 - 10:30	1:30							Report from ICFA working groups
		10:30 - 11:00	0:30							JAERI workshop Summary

## SPECIAL EVENTS

### **1. Welcoming Reception**

Monday, July 14 from 6:00 p.m. to 8:00 p.m. at the restaurant "Bread Basket" in the Kyoto Research Park, Conference site.

It is a great of pleasure for JAERI-Kansai to invite all the workshop attendees and their guests to this event.

### **2. Commemorative Photography**

Wednesday, July 16 at 5:00 p.m. at the gate of the Kyoto Research Park, Conference site.

### **3. Banquet**

Wednesday, July 16 from 6:00 p.m. to 7:00 p.m. at a Japanese style restaurant "ROKUSEI", near Gion, Kyoto.

The bus will leave for Banquet from Conference site at **5:30 p.m.** Attendance at this event is covered in the registration fees. Bringing guest tickets may be purchased for ¥3,000(Yen) per person at the registration desk. After the banquet, everyone can enjoy the Gion Festival Eve and/or the Gion Corner (one of optional tours).

### **4. "Gion Corner" after the Banquet (Optional Tours-1)**

Wednesday, July 16 from 7:40 p.m. at Gion Corner.

After the banquet, the bus will leave for the Gion Corner, 1st Floor of Yasaka Hall, Gion, Kyoto.

This place offers visitors a chance to enjoy traditional Japanese arts such as the tea ceremony, flower arrangement as well as Japanese performance of Bunraku (puppets), Kyo-mai (Kyoto-style dance) of Geisha girls etc.. The entry fee for this tour is ¥2,500 Yen.

### **5. Gion Festival "Yamahoko Junko" (Optional Tours-2)**

Thursday, July 17 in the morning.

The bus will pick up the participator at each hotels (**HOTEL KEIHAN (EL INN) 9:00, NEW MIYAKO HOTEL 9:05, RIHGA ROYAL HOTEL 9:10, GINKAKU 9:15**).

This is the climax of the Gion Festival. A sightseeing of the parade of Yamahoko (decorated traditional floats) at a special gallery is also scheduled on the morning of July 17.

# Joint plenary session

## Monday, July 14

[Science Hall]

- |       |   |       |  |   |
|-------|---|-------|--|---|
| 8:00  | — | 9:45  | [ Registration ]   |   |
|       |   |       | [ Coffee ]   |   |
| 9:45  | — | 11:15 | (Chairman) K.Nakajima  |   |
| 9:45  | — | 10:15 | [Welcome Address]  |   |
| 10:15 | — | 10:45 | Y.Nishida<br>(Utsunomiya U.)                                 | "Plasma Based Cross-Field Particle<br>Acceleration with High Power Microwave"       |
| 10:45 | — | 11:15 | C.Clayton<br>(UCLA)  | "Second Generation Beatwave Experiments<br>at UCLA"                                 |
| 11:15 | — | 11:45 | [ Coffee ]   |   |
| 11:45 | — | 13:15 | (Chairman) D.Umstadter                                       |   |
| 11:45 | — | 12:15 | H.Dewa<br>(JAERI)  | "KEK-JAERI-U.Tokyo Experiments of<br>High Energy Gain Laser Wakefield Acceleration" |
| 12:15 | — | 12:45 | M.Downer<br>(University of Texas)                            | "Laser Wakefield Acceleration Experiments"  |
| 12:45 | — | 13:15 | F.Amiranoff<br>(LULI)  | "The Laser Wakefield Program at<br>Ecole Polytechnique"                             |
| 13:15 | — | 14:40 | [ Lunch ]  |   |
| 14:40 | — | 15:00 | (Chairman) W.Gai   |   |
| 14:40 | — | 15:00 | N.Barov<br>(UCLA)  | "The UCLA/ANL Plasma Wakefield Experiment"  |
| 15:00 | — | 15:20 | A.M.Koudriavtsev<br>(Budker Institute of<br>Nuclear Physics) | "Plasma Wake-Field Acceleration for<br>High Energies: Physics and Perspectives"     |
| 15:20 | — | 15:40 | R.Assmann<br>(SLAC)  | "Proposal for a 1GeV Plasma-Wakefield<br>Acceleration Experiment at SLAC"           |
| 15:40 | — | 16:00 | P.Chen<br>(SLAC)   | "Proposal for a FFTB Plasma Lens Experiment<br>at SLAC"                             |
| 16:00 | — | 16:30 | [ Coffee ]   |   |
| 16:30 | — | 18:00 | (Chairman) Y.Kitagawa  |   |
| 16:30 | — | 18:00 | Working Group Introductory Talks and Organization            |   |
| 18:00 | — | 20:00 | [ Reception ]  |   |

# Joint plenary session

## Wednesday, July 16

[Science Hall]

14:00	—	17:00	(Chairman)	H.Takuma	
14:00	—	14:30	C.Barty	" From T-cubed to U-cubed: The Evolution of Ultrafast, Ultrabright, Ultrapowerful Amplification Systems"	
14:30	—	15:00	K.Yamakawa	" Development of an Ultrahigh Brightness Laser Source at JAERI"	
15:00	—	15:30	J.P.Chambaret	" Towards Ultra-high Peak Power with Femtosecond Laser at High Repetition Rate"	
15:30	—	16:00	[ Coffee ]		
16:00	—	16:30	G.Mourou	"Ultrahigh Peak Power Laser for Particle Acceleration : Present and Future"	
16:30	—	17:00	T.Tajima	"High Field Science"	

# Joint plenary session

**Friday, July 18**

[AV ROOM]

8:30 - 9:00 [Coffee]

9:00 - 11:00 (Chairman) K.Hirata  
9:00 - 10:30 "Report from ICFA working groups"

10:30 - 11:00 T.Arisawa (JAERI) "JAERI workshop Summary"

First JAERI-Kansai International Workshop  
on  
Ultrashort-Pulse Ultrahigh-Power Lasers  
and Simulations for Laser-Plasma Interactions

14 to 18 July 1997  
Kyoto Research Park  
Kyoto, JAPAN

**organized by International Committee for Future Accelerators (ICFA)  
hosted by High Energy Accelerator Research Organization (KEK)  
and Japan Atomic Energy Research Institute (JAERI)**

**joined by  
13th Advanced ICFA Beam Dynamics Workshop  
and 1st ICFA Novel and Advanced Accelerator Workshop:  
the Second Generation Plasma Accelerators**

as

*Joint ICFA/JAERI-Kansai International Workshop '97*

## JAERI workshop

Tuesday, July 15

[AV ROOM]

8:30	—	9:00	[ Coffee ]	
9:00	—	10:30	(Chairman)	K.Mima
9:00	—	9:30	Y.Kurihara (KEK)	"Polarized Positron Generation for JLC using a High Power Pico-second CO <sub>2</sub> Laser System"
9:30	—	10:00	J.MENDONCA (INSTITUTE SUPERIOR TECNICO)	"Recent Result on Photon Acceleration"
10:00	—	10:30	I.Pogorelsky (BNL)	"Staged Electron Laser Accelerator STELLA Experiment at Brookhaven ATF"
10:30	—	11:00	[ Coffee ]	
11:00	—	12:30	(Chairman)	R.More
11:00	—	11:30	Y.Ueshima (JAERI)	"Simulation of Intense Laser and Dense Matter Interactions - X ray Generation and Laser absorption -"
11:30	—	12:00	A.ANDREEV (Visiting Prof. in ILE Osaka U.)	"Scattering and Absorption of Multy TW Picosecond Laser Pulse by Solid Targets"
12:00	—	12:30	K.Mima (ILE, Osaka U.)	"Intense Short Pulse Propagation and Interactions in Overdense Plasmas"
12:30	—	14:00	[ Lunch ]	
14:00	—	15:30	(Chairman)	M.Skoric
14:00	—	14:30	H.Takabe (ILE, Osaka U.)	"Integrated Code Development for Studying Laser Driven Plasma Physics"
14:30	—	15:00	K.Nishihara (Osaka U.)	"3d Particle Simulations on Ultra Short Laser Interaction"
15:00	—	15:30	T.Zolotoukhina (AIST)	"Energy Transfer in the Process of Diatomic-Surface Collision"
15:30	—	16:00	[ Coffee ]	
16:00	—	17:30	(Chairman)	K.Nishihara
16:00	—	16:30	K.Moribayashi (JAERI)	"Ultrafast Atomic Process in X-ray Emission by Inner-shell Ionization". Kengo Moribayashi, Akira Sasaki, and Toshiki Tajima
16:30	—	17:00	M.Skoric (Vinca Institute /JAERI)	"Stimulated Raman Back-scattering at High Laser Intensities"
17:00	—	17:30	T.Utsumi (JAERI)	"Plasma Simulation with the Differential Algebraic-CIP Scheme"

## JAERI workshop

Wednesday, July 16

[AV ROOM]

- 8:30 - 9:00 [ Coffee ]
- 9:00 - 10:30 (Chairman) J.Koga  
 9:00 - 9:30 J.Chihara "Correlations in a Partially Degenerate  
 (JAERI) Electron Plasma"
- 9:30 - 10:00 T.Kato "Time Dependent H-like and He-like  
 (NIFS) Al Lines Produced by Ultra-Short Pulse Laser"
- 10:00 - 10:30 R.More "Theory and Simulation of Short-Pulse Laser  
 (Lawrence Livermore Interactions". R.More, R.Walling, D.Price,  
 National Laboratory) G.Guethlein, A.Osterheld, J.Dunn and  
 R.Stewart
- 10:30 - 11:00 [ Coffee ]
- 11:00 - 12:30 (Chairman) H.Takabe  
 11:00 - 11:30 A.Sasaki "Modeling of collisional excited X-ray lasers  
 (JAERI) using short pulse laser pumping"
- 11:30 - 12:00 Y.Kishimoto "Cluster Plasma and its Linear and Nonlinear  
 (JAERI) Properties"
- 12:00 - 12:30 S.Peng "Design of Optimal Array Processors for  
 (Aizu U.) Division-Free Linear System Solving"
- 12:30 - 14:00 [ Lunch ]

## JAERI workshop

Thursday, July 17

[AV ROOM]

- 9:00 - 14:00 [ Gion Festival ]
- 14:00 - 15:40 (Chairman) T.Matoba
- 14:00 - 14:25 T.Itoh (JAERI) "Numerical Simulation For Extremely Chirped Pulse Using An Optical Fiber"
- 14:25 - 14:50 I.Pogorelsky (BNL) "Emerging Terawatt Picosecond CO<sub>2</sub> Laser Technology"
- 14:50 - 15:15 S.Biswal (University of Michigan) "Chirped Pulse Amplification in a Ytterbium glass Regenerative Amplifier"
- 15:15 - 15:40 A.Nishimura (JAERI) "Flashlamp Pumped Ti:S Free-Running Laser for Ytterbium Glass CPA"
- 15:40 - 16:00 [ Coffee ]
- 16:00 - 18:05 (Chairman) G.Mourou
- 16:00 - 16:25 S.Matsuoka (JAERI) "Efficient and High Energy Ti:Sapphire Amplifiers for Ultra-Short Pulse Amplification". Shinichi Matsuoka, Makoto Aoyama, Koichi Yamakawa
- 16:25 - 16:50 Y.Maruyama (JAERI) "R&D of LD-Pumped High Average Power Solid-State Laser for the Pumping of High Average Power Ti:sapphire CPA system"
- 16:50 - 17:15 S.Harayama (JAERI) "Development of All Solid-State, High Average Power Ultra-Short Pulse Laser for X-ray Generation"
- 17:15 - 17:40 S.Konno (Mitsubishi Electric Corporation Advanced Research R&D Center) "80W-cw-TEM<sub>00</sub> IR Beam Generation by Use of a Laser-Diode-Side-Pumped Nd:YAG Rod Laser". Susumu Konno, Shuichi Fujikawa, and Koji Yasui
- 17:40 - 18:05 N.Umezu (SONY Corp. Research Center) "Reliability of a Czochralski-Grown  $\beta$ -BaB<sub>2</sub>O<sub>4</sub> Crystal"

**13th Advanced ICFA Beam Dynamics Workshop  
and 1st ICFA Novel and Advanced Accelerator Workshop:  
*the Second Generation Plasma Accelerators***

**14 to 18 July 1997**

**Kyoto Research Park**

**Kyoto, JAPAN**

organized by International Committee for Future Accelerators (ICFA)  
hosted by High Energy Accelerator Research Organization (KEK)  
and Japan Atomic Energy Research Institute (JAERI)

joined by  
1st JAERI Workshop on Ultrashort-Pulse Ultrahigh-Power Lasers  
and Simulations for Laser-Plasma Interactions

as

***Joint ICFA/JAERI-Kansai International Workshop '97***

## Program

July 14 (Mon)

800-945 registration

945-1115 K.Nakajima, chairman

945-1015 welcome

Hirata(ICFA), Amiranoff(ICFA), Ohno(JAERI)

1015-1045 Y. Nishida(Utsunomiya U. ) Plasma Based Cross-Field Particle Acceleration  
with High Power Microwave

1045-1115 C. Clayton(UCLA) Second Generation Beatwave Experiments at UCLA

1115-1145 coffee

1145-1315 D.Umstadter, chairman

1145-1215 H. Dewa(JAERI) KEK-JAERI-U.Tokyo Experiments of High Energy Gain  
Laser Wakefield Acceleration

1215-1245 M. Downer(U.Texas, Austin) Laser Wakefield Acceleration Experiments

1245-1315 F. Amiranoff(LULI) The Laser Wakefield Program at Ecole Polytechnique

1315-1440 lunch

1440-1600 W.Gai, chairman

1440-1500 N.Barov(UCLA) The UCLA/ANL Plasma Wakefield Experiment

1500-1520 A.M.Kudryavtsev(BINP) Plasma Wake-Field Acceleration for High  
Energies: Physics and Perspectives

1520-1540 R. Assmann(SLAC) Proposal for a 1GeV Plasma-Wakefield Acceleration  
Experiment at SLAC

1540-1600 P. Chen(SLAC) Proposal for a FFTB Plasma Lens Experiment at SLAC

1600-1630 coffee

1630-1800 Y. Kitagawa, chairman

introductory talks by working group chairmen (J.Rosenzweig, T.Katsouleas, T.Tajima)

July 15 (Tue)-17 (Thu)

Working Group Sessions

Group I injection and dynamics of accelerated beams,  
chaired by K. Yokoya, and J.Rosenzweig

Group II dynamics of plasma-wave drivers (lasers in LWFA and beams in PWFA) and plasmas  
chaired by T. Katsouleas and K.Nakajima

Group III near-term and far-term applications of plasma accelerators  
chaired by T.Tajima and P.Chen

July 18 (Fri)

900-1030 H.Hirata, chairman

Working Group Summary Reports and Closing

to be followed by JAERI Workshop Summary

## Proposed Talks at the Working Group Sessions

*If you want to make talks in addition to those listed below,  
(or if you find anything wrong in the list),  
please contact the working group chairmen,  
preferably within July 14, Monday.*

### Group I

- D.Bernard: Electron Capture in the Laser Wake-Field Acceleration Experiment
- R.Hemker: Cathodeless, High Brightness Electron Beam Production by Multiple Laser Pulses in Plasmas
- N.Kirihara:  $V_p \times B$  Electron Linear Accelerator with TE-wave Assisted by Plasma for Beam stabilization
- F.Pegoraro: Nonlinear Electrodynamics of the Interaction of Ultraintense Laser Pulses with a Thin Foil
- M.Uesaka: Femtosecond Electron Injection for Laser Wakefield Acceleration
- D.Umstadter: Laser Injection and Wakefield Acceleration in a Guided Channel
- X.Wang: Femto-Second Micro-bunched Electron Beam Generation using IFEL

### Group II

- N.Andreev: The Problems of Laser Wake Field Acceleration in Plasma Channels
- S.Bulanov: Variety of Nonlinear Wave-Breaking
- P.Chen: Laser Pulse Shaping and the Laser-Plasma Coupling Efficiency
- M.Downer : Lasers for Accelerators
- W.Gai: High Current Electron Drive Beam for Plasma Wakefield Acceleration
- H.Hojo: Particle Acceleration by Subcycle Laser Pulses
- J.Koga/Y.Kishimoto: Simulation of Short Pulse Laser Propagation and Wake Field Generation Including Ionization and Polarization Effects
- K.Lotov: Simulation of Ultrarelativistic Beam Dynamics in Plasma Wake-Field Accelerator
- M.Mori: Ultra Intense Glass Laser System and Laser-Plasma Interactions
- K.Nakajima: Developments of Laser Wakefield Accelerators at JAERI-Kansai
- R.Sugihara : Electron Acceleration by Two Colinear, Overlapping Laser Beams
- L.Tsintsadze: Nonlinear Wakefields in an Electron-Positron-Ion Plasma

Group III

D.Bernard: One GeV Acceleration with Laser Wake-Field in the Linear Regime

P.Chen: Testing Unruh Radiation in Plasma Wavefronts

I.Pogorelsky : Prospects for LWFA and electron-positron colliders using CO<sub>2</sub> laser drivers

A.Ogata : Laser/Plasma Accelerator in Terminology of RF Linac

T.Tajima : Laser Collider at a Quantum Operating Regime

Joint ICFA/JAERI-Kansai International Workshop '97  
July 14 - 18, 1997

List of the Registrants(106) and Participants(106)

○ : Registrants  
● : Participants

<u>Name</u>	<u>Affiliation</u>
<b>A</b>	
○ ● Akahane, Yutaka	JAERI, JAPAN
○ ● Amiranoff, Francois	LULI, FRANCE
○ ● ANDREEV, Alexandre A.	Visiting Prof. in ILE Osaka U., JAPAN
○ ● Andreev, Nikolai E.	HEDRC of RAS, RUSSIA
○ ● Arisawa, Takashi	JAERI, JAPAN
○ ● Assmann, Ralph W.	SLAC, U. S. A.
<b>B</b>	
○ ● Barov, Nikolai	ANL, U. S. A.
○ ● Barty, Christopher P. J.	Univ. California, San Diego, U. S. A.
○ ● Bernard, Denis	LPNHE, Ecole Polytechnique, FRANCE
○ ● Biswal, Subrat	University of Michigan,
○ ● Bulanov, Sergei V.	General Phys. Inst. , Moscow, RUSSIA
<b>C</b>	
○ ● CHAMBARET, Jean - Paul	LOA - ENSTA, FRANCE
○ ● Chen, Pisin	SLAC, U. S. A.
○ ● Chihara, Jyunzo	JAERI, JAPAN
○ ● Clayton, Chris	UCLA, U. S. A.
<b>D</b>	
○ ● Dewa, Hideki	JAERI, JAPAN
○ ● Downer, Mike	University of Texas , U. S. A.
<b>E</b>	
○ ● Endo, Akira	SHI, JAPAN
<b>F</b>	
○ ● Ferrario, Massimo	INFN-LNF, ITALY
<b>G</b>	
○ ● Gai, Wei	ANL, U. S. A.
<b>H</b>	
○ ● Harayama, Sayaka	JAERI, JAPAN
○ ● Hatsuda, Yoshio	NEC G&E Div,
○ ● Hemker, Roy G	UCLA, U. S. A.
○ ● Hirata, Kohji	KEK, JAPAN
○ ● Hizanidis, Kyriakos	NATIONAL TECHNICAL UNIVERSITY OF ATHENS, GREECE
○ ● Hojo, Hitoshi	Tsukuba U. , JAPAN
<b>I</b>	
○ ● Ihara, Hitoshi	JAERI, JAPAN
○ ● Iizumi, Masashi	JAERI, JAPAN
○ ● Ikegami, Masanori	NSRF, ICR, Kyoto U. , JAPAN
○ ● Inoue, Makoto	Kyoto U. , JAPAN
○ ● Itoh, Tamitake	JAERI, JAPAN
<b>K</b>	
○ ● Kando, Masaki	Kyoto U. /JAERI, JAPAN
○ ● Kato, Takako	NIFS, JAPAN
○ ● Katsouleas, Thomas C.	Univ. Southern California ,Dept. EE-Electrophysics, U. S. A.
○ ● Kawachi, Tetsuya	RIKEN, JAPAN
○ ● Kawanishi, Shun-ichi	JAERI, JAPAN
○ ● Kirihara, Naotoshi	Utsunomiya U. , JAPAN
○ ● Kishimoto, Yasuaki	JAERI, JAPAN
○ ● Kobayashi, Katsuyuki	Femtosecond Technology Research Association, JAPAN
○ ● Koga, James	JAERI, JAPAN
○ ● Konno, Susumu	Mitsubishi Electric Corporation Advanced Research R&D Center, JAPAN
○ ● Kotaki, Hideyuki	JAERI, JAPAN
○ ● Koudriavtsev, Andrey M.	Budker Institute of Nuclear Physics , RUSSIA
○ ● Koyama, Kazuyoshi	JAPAN
○ ● Kumada, Masayuki	NIRS, JAPAN
○ ● Kurihara, Yoshimasa	KEK, JAPAN
○ ● Kuroda, Hiroto	Institute for Solid State Physics, Univ. of Tokyo, JAPAN
<b>L</b>	
○ ● Lotov, Konstantin V.	Budker Institute of Nuclear Physics , RUSSIA
<b>M</b>	
○ ● Maruyama, Tomoyuki	JAERI, JAPAN

- ● Maruyama, Yoichiro JAERI, JAPAN
- ● Matoba, Tooru JAERI, JAPAN
- ● Matsuoka, Shinichi JAERI, JAPAN
- ● Matsushima, Isao ETL, JAPAN
- ● MENDONCA, J. T. INSTITUTE SUPERIOR TECNICO, PORTUGAL
- ● MIGUS, Arnold LULI, FRANCE
- ● Mima, Kunioki ILE, Osaka U., JAPAN
- ● More, Richard Lawrence Livermore National Laboratory, U. S. A.
- ● Mori, Michiaki ILE, Osaka U., JAPAN
- ● Mori, Warren B. UCLA, U. S. A.
- ● Moribayashi, Kengo JAERI, JAPAN
- ● Mourou, Gerald U. Michigan, U. S. A.
- N**
- ● Naito, Kenta NISSIN ELECTRIC CO. LTD, JAPAN
- ● Nakajima, Kazuhisa KEK, JAPAN
- ● Nakanishi, Hiroshi KEK, JAPAN
- ● Nakano, Masafumi JAERI, JAPAN
- ● Nees, John University of Michigan, U. S. A
- ● Nishida, Yasushi Utsunomiya U., JAPAN
- ● Nishihara, Katsunobu Osaka U., JAPAN
- ● Nishimura, Akihiko JAERI, JAPAN
- ● Noda, Akira Kyoto U., JAPAN
- O**
- ● Ogata, Atsushi KEK, JAPAN
- ● Ohno, Hideo JAERI, JAPAN
- ● Okamoto, Hiromi Kyoto U., JAPAN
- P**
- ● Pegoraro, Francesco University of Pisa, ITALY
- ● Peng, Shietung Aizu U., JAPAN
- ● Petracca, Stefania University of Salerno/Canon Fellow, ITALY
- ● Pogorelsky, Igor BNL, U. S. A.
- R**
- ● Rosenzweig, James B. UCLA, U. S. A.
- ● Rousse, Antoine LOA - ENSTA, FRANCE
- ● Ruhl, Hartmut Post Doc. /ILE, Osaka U., JAPAN
- S**
- ● Sakai, Jun-ichi Toyama U., JAPAN
- ● Sasaki, Akira JAERI, JAPAN
- ● Sasuga, Tsuneo JAERI, JAPAN
- ● Sentoku, Yasuhiko Student/Osaka U., JAPAN
- ● Shadwick, Brad Physics Department, University of California at Berkeley, U. S. A
- ● Skoric, Milos M. Vinca Institute /JAERI, Yugoslavia
- ● Sugihara, Ryo Nagoya U., JAPAN
- ● Sugiyama, Akira JAERI, JAPAN
- T**
- ● Tajima, Toshiki UT Austin/JAERI, U. S. A.
- ● Takabe, Hideaki ILE, Osaka U., JAPAN
- ● Takuma, Hiroshi JAERI, JAPAN
- ● Tani, Keiji NASDA, JAPAN
- ● Tsintsadze, Levan ILE, Osaka U., JAPAN
- ● Tsuchida, Noboru JAERI, JAPAN
- ● Tsunemi, Akira BNL, U. S. A.
- U**
- ● Uesaka, Mitsuru NERL, U. Tokyo, JAPAN
- ● Ueshima, Yutaka JAERI, JAPAN
- ● Umezu, Nobuhiko SONY Corp. Research Center, JAPAN
- ● Umstadter, Donald U. Michigan, U. S. A
- ● Utsumi, Takayuki JAERI, JAPAN
- W**
- ● Wang, Xijie ATF/BNL, U. S. A.
- ● Washio, Masakazu SHI, JAPAN
- Y**
- ● Yamakawa, Koichi JAERI, JAPAN
- ● Yamanaka, Chiyoe Institute for Laser Technology, JAPAN
- ● Yokoya, Kaoru KEK, JAPAN
- ● Yoshida, Norimasa Toshiba Co., JAPAN
- ● Yoshikawa, Hiroshi JAERI, JAPAN
- ● Yugami, Noboru Utsunomiya U., JAPAN
- Z**
- ● Zolotoukhina, Tatiana N. AIST, JAPAN

## Author Index

<b>A</b>			
Akaoka, Katsuaki	JAERI		22
Andreev, A.A.	Vavilov State Optical Institute		4
Arisawa, Takashi	JAERI	19 21	22
<b>B</b>			
Babzien, M.	BNL		2
Ben-Zvi, I.	SUNY at Stony Brook		2
Biswal, Subrat	Univ. Michigan	18	19
<b>C</b>			
Camino, F.	SUNY at Stony Brook		2
Chihara, Junzo	JAERI		10
Cline, D.B.	UCLA		2
<b>D</b>			
Dias, J.M.	Institute Superior Tecnico		1
Downer, Mike.C.	Univ. of Texas		14
<b>E</b>			
Erickson, Edward	EEA		19
<b>F</b>			
Fiorito, R.B.	NSWC		2
Fujikawa, Shuichi	Advanced Technology R&D Center, Mitsubishi Electric Corporation		23
Fukui, Tatsuo	Research Center, Sony Corporation		24
<b>G</b>			
Gallardo, J.C.	BNL		2
Gottschalk, S.C.	STI Optronics Inc.		2
Graziani, Frank	LLNL		12
Guethlein, Gary	LLNL		12
<b>H</b>			
Harayama, Sayaka	JAERI	21	22
He, P.	UCLA		2
<b>I</b>			
Itoh, Tamitake	JAERI		16
<b>J</b>			
Jovanovic, Moma	Univ. of Nis		8
<b>K</b>			
Kato, Masaaki	JAERI	21	22
Kato, Masatoshi	NIFS		11
Kato, Takako	NIFS		11
Kimura, W.D.	STI Optronics Inc.		2
Kishimoto, Yasuaki	JAERI	3	14
Kondo, Kenji	Research Center, Sony Corporation		24
Konno, Susumu	Advanced Technology R&D Center, Mitsubishi Electric Corporation		23
Kubota, Shigeo	Research Center, Sony Corporation		24
Kusche, K.P.	BNL/STI Optronics Inc.		2
<b>L</b>			
Levatin, Joann	LLNL		12
Libby, Steven	LLNL		12
Liu, Y.	UCLA		2
<b>M</b>			
Maluckov, Aleksandra	Univ. of Nis		8

Maruyama, Yoichiro	JAERI	19	21	22
Matoba, Tohru	JAERI	16	21	22
Matsuoka, Shinichi	JAERI			20
Mendonca, J.T.	Institute Superior Tecnico			1
Mima, Kunioki	ILE, Osaka Univ.			5
More, Richard	LLNL	11	12	
Moribayashi, Kengo	JAERI	7	13	
Morita, Ryuji	Hokkaido Univ.			16
Mourou, Gerard	Univ. Michigan	18	19	
<b>N</b>				
Nagatomo, Hideo	ILE, Osaka Univ.			5
Naruo, Syuji	ILE, Osaka Univ.			5
Nees, John	Univ. Michigan	18	19	
Nishihara, Katsunobu	ILE, Osaka Univ.			6
Nishimura, Akihiko	JAERI	16	18	19
Niwa, Yoshito	JAERI		21	22
<b>O</b>				
Oba, Masaki	JAERI			21
Ohnishi, Naofumi	ILE, Osaka Univ.			5
Ohzu, Akira	JAERI			19
Okamoto, Takashi	ILE, Osaka Univ.			6
Okamoto, Tsutomu	Research Center, Sony Corporation			24
Osterheld, Al	LLNL			11
Owada, Susumu	RASEL			19
<b>P</b>				
Pantell, R.H.	Stanford Univ.			2
Pastwick, L.J.	STI Optronics Inc.			2
Peng, Shietung	Univ. of Aizu			15
Platonov, K.Yu.	Vavilov State Optical Institute			4
Pogorelsky, I.V.	BNL	2	17	
Price, Dwight	LLNL			12
<b>Q</b>				
Quimby, D.C.	STI Optronics Inc.			2
<b>R</b>				
Robinson, K.E.	STI Optronics Inc.			2
Rule, D.W.	NSWC			2
<b>S</b>				
Sandweiss, J.	Yale Univ.			2
Sasaki, Akira	JAERI	3	7	8 13
Satou, Sousuke	RASEL			19
Sedukhin, Igor	Hiwada Electronic Corp.			15
Sedukhin, Stanislav	Univ. of Aizu			15
Sentoku, Yasuhiko	ILE, Osaka Univ.			3
Shepherd, Ronnie	LLNL			11
Silva, L.O.	Institute Superior Tecnico / UCLA			1
Skaritka, J.	BNL			2
Skoric, Milos.M.	Vinca Institute			8
Steinhauser, L.C.	STI Optronics Inc.			2
Stewart, Rick	LLNL			12
Sugiyama, Akira	JAERI			19
Sunahara, Atsusi	ILE, Osaka Univ.			5

<b>T</b>						
Tajima, Toshiki	JAERI/Univ. of Texas	3	7	8	13	14
Takabe, Hideaki	ILE, Osaka Univ.					5
Takuma, Hiroshi	JAERI	16	18	19	21	22
Tanaka, K.A.	ILE, Osaka Univ.					4
Tatsuki, Kouichi	Research Center, Sony Corporation					24
Tei, Kazuyoku	JAERI			16	21	22
<b>U</b>						
Ueshima, Yutaka	JAERI					3
Umezu, Nobuhiko	Research Center, Sony Corporation					24
Utsumi, Takayuki	JAERI			9	13	
<b>V</b>						
vanSteenbergen, A.	BNL					2
<b>W</b>						
Wada, Hiroyuki	Research Center, Sony Corporation					24
Walling, Rosemary	LLNL					12
<b>Y</b>						
Yakimenko, V.	BNL					2
Yamakawa, Koichi	JAERI					20
Yamashita, Mikio	Hokkaido Univ.					16
Yasui, Hidekazu	ILE, Osaka Univ.					6
Yasui, Koji	Advanced Technology R&D Center, Mitsubishi Electric Corporation					23
Young, Bruce	LLNL					11

## Keyword Index

<b>A</b>	
Adaptive optics	22
All-solid-state CW UV laser	24
Anomalous absorption	8
Array processors	15
Atomic kinetics	13
Atomic models	12
Atomic structure	10
<b>B</b>	
BBO	24
Boltzmann equation	9
Bremsstrahlung emission	3
<b>C</b>	
Carbon atom	7
Chirped pulse	16
Chirped pulse amplification (CPA)	18 19 20 22
Cluster plasma	14
Czochralski	24
<b>D</b>	
Degenerate electron plasma	10
Dense plasma	6
Dependence analysis	15
Differential Algebraic CIP scheme	9
<b>E</b>	
Electric conductivity	6
<b>F</b>	
Flashlamp pumping	19
Free running	19
<b>G</b>	
Grain narrowing	20
Grain saturation	20
<b>H</b>	
H and He-like Al spectra	11
High energy storage density laser materials	18
High intensity short pulse X-ray emission	7
High peak power laser	22
High power laser	14
Hollow fiber	16
<b>I</b>	
Implosion	5
Inhomogeneous plasma	4
Inner-shell ionization	7
Inner-shell X-ray laser	3
Integrated code	5
Ionization	10 11
<b>L</b>	
Larmor radiation	3
Laser diode	21
Laser fusion	5
Laser interaction	12

Laser plasma	8
Laser produced plasma	13
Laser scanning tomography	24
LD-pumped laser	22
Linear systems	15
Liquid metal	10
<b>M</b>	
Master oscillator power amplifier	21
Multi-pass amplification	22
<b>N</b>	
Nd:YAG	21
Nonlinear crystal	21
Nonlinear fiber	16
Nonlinear propagation	16
Non-LTE atomic kinetics	12
Numerical algorithms	15
<b>O</b>	
Optical properties	12
<b>P</b>	
Particle-in cell simulation	14
Petawatt laser	18
Photolithography	24
Plasma	10
Polarization mode	14
Pulse stretcher	16
<b>R</b>	
Radial distribution function	10
Rayleigh-Taylor instability	5
Recombination	11
Regenerative pulse shaping	20
Resonant absorption	4
Rezoning	5
<b>S</b>	
2-D ALE code	5
Self focusing	6
Short laser pulse	4
Short-pulse intense X-ray	3
Short-pulse ultra high intensity laser	3
Stimulated Raman scattering	8
Stochastic motion	14
Surface mode	14
Symmetric split-step Fourier method	16
Systolic processing	15
<b>T</b>	
Ti:sapphire	19
Time evolution of X-ray	11
Top seeded solution growth	24
<b>U</b>	
Ultra fast atomic process	7
Ultra short pulse	6
Ultra short pulse laser	22

Ultra-short pulse	12
Ultra-short pulse laser	11
<b>V</b>	
Vlasov equation	9
<b>W</b>	
Wavefront compensation	22
<b>X</b>	
X-ray generation	14
X-ray laser	7 13
X-ray lasers	8
<b>Y</b>	
Ytterbium glass	18 19
<b>Z</b>	
Zigzag slab crystal	21

# 国際単位系 (SI) と換算表

表1 SI基本単位および補助単位

量	名称	記号
長さ	メートル	m
質量	キログラム	kg
時間	秒	s
電流	アンペア	A
熱力学温度	ケルビン	K
物質質量	モル	mol
光度	カンデラ	cd
平面角	ラジアン	rad
立体角	ステラジアン	sr

表2 SIと併用される単位

名称	記号
分, 時, 日	min, h, d
度, 分, 秒	°, ', "
リットル	l, L
トン	t
電子ボルト	eV
原子質量単位	u

1 eV=1.60218×10<sup>-19</sup>J  
1 u=1.66054×10<sup>-27</sup>kg

表5 SI接頭語

倍数	接頭語	記号
10 <sup>18</sup>	エクサ	E
10 <sup>15</sup>	ペタ	P
10 <sup>12</sup>	テラ	T
10 <sup>9</sup>	ギガ	G
10 <sup>6</sup>	メガ	M
10 <sup>3</sup>	キロ	k
10 <sup>2</sup>	ヘクト	h
10 <sup>1</sup>	デカ	da
10 <sup>-1</sup>	デシ	d
10 <sup>-2</sup>	センチ	c
10 <sup>-3</sup>	ミリ	m
10 <sup>-6</sup>	マイクロ	μ
10 <sup>-9</sup>	ナノ	n
10 <sup>-12</sup>	ピコ	p
10 <sup>-15</sup>	フェムト	f
10 <sup>-18</sup>	アト	a

表3 固有の名称をもつSI組立単位

量	名称	記号	他のSI単位による表現
周波数	ヘルツ	Hz	s <sup>-1</sup>
力	ニュートン	N	m·kg/s <sup>2</sup>
圧力, 応力	パスカル	Pa	N/m <sup>2</sup>
エネルギー, 仕事, 熱量	ジュール	J	N·m
工率, 放射束	ワット	W	J/s
電気量, 電荷	クーロン	C	A·s
電位, 電圧, 起電力	ボルト	V	W/A
静電容量	ファラド	F	C/V
電気抵抗	オーム	Ω	V/A
コンダクタンス	ジーメンズ	S	A/V
磁束	ウェーバ	Wb	V·s
磁束密度	テスラ	T	Wb/m <sup>2</sup>
インダクタンス	ヘンリー	H	Wb/A
セルシウス温度	セルシウス度	°C	
光強度	ルーメン	lm	cd·sr
照射線量	ルクス	lx	lm/m <sup>2</sup>
放射線量	ベクレル	Bq	s <sup>-1</sup>
吸収線量	グレイ	Gy	J/kg
線量等量	シーベルト	Sv	J/kg

表4 SIと共に暫定的に維持される単位

名称	記号
オングストローム	Å
バ	b
バル	bar
ガリ	Gal
キュリー	Ci
レントゲン	R
ラド	rad
レム	rem

1 Å=0.1nm=10<sup>-10</sup>m  
1 b=100fm<sup>2</sup>=10<sup>-28</sup>m<sup>2</sup>  
1 bar=0.1MPa=10<sup>5</sup>Pa  
1 Gal=1cm/s<sup>2</sup>=10<sup>-2</sup>m/s<sup>2</sup>  
1 Ci=3.7×10<sup>10</sup>Bq  
1 R=2.58×10<sup>-4</sup>C/kg  
1 rad=1cGy=10<sup>-2</sup>Gy  
1 rem=1cSv=10<sup>-2</sup>Sv

(注)

- 表1-5は「国際単位系」第5版, 国際度量衡局1985年刊行による。ただし, 1 eVおよび1 uの値はCODATAの1986年推奨値によった。
- 表4には海里, ノット, アール, ヘクタールも含まれているが日常の単位なのでここでは省略した。
- barは, JISでは流体の圧力を表わす場合に限り表2のカテゴリーに分類されている。
- E C閣僚理事会指令では bar, barnおよび「血圧の単位」mmHgを表2のカテゴリーに入れている。

## 換 算 表

力	N(=10 <sup>5</sup> dyn)	kgf	lbf
	1	0.101972	0.224809
	9.80665	1	2.20462
	4.44822	0.453592	1

粘 度 1 Pa·s(N·s/m<sup>2</sup>)=10 P(ポアズ)(g/(cm·s))

動粘度 1 m<sup>2</sup>/s=10<sup>4</sup>St(ストークス)(cm<sup>2</sup>/s)

圧	MPa(=10bar)	kgf/cm <sup>2</sup>	atm	mmHg(Torr)	lbf/in <sup>2</sup> (psi)
	1	10.1972	9.86923	750062×10 <sup>3</sup>	145.038
力	0.0980665	1	0.967841	735.559	14.2233
	0.101325	1.03323	1	760	14.6959
	1.33322×10 <sup>-4</sup>	1.35951×10 <sup>-3</sup>	1.31579×10 <sup>-3</sup>	1	1.93368×10 <sup>-2</sup>
	6.89476×10 <sup>-3</sup>	7.03070×10 <sup>-2</sup>	6.80460×10 <sup>-2</sup>	51.7149	1

エネルギー・仕事・熱量	J(=10 <sup>7</sup> erg)	kgf·m	kW·h	cal(計量法)	Btu	ft·lbf	eV
	1	0.101972	2.77778×10 <sup>-7</sup>	0.238889	9.47813×10 <sup>-4</sup>	0.737562	6.24150×10 <sup>18</sup>
	9.80665	1	2.72407×10 <sup>-6</sup>	2.34270	9.29487×10 <sup>-3</sup>	7.23301	6.12082×10 <sup>19</sup>
	3.6×10 <sup>6</sup>	3.67098×10 <sup>5</sup>	1	8.59999×10 <sup>5</sup>	3412.13	2.65522×10 <sup>6</sup>	2.24694×10 <sup>25</sup>
	4.18605	0.426858	1.16279×10 <sup>-6</sup>	1	3.96759×10 <sup>-3</sup>	3.08747	2.61272×10 <sup>19</sup>
	1055.06	107.586	2.93072×10 <sup>-4</sup>	252.042	1	778.172	6.58515×10 <sup>21</sup>
	1.35582	0.138255	3.76616×10 <sup>-7</sup>	0.323890	1.28506×10 <sup>-3</sup>	1	8.46233×10 <sup>18</sup>
	1.60218×10 <sup>-19</sup>	1.63377×10 <sup>-20</sup>	4.45050×10 <sup>-26</sup>	3.82743×10 <sup>-20</sup>	1.51857×10 <sup>-22</sup>	1.18171×10 <sup>-19</sup>	1

1 cal= 4.18605J (計量法)  
= 4.184J (熱化学)  
= 4.1855J (15°C)  
= 4.1868J (国際蒸気表)  
仕事率 1 PS(仏馬力)  
= 75 kgf·m/s  
= 735.499W

放射能	Bq	Ci
	1	2.70270×10 <sup>-11</sup>
	3.7×10 <sup>10</sup>	1

吸収線量	Gy	rad
	1	100
	0.01	1

照射線量	C/kg	R
	1	3876
	2.58×10 <sup>-4</sup>	1

線量当量	Sv	rem
	1	100
	0.01	1

PROCEEDINGS OF THE FIRST JAERI-KANSAI INTERNATIONAL WORKSHOP ON ULTRASHORT-PULSE ULTRAHIGH-POWER LASERS AND SIMULATION FOR LASER-PLASMA INTERACTIONS JULY 14-18, 1997, KYOTO RESEARCH PARK, KYOTO, JAPAN